Decoherence and optical response of low-dimensional Bose gases

Rémy Vatré

Laboratoire Kastler Brossel — Collège de France

Thèse de doctorat de Sorbonne Université

préparée par

Rémy Vatré

Decoherence and optical response of low-dimensional Bose gases

---

Soutenue le 24 mai 2023 devant le jury composé de :

M. David Clément	Rapporteur
M. Christof Weitenberg	Rapporteur
Mme. Corinna Kollath	Examinatrice
M. Gwendal Fève	Président du jury
M. Jérôme Beugnon	Membre invité
M. Fabrice Gerbier	Directeur de thèse

Travail réalisé au laboratoire Kastler Brossel, au sein du Collège de France.

Abstract

In this manuscript, I present experimental studies on the interaction between ultracold quantum gases of bosons and resonant light. Ytterbium, with its two valence electrons, is an atom of choice for such quantum simulations because it has both a broad $^1S_0$–$^1P_1$ and a narrow $^1S_0$–$^3P_1$ intercombination line, commonly used for laser cooling.

In a first series of experiments, I study the decoherence of the gas induced by a controlled amount of light scattering. An ytterbium quantum gas is loaded into optical lattices and optically driven by resonant light addressing the intercombination transition. The many cycles of absorption and spontaneous emissions lead to momentum diffusion and thus decoherence, which I study through the momentum distribution of the gas. In the later stages of the dynamics, I observe a regime of algebraic decay of coherence resulting from the build-up of correlations. The early exponential regime of decoherence gives us information about the initial state of the system.

In a second series of experiments, an ytterbium quantum gas is loaded in a single plane of a large-period optical lattice, which realizes an effective two-dimensional system. This two-dimensional gas is probed in-situ using a high-resolution imaging system allowing a precise characterization of its thermodynamic properties. I characterize the optical response of such as system by measuring the transmission and the phase shift it imparts to light near resonance with the broad transition.

Résumé

Dans ce manuscrit, je présente des études expérimentales sur l'interaction entre des gaz quantiques ultrafroids de bosons et de la lumière résonante. L'ytterbium, avec ses deux électrons de valence, est un atome de choix pour de telles simulations quantiques car il possède à la fois une raie large $^1S_0$–$^1P_1$ et une raie d'intercombinaison étroite $^1S_0$–$^3P_1$, couramment utilisées pour le refroidissement laser.

Dans une première série d'expériences, j'étudie la décohérence du gaz induite par une quantité contrôlée de diffusion de lumière. Un gaz quantique d'ytterbium est chargé dans des réseaux optiques et la transition d'intercombinaison est excitée par de la lumière résonante. Les nombreux cycles d'absorption et d'émissions spontanées conduisent à de la diffusion en impulsion et donc à de la décohérence, ce que j'étudie à travers la distribution en impulsion du gaz. Aux temps longs de l'évolution du système, j'observe un régime de décohérence algébrique résultant de l'accumulation de corrélations. Le régime exponentiel de décohérence aux temps courts nous renseigne sur l'état initial du système.

Dans une deuxième série d'expériences, un gaz quantique d'ytterbium est chargé dans un seul plan d'un réseau optique de grand pas, ce qui réalise en pratique un système bidimensionnel. Ce gaz bidimensionnel est sondé in situ à l'aide d'un système d'imagerie à haute résolution permettant une caractérisation précise de ses propriétés thermodynamiques. Je caractérise la réponse optique d'un tel système en mesurant la transmission et le déphasage qu'il imprime à de la lumière proche de résonance avec la transition large.

Remerciements

Les bienfaits sont agréables tant que l'on peut s'en acquitter

Montaigne

Je veux donc remercier ici toutes celles et ceux à qui je suis redevable pour m'avoir accompagné, d'une manière ou d'une autre, pendant mes quatre années de thèse.

Tout d'abord, je tiens à remercier mes trois encadrants de thèse: Fabrice Gerbier, Jérôme Beugnon et Raphael Lopes. J'ai pour chacun d'entre vous un profond respect, à la fois scientifique et humain. Je vous suis extrêmement reconaissant pour tout ce que vous avez fait pour moi, et pour tout ce que j'ai appris auprès de vous.

Je souhaite également remercier chaleureusement les membres de mon jury, David Clément et Christoph Weitenberg pour avoir rapporté ma thèse, Corinna Kollath et Gwendal Fève pour avoir examiné pour travail.

Ce travail n'aurait bien sûr jamais été possible sans ceux qui m'ont précédé sur le projet Ytterbium. Je remercie particulièrement Raphaël Bouganne, Manel Bosch Aguilera et Alexis Ghermaoui, à qui je dois beaucoup pour m'avoir formé sur l'expérience avec une grande pédagogie et une aussi grande patience. J'espère avoir été à la hauteur de l'exemple que vous m'avez donné.

Si ma thèse n'a pas été une expérience solitaire, c'est avant tout grâce aux deux doctorants qui sont arrivés à peu près en même temps que moi: Chloé Maury et Aurélien Fabre. Je me souviendrais toujours de cette époque de nos vies avec un grand sourire, et vous y êtes certainement pour quelque chose. Mais vous n'avez pas été les seuls, et je remercie généralement tous ceux qui sont passés par le deuxième étage de l'Institut de Physique du Collège de France, et particulièrement Brice Bakkali-Hassani, Tanish Satoor, Alexandre Evrard, Édouard Le Cerf, Raphaël Saint-Jalm et Thomas Chalopin.

Je remercie toutes les équipes administratives et techniques, du Collège de France comme du Laboratoire Kastler Brossel, et notamment Carmen Toderasc. Merci également à ceux qui ont participé au suivi de ma thèse, Antoine Heidmann, Tarik Yefsah, et surtout mon parrain Romain Long.

Mille mercis à mes amis, ceux qui sont fêté ma soutenance avec moi et ceux qui n'ont hélas pas pu. Je pense particulièrement aux amis de la Botulus, où je me suis invité maintes et maintes fois, à Kenneth et Sooshin et nos longues sessions Zoom, à Sarah, à Jonathan et à Oliver.

Je dois beaucoup à mes parents pour leur soutien infaillible pendant toute ma scolarité, dont cette thèse est (enfin) l'aboutissement. Je remercie évidemment Flore et Paul, et j'ai une pensée particulière pour Mamie Nelly et Papy Michel. Et bien sûr, merci Thomas pour m'avoir accompagné toutes ces années.

Contents

Introduction

Quantum mechanics is about a century old and, thanks to extensive experimental and theoretical work, has risen to the status of a fully established theory with impressive predictive power for countless physical phenomena. Yet, to this day, quantum systems composed of a large number of particles often elude a complete physical understanding. High-temperature superconductivity is perhaps the most emblematic example of a phenomenon that continues to pose not only theoretical but also computational challenges, even for modern computers, because as the number of particles in a quantum system increases, the computational power required to describe it accurately grows exponentially. Many other quantum systems are at the heart of very active areas of current research, such as topological insulators (Hasan et al. 2010). In 1982, Richard Feynman proposed a new and complementary approach to study many-body quantum systems: *"Let the computer itsef be built of quantum mechanical elements which obey quantum mechanical laws"* (Feynman 1982). The general idea of this *quantum simulation* approach is to find a model quantum system that is equivalent to other quantum systems of interest, but more convenient for experimentalists. In concrete terms, it could be easier to tune some parameters with the model system, which would allow for a more fundamental understanding of the quantum system of interest.

Ultracold quantum gases are great tools for quantum simulation (Bloch et al. 2012) and rank among the leading model quantum systems along with trapped ions, superconducting qubits, and photonic quantum systems (Blatt et al. 2012, Houck et al. 2012, Aspuru-Guzik et al. 2012). In the 1970s and the 1980s, technological progress on lasers has enabled significant advances in the study of the interaction of light and matter. In particular, it led to the development of laser cooling, which, combined with various trapping techniques, realized dilute gases of neutral alkali atoms with temperature well below a mK. Nowadays, a wide variety of atoms, such as metastable noble gases (Vassen et al. 2012), alkaline-earth atoms (Stellmer et al. 2009), lanthanides (Lu et al. 2011), and a few others, have been cooled to ultracold temperatures, and the field of ultracold molecules is also rapidly growing (Carr et al. 2009). In 1995, bosons were evaporatively cooled to sufficiently low temperatures to form a new state of matter, a Bose-Einstein condensate (Anderson et al. 1995, Bradley et al. 1995, Davis et al. 1995). Predicted by Einstein (1924), this phase exhibits superfluid behavior, among many other interesting properties that have been studied extensively over the past three decades (Pitaevskii et al. 2003).

The physics of ideal and weakly-interacting quantum gases is largely described by relatively simple theoretical tools (Dalfovo et al. 1999, Giorgini et al. 2008). To simulate quantum many-body systems, there are numerous ways to enhance interactions and induce strong correlations in ultracold gases (Bloch et al. 2008). In particular, Feshbach resonances are an excellent way to control the strength of interactions and even access a unitary regime where

the interactions are as high as allowed by quantum scattering theory (Chin et al. 2010). Atoms with long-range dipolar interactions, such as erbium and dysprosium, have also been brought to quantum degeneracy (Aikawa et al. 2012), leading to experimental evidence of a supersolid phase, a superfluid phase with a spontaneously-broken translational invariance (Chomaz et al. 2022). Various schemes have also been proposed to simulate the fractional quantum Hall effect, which results from the interplay between interactions and orbital magnetism, with (neutral) ultracold atoms under an artificial magnetic field (Jaksch et al. 2003, Dalibard et al. 2011). One such scheme was the motivation to start the Ytterbium project in our group (Gerbier et al. 2010).

Another way to study many-body physics with ultracold gases is to increase the external confinement of the atoms. A two-dimensional gas can even obtained by freezing the atomic motion in one direction with strong external confinement, and a one-dimensional gas is obtained by freezing the atomic motion in two directions. For bosons in reduced dimensions (Petrov et al. 2004), traditional Bose-Einstein condensation is not possible in low dimensions. In two dimensions a superfluid transition still exists thanks to a mechanism theorized by Berezinskii, Kosterlitz and Thouless (Berezinsky 1972, Kosterlitz et al. 1973). A transition compatible with this mechanism was experimentally observed in an ultracold atomic gas by Hadzibabic et al. (2006). Quantum physics in one dimension is arguably even less intuitive than in two dimensions because of the increased role of fluctuations (Giamarchi 2003). Fortunately, many theoretical and computational tools are available to model one-dimensional quantum systems, from Luttinger liquid theory to exact methods such as the Bose-Fermi mapping and the Bethe ansatz (Cazalilla et al. 2011).

Strong confinement of the atoms is often achieved by trapping them in one node of periodic light trapping potentials, also known as optical lattices. By trapping one atom per node in three-dimensional optical lattices, one can perform controlled quantum simulations of popular condensed matter lattice models such as the Bose and Fermi-Hubbard models (Jaksch et al. 1998). In a seminal experiment, Greiner et al. (2002) probed the celebrated superfluid-to-Mott insulator transition for the first time. This observation has triggered an explosion of the field of quantum gases in optical lattices due to the wide range of physical models that can be studied, from the weakly to strongly-interacting regime, with bosons, fermions, or mixtures thereof (Gross et al. 2017). A remarkable experimental achievement in the field has been the quantum gas microscope, i.e. the detection of quantum gases in optical lattices with single site resolution (Bakr et al. 2009, Sherson et al. 2010). As an example, quantum gas microscopes have been instrumental to reveal the phenomenon of many-body localization (Abanin et al. 2019), an example of out-of-equilibrium quantum physics where thermalization is suppressed due to the interplay between interactions and disorder.

The interaction of matter and light is a topic that goes back to the origins of quantum mechanics (Einstein 1905). In the field of ultracold quantum gases, light is most commonly seen as the tool of choice for probing atomic properties. However, an equally interesting problem is how the response of a material system to light is affected by many-body effects. Both of these aspects of light-matter interaction are well suited to quantum simulation because of their complexity. For that purpose, ultracold quantum gases of alkaline-earth and alkaline earth-like atoms, such as strontium and ytterbium, make great quantum simulators because of the simplicity of their electronic structure compared to alkalis (Bromley et al. 2016).

The quantum description of light-matter interaction is related to the notion of open quantum systems. The system of interest $\mathcal{S}$ (e.g. trapped ultracold atoms) and the environment $\mathcal{E}$ (e.g. the electromagnetic field or untrapped atomic states) form a closed quantum system that is too complex to study in its full generality. If the environment $\mathcal{E}$ behaves under the right conditions, the evolution of the system of interest $\mathcal{S}$ can be studied on its own in a rather simple way through a quantum master equation (Haroche et al. 2006). The inter-

action of a quantum system with its environment is linked to quantum dissipation, and the interaction of an atomic system with a photon bath is a prime example that has been studied in great details (Dalibard et al. 1985, Cohen-Tannoudji et al. 1992). Shining resonant light on ultracold quantum gases generally results in losses and heating. If the system was cold enough to initially have some quantum coherence, the interaction with the electromagnetic environment gradually destroys this coherence as quantum information is transferred to the environment. Cavity quantum electrodynamics experiments have studied in detail the evolution of a single quantum particle in a controlled environment (Raimond et al. 2001, Blais et al. 2021), but the surface has only been scratched with respect to dissipation in many-body quantum systems.

It is essential to understand open quantum many-body systems in order to scale up quantum simulators. Moreover, open quantum many-body systems are themselves interesting subjects for quantum simulation, where the interplay of dissipation and interactions can lead to new phenomena. The role of interactions in the decoherence of an open system has been the subject of theoretical (Sieberer et al. 2016, Weimer et al. 2021) and experimental (Raitzsch et al. 2009, Baumann et al. 2010, Barreiro et al. 2011, Ates et al. 2012) efforts in recent years. For example, a celebrated phenomena pertaining to many-body quantum dissipation is the quantum Zeno effect, which is the inhibition of coherent dynamics under frequent measurements (Misra et al. 1977, Itano et al. 1990). The slowing down of atomic losses, which can be considered as an unread measurement of the atom number, has been observed experimentally in many experiments (Syassen et al. 2008, Barontini et al. 2013, Sponselee et al. 2018), including ours (Ghermaoui 2020).

The counterpart of the atomic response is the optical response, i.e. the effect of the atoms on the light. Typically, an atomic cloud absorbs and re-emits photons, thus scattering the probing electromagnetic field. The optical response of non-interacting particles can be computed easily (Born et al. 1999), but the physics is much more elusive when it comes to a dense medium (Guerin et al. 2017). In particular, the atoms can interact by exchanging photons, leading to dipole-dipole interactions (Morice et al. 1995). This leads to a broadening and a shift of the resonance line, as well as subradiance or superradiance (Guerin et al. 2016, Araújo et al. 2016, Roof et al. 2016, Corman et al. 2017, Jennewein et al. 2018). Due to conflicting experimental results in different geometries and with multilevel atoms, the state of the field is not entirely clear at this time, calling for a replication of collective scattering experiments using atoms with two-level transitions Bromley et al. (2016).

This manuscript reports on experiments carried out during my thesis at the Laboratoire Kastler Brossel at the Collège de France in Paris. We performed experiments on ultracold ytterbium quantum gases, on which we provide a theoretical and experimental background in Part I of this manuscript. More specifically, we successively studied the effect of near-resonant light on ultracold quantum gases of bosons in optical lattices, as detailed in Part II, and the effect of bulk two-dimensional quantum gases of ytterbium on near-resonant light, as detailed in Part III. The manuscript contains seven chapters, which are organized as follows:

Chapter 1 provides the theoretical tools on which we will rely throughout the manuscript. Starting with the basic description of weakly-interacting Bose-Einstein condensates in three dimensions, we then review the main features of the Bose gas in low dimensions. Finally, we present the basics of quantum gases in optical lattices, in particular in the framework of the Bose-Hubbard model.

Chapter 2 describes the experimental setup on which I worked during my thesis. The main aspects are the realization of three-dimensional Bose-Einstein condensates of ^{174}Yb, their characterization through time-of-flight absorption imaging, and their loading in three-

dimensional optical lattices. This chapter focuses particularly on the state of the experiment for the first two years of my thesis, which corresponds to the results presented in Chapters 3 to 5.

Chapter 3 provides more details on the physics of the one-dimensional Bose gas, in the continuum and on a lattice, which is essential for the experiments reported in Part II. Experimental data on the momentum distribution of one-dimensional bosons is analyzed using the theoretical tools introduced.

Chapter 4 presents a series of experiments showing the existence of an algebraic regime of decoherence at long times when a quantum gases of bosons in an optical lattice is subjected to many cycles of absorption and spontaneous emission by near-resonant light. In this chapter, we also give more details on open quantum systems and on the quantum description of spontaneous emission.

Chapter 5 demonstrates that the same decoherence experiment as in Chapter 4 can also be used as a probe for the initial state of the system by studying the short-time dissipative dynamics and applying quantum linear response theory to the open system. We benchmark this method by applying it to a quantum many-body system which is well understood at equilibrium, namely the one-dimensional Bose gas.

Chapter 6 describes the experimental improvements we have made to the setup midway through my thesis. These improvements include a new imaging system to probe the atoms in-situ with a high spatial resolution ($\approx 1\,\mu m$) and a large-period optical lattice to prepare a single two-dimensional Bose gas. This chapter provides detailed calibrations of the new experimental tools, as well as various perspectives for taking the experiment further.

Chapter 7 reports on a study of the optical response of a bulk two-dimensional Bose-Einstein condensate through a complete measurement of its complex transmission coefficient. The experimental data are compared with different theoretical approaches as well as with numerical simulations.

Part I

General features of bosonic quantum gases of ytterbium

CHAPTER 1

Theoretical background on ultracold bosonic gases

Introduction

During my thesis, we have studied ultracold quantum gases of bosons in a wide variety of configurations. Starting from three-dimensional Bose-Einstein condensates, we have studied Bose gases in one dimension, as discussed in Part II, and in two dimensions, as discussed in Part III. In addition, we have also studied quantum gases of bosons in periodic light potentials, also known as optical lattices. In this chapter, we aim to describe the many theoretical aspects related to the ultracold quantum gases studied in this manuscript. As the physics involved is very rich, we focus on the essential features.

In the first section, we focus on the description of a Bose-Einstein condensate in a harmonic trap and with weak contact interactions. We describe Bose gases in dimension $d = 3$ and derive the density distribution of a condensate with a mean-field formalism.

In the second section, we discuss Bose gases in low dimensions $d = 1$ or 2, where phase fluctuations play a more important role and true condensation is forbidden in the thermodynamic limit. Using first and second-order correlation functions, we highlight the essential differences coming from the reduction of dimensionality, and we describe the properties of the low-dimensional quasi-condensates.

In the third section, we focus on bosonic quantum gases in optical lattices. After a reminder on band theory, we derive the Bose-Hubbard Hamiltonian. This celebrated model describes bosons with on-site interactions in a single-band approximation and by considering a tight-binding regime. We then present some important features of the Bose-Hubbard model that are relevant to our experiments, in particular its phase diagram.

1.1 Weakly-interacting Bose-Einstein condensates in three dimensions

1.1.1 Introduction without interactions

In the absence of interactions, the behavior of a gas of N bosons is determined by the single-particle Hamilotnian

$$\hat{H}(\hat{\boldsymbol{r}}, \hat{\boldsymbol{p}}) = \frac{\hat{\boldsymbol{p}}^2}{2m} + V_{\text{trap}}(\hat{\boldsymbol{r}}), \tag{1.1.1}$$

where $V_{\text{trap}}(\boldsymbol{r})$ is a trapping potential that has a minimum in $r = 0$. In the thermodynamic limit ($N \to \infty$ at fixed density), the semi-classical phase-space density of a non-interacting Bose gas of temperature T and chemical potential $-\infty < \mu < V_{\text{trap}}(0)$ reads

$$\mathcal{W}(\boldsymbol{r}, \boldsymbol{p}) = \frac{1}{h^d} \frac{1}{\mathrm{e}^{\beta[H(\boldsymbol{r},\boldsymbol{p})-\mu]} - 1} = \frac{1}{h^d} \mathrm{Li}_0\Big(\mathrm{e}^{\beta[\mu - H(\boldsymbol{r},\boldsymbol{p})]}\Big) \tag{1.1.2}$$

with d the dimension, $\beta = 1/k_{\mathrm{B}}T$ and $\mathrm{Li}_\alpha(x) = \sum_n x^n/n^\alpha$, a so-called polylog function of order α (Bagnato et al. 1987, Castin 2001). In three dimensions (3D), integration over $\boldsymbol{p}$ yields

$$\mathcal{D}_{3\mathrm{D}}(x, y) \equiv n_{3\mathrm{D}}(\boldsymbol{r})\lambda_{\text{th}}^3 = \mathrm{Li}_{3/2}\Big(\mathrm{e}^{\beta[\mu - V_{\text{trap}}(\boldsymbol{r})]}\Big) < \mathrm{Li}_{3/2}(1) \tag{1.1.3}$$

where we have defined the thermal de Broglie wavelength $\lambda_{\text{th}} = h/\sqrt{2\pi m k_{\mathrm{B}} T}$ and the 3D atomic density $n_{3\mathrm{D}}$. Equation (1.1.3) implies that the atomic density $n_{3\mathrm{D}}$ is bounded from above as μ is increased towards $V_{\text{trap}}(0)$. To elucidate this apparently strange result, Einstein (1924) pointed out that for bosons the contribution of the single-particle ground state must be considered separately from that of the excited states even in the thermodynamic limit. Equation(1.1.3) then corresponds to the excited state density, which is bounded. This implies that, as μ is increased, the ground state density can increase without bounds. This leads

to the formation of a *Bose-Einstein condensate*, where a macroscopic number of atoms are condensing in the ground state.

Note that Bose-Einstein condensation does not exist in the thermodynamic limit in low dimensions at finite temperature. In the case of a 2D and 1D ideal gas, integration over $\boldsymbol{p}$ of the phase-space density yields

$$\mathcal{D}_{2D}(x,y) \equiv n_{2D}(x,y)\lambda_{th}^2 = \mathrm{Li}_1\Big(e^{\beta[\mu - V_{trap}(x,y)]}\Big) = -\ln\Big(1 - e^{\beta[\mu - V_{trap}(x,y)]}\Big), \tag{1.1.4}$$

$$\mathcal{D}_{1D}(x,y) \equiv n_{1D}(x)\lambda_{th} = \mathrm{Li}_{1/2}\Big(e^{\beta[\mu - V_{trap}(x,y)]}\Big), \tag{1.1.5}$$

which are not bounded from above.

1.1.2 Mean-field description

Interactions between atoms cannot be dismissed when the density becomes high enough to reach Bose-Einstein condensation. In most cases, the interactions are two-body and short-ranged, and the interaction potential can be modeled by

$$U(\boldsymbol{r}) = g_{3D}\delta(\boldsymbol{r}) \quad \text{with} \quad g_{3D} = \frac{4\pi\hbar^2 a}{m} \tag{1.1.6}$$

to reproduce the same scattering amplitude as the true potential (Dalibard 2021). The characteristic length a is called the s-wave scattering length.

For a gas of N bosons interacting pair-wise, we then consider the Hamiltonian

$$\begin{aligned}\hat{H} = &\int \mathrm{d}^3 r \left(\frac{\hbar^2}{2m}\nabla\hat{\Psi}^\dagger(\boldsymbol{r})\cdot\nabla\hat{\Psi}(\boldsymbol{r}) + \hat{\Psi}^\dagger(\boldsymbol{r})V_{trap}(\boldsymbol{r})\hat{\Psi}(\boldsymbol{r})\right) \\ &+ \frac{1}{2}\iint \mathrm{d}^3 r_1 \mathrm{d}^3 r_2\, \hat{\Psi}^\dagger(\boldsymbol{r}_1)\hat{\Psi}^\dagger(\boldsymbol{r}_2)U(\boldsymbol{r}_1 - \boldsymbol{r}_2)\hat{\Psi}(\boldsymbol{r}_2)\hat{\Psi}(\boldsymbol{r}_1).\end{aligned} \tag{1.1.7}$$

At zero temperature, the simple theoretical approach is a *classical field formalism*. This formalism is equivalent to a mean-field approximation describing the many-bound ground state as a product state

$$\Psi(\boldsymbol{r}_1, ..., \boldsymbol{r}_N) \simeq \psi(\boldsymbol{r}_1)...\psi(\boldsymbol{r}_N) \tag{1.1.8}$$

with the single-particle wavefunction ψ being the "classical field". The expectation value of the Hamiltonian is an energy functional $E[\psi]$, which is minimized by the solution of the *Gross-Pitaevskii equation*

$$-\frac{\hbar^2}{2m}\Delta\psi(\boldsymbol{r}) + V_{trap}(\boldsymbol{r})\psi(\boldsymbol{r}) + g_{3D}|\psi(\boldsymbol{r})|^2\psi(\boldsymbol{r}) = \mu_0\psi(\boldsymbol{r}). \tag{1.1.9}$$

The mean-field approximation is valid in the dilute and weakly-interacting regime, i.e. when the scattering length a is much smaller than the average distance between atoms. This condition is usually put in the form $n_{3D}a^3 \ll 1$.

Let us now consider the case of a BEC trapped by a harmonic potential with frequencies $(\omega_x, \omega_y, \omega_z)$. For each direction i, there are two lengths in the GP equation: the actual size of the cloud σ_i and the size of the single-particle ground state in the harmonic potential $a_{ho,i} = \sqrt{\hbar/m\omega_i}$, with $\sigma_i \geqslant a_{ho,i}$. The kinetic energy per atom within the mean-field approximation is on the order of

$$e_{kin} \sim \frac{\hbar^2}{2m\sigma_i^2} < \frac{\hbar^2}{2ma_{ho,i}^2} = \frac{\hbar\omega_i}{2}. \tag{1.1.10}$$

In the Thomas-Fermi limit $\mu_0 \gg \hbar\omega_i$, we neglect the kinetic term in equation (1.1.9). A 3D BEC can be described in the Thomas-Fermi limit for the three directions, and the density of the ground state is an inverted parabola

$$n_{3D}(\boldsymbol{r}) = N|\psi(\boldsymbol{r})|^2 = \max\left[\frac{\mu_0 - V_{\text{trap}}(\boldsymbol{r})}{g}, 0\right]. \tag{1.1.11}$$

This is equivalent to writing the thermodynamic equation $\mu_0 = g_{3D}n(\boldsymbol{r}) + V_{\text{trap}}(\boldsymbol{r})$, corresponding to a hydrodynamic equilibrium.

1.2 Weakly-interacting Bose gases in reduced dimensions

1.2.1 Mean-field description

We start by presenting the mean-field description of Bose-Einstein condensates in low dimensions. We mentioned earlier that true Bose-Einstein condensation does not exist in low dimensions, so the mean-field description cannot capture all the relevant physics. However, it already highlights a few important differences with the 3D case, and we will see in section 1.2.2 that it remains useful in certain conditions.

1.2.1.1 Effective interaction strength in low dimensions

For concreteness, we first consider a 2D harmonic trap

$$V_{\text{trap}}(\boldsymbol{r}) = V_{2D}(x, y) + \frac{1}{2}m\omega_z^2 z^2 \tag{1.2.1}$$

where $\omega_z \gg \omega_x, \omega_y$. We separate the dimensions in the ground state single-particle wavefunction

$$\psi(\boldsymbol{r}) = \phi(x, y)\chi_0(z). \tag{1.2.2}$$

At $T = 0$, the atoms occupy the ground state of the transverse harmonic oscillator, described by the transverse wavefunction χ_0. At finite temperature, the gas will be considered to be 2D if the transverse degrees of freedom are frozen, i.e. if $k_B T, |\mu| \ll \hbar\omega_z$ in 2D. The classical field energy minimization functional yields a 2D version of the Gross-Pitaevskii equation

$$-\frac{\hbar^2}{2m}\Delta\phi + g_{2D}|\phi|^2\phi = (\mu - V_{2D})\phi, \tag{1.2.3}$$

and in the Thomas-Fermi limit we write

$$n_{2D}(x, y) = \max\left[\frac{\mu - V_{2D}(x, y)}{g_{2D}}, 0\right]. \tag{1.2.4}$$

The 2D interaction strength g_{2D} reads

$$g_{2D} = g_{3D}\int \mathrm{d}z|\chi_0(z)|^4 = \frac{\hbar^2}{m}\frac{\sqrt{8\pi}a}{a_{\text{ho},z}}. \tag{1.2.5}$$

In 1D, the same procedure can be applied with $\psi(\boldsymbol{r}) = \phi(x)\chi_0(y, z)$. The main difference is that the 1D interaction strength reads

$$g_{1D} = g_{3D}\iint \mathrm{d}y\mathrm{d}z|\chi_0(y, z)|^4 = 2\hbar\omega_\perp a. \tag{1.2.6}$$

Note that the existence of 2D and 1D interaction strengths g_{2D} and g_{1D} does not imply that the kinematics of the collisions are 2D or 1D in our gas: the scattering length a and the range of the interactions remain small compared to $a_{\mathrm{ho},z}$ and $a_{\mathrm{ho},\perp} = \sqrt{\hbar/m\omega_\perp}$. For this reason, the kinematics of the collisions remain 3D and our systems should be called more rigorously *quasi-two/one-dimensional* gases (Petrov et al. 2000; 2001). We will not use this denomination for the sake of simplicity.

1.2.1.2 Dimensionless interaction parameter

In all dimensions, it is convenient to define a dimensionless interaction parameter which compares the kinetic energy and the interaction energy in order to separate the weakly and the strongly-interacting regime. In dimension d and at $T = 0$, the typical length is the mean interparticle distance $n_{d\mathrm{D}}^{1/d}$. In order to form a dimensionless parameter, it is common to compare the mean-field interaction energy $g n_{d\mathrm{D}}$ with the kinetic energy of a strongly-interacting system $\sim \hbar^2 n_{d\mathrm{D}}^{2/d}/2m$. The dimensionless parameters in all dimensions are reported in table 1.1.

Dimension	3D	2D	1D
Name		$\tilde{g}$	γ
$E_{\mathrm{int}}/E_{\mathrm{kin}}$	$2\pi n_{3\mathrm{D}}^{1/3} a$	$\sqrt{8\pi} a/a_{\mathrm{ho},z}$	$2a/(a_\perp^2 n)$

Table 1.1: Dimensionless interaction parameter in all dimensions.

The different dimensionless interaction parameters scale differently with the density. In 3D we recognize the weakly-interacting condition $n_{3\mathrm{D}} a^3 \ll 1$. In 2D, the dimensionless interaction parameter $\tilde{g}$ is independent of the density, a consequence of the scale invariance of a quasi-2D gas with weak contact interactions (Saint-Jalm et al. 2019). In 1D, the kinetic energy increases more rapidly than the interaction energy when the density is increased. Counter-intuitively, this means that the strongly-interacting regime can be achieved by reducing the 1D density (Olshanii 1998).

1.2.2 Quasi-condensates and quasi-long-range order

As we mentioned, the mean-field approach is far from a complete description of low dimensional Bose gases. Indeed, the general Mermin–Wagner–Hohenberg theorem states that, in dimension $d \leqslant 2$, no continuous symmetry can be spontaneously broken for a finite-temperature system with short-range interactions (Mermin et al. 1966, Hohenberg 1967). This implies that true Bose-Einstein condensation does not exist in the thermodynamic limit in low dimensions. In order to complete our description of low-dimensional Bose gases, we need to introduce correlation functions and the notion of quasi-condensates and of quasi-long-range order.

The commonly accepted criterion for true Bose-Einstein condensation is that the first-order correlation function

$$g_1(\boldsymbol{r}) = \frac{\langle \hat{\Psi}^\dagger(\boldsymbol{r})\hat{\Psi}(0)\rangle}{\langle \hat{\Psi}^\dagger(0)\hat{\Psi}(0)\rangle} \tag{1.2.7}$$

has a finite value at infinite distance, following a proposal by Penrose et al. (1956). This property is called long-range order, and is verified for ideal and weakly-interacting 3D BECs.

We now go beyond the classical field description and introduce the quantum field

$$\hat{\Psi} = \mathrm{e}^{\mathrm{i}\hat{\theta}}\sqrt{n + \delta\hat{n}}, \tag{1.2.8}$$

where $\delta\hat{n}$ and $\hat{\theta}$ describe the density and phase fluctuations respectively. Density fluctuations are captured by the second-order correlation function

$$g_2(\boldsymbol{r}) = \frac{\langle n(\boldsymbol{r})n(0)\rangle}{n^2} \tag{1.2.9}$$

As a result of bunching and anti-bunching, $g_2(0) = 2$ for an ideal gas of bosons above condensation and $g_2(0) = 0$ for an ideal gas of fermions (Jeltes et al. 2007). For a weakly-interacting gas of bosons at low temperature $k_B T \ll \mu$, $g_2 \to 0$ on a scale l_c on the order of the healing length ξ. On larger length scales $r \gg l_c$, the density fluctuations are suppressed ($g_2(0) - 1 \ll 1$). Taking $\delta\hat{n} = 0$ in equation (1.2.8), the quantum field can be approximated as

$$\hat{\phi} \simeq \sqrt{n}\exp\left(\mathrm{i}\hat{\theta}\right). \tag{1.2.10}$$

Such a system with a fluctuating phase but no density fluctuations is called a *quasi-condensate*. The first-order correlation function is dominated by phase fluctuations

$$g_1(\boldsymbol{r}) \simeq \exp\left[-\frac{1}{2}\langle\hat{\theta}(\boldsymbol{r}) - \hat{\theta}(0)\rangle^2\right]. \tag{1.2.11}$$

A complete theoretical formalism to describe quasi-condensates is discussed in Mora et al. (2003) and Castin (2004).

The singularity of the 2D case is the existence of a genuine phase transition to a superfluid state, called the Berezinskii–Kosterlitz–Thouless (BKT) transition (Berezinsky 1972, Kosterlitz et al. 1973). Just above the critical point T_c of this transition, the gas does not possess long-range or quasi-long-range order: the first-order correlation function decays exponentially. Below T_c, we observe the apparition of bound pairs of vortices which result in an algebraic decay of the first-order correlation function

$$g_1(r) \simeq \left(\frac{r}{\lambda_{\mathrm{th}}}\right)^{-\alpha}, \tag{1.2.12}$$

which is called quasi-long-range order. The exponent α is the inverse of the phase-space density of the superfluid fraction which appears at $T < T_c$. Finally, at zero temperature, there is a true condensate and the first-order correlation function has a finite value at infinite distance. Strictly speaking, the result 1.2.12 holds only in the thermodynamic limit. For a finite 2D system at finite temperature, quasi-long range order leads to a true BEC if the thermal length is much larger than the system size

$$\lambda_{\mathrm{th}} \gg L. \tag{1.2.13}$$

In 1D, there is no phase transition. Even at zero temperature, a 1D system only exhibits quasi-long-range order

$$g_1(x) \simeq \left(\frac{|x|}{\xi_{1\mathrm{D}}}\right)^{-\sqrt{\gamma}/2\pi}, \tag{1.2.14}$$

where $\xi_{1\mathrm{D}} = n/\sqrt{2\gamma}$ is the 1D healing length. At finite temperature T, the asymptotic behavior of $g_1(x)$ is an exponential decay

$$g_1(x) \simeq \exp\left(-\frac{|x|}{l_\phi}\right), \tag{1.2.15}$$

where we have defined a phase coherence length

$$l_\phi = \frac{2\hbar^2 n}{m k_B T}. \tag{1.2.16}$$

Nevertheless, true condensation is possible for a finite 1D system if the phase coherence length is much larger than the thermal length

$$l_\phi \gg \lambda_{\mathrm{th}} \gg L. \tag{1.2.17}$$

Indeed, the first-order correlation function still has finite values over the finite sample in this case.

1.3 Ultracold bosons on optical lattices

We now turn to the physics of bosonic quantum gases loaded in periodic light potentials known as optical lattices, an experimental tool that we will use throughout this manuscript and in particular in Part II. The standing wave obtained by retroreflecting an off-resonant laser beam creates, via the dipole force, a periodic potential of the form

$$V_{\mathrm{L}}(x) = V_0 \sin^2(k_{\mathrm{L}} x), \tag{1.3.1}$$

with period $d = \pi/k_{\mathrm{L}} = \lambda/2$, as sketched in figure 1.1.

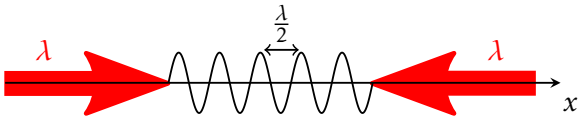

Figure 1.1 Sketch of the interference of two counter-propagating plane waves. The resulting standing plane wave of period $d = \lambda/2$ forms a 1D lattice potential.

1.3.1 Reminder on band theory

The Hamiltonian of an atom in a 1D optical lattice,

$$\hat{H} = \frac{\hat{p}^2}{2m} + V_{\mathrm{L}}(\hat{x}), \tag{1.3.2}$$

commutes with the translation operator $\hat{T}_d = \exp(\mathrm{i}\hat{p}d/\hbar)$. The eigenstates of the Hamiltonian obey Bloch theorem

$$\phi_{n,q}(x) = \mathrm{e}^{\mathrm{i}qx} u_{n,q}(x), \tag{1.3.3}$$

where q is the quasi-momentum. We restrict q to the first Brillouin zone (BZ1) $(-k_{\mathrm{L}}, k_{\mathrm{L}}] = (-\pi/d, \pi/d]$. q is quantized in a finite system with periodic boundary conditions. $u_{n,q}$ is called a Bloch function and is periodic with period d.

The energy spectrum splits into allowed energy bands, corresponding to the eigenenergies $E_n(q)$ of the eigenstates $\phi_{n,q}$, and forbidden regions. n corresponds to the band number in the energy spectrum, with $n = 0$ corresponding to the ground band. The first three energy bands are shown in figure 1.2 for different lattice depths V_0. In the free space limit ($V_0 = 0$), the band structure is obtained by "folding" the kinetic energy parabola. As the lattice gets deeper, gaps open at the crossing points $\pm k_{\mathrm{L}}$ and the bands progressively become flatter.

To describe efficiently interacting systems, it is convenient to introduce the Wannier functions. They are defined from the Bloch waves $\phi_{n,q}(x)$ by a Fourier transform

$$w_n(x - x_i) = \frac{1}{\sqrt{N_{\mathrm{s}}}} \sum_{q \in \mathrm{BZ1}} \mathrm{e}^{-\mathrm{i}qx_i} \phi_{n,q}(x). \tag{1.3.4}$$

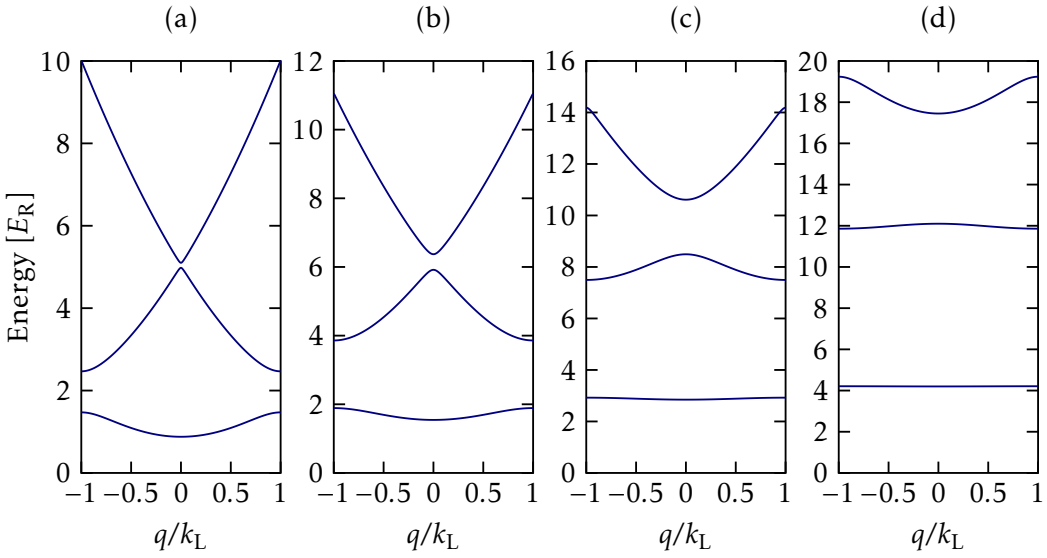

Figure 1.2 Band structure of a 1D lattice for (a) $V_0 = 2E_R$, (b) $V_0 = 4E_R$, (c) $V_0 = 10E_R$, and (d) $V_0 = 20E_R$. Only the first three bands are shown.

where N_s is the number of sites. Like Bloch functions, Wannier functions form an orthonormal basis of the Hilbert space and describe position eigenstates, while Bloch functions describe momentum eigenstates. The Wannier function of the ground and first excited bands are shown in figure 1.3. The Hamiltonian is not diagonal in the Wannier basis and reads

$$\hat{H} = -\sum_{n,i,j} J_n(i-j)|w_{n,i}\rangle\langle w_{n,j}|, \tag{1.3.5}$$

where the matrix elements $J_n(i-j)$ are defined as

$$J_n(i-j) = \int \mathrm{d}x w_n^*(x-x_j)\left(\frac{\hbar^2\nabla^2}{2m} - V_L(x)\right)w_n(x-x_i). \tag{1.3.6}$$

As shown in figure 1.3, the Wannier functions become more localized around the sites as the lattice depth is increased. The overlap between neighbouring Wannier functions is therefore small for deep enough lattices. In the tight-binding limit, we only consider the first two terms $J_n(0)$ (the mean energy of the band) and $J_n(1)$ (the nearest-neighbour tunnelling). We discuss the regime of validity of this approximation below.

We are interested in the behavior of a quantum gas of bosons in an optical lattice. In 3D, the band theory applies with a vector band number $\boldsymbol{n}$. Assuming the atoms are cold enough so that the ground band can be adiabatically loaded, we neglect all excited bands $n_{x/y/z} \neq 0$. Then, we assume that the lattice is deep enough to consider the tight-binding limit $J_0(1) \gg J_0(i>1)$. By redefining the energy so that $J_0(0) = 0$, we obtain a tight-binding Hamiltonian

$$\hat{H} = -J\sum_m \left(\hat{a}_{m+1}^\dagger \hat{a}_m + \hat{a}_m^\dagger \hat{a}_{m+1}\right), \tag{1.3.7}$$

where $J \equiv J_0(1)$ and the operator $\hat{a}_m^\dagger$ creates an atom in the Wannier function localized at site m (in the ground band). In momentum space, the Bloch wavefunction annihilation operator reads

$$\hat{a}_q = \frac{1}{\sqrt{N_s}}\sum_m \mathrm{e}^{\mathrm{i}mqd}\hat{a}_m. \tag{1.3.8}$$

In the Bloch basis, the tight-binding Hamiltonian is diagonal and reads $\hat{H} = \sum_q \mathcal{E}_q \hat{a}_q^\dagger \hat{a}_q$. The eigenenergies take the simple form $\mathcal{E}_q = -2J\cos qd$.

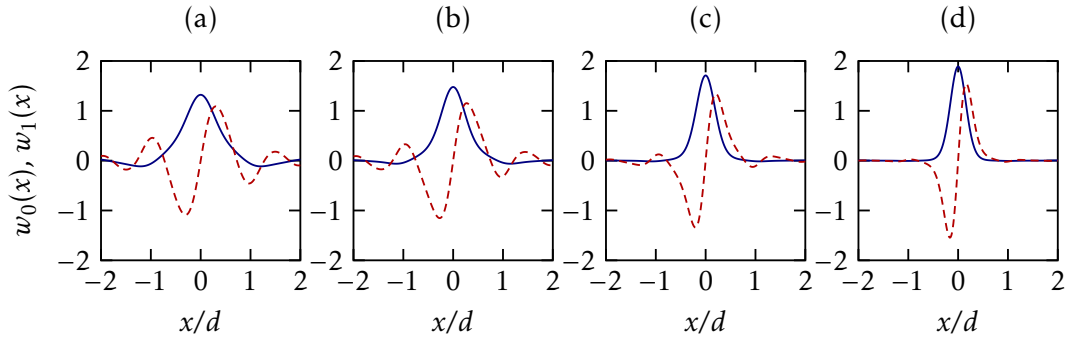

Figure 1.3 Wannier functions of a 1D lattice for (a) $V_0 = 2E_R$, (b) $V_0 = 4E_R$, (c) $V_0 = 10E_R$, and (d) $V_0 = 20E_R$. We show Wannier function of the ground band (solid line) and the first excited band (dashed line).

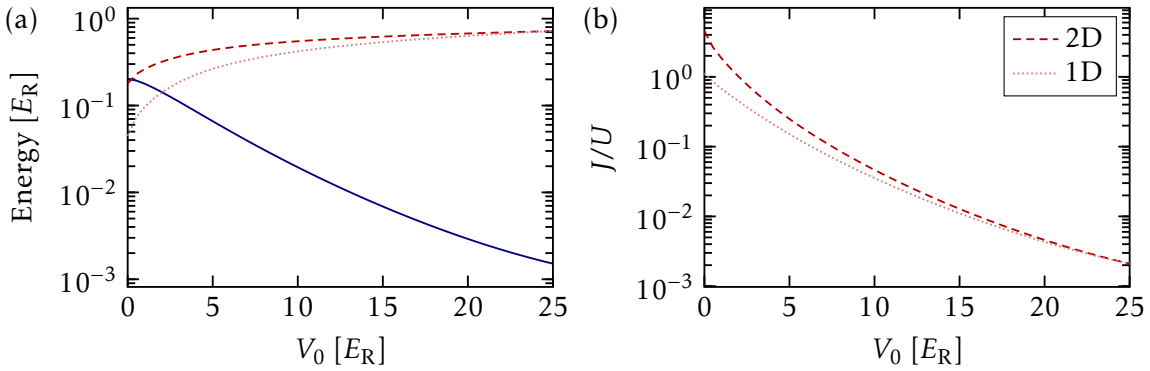

Figure 1.4 (a) Energy scales of the Bose-Hubbard model, in units of the recoil energy E_R. The solid line corresponds to J as a function of V_0. The dashed line corresponds to U for a 2D lattice such that $V_x = V_y = V_0$ and $V_z = 27E_R$. The dotted line corresponds to U for a 1D lattice such that $V_x = V_0$, $V_y = 25E_R$ and $V_z = 27E_R$. (b) J/U, with the same conventions.

1.3.2 Bose-Hubbard model

1.3.2.1 On-site interactions

We want to add interactions between the bosons to the single-band tight-binding model. In second quantization, the contact-interaction Hamiltonian reads

$$\hat{H}_{\text{int}} = \frac{g}{2}\int \mathrm{d}\boldsymbol{r}\hat{\Psi}^\dagger(\boldsymbol{r})\hat{\Psi}^\dagger(\boldsymbol{r})\hat{\Psi}(\boldsymbol{r})\hat{\Psi}(\boldsymbol{r}), \tag{1.3.9}$$

where $\hat{\Psi}(\boldsymbol{r})$ annihilates an atom at position $\boldsymbol{r}$ and g is the interaction strength in the dimension of the problem. In the single-band approximation and tight-binding limit, we write the field operator as $\hat{\Psi}(\boldsymbol{r}) = \sum_m w(\boldsymbol{r}-\boldsymbol{r}_m)\hat{a}_m$, yielding

$$\hat{H}_{\text{int}} = \sum_{mnlp}\frac{U_{mnlp}}{2}\hat{a}_m^\dagger\hat{a}_n^\dagger\hat{a}_l\hat{a}_p. \tag{1.3.10}$$

We consider only the dominant term $m = n = l = p$ corresponding to on-site interactions

$$U \equiv U_{mmmm} = g\int \mathrm{d}\boldsymbol{r}|w(\boldsymbol{r})|^4. \tag{1.3.11}$$

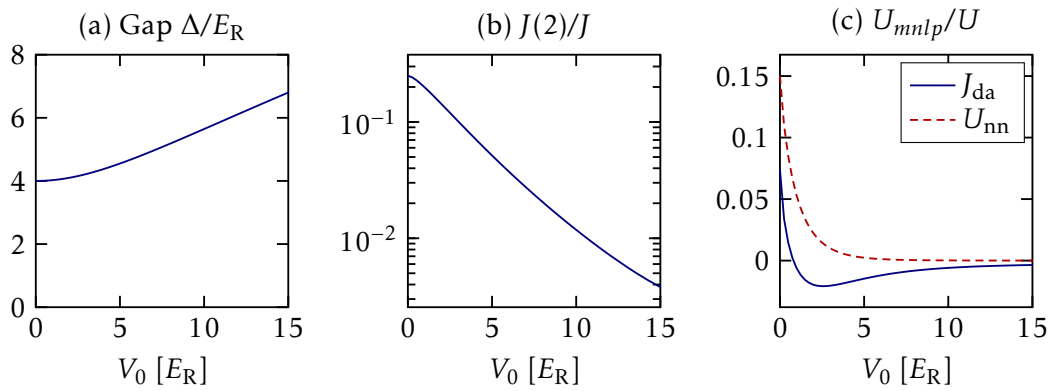

Figure 1.5 Validity of the Bose-Hubbard model as a function of the lattice depth. (a) Gap Δ (solid line). (b) Validity of the tight-binding approximation with $J(2)/J$. (c) Validity of the on-site interaction model: J_{da}/U (solid line) and U_{nn}/U (dashed line).

We discuss the regime of validity of this approximation below. Finally, we obtain the Bose-Hubbard Hamiltonian

$$\hat{H}_{BH} = -J\sum_m (\hat{a}^\dagger_{m+1}\hat{a}_m + \hat{a}^\dagger_m\hat{a}_{m+1}) + \frac{U}{2}\sum_m \hat{n}_m(\hat{n}_m - 1). \tag{1.3.12}$$

The energy scale U and J are usually expressed in units of the recoil energy $E_R = \hbar^2 k_L^2/2m$, the natural energy unit arising for a periodic potential of period π/k_L.

1.3.2.2 Validity of the Bose-Hubbard model

Let us discuss in this subsection the validity of the Bose-Hubbard model. First, to study the validity of the single-band approximation, we show in figure 1.5(a) the gap, defined as $\Delta = E_1(q=0) - E_0(q=0)$, as a function of the lattice depth. We observe that $\Delta > 4E_R$, and we will see later that the chemical potential in our 1D Bose-Hubbard systems is on the order of $0.1E_R$. We can thus use band theory in a single-band approximation even if there is no lattice for 1D gases.

Then, to study the validity of the tight-binding approximation, we show in figure 1.5(b) the next-nearest-neighbor tunneling term $J(2)$ in units of the nearest-neighbor tunneling term $J \equiv J(1)$. We observe that the tight-binding approximation is valid up to 10% for $V_0 \simeq 3.0E_R$.

We now turn to the validity of the on-site interaction model. The leading terms U_{mnlp} (after $U \equiv U_{mmmm}$) in the interacting Hamiltonian from equation (1.3.10) are the following:

- If one index is different (e.g. $m = n = l = p \pm 1$), we obtain a density-assisted tunnelling Hamilonian

$$\hat{H}_{da} = \sum_m J_{da}\hat{a}^\dagger_m(\hat{n}_m + \hat{n}_{m+1})\hat{a}_{m+1} \quad \text{with} \quad J_{da} = g\int d\boldsymbol{r} w^*(\boldsymbol{r})|w(\boldsymbol{r})|^2 w(\boldsymbol{r} + d\boldsymbol{e}_x). \tag{1.3.13}$$

  We show J_{da}/U as a function of the lattice depth in figure 1.5(c).

- If two indices are different and $m = n = l \pm 1 = p \pm 1$, we obtain a nearest-neighbor interaction Hamiltonian

$$\hat{H}_{nn} = \sum_m \frac{U_{nn}}{2}\hat{n}_m\hat{n}_{m+1} \quad \text{with} \quad U_{nn} = g\int d\boldsymbol{r}|w(\boldsymbol{r})|^2|w(\boldsymbol{r} + d\boldsymbol{e}_x)|^2. \tag{1.3.14}$$

  We show U_{nn}/U as a function of the lattice depth in figure 1.5(c).

χ	$J(2)/J$	J_{da}/U	U_{nn}/U
$V_0(\chi = 0.1)\ [E_{\mathrm{R}}]$	3.0	0	0.3
$V_0(\chi = 0.01)\ [E_{\mathrm{R}}]$	10.6	0.6	3.0

Table 1.2: Validity limits of the Bose-Hubbard model: for a lattice depth V_0 greater than $V_0(\chi = x)$, the validity parameter χ is smaller than x. We consider $x = 10\%$ and $x = 1\%$.

- If two indices are different and $m = l = n \pm 1 = p \pm 1$, we obtain a cotunnelling Hamiltonian
$$\hat{H}_{\mathrm{co}} = \sum_m \frac{J_{\mathrm{co}}}{2} \hat{a}_m^{\dagger 2} \hat{a}_{m+1}^2 \quad \text{with} \quad J_{\mathrm{co}} = g \int \mathrm{d}\boldsymbol{r} w^*(\boldsymbol{r})^2 w(\boldsymbol{r} + d\boldsymbol{e}_x)^2. \tag{1.3.15}$$
We have $U_{\mathrm{nn}} = J_{\mathrm{co}}$ if the Wannier functions are chosen to be real, which is why we do not show the cotunneling coefficient in figure 1.5(c).

In table 1.2, we compile the validity limits of the different approximations of the Bose-Hubbard model. We observe that the most limiting approximation is the tight-binding approximation. The on-site interaction approximation is valid for lattice depths that are an order of magnitude smaller. However, note that, although in low dimensions the single-band approximation is not the most limiting approximation, this is not necessarily true in 3D where typically $\mu \sim E_{\mathrm{R}}$.

1.3.3 Phase diagram of a uniform system

1.3.3.1 Two phases

By taking the opposite limits $J = 0$ and $U = 0$, we can see that (at least) two phases can exist in the Bose-Hubbard model Zwerger (2003). In the non-interacting limit $U = 0$, the ground state is an ideal Bose-Einstein condensate. This phase is well-described by a product of coherent states over the sites i
$$|\Psi_{\mathrm{SF}}\rangle = \prod_i \sum_n \mathrm{e}^{-|\alpha|^2/2} \frac{\alpha^n}{\sqrt{n!}} |n\rangle_i . \tag{1.3.16}$$
For small but finite U, this phase is called the superfluid phase. In the opposite limit $J = 0$, also known as the atomic limit, there is no phase correlation between the sites and the ground state is a product of Fock states
$$|\Psi_{\mathrm{MI}}\rangle = \prod_i |\bar{n}\rangle_i . \tag{1.3.17}$$
This phase is called the Mott insulator and has an integer filling $\bar{n}$ (note that the filling and the density are simply related by $\bar{n} = nd^D$ where d is the lattice spacing and D is the dimension).

For an arbitrary J/U, the Bose-Hubbard model cannot be solved analytically. However, the phase diagram of the Bose-Hubbard model has been extensively studied by numerical approaches, including quantum Monte Carlo (QMC) and density matrix renormalization group (DMRG) techniques (Pollet 2012, Kühner et al. 1998). In this manuscript, we focus on 2D square and 1D lattice Bose-Hubbard models. In the rest of this section, we show that it can be well captured with simple theoretical tools, but also that two slightly different approaches must be used in 2D and 1D respectively.

A Bose gas in a lattice in the superfluid regime retains the phase coherence properties of the BEC: the first-order correlation function has a finite value at infinite distance in the thermodynamic limit and in 3D. In the Mott insulating regime however, the first-order correlation function decays exponentially (Zwerger 2003). In the next chapter, we will see how

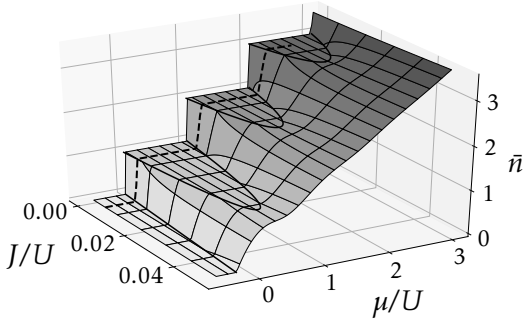

Figure 1.6 Phase diagram of the 2D Bose-Hubbard model at $T = 0$, calculated by numerically minimizing the Gutzwiller energy. The dashed line corresponds to the density profile in the local density approximation.

the disappearance of long-range order can be probed experimentally in time-of-flight experiments (Greiner et al. 2002). Higher-order correlations are still present in a Mott insulator, and can be probed in quantum gas microscopes accessing the density distribution of 2D lattices (Bakr et al. 2009, Sherson et al. 2010).

1.3.3.2 Mean-field approach

In two (or higher) dimensions, the ground state of the Bose-Hubbard Hamiltonian can be qualitatively captured by a factorization ansatz called the Gutzwiller wavefunction

$$|\Psi_G\rangle = \prod_i \sum_n c(n)|n\rangle_i . \tag{1.3.18}$$

where $|n\rangle_i$ is a Fock state where n atoms are present on site i. The Gutzwiller wavefunction interpolates between the ground states in the opposite limits $J = 0$ and $U = 0$, given in equation (1.3.16) and equation (1.3.17).

For a given chemical potential μ, numerical minimization of the Gutwiller free energy $\langle\Psi_G|\hat{H}_{BH} - \mu\sum_i \hat{n}_i|\Psi_G\rangle$ gives access to the density for any $(J/U, \mu/U)$ through

$$\bar{n} = \sum_n n|c(n)|^2. \tag{1.3.19}$$

We obtain the phase diagram shown in figure 1.6(a) for an isotropic 2D square lattice. We observe characteristic lobes corresponding to Mott insulators with filling $\bar{n} \in \mathbb{N}^*$. In the rest of the phase diagram, the gas is in the superfluid phase. The phase diagram is qualitatively the same in one dimension, and we discuss the quantitative differences in Chapter 3.

1.3.4 Non-uniform system in the local density approximation

The laser beams creating lattice potentials are not plane waves and typically have a Gaussian shape, as discussed in the next chapter. Approximating the Gaussian envelope with a harmonic $V_{trap}(\boldsymbol{r}) = \kappa(x^2 + y^2)$, we write

$$\hat{H}'_{BH} = \hat{H}_{BH} + \hat{V}_{trap} \quad \text{with} \quad \hat{V}_{trap} \simeq \sum_m \kappa \boldsymbol{r}_m^2 \hat{a}_m^\dagger \hat{a}_m. \tag{1.3.20}$$

If $V_{trap}(\boldsymbol{r})$ is weak enough, Bloch theorem remains a good approximation and we can apply a local density approximation. In the grand-canonical ensemble, we associate a chemical potential $\mu'(\boldsymbol{r}) = \mu_0 - V(\boldsymbol{r})$ to any point $\boldsymbol{r}$ and write

$$K'_{BH} = H'_{BH} - \mu_0 N = H_{BH} - \mu' N. \tag{1.3.21}$$

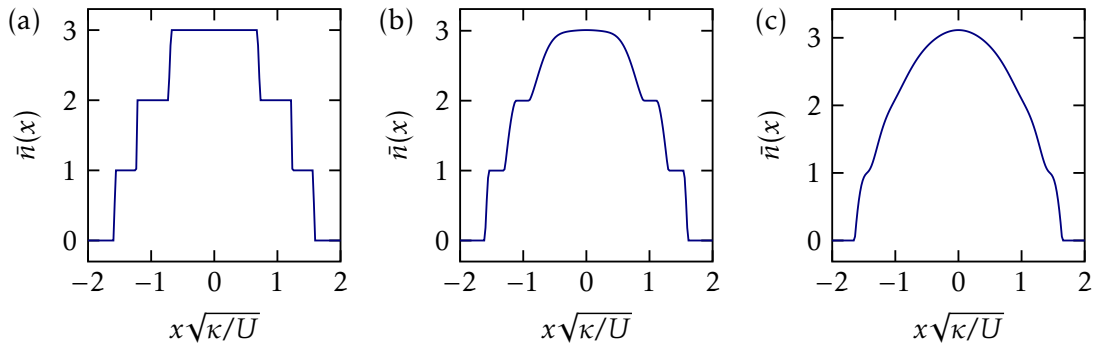

Figure 1.7 (a-c) Shell structure for a 2D trapped Mott insulator at $T = 0$ for $\mu_0/U = 2.5$: (a) $J/U = 0.002$, (b) $J/U = 0.02$, and (c) $J/U = 0.2$. The behavior is qualitatively the same in 1D. $\sqrt{U/\kappa}$ is the typical distance set by the external trapping potential.

The density profile can then be deduced by using the uniform phase diagram, as shown in figure 1.6(a) with a dashed line. We find that the density profile resembles a Thomas-Fermi profile in the superfluid regime, and exhibits a characteristic shell-like structure in the Mott insulating phase, as shown in figure 1.7(b-d).

Conclusion

In this chapter, we have presented the essential theoretical tools for this manuscript. After introducing the notion of Bose-Einstein condensation with the ideal gas, we have presented the mean-field formalism describing a zero temperature weakly-interacting 3D Bose-Einstein condensate. We then turned to the description of low-dimensional Bose gases ($d = 2$ and 1). After highlighting the differences in the mean-field approach, we have described the correlation properties of low-dimensional Bose gases, with the emphasis on the differences between 2D and 1D. We explained that true Bose-Einstein condensation does not exist in low dimensions, but we presented the notions of quasi-Bose-Einstein condensates and of quasi-long-range order, which allows us to retrieve condensation for finite systems. Finally, in a third part, we focused on the behavior of bosons in periodic trapping potentials, also known as optical lattices. We presented the essential aspects of band theory, and made two key approximations to derive the Bose-Hubbard Hamiltonian: a single-band approximation and a tight-binding limit. Finally, we described the phase diagram of the Bose-Hubbard model, its ground state for a harmonically-trapped system, and the correlation properties of the two phases: the superfluid phase and the Mott insulating phase.

CHAPTER 2

Experimental background on ultracold bosonic ytterbium

Introduction

In this chapter, we present the experimental apparatus on which I have performed the experiments reported in this thesis. The control and maintenance of this complex machine is an important part of the experimental work. The aim of this chapter is to present some key specificities of this experiment, and not an exhaustive account of laser cooling and trapping (Metcalf et al. 1999), experimental realization of Bose-Einstein condensates (Ketterle et al. 1999) or quantum gases in optical lattices (Bloch et al. 2008). More technical details can be found in the theses of my predecessors (Scholl 2014, Dareau 2015, Bouganne 2018, Bosch Aguilera 2019, Ghermaoui 2020).

In section 2.1, we present the relevant properties of the Ytterbium atom. We introduce the two important electronic transitions, the $\lambda_b = 399\,\text{nm}$ transition with a broad linewidth, which we call the "blue transition", and the $\lambda_g = 556\,\text{nm}$ transition with a narrow transition, which we call the "green transition". We use lasers close to the blue and green resonances to cool down and detect the atoms. We also describe how we can trap the atoms in light potentials created by lasers far off resonance. In these *optical traps*, the depth of the trap is related to the intensity of the light and to the atomic polarizability (Grimm et al. 2000). We show calculations for the latter (Dzuba et al. 2010).

In section 2.2, we detail the various stages of the experimental sequence to produce Bose-Einstein condensates (BECs) of Yb, the starting point for all subsequent experimental studies in this manuscript. The main steps of the experimental sequence are as follow. In a ultra-high vacuum system, we first slow down the atomic beam from an Yb oven with a Zeeman slower, so that it can be trapped and cooled in a magneto-optical trap. The Yb gas is then transferred to a crossed optical dipole trap. Evaporative cooling is used to increase the phase-space density to reach Bose-Einstein condensation.

In section 2.3, we describe time-of-flight absorption imaging, the method used to probe the atoms at the end of each experimental realization. This technique gives us access to the momentum distribution of the trapped cloud [at least when interactions can be neglected (Castin et al. 1996, Gerbier et al. 2008)], integrated along the line of sight of the imaging system. We describe absorption imaging in the experimentally relevant low-intensity limit and for dilute gases. The case of optically dense gases will be discussed further in Chapter 7. We also explain how the images are processed with a "best-reference picture" algorithm to improve the atom detection (Ockeloen et al. 2010).

Finally, in section 2.4, we describe the loading of Yb Bose-Einstein condensates into a cubic optical lattice to realize stacks of 2D or 1D Bose-Hubbard systems. The optical setup as well as the loading sequence are detailed. We also present a brief discussion of the experimental studies of the 2D and 1D superfluid to Mott insulator transitions.

2.1 Properties of the Yb atom

Ytterbium is a lanthanide with atomic number 70, usually found as a solid metal. It is an alkaline-earth-like atom, which means that it has complete inner shells and a complete s outer shell with two electrons. Bosonic ^{174}Yb, which is used in this manuscript, is the most abundant isotope, while ^{173}Yb is the most abundant fermionic isotope.

2.1.1 Relevant electronic transitions of ^{174}Yb

The low-energy electronic structure of ^{174}Yb is shown in figure 2.1, with the wavelength and linewidth of the relevant electronic transitions. We use the spectroscopic notation $^{2S+1}\mathrm{L}_J$, where S is the total electronic spin, L is the total electronic orbital momentum and $J = \mathrm{L} + S$ is the total electronic angular momentum. The nuclear spin I is always zero for bosonic

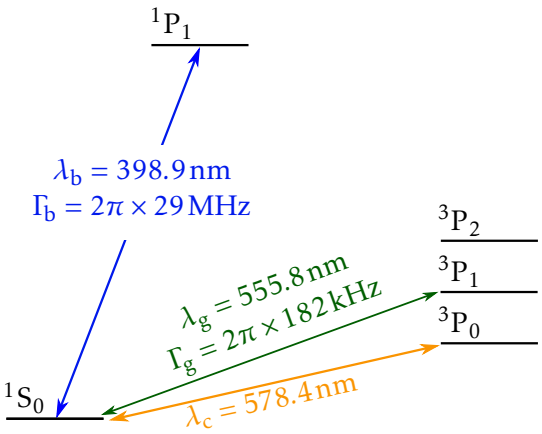

Figure 2.1 Scheme of the lowest energy levels of ^{174}Yb. The $\lambda_b = 399\,nm$ blue transition and the $\lambda_g = 556\,nm$ green transition are the two essential transitions in this manuscript. The $\lambda_c = 578\,nm$ "clock" transition is only briefly mentioned in section 2.1.1 and in Chapter 5.

isotopes of ytterbium. Not shown in this figure are the Zeeman sublevels, which appear in the presence of a magnetic field for states with $J > 0$.

The two valence electrons of Yb largely determine its electronic structure, and can pair in a spin-singlet state $S = 0$ or in a spin-triplet state $S = 1$. The ground state is the $^1S_0$ spin-singlet. The zero total electronic angular momentum $F = J + I = 0$ of the ground state implies the absence of hyperfine structure. This electronic structure, much simpler than that of alkaline atoms, simplifies greatly the study of atom-light interaction (see Chapters 3 and 6). However, it also implies the absence of sub-Doppler cooling mechanisms (Dalibard et al. 1989). Magnetic trapping of bosonic ytterbium is also not an option since the total angular momentum of the electronic ground state is zero, making Ytterbium atoms in their electronic ground state insensitive to magnetic fields. For that reason, optical dipole traps are essential in our experiment, as we will see in the next section.

The spin-orbit interaction splits the spin-triplet ^3P into three levels with electronic angular momentum J (0, 1 and 2). Transitions between singlet and triplet states are forbidden in the electric dipole approximation, owing to the selection rules $\Delta J = 0, \pm 1$ and $\Delta S = 0$ if one neglects spin-orbit coupling. Only the blue transition $^1S_0$–$^1P_1$ is allowed in this framework. However, some transitions, such as the green *intercombination* transition $^1S_0$–$^3P_1$, are weakly allowed due to spin-orbit coupling, but with a linewidth about two orders of magnitude smaller than the allowed $^1S_0$–$^1P_1$ transition. In this manuscript, we will use almost exclusively the blue and green transitions, for laser cooling and absorption imaging as well as for inducing interesting physics. We will denote by (λ_b, Γ_b) and (λ_g, Γ_g) their respective wavelengths and linewidths.

The $^1S_0$–$^3P_0$ and $^1S_0$–$^3P_2$ transitions are "doubly forbidden", because they violate the $J = 0 \nleftrightarrow J = 0$ and $\Delta J = 0, \pm 1$ selection rules respectively (in addition to $\Delta S = 0$). Due to the vanishingly small linewidth of the transition, the two states $^3P_0$ and $^3P_2$ are metastable. These transitions are used in optical clocks with great success (Ludlow et al. 2015) and they are thus called *clock* transitions. In our experiment, we addressed exclusively the excited metastable state $^3P_0$ (Bouganne et al. 2017), which does not have a hyperfine structure and is insensitive to magnetic fields ($J = 0$). We refer to $^1S_0$–$^3P_0$ as the clock transition and we denote its wavelength by $\lambda_c = 578.4\,nm$. Although it is doubly forbidden, it can be addressed by turning on a static magnetic field (roughly 180 G) mixing the $^3P_0$ and $^3P_1$ states. Even then, the lifetime of the $^3P_0$ state is longer than all experimental times, so we consider $\Gamma_c = 0$ (calculations predict $\sim 20\,mHz$ for a 180 G magnetic field).

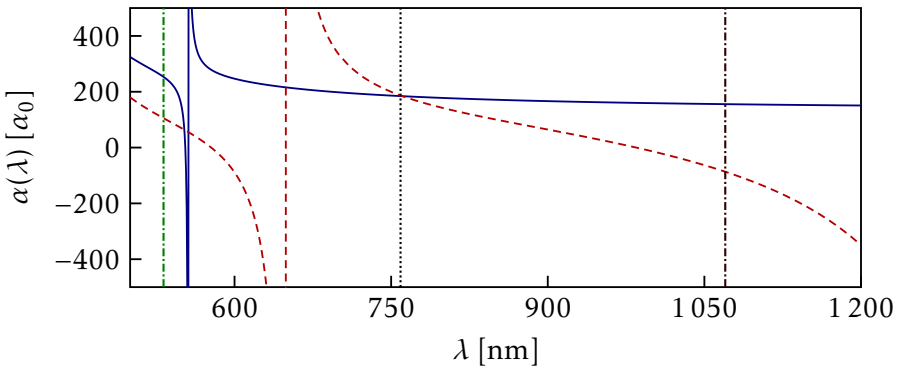

Figure 2.2 Real part of the atomic polarizability for the ground state $^1S_0$ (solid blue) and metastable excited state $^3P_0$ (dashed red), in units of the atomic polarisability $\alpha_0 = 4\pi\epsilon_0 a_0^2$ (Dzuba et al. 2010). The dotted vertical line indicate the magic wavelength ($\lambda_m = 759\,\text{nm}$). The wavelengths of the crossed dipole trap ($\lambda_{DT1} = 532\,\text{nm}$ and $\lambda_{DT1} = 1070\,\text{nm}$) are shown as vertical dash-dotted lines.

2.1.2 Polarizability and light potentials

In addition to near-resonant light for cooling and probing the atoms, far-off-resonance light can be used to create attractive or repulsive light potentials (Grimm et al. 2000). If $\alpha_i(\lambda)$ is the polarizability of an atom in its internal state i at wavelength λ, we have

$$V_i(\boldsymbol{r}, \lambda) = -\frac{1}{2\epsilon_0 c}\,\text{Re}[\alpha_i(\lambda)]I(\boldsymbol{r}) \tag{2.1.1}$$

where $I(\boldsymbol{r})$ is the light intensity. Figure 2.2 shows a calculation of the real part of the polarizability of the ground state (solid line) as a function of the wavelength, taken from Dzuba et al. (2010). We can see that, due to the simple electronic structure of Yb, $\text{Re}[\alpha(\lambda)] > 0$ for most wavelengths, except near resonance. This means that we can only create attractive potentials with Yb if we want to avoid substantial heating.

For completeness, we also present calculations of the polarizability of the excited metastable state $^3P_0$ (dashed line in figure 2.2). We observe that the two polarizabilities cross at $\lambda_m = 759.4\,\text{nm}$ (marked as a vertical dotted line in figure 2.2). The light potential seen by ground and excited is the same at this wavelength, and it is therefore called a *magic* wavelength. The use of such a wavelength is essential in optical clock experiments, and the retro-reflected optical lattices in our experiment (see section 2.4) are at the magic wavelength.

2.2 Preparation of ytterbium Bose-Einstein condensates

In this section, we detail the experimental steps leading to the Bose-Einstein condensation of Yb. The experiment operates in the ultra high vacuum (UHV) regime to minimize collisions between the ultracold gas and residual background atoms at room temperature. As shown in figure 2.3, the experiment has three sections, separated by differential pumping stages,

1. the oven section ($P \approx 10^{-8}\,\text{mbar}$),
2. the Magneto-Optical Trap (MOT) chamber ($P \approx 10^{-10}\,\text{mbar}$),
3. the science chamber ($P < 10^{-11}\,\text{mbar}$).

The experiment uses a total of five ion pumps (not shown in figure 2.3): two in the oven section, one at the entrance of the Zeeman slower, one in the MOT chamber, and one in the science chamber. In addition, a getter pump is also located in the science chamber.

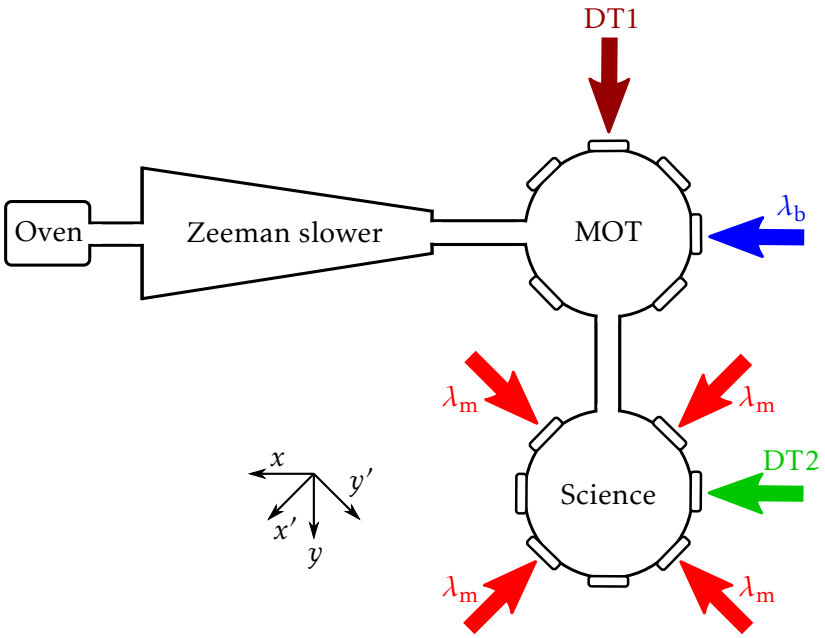

Figure 2.3 Top-view schematic presenting the different sections of the experiment as well as the optical beams necessary for laser cooling and trapping. Only 4 of the MOT beams are represented, the two remaining being in the vertical direction.

2.2.1 Zeeman slower and magneto-optical trap

We create a vapour of Ytterbium by heating a metallic oven to $\sim 410°C$. A collimation tube extracts an atomic beam for that oven. The atomic beam is slowed from about 300 m/s to about 10 m/s by a counter-propagating resonant laser beam, as shown in figure 2.3. Since the radiation force exerted by the beam is proportional to the linewidth of the transition, the laser is chosen to be resonant with the large blue transition at $\lambda_b = 399\,\text{nm}$. In order to maintain the resonance when the atoms are slowed down despite the Doppler effect, we use a Zeeman slower, i.e. a suitably designed solenoid generating a magnetic field gradient such that the Zeeman effect compensates the Doppler shift of the decelerated beam all the way to the MOT chamber (Phillips et al. 1982).

The atoms are then cooled and trapped in a MOT, which is made of

- Three pairs of near-resonant counter-propagating beams, which create a friction force and slow down the atoms,
- A quadrupole magnetic field which adds a spring-like component to the optical force and traps the atoms at the center of the MOT chamber.

As mentioned before, sub-Doppler cooling mechanisms are not available for the ground state of ^{174}Yb. The minimum temperature that can be reached with a transition of linewidth Γ is then given by the Doppler temperature

$$T_{\text{Doppler}} = \frac{\hbar\Gamma}{2k_B}. \tag{2.2.1}$$

For this reason, the MOT is chosen to be near resonance of the narrow green transition at $\lambda_g = 556\,\text{nm}$. Another reason is the presence of weak decay channels from the $^1P_1$ state (not represented in figure 2.1) which limits the atom number achievable in a "standard" MOT operating near the broad blue transition at $\lambda_b = 399\,\text{nm}$ (Honda et al. 1999). The downside

of a green MOT is a lower capture velocity

$$v_{\text{capture}} \simeq \sqrt{\frac{w\hbar k\Gamma_{\text{g}}}{m}}, \tag{2.2.2}$$

where w is the waist of the MOT beams. In optimal working conditions, we load about 2×10^8 atoms into the MOT in 6 s. The loading step is followed by a Doppler cooling step, leading to a temperature on the order of 10 µK (Dareau 2015).

The blue and green laser light at $\lambda_{\text{b}} = 399\,\text{nm}$ and $\lambda_{\text{g}} = 556\,\text{nm}$ are both obtained by frequency doubling. For $\lambda_{\text{b}} = 399\,\text{nm}$, a commercial laser (TA pro, Toptica) sends 1.2 W of 798 nm light to a doubling cavity made of a non-linear crystal at the center of four mirrors in a bow-tie configuration. For the first part of my thesis (and the data presented in Part II), we used a homemade doubling cavity (Dareau 2015). In the course of my thesis, we changed to a commercial doubling cavity (SHG pro, Toptica). This change significantly improved the stability of the experiment over one day. For $\lambda_{\text{g}} = 556\,\text{nm}$, a commercial laser (Koheras Adjustik, NKT photonics seed + Elysa, Quantel laser or Orange One, Menlo system amplifier) sends 1.5 W of 1112 nm light to another homemade doubling cavity with a ppSLT crystal (Covesion). For each system, two feedback loops are used: one to maintain the resonance condition of the cavity and one for frequency locking. The cavity lock generates the error signal from the intra-cavity power and feedbacks to a piezoelectric motor placed on one of the cavity mirrors. The blue light frequency is locked by modulation transfer spectroscopy on an Yb hollow cathod lamp (Bouganne 2018) and the green light frequency is locked by saturated absorption spectroscopy to a diiode gas confined in a glass cell (Dareau 2015).

2.2.2 Optical dipole traps and evaporative cooling

At the end of the MOT loading stage, the magnetic gradient is increased to compress the cloud and the magnetic quadrupole is moved to coincide with the focal point of a high-intensity laser beam. This infrared laser (YLR-50-LP-AC-Y12, IPG Photonics) is very red-detuned with respect to the two resonances ($\lambda = 1070\,\text{nm}$) and thus creates an attractive potential proportional to its intensity, as seen in section 2.1.2. Optical beams in the experiment typically come from optical fibers and their propagation is well described by Gaussian optics. The first dipole trap (DT1) potential can then be expressed as

$$V_{\text{DT1}}(r,z) = -\frac{1}{2\epsilon_0 c}\,\text{Re}[\alpha_i(\lambda)]I_{\text{DT1}}(r,z) = -V_1\,\text{e}^{-2r^2/w^2(z)}. \tag{2.2.3}$$

Here, V_1 is the depth of the dipole trap and is proportional to the power P of the beam,

$$V_1 = \frac{P}{\pi\epsilon_0 c w_1^2}\text{Re}[\alpha(\lambda_{\text{DT1}})], \tag{2.2.4}$$

z is the propagation axis of the beam and r is the distance from the propagation axis. We have defined the Gaussian *waist* at position z, $w(z)$, which corresponds to the radius at $1/\text{e}^2$ of the beam,

$$w(z) = w_1\sqrt{1+\frac{z^2}{z_{\text{R}}^2}}. \tag{2.2.5}$$

Here, w_1 is the waist at the focus of the beam and $z_{\text{R}} = \pi w_1^2/\lambda$ is the Rayleigh length. In the following, we will simply refer to w_1 as "the" waist of the beam.

Atoms trapped by an optical dipole trap typically have small energies compared to V_1. As such, the dipole trap potential can be approximated as harmonic for (almost) all practical purposes,

$$V_{\text{DT1}}(r,z) \approx -V_1 + \frac{1}{2}m(\omega_r^2 r^2 + \omega_z^2 z^2). \tag{2.2.6}$$

The radial frequency is determined by the waist and the axial frequency by the Rayleigh length,

$$\omega_r = \sqrt{\frac{4V_1}{mw_1^2}}, \quad \omega_z = \sqrt{\frac{2V_1}{mz_R^2}}. \tag{2.2.7}$$

From the calculated value of $\mathrm{Re}[\alpha(\lambda_{DT1})] = 164\,\alpha_0$ and given the $w_1 \approx 40\,\mu\mathrm{m}$ waist, we estimate the trap depth to be $V_1 \approx k_B \times 600\,\mu\mathrm{K}$, much higher than the MOT temperature (Bouganne 2018). We are able to transfer approximately 1.2×10^7 atoms from the MOT to the DT1, corresponding to a transfer efficiency on the order of 5 %.

After loading, the DT1 is moved from the MOT chamber to the science chamber. Using a corner cube mirror, the beam focus is translated by over 18 cm in 1.5 s. About 20 % of the atoms are lost during the transport stage, which is compatible with the natural evaporation and losses expected during the transport time (Scholl 2014). In the science chamber, we perform evaporative cooling in a crossed dipole trap (CDT). The CDT consists of the DT1 and an additionnal DT2 (Verdi V-6, Coherent) at wavelength $\lambda_{DT2} = 532\,\mathrm{nm}$ and with a $w_2 \approx 16\,\mu\mathrm{m}$ waist. A power of about 1 W is available, which corresponds to a trap depth $V_0 \approx k_B \times 100\,\mu\mathrm{K}$. The trapping frequencies of the CDT are given by the quadratic sum of the frequencies of each DT $\omega_i^2 = (\omega_{i,DT1}^2 + \omega_{i,DT2}^2)^{1/2}$. The axial frequencies ω_{z1}, ω_{z2} being negligible compared to the radial frequencies ω_{r1}, ω_{r2}, we thus have

$$\omega_x \simeq \omega_{r1}, \quad \omega_y \simeq \omega_{r2}, \quad \omega_z = \left(\omega_{r1}^2 + \omega_{r2}^2\right)^{1/2} \tag{2.2.8}$$

with the (x, y, z) axes defined in figure 2.3.

Evaporative cooling is performed by ramping down the CDT depth through the powers of DT1 and DT2. The power of DT2 is controlled by the radio-frequency amplitude of an AOM, like all lasers on the experiment except the high power DT1 laser. The power of DT1 is decreased in two steps: first, a half-wave plate placed in front of a Glan-Taylor prism is rotated to reduce the power by a factor of ~ 100. Then, the laser pump power is tuned to reduce the output power by an additional factor of 10. Only in the second step is the power servo-looped.

The evaporation lasts 4 s and yields a Bose-Einstein condensate of 6 to 8×10^4 atoms with no discernible thermal fraction. Shot-to-shot atom number fluctuations are smaller than 5 %. The CDT frequencies where measured to be $(\omega_x, \omega_y, \omega_z) = 2\pi \times (60, 230, 260)\,\mathrm{Hz}$. The chemical potential is then

$$\mu_0 = \frac{\hbar\bar{\omega}}{2}\left(\frac{15N_{at}a}{\bar{a}_{ho}}\right)^{2/5} \approx h \times 3\,\mathrm{kHz}, \tag{2.2.9}$$

where $a = 105\,a_0$ is the s-wave scattering length (Kitagawa et al. 2008, Borkowski et al. 2017) and $\bar{\omega} = (\omega_x\omega_y\omega_z)^{1/3}$, with $\bar{a}_{ho} = \sqrt{\hbar/m\bar{\omega}}$. The Thomas-Fermi condition $\mu \gg \hbar\omega_{x,y,z}$ is therefore well satisfied. The Thomas-Fermi radii are $(R_x, R_y, R_z) = (9.5, 2.5, 2.2)\,\mu\mathrm{m}$ and the maximum (3D) density is $n_0 = 15N_{at}/8\pi R_x R_y R_z \approx 7 \times 10^{20}\,\mathrm{m}^{-3}$.

2.3 Time-of-flight absorption imaging

2.3.1 Absorption imaging

In order to detect and probe the atoms, we use absorption imaging, where a resonant beam is sent to the atoms for a time t_p (typically 20 µs) and then imaged on a CCD camera. After a waiting time (typically 200 ms) ensuring there are no more atoms in the field of view and the camera has had enough time to reset, a second image of the beam is taken. In the experiments

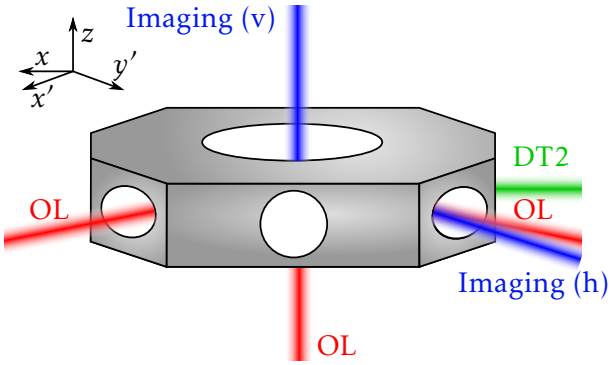

Figure 2.4 Side-view schematic of the science chamber, which from the top is a regular octogon. For clarity, only the incoming beams are represented. DT1 is not represented and is coming towards the reader. OL stands for optical lattice. The axes x and y are aligned with DT2 and DT1 respectively, while the axes x' and y' are aligned with the horizontal optical lattices.

described in Part II, we use the blue transition near 399 nm. In Chapter 7, we discuss the advantages and disadvantages of the blue and green transitions for in-situ imaging.

The reduction of the intensity due to absorption is given by the Beer-Lambert law, which, at resonance, reads

$$T \equiv \frac{I_\mathrm{f}(x,y)}{I_\mathrm{i}(x,y)} = \exp\left(-\sigma_0 \int n(x,y,z)\mathrm{d}z\right), \tag{2.3.1}$$

where T is the transmission, n is the 3D density and $\sigma_0 = 3\lambda^2/2\pi$ is the resonant absorption cross section (Ketterle et al. 1999). I_f is the intensity after the atoms, corresponding to the first image, and I_i is the intensity before the atoms, corresponding to the second image. We define the optical density

$$\mathrm{OD}(x,y) \equiv \sigma_0 \int n(x,y,z)\mathrm{d}z = -\ln[T(x,y)]. \tag{2.3.2}$$

Equation (2.3.1) holds provided the imaging intensity I_i is small compared to the saturation intensity $I_{\mathrm{sat},0} = \hbar\Gamma\omega^3/12\pi c^2$ of the transition (Ketterle et al. 1999).

We use one of two imaging systems in orthogonal directions, as shown in figure 2.4: a horizontal imaging system with a magnification of 2, and a vertical imaging system with a magnification of 5. In Chapter 5, we discuss the installation of a high-resolution vertical imaging system, replacing the one described here and used in Part II of this manuscript.

Any effect that causes a fraction of the light to not address the atoms will lead to an underestimation of the density. In particular, care must be taken to ensure that frequency of the imaging light is set to resonance. The blue imaging transition is a $J = 0 \leftrightarrow J = 1$ transition, as explained in section 2.1.1, for which all Clebsch-Gordan coefficients are equal to 1. Experimentally, we sometimes use a high vertical magnetic field (on the order of 300 G). In that case, the polarization must be chosen accordingly. For horizontal imaging, the polarization is linear and vertical to address the π-transition ($m_\mathrm{F} = 0 \leftrightarrow m_\mathrm{F} = 0$), which is insensitive to the magnetic field. For vertical imaging, the polarization is circular to address one of the σ-transitions ($m_\mathrm{F} = 0 \leftrightarrow m_\mathrm{F} = \pm 1$), which are sensitive to the magnetific field. Magnetic field fluctuations (typically a few mG) are negligible in practice because the blue transition is broad ($\Gamma_\mathrm{b} \simeq 2\pi \times 29$ MHz).

2.3.2 Imaging after a time-of-flight

2.3.2.1 Imaging Bose-Einstein condensates

The peak density of the 3D BEC integrated along the vertical direction is $n_{2D,0} = 4n_0R_z/3 \simeq 2 \times 10^3\,\mu\text{m}^{-2}$, with n_0 the peak 3D density and R_z the vertical Thomas-Fermi radius. The corresponding optical depth is $\text{OD} = \sigma_0 n_{2D,0} \simeq 156$, which corresponds to a vanishing transmission far below any realistic value for experimental detection. In addition, many additional problems arise when measuring the in-situ distribution of atoms, from atomic motion to collective scattering of photons. These phenomena will be discussed in Part III in greater details, but for the time being our purpose is to get rid of them.

To probe our quantum gases, we therefore use the technique called *time-of-flight* (tof) imaging. We suddenly release the cloud from all trapping potentials simultaneously. The cloud falls due to gravity and also expands due to the initial velocity distribution and to the conversion of interaction energy into kinetic energy. Neglecting the latter, the density distribution after a sufficiently long tof (typically 20 ms) reflects the initial momentum distribution of the trapped cloud. If $n(\boldsymbol{k})$ is the momentum distribution of the trapped cloud, then

$$n_{\text{tof}}(\boldsymbol{r}, \text{tof} = t) \approx \left(\frac{m}{\hbar t}\right)^3 \tilde{n}\left(\boldsymbol{k} = \frac{m\boldsymbol{r}}{\hbar t}\right). \tag{2.3.3}$$

However, neglecting the effect of interactions in the expansion is not a good approximation in the case of a Bose-Einstein condensate. Castin et al. (1996) showed that the expansion of a BEC released from a 3D harmonic trap follows

$$n_{\text{tof}}(\boldsymbol{r}, t) = \frac{1}{\Lambda(t)} n\left(\left\{\frac{r_i}{\lambda_i(t)}\right\}\right), \tag{2.3.4}$$

with $\Lambda = \lambda_x\lambda_y\lambda_z$. The evolution of the dilatation coefficients $\lambda_i(t)$ is given by

$$\frac{\mathrm{d}^2}{\mathrm{d}t^2}\lambda_i(t) = \frac{\omega_i}{\Lambda(t)\lambda_i(t)}, \tag{2.3.5}$$

and can be calculated numerically. In Chapter 5, we will discuss the expansion of a BEC released from a very anistropic harmonic trap realizing a 2D BEC.

2.3.2.2 Imaging atoms in optical lattices

In section 2.4, we describe the loading of the 3D BEC into a cubic optical lattice. For the same reason as for a BEC, the in-situ density distribution is not accessible experimentally. Gerbier et al. (2008) have shown that, for atoms relased from optical lattices, the effect of interactions on the tof density distribution is usually negligible compared to finite-tof effects. Neglecting the latter as well, the density distribution after a sufficiently long tof t reads

$$n_{\text{tof}}(\boldsymbol{r}, \text{tof} = t) \approx \left(\frac{m}{\hbar t}\right)^3 \left|\tilde{w}_0\left(\boldsymbol{k} = \frac{m\boldsymbol{r}}{\hbar t}\right)\right|^2 S\left(\boldsymbol{k} = \frac{m\boldsymbol{r}}{\hbar t}\right) \tag{2.3.6}$$

where $\tilde{w}_0(\boldsymbol{k})$ is the Fourier transform of the ground band Wannier function and $|\tilde{w}_0(\boldsymbol{k})|^2$ is often called the Wannier envelope. As detailed in section 2.4, the tof density distribution equation (2.3.6) presents an interference pattern coming from the quasi-momentum distribution

$$S(\boldsymbol{k}) = \sum_{l,m} \mathrm{e}^{\mathrm{i}\boldsymbol{k}\cdot(\boldsymbol{r}_l - \boldsymbol{r}_m)} \langle \hat{a}_l^\dagger \hat{a}_m \rangle, \tag{2.3.7}$$

which is the Fourier transform of the lattice first-order correlation function $\langle \hat{a}_l^\dagger \hat{a}_m \rangle$.

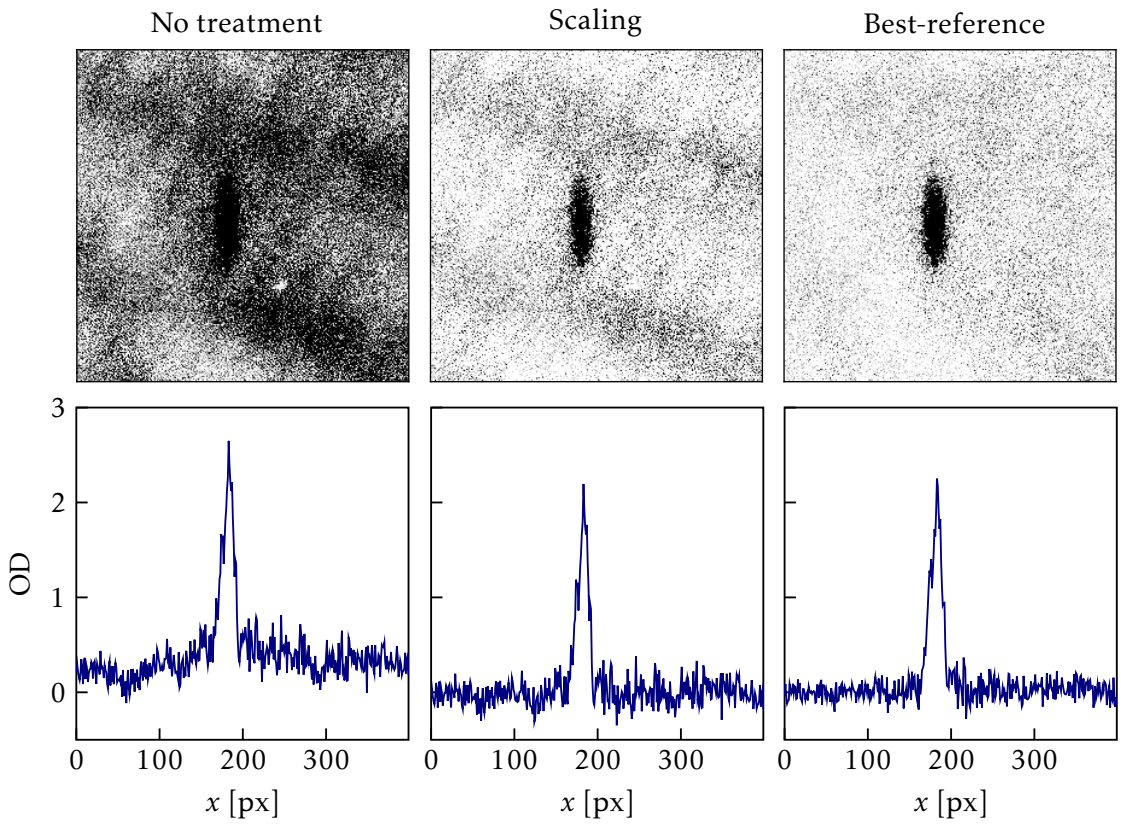

Figure 2.5 Optical depths computed from the same two pictures, without treatment, with a scaling treatment and with the best-reference picture algorithm.

2.3.3 Best-reference algorithm

As mentioned above, two images are taken for each experimental sequence. Both are images of the imaging light beam, but the first image S contains the shadow of the atoms, while the second image R is used as a reference without atoms. However, problems can still arise if the imaging beam changes slightly during the 200 ms between the two images. If the beam intensity is slightly different for the two images, this gives rise to an offset in the OD, i.e. the log of transmission in equation (2.3.2). This can be corrected by a *scaling* treatment: a numerical factor is introduced to ensure that a selected region of the image without atoms has the same average intensity for both images.

The scaling treatment is however insufficient: the beam profile exhibits many fringes and speckle grains and, because of various factors such as a displacement of the beam during the off time, the patterns of the beam are imperfectly canceled when taking the ratio of the two images. We observe this in the absorption images by the appearance of a variety of spurious background patterns, as shown in figure 2.5. They are corrected by a *best-reference picture algorithm* (BRPA). When we collect experimental data, we typically take at least 50 images with different experimental parameters, but without changing the imaging system. The idea of the BRPA is to use all the reference images $\{R_i\}$ to create a best-reference image $Q = \sum_i c_i R_i$, which is a linear combination of all reference images (Ockeloen et al. 2010). This best-reference image minimizes the quantity $\sum_{i,j}(S_{i,j} - Q_{i,j})^2$, where i and j span all a pixels of the selected region with no atoms. More details about the BRPA can be found in Bouganne (2018).

Figure 2.5 compares the performance of the scaling treatment and the BRPA against an untreated OD image. We observe that the BRPA further improves the quality of the back-

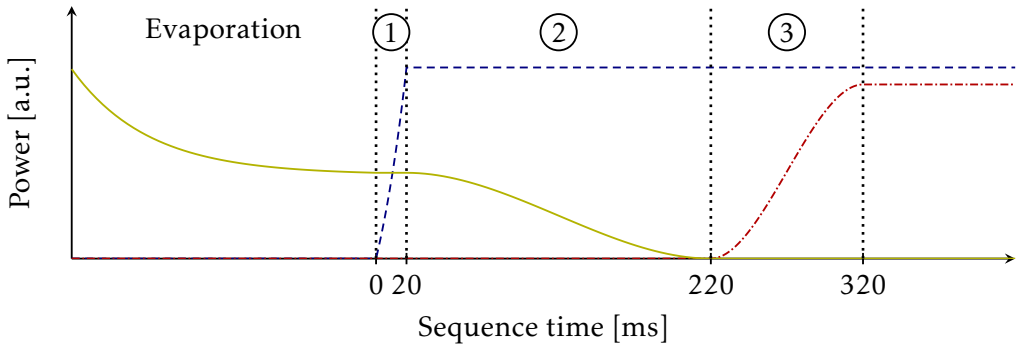

Figure 2.6 Experimental loading sequence of the 3D optical lattice, starting from 3D BEC evaporation. We show the power of the CDT (solid line) as well as the power of the vertical (dashed line) and horizontal (dash-dotted line) lattices as a function of time.

ground with respect to the scaling treatment by removing unwanted patterns. The BRPA is applied on all images presented in this manuscript, both for tof images in Part II and for the in-situ images in Part III.

2.4 Loading a three-dimensional cubic optical lattice

2.4.1 Experimental setup

The geometry of the 3D optical lattices is shown on figure 2.4. There are three retro-reflected beams in the (x', y', z) directions making a cubic optical lattice. We define (x', y') as horizontal axes 45° away from the (x, y)-axes defined by the dipole traps DT1 and DT2. The laser source is a Ti:Sapphire laser (SolsTiS, M Squared), which we set to the magic wavelength $\lambda_m = 759\,\text{nm}$ and split in 3 for the 3 arms of the lattice. During my thesis, the available power of the laser decreased from 4 W to 1 W. An additional laser (TA pro, Toptica), providing a power of 2 W, was used to realize the vertical lattice and obtain the results presented in Part II.

The optical beams creating the cubic optical lattice are fibered and therefore Gaussian-shaped. This creates an approximate harmonic trapping potential in addition to the periodic potential coming from the retro-reflection. The waists of the horizontal lattices are about 120 µm, while the waist of the vertical lattice is about 150 µm. As a result, the trapping frequencies of the additional harmonic potential created by the Gaussian envelope of the beams are $(\omega_x, \omega_y, \omega_z) \approx 2\pi \times (40, 40, 30)\,\text{Hz}$. With the available power, we were able to achieve lattice depths of about $25\,E_R$ for each lattice. The lattice depth can be accurately calibrated using a Kapitza-Dirac technique as shown in Appendix A.1.

The power of each optical lattice is regulated by AOMs and a servo-loop. To avoid interferences between the lattices in the x, y and z directions, their frequencies are detuned by tens of MHz by the AOMs. The resulting beatings are very fast compared to atomic motion frequencies, which are at most a few tens of kHz for the frequencies in a well of the periodic potential. Moreover, we set the polarizations of optical lattice beams propagating in different directions to be mutually orthogonal.

2.4.2 Loading sequence

The loading sequence, shown in figure 2.6, contains three steps.

1. First, the vertical lattice is turned on by a 20 ms exponential ramp, so as to slice the 3D BEC into a stack of 2D BECs.

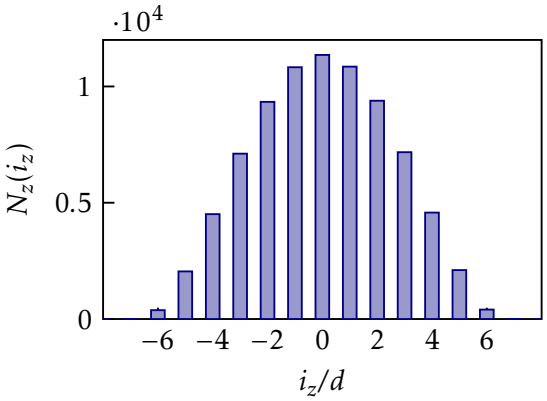

Figure 2.7 Atom number distribution for the stack of 2D gases for $V_z = 27E_R$ and $N = 6\times10^4$ atoms.

2. Then, the CDT is slowly ramped down in 200 ms, so as to let the 2D BECs expand in the horizontal plane.

3. Finally, the horizontal lattices are adiabatically ramped up in 100 ms to their final values.

The reason for the fast ramp-up of the vertical lattice is gravity, which makes adiabatic transfer more difficult because we also want to switch off the CDT at the same time. The vertical slicing of the 3D BEC results in a stack of about $R_z/d \simeq 10$ 2D BECs. In Part II of this manuscript, we will also study stacks of 1D systems. To realize 1D systems, the horizontal lattice along y is ramped up adiabatically to the maximum available power.

2.4.3 Plane loading model

We now present our loading model relying the experimental loading sequence. First, we model the fast ramp-up of the vertical lattice as "slicing" the 3D BEC, resulting in a stack of $2R_z/d \simeq 10$ 2D BECs. If $j = 0$ is the site holding the central plane 2D BEC, the number of atoms in 2D BEC j is given by

$$N_z(i_z) = \int_{z_{i_z}-d/2}^{z_{i_z}+d/2} \mathrm{d}z \int \mathrm{d}^2\rho\, n_{\mathrm{TF}}(\boldsymbol{r}). \tag{2.4.1}$$

In figure 2.7(a), we show the atom number distribution in the different planes, calculated using equation (2.4.1).

We then calculate the density distribution inside a plane for an isotropic 2D lattice using the Gutzwiller ansatz and the local density approximation, as discussed in Chapter 1. The tube loading model is discussed in the next chapter.

2.4.4 Superfluid-to-Mott insulator transition

By varying the lattice depth V_x in 1D and (V_x, V_y) in 2D, we probe the transition between superfluid and Mott insulator. Using the tof absorption imaging described in section 2.3, we measure the initial momentum distribution of our system before performing experiments such as those presented in Part II. In figure 2.8(a), we show experimental images across the transition from superfluid to Mott insulator in 2D. These tof images indicate the loss of long-range coherence when J/U is decreased through the variation of the lattice depth. The destruction of long-range coherence is thus indicated by a broadening, and finally by

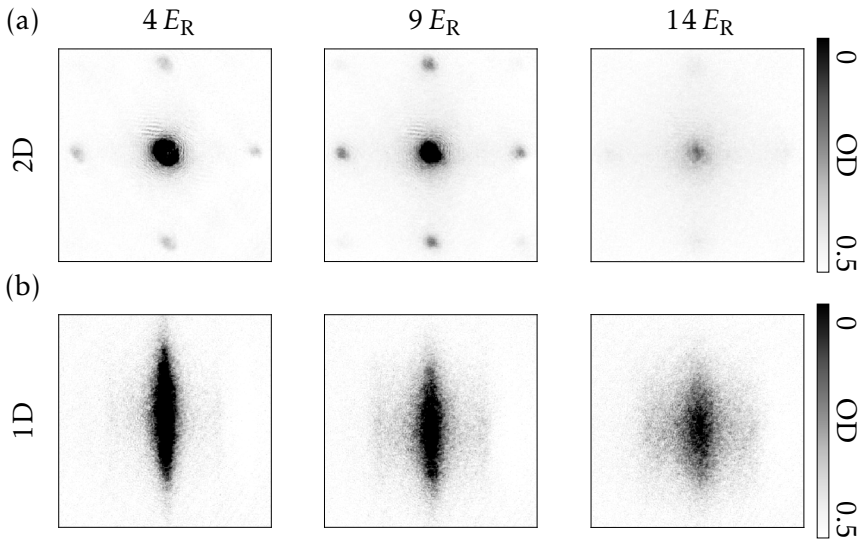

Figure 2.8 Superfluid to Mott insulator transition in stacks of 2D (a) and 1D (b) Bose-Hubbard systems. We show the momentum distribution of the lattice cloud, obtained through tof imaging.

	$(J/U)_c^{n=1}$		$(J/U)_c^{n=2}$
Dimension	MF	QMC	QMC
3D	0.029	0.034	0.020
2D	0.043	0.059	0.035
1D	0.086	~ 0.3	~ 0.2

Table 2.1: Critical values $(J/U)_c$ of the Mott insulator transition. For $\bar{n} = 1$, we compare mean-field values (Zwerger 2003) to quantum Monte Carlo simulations (Capogrosso-Sansone et al. 2007; 2008, Teichmann et al. 2009). See Kühner et al. (1998) for 1D values.

a disappearance of the central peak at $\boldsymbol{k} = 0$. When going to the Mott insulating phase and back, the reappearance of sharp peaks indicates that the loss of single-particle coherence is indeed due to the Mott insulator transition and not merely heating effects.

The first observation of the superfluid-to-Mott insulator transition was reported in Greiner et al. (2002) for 3D optical lattices, following a proposal by Jaksch et al. (1998). The 2D Mott insulator transition is somewhat comparable to the 3D Mott insulator transition. The 3D and 2D critical values calculated with quantum Monte Carlo (QMC) simulations are relatively close to the mean field approximation, as shown in table 2.1 (Zwerger 2003, Capogrosso-Sansone et al. 2007; 2008). The 2D Mott insulator transition was experimentally studied in Spielman et al. (2007), and the results were in good agreement with the predicted value for the transition for a unit filling $\bar{n} = 1$ (Elstner et al. 1999, Capogrosso-Sansone et al. 2008).

The 1D Mott insulator transition is more complicated, as we will see in Chapter 3. To summarize briefly, the Mott insulator transition occurs much earlier (Kühner et al. 1998). In table 2.1, we give approximate values, as different methods used in the literature result in slightly different values (Kühner et al. 1998, Zakrzewski et al. 2008, Ejima et al. 2011, Danshita et al. 2011). Experimentally, this transition was first studied in Stöferle et al. (2004). By probing the excitation spectrum with Bragg spectroscopy, the authors found that the Mott insulating phase appeared gradually for J/U between 0.25 and 0.13. In figure 2.8(b), we show experimental images taken during this thesis probing the transition in 1D. These data will be analyzed in Chapter 4.

Conclusion

In this chapter, we have presented the essential characteristics of the apparatus used to perform the experiments detailed in Parts II and III. First, we presented the key properties of ^{174}Yb, i.e its low-energy electronic transitions and its atomic polarizabilty. Then, we described the experimental steps we follow to prepare Yb Bose-Einstein condensates: atomic beam generation, Zeeman slowing, magneto-optical trapping, transport and finally evaporative cooling. We have emphasized the importance of optical dipole traps, which are omnipresent in this manuscript. We also presented our horizontal and vertical imaging systems, which we use to probe the atoms at the end of the experiments described in Part II. Absorption imaging is performed after a time-of-flight, which transforms the initial position distribution into a momentum distribution. Finally, we presented the experimental setup to realize the stacks of 2D or 1D Bose-Hubbard systems that are the starting point of the experiments in Part II. It consists of a cubic optical lattice in which the BEC is loaded according to a sequence that we have described. We have presented our model for calculating the atom number distribution in the different planes, and we have looked at the initial momentum distribution of the experiments presented in Part II by probing the superfluid-to-Mott insulator transition.

CHAPTER 3

One-dimensional bosons: theory and experiment

Introduction

In this chapter, we focus on the physics of one-dimensional Bose gases, which is very different from its 3D and 2D counterparts. In Chapter 1, we already discussed some of the key features of weakly-interacting 1D Bose gases, including the concepts of quasi-condensates and quasi-long-range order. The experiments in Part II rely on 1D Bose gases that can be made strongly interacting with an optical lattice. To better understand these systems, we present here a more detailed theoretical and experimental background on 1D Bose gases. Specifically, we develop a model for our experiment using newly introduced theoretical tools, and compare this model to experimental data on the momentum distribution of our 1D Bose gases.

One of the main advantages of studying 1D Bose gases is that, in addition to efficient computational approaches, there are also exact solutions (Bethe ansatz, Tonks-Girardeau gas) as well as powerful approximate descriptions, such as Luttinger liquid theory (Cazalilla et al. 2011). This low-energy theory predicts that correlation functions in 1D decay algebraically and that all the power-law exponents depend on a single parameter, the Luttinger parameter K. Experimental measurements of the Luttinger parameter for various physical systems have been an increasingly important topic in the past two decades. Although much work has been done with condensed matter systems (Schwartz et al. 1998, Bockrath et al. 1999, Denlinger et al. 1999, Chang 2003, Klanjšek et al. 2008), the lack of tunability and shielding from the Coulomb interaction make cold atoms more suitable for such studies.

On the one hand, atom chip experiments have achieved very well controlled 1D systems and correlation functions have been studied extensively (Trebbia et al. 2006, Hofferberth et al. 2007; 2008). However, these systems have not yet reached a high enough interaction strength for Luttinger liquid theory to become more relevant than the hydrodynamic quasi-condensate approach discussed in Chapter 1. On the other hand, optical lattices can also provide effective 1D systems, but so far most experimental studies have been on inhomogeneous stacks of 1D systems (Paredes et al. 2004, Kinoshita et al. 2004). The harmonic confining potential causes a position-dependent chemical potential that prevents accurate determination of K. Different tubes also have different populations, as we will discuss in this Chapter, and the Luttinger parameter can depend strongly on the density. Experiments with homogeneous and resolvable 1D systems are certainly the way forward (Endres et al. 2011). Nevertheless, in this chapter we present Luttinger liquid theory and compare its predictions to the initial momentum distribution of our stacks of 1D lattice gases.

In section 3.1, we present Luttinger liquid theory for continuum and lattice systems, focusing on the first-order correlation function $g_1(x)$, which is closely related to the density distribution after a time-of-flight. In section 3.2, we describe a loading model of our stacks of tubes and, for small lattice depths, we calculate a Luttinger parameter that is averaged over the whole system. In section 3.3, we analyze the measured time-of-flight momentum distribution for different lattice depths and extract the average first-order correlation function of the system.

3.1 Luttinger liquid theory

A powerful approach to describe the low-energy physics of one-dimensional gases is Luttinger liquid (LL) theory. This universal theory applies to any interaction strength (Tomonaga 1950, Luttinger 1963, Haldane 1981b), and relies on an approach called *bosonization* or *harmonic-fluid approach* (Haldane 1981a): two quantum fields $\hat{\phi}$ and $\hat{\theta}$ describe respectively the density and phase fluctuations. The most standard form of the Luttinger liquid

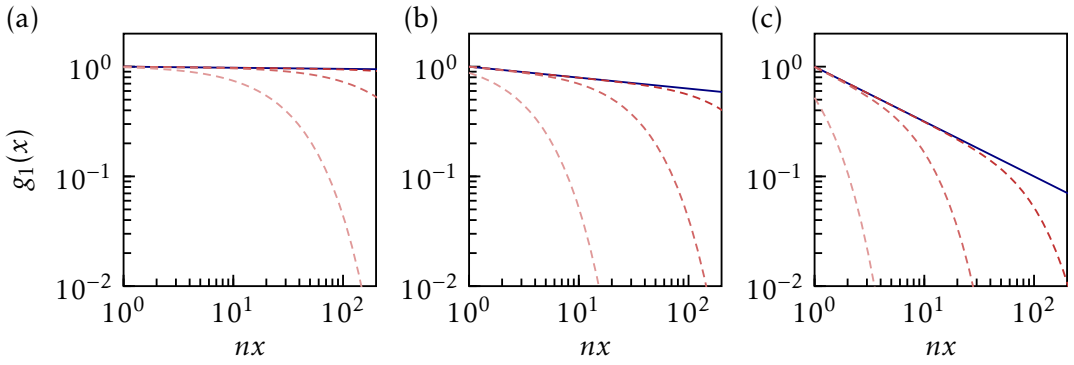

Figure 3.1 Comparison of g_1 for (a) $K = 50$, (b) $K = 5$ and (c) $K = 1$. The solid line corresponds to the zero-temperature behavior. The three dashed lines correspond to, from darker to brighter, $nl_T = 100$, $nl_T = 10$ and $nl_T = 1$.

Hamiltonian reads

$$\hat{H}_{\mathrm{LL}} = \frac{\hbar v}{2\pi} \int \mathrm{d}x \left(K \frac{\partial \hat{\phi}^\dagger}{\partial x} \frac{\partial \hat{\phi}}{\partial x} + \frac{1}{K} \frac{\partial \hat{\theta}^\dagger}{\partial x} \frac{\partial \hat{\theta}}{\partial x} \right), \tag{3.1.1}$$

where K is called the Luttinger parameter and v the sound velocity. The essential aspect of LL theory is that zero-temperature correlation functions can be expressed by simple power laws, and the exponents depend only on the Luttinger parameter K.

3.1.1 Homogeneous system

Let us first start a homogeneous 1D gas. As a low-energy theory, LL theory only provides the asymptotic behavior of the correlation functions at large distances (or small momenta). For example, at zero temperature, the first and second-order correlation functions of the homogenenous 1D gas read

$$g_1(x) \approx A_0 \frac{1}{(n|x|)^{1/2K}} + \ldots \tag{3.1.2}$$

$$g_2(x) \approx 1 - \frac{K}{2\pi^2} \frac{1}{(n|x|)^2} + \ldots \tag{3.1.3}$$

in position space. Hereafter, n is the 1D density in position space. On the other hand, at finite temperature, the first and second-order correlation functions decay as

$$g_1(x) \approx A_1 \left[\frac{\pi}{n l_T \sinh(\pi x / l_T)} \right]^{1/2K} + \ldots \tag{3.1.4}$$

$$g_2(x) \approx 1 - \frac{K}{2\pi^2} \left[\frac{\pi}{n l_T \sinh(\pi x / l_T)} \right]^2 + \ldots \tag{3.1.5}$$

where we have defined a thermal length $l_T = \hbar v / k_{\mathrm{B}} T$ (Cazalilla 2004a). These equations capture the crossover between an algebraic decay for $|x| \ll l_T$ and an exponential decay for $|x| \gg l_T$, as shown in figure 3.1. This behavior is consistent with the existence of quasi-condensates in 1D when T is finite but low enough for l_T to be larger than the system size.

Knowing this, the question now is how to determine the Luttinger parameters K and v. A homogeneous gas of one-dimensional bosons is described by the Lieb-Liniger model,

$$\hat{H} = \int \mathrm{d}x \left(\frac{\hbar^2}{2m} \frac{\partial \hat{\phi}^\dagger}{\partial x} \frac{\partial \hat{\phi}}{\partial x} + \frac{g_{1\mathrm{D}}}{2} \hat{\phi}^\dagger \hat{\phi}^\dagger \hat{\phi} \hat{\phi} \right), \tag{3.1.6}$$

for which there is an exact solution called the Bethe ansatz. Although the model and the solution are valid for any interaction strength and energy scale, it is difficult to calculate and express correlation functions using the Bethe ansatz. LL theory then becomes very convenient for this purpose, and the Bethe ansatz allows the derivation of the Luttinger parameters K and v for any interaction parameter γ, as shown in figure 3.2 adapted from Cazalilla (2004a). In Chapter 1, we introduced the 1D dimensionless interaction parameter $\gamma = mg_{1D}/\hbar^2 n$, with $g_{1D} = 2\hbar\omega_\perp a$ the 1D interaction strength, a the 3D scattering length, and $\omega_\perp$ the transverse confinement frequency. Although an exact calculation of the Luttinger parameters is available for all values of γ, the weakly and the strongly-interacting regimes are simple enough to be worth describing.

For weak interactions ($\gamma \ll 1$), the LL Hamiltonian can be identified with the Bogoliubov Hamiltonian describing the 1D quasi-condensates discussed in Chapter 1. The Luttinger parameters resulting from the identification read

$$K \approx \frac{\pi}{\sqrt{\gamma}}, \tag{3.1.7}$$

$$v \approx v_s = \sqrt{\frac{g_{1D} n}{m}}. \tag{3.1.8}$$

Combining equation(3.1.2) and equation(3.1.7), we retrieve that there is a quasi-Bose-Einstein condensation at zero temperature for finite weakly-interacting 1D gases: the smaller the interaction parameter γ, the larger the Luttinger parameter K and the slower the decay of the first-order correlation function.

In the opposite limit ($\gamma \gg 1$), strongly-interacting bosons can be mapped to hardcore bosons, which can themselves be mapped to free fermions. This exactly solvable model, called the Tonks-Girardeau gas, leads to

$$K \approx 1, \tag{3.1.9}$$

$$v \approx v_F = \frac{\hbar\pi n}{m} \tag{3.1.10}$$

at zero temperature, which means that the first-order correlation function decays as a power-law with an exponent 1/2. Refer to Appendix A.2 for more details on the Tonks-Girardeau gas.

3.1.2 Lattice system

Probing the strongly-interacting regime in the continuum is not easy, and optical lattices provide a simple way to increase the interactions. We thus turn to Luttinger liquid theory for bosons in lattices. However, describing lattice gases with LL theory and extracting the Luttinger parameters is more complicated. The Bose-Hubbard model can be described as a Luttinger liquid for non-integer filling, and also for integer filling in the superfluid regime: a Mott insulator is not a Luttinger liquid because the gap prevents an accurate low-energy description of the system (Cazalilla et al. 2011). The 1D Bose-Hubbard model cannot be solved exactly with the Bethe ansatz, but approximate and numerical calculations are available for the Luttinger parameter and the sound velocity (see Kiely et al. (2022) for a recent paper).

3.1.2.1 Phase diagram of the one-dimensional Bose-Hubbard model

Before discussing the Luttinger parameters in the Bose-Hubbard model, we need to know more about the phase diagram of the 1D Bose-Hubbard model. In particular, we need to determine the equation of state $\bar{n}(J, U)$ relating the tunneling coefficient J and the interaction strength U to the lattice filling $\bar{n} = nd$ (with d the lattice spacing). Although the phase

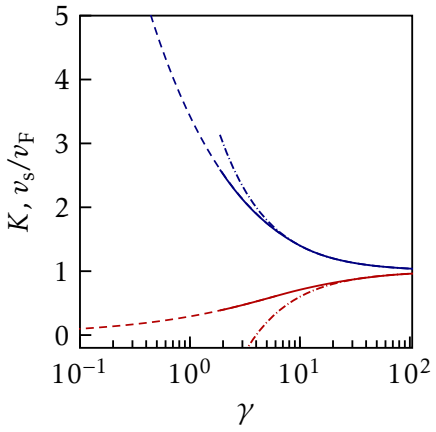

Figure 3.2 Luttinger parameter K (blue) and sound velocity v_s/v_F (red) for the Lieb-Liniger model as a function of the one-dimensional interaction parameter $\gamma = mg_{1D}/\hbar^2 n$. Dashed and dash-dotted lines correspond to known asymptotic limits. Adapted from Cazalilla (2004a).

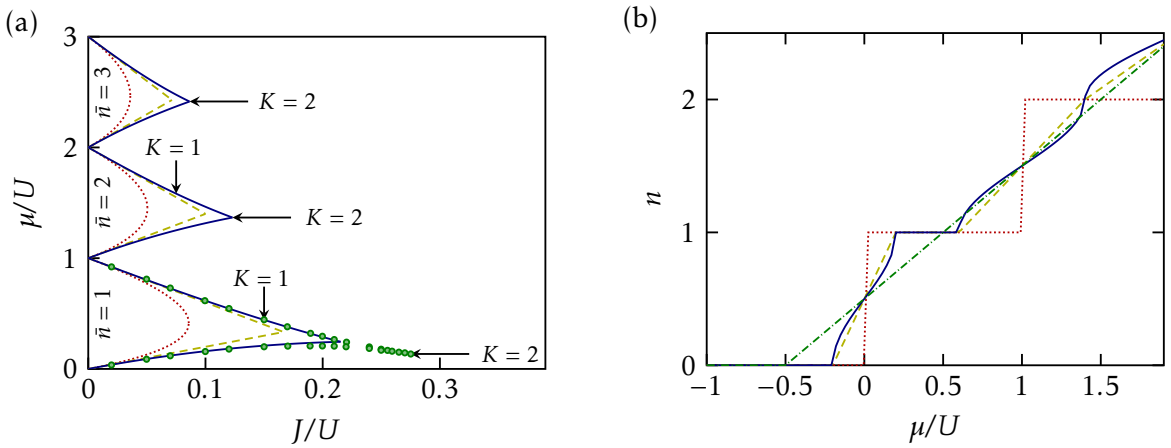

Figure 3.3 (a) Phase diagram of the 1D Bose-Hubbard model, including mean-field calculations (dotted lines), first-order (dashed lines) and third-order (solid lines) strong-coupling expansions, and DMRG calculations (circles) from Kühner et al. (2000). The Luttinger parameter K is shown at the Mott-U and Mott-δ transitions. (b) Equation of state $\bar{n}(J/U, \mu/U)$ for $J/U = 0.1$: the solid line corresponds to the hardcore boson calculations, and the dashed line to the simplified Gutzwiller variational approach. The dotted line corresponds to the $J = 0$ limit and the dash-dotted line corresponds to the $J/U \gg 1$ Thomas-Fermi limit.

diagram of the 1D Bose-Hubbard model presents Mott-insulating lobes as in higher dimensions, the shape of the lobes differs: mean-field calculations fail and reentrant and pointed lobes can be observed with strong-coupling expansions (Freericks et al. 1994) or density-matrix renormalization group calculations (Kühner et al. 1998), as shown in figure 3.3(a). The equation of state is also not well approximated by a mean-field description in 1D, and advanced numerical simulations should be the way to calculate it. In order to derive an analytical model, we distinguish two regimes where the equation of state takes a rather simple form.

On the one hand, in the weakly-interacting limit $J/U \gg 1$, the equation of state is a Thomas-Fermi one

$$\bar{n}_{J/U \gg 1} = \max\left[\frac{\mu}{U} + \frac{1}{2}, 0\right]. \tag{3.1.11}$$

On the other hand, in the atomic limit $J = 0$, we have

$$\bar{n}_0 \equiv \bar{n}_{J=0} = \mathrm{Int}\left(\frac{\mu}{U}\right) + 1 \tag{3.1.12}$$

where Int is the floor function. We propose two approaches to determine the equation of state in the regime $J/U \ll 1$. First, we can use a Gutzwiller variational approach akin to the one we used in Chapter 2. To make it even simpler, we restrict the study to two Fock states, $|\bar{n}_0\rangle$ and $|\bar{n}_0 - 1\rangle$.

$$|\Psi_{\mathrm{red}}\rangle = \prod_i \Big[c_1 |\bar{n}_0 - 1\rangle_i + c_2 |\bar{n}_0\rangle_i \Big]. \tag{3.1.13}$$

With this approach, one finds that the Mott lobes are triangles defined by

$$U(n_0 - 1) + 2Jn_0 < \mu < Un_0 - 2J(n_0 + 1). \tag{3.1.14}$$

These triangles are shown in figure 3.3(a) as a dashed line, and compared to the traditional Gutzwiller mean-field approach which is shown as a dotted line. As expected, the two approaches are consistent when $J/U \ll 1$. On the other hand, the simplified Gutzwiller ansatz gives a better account of the expected shape of the Mott lobes than the traditional mean-field approach. As for the equation of state, the density is trivially $\bar{n}_0$ in the Mott lobes. Between the Mott lobes, the simplified Gutzwiller approach finds that the density interpolates linearly between $\bar{n}_0 - 1$ and $\bar{n}_0$. In the end, we have

$$\bar{n}_{J/U\gg 1}(\mu, J) = \begin{cases} \bar{n}_0 - 1 & \text{if } \mu - U(\bar{n}_0 - 1) < -2J\bar{n}_0 \\ \bar{n}_0 - \frac{1}{2} + \frac{\mu - U(\bar{n}_0 - 1)}{4J\bar{n}_0} & \text{if } |\mu - U(\bar{n}_0 - 1)| < 2J\bar{n}_0 \\ \bar{n}_0 & \text{if } \mu - U(\bar{n}_0 - 1) > 2J\bar{n}_0 \end{cases} \tag{3.1.15}$$

A more refined approach relies on the notion of a Tonks-Girardeau gas, i.e. a 1D gas of hardcore bosons. After calculations detailed in Appendix A.2, we obtain

$$\bar{n}_{J/U\gg 1}(\mu, J) = \begin{cases} \bar{n}_0 - 1 & \text{if } \mu - U(\bar{n}_0 - 1) < -2J\bar{n}_0 \\ \bar{n}_0 - 1 + \frac{1}{\pi} \arccos\left(\frac{U(\bar{n}_0 - 1) - \mu}{2J}\right) & \text{if } |\mu - U(\bar{n}_0 - 1)| < 2J\bar{n}_0 \\ \bar{n}_0 & \text{if } \mu - U(\bar{n}_0 - 1) > 2J\bar{n}_0 \end{cases} \tag{3.1.16}$$

The different approaches and regimes are compared in figure 3.3(b). We observe that the reduced Gutzwiller and harcore boson approaches are very similar.

Note that refinements to the first-order strong-coupling expansion such as higher-order expansions or DMRG calculations are not very relevant for our experiment setup: in our harmonically-trapped systems, only a small fraction of the atoms will be impacted by these corrections. In particular, DMRG calculations for $\bar{n} = 1$ give $(J/U)_c \simeq 0.297$ (as mentioned in the previous chapter), but this corresponds to a vanishingly small region of the phase diagram in figure 3.3(a). In a trap, it is unclear whether a *barn* = 1 Mott domain survives beyond the local-density approximation in the range $0.2 \lesssim J/U \lesssim 0.3$, where the domain width is very small. To obtain a more robust estimate of the location of the Mott transition for a trapped gas, we will rather use the first-order expansion. For $\bar{n} = 1$, this yields $(J/U)_c \approx 0.17$ and $V_c \approx 4.9E_R$ and, for $\bar{n} = 2$, $(J/U)_c \approx 0.1$ and $V_c \approx 6.7E_R$.

3.1.2.2 Luttinger exponent on a lattice

We now return to Luttinger liquid theory for bosons in optical lattices. As mentioned above, a Luttinger exponent K is defined in the superfluid region, i.e. outside the lobes. K also takes critical values at the Mott transition. On the one hand, a Luttinger parameter $K = 2$ is found

at the Mott transition at fixed commensurate filling $\bar{n}$ and varying J/U, also known as the Mott-U transition. By finding the value of J/U for which $K = 2$, Kühner et al. (2000) found the critical point to be $(J/U)_c = 0.297 \pm 0.01$ for $\bar{n} = 1$. We also note that this transition is of Kosterlitz-Thouless type, like the 2D superfluid transition. On the other hand, the Mott-δ transition (or commensurate-incommensurate transition), for which the filling is varied at fixed J/U, has a Luttinger exponent of $K = 1$ at the critical point. A schematic summary is presented in figure 3.3(a). A notable consequence of this description is that for sufficiently strong interactions, a very weak periodic potential can induce a Mott transition in a commensurate system (Büchler et al. 2003). For example, for $\bar{n} = 1$, the interactions must be strong enough that $K < 2$. This was experimentally observed by Haller et al. (2010).

In the strongly-interacting regime $J/U \ll 1$ and for filling factors $\bar{n} \leqslant 1$, a lattice system can also be described as a Tonks-Girardeau gas of impenetrable bosons. For the Luttinger parameter, Cazalilla (2004b) has shown

$$K \simeq 1 + \frac{4J}{\pi U}\sin(\pi\bar{n}), \tag{3.1.17}$$

$$v_s \simeq \frac{Jd}{\hbar}\sin(\pi\bar{n})\left[1 - \frac{4J}{U}\bar{n}\cos(\pi\bar{n})\right] \tag{3.1.18}$$

with a strong-coupling expansion. This does not mean that a unit-filling Mott insulator is a Luttinger liquid with $K = 1$, but that $K \to 1$ as $\bar{n}$ approaches 1 at fixed J/U. In the Mott insulating regime of a trapped gas, due to the varying chemical potential, some regions will be commensurate and form Mott insulators, while others will be incommensurate and remain within the framework of LL theory. Equation (3.1.17) will apply for the latter, while the former have exponentially decaying correlation functions (the Luttinger parameter is not defined).

On the other hand, in the weakly-interacting regime $J/U \gg 1$, one can account for the lattice by renormalizing the continuum. In the superfluid regime (typically $V < 3E_R$ in our experiment), the system is well described by the Bose-Hubbard Hamiltonian because the tight-binding approximation is not fully valid, as discussed in Chapter 1. However, we can use a single-band description if the chemical potential and the temperature are small compared to the width of the ground band. Such a description is still valid even for $V = 0$ if $\mu, k_B T \ll 4E_R$. Since LL theory is a low-energy description, we can focus on small quasi-momenta and approximate the ground band by a parabola with an effective mass $m^* \geqslant m$. This leads to an effective interaction parameter

$$\gamma^* = \frac{m^*(Ud)}{\hbar^2(\bar{n}/d)}, \tag{3.1.19}$$

and an effective Fermi velocity $v_F^* = \pi\hbar(\bar{n}/d)/m^*$. In the tight-binding regime, we have $\hbar^2/m^* \simeq Jd^2$. This leads to $\gamma^* \simeq U/J\bar{n}$ and $v_F^* \simeq (Jd/\hbar)\pi\bar{n}$.

3.2 Modeling the experimental system

In this section, we propose a model to describe our experimental system using the theoretical tools presented above.

3.2.1 Experimental tube loading model

As discussed in Chapter 2, when loading stacks of 1D systems, we ramp up one of the horizontal lattice adiabatically. To calculate the population distribution of the tubes assuming perfect adiabaticity, we need the 1D equation of state $n(\mu/U, J/U)$ described in the previous

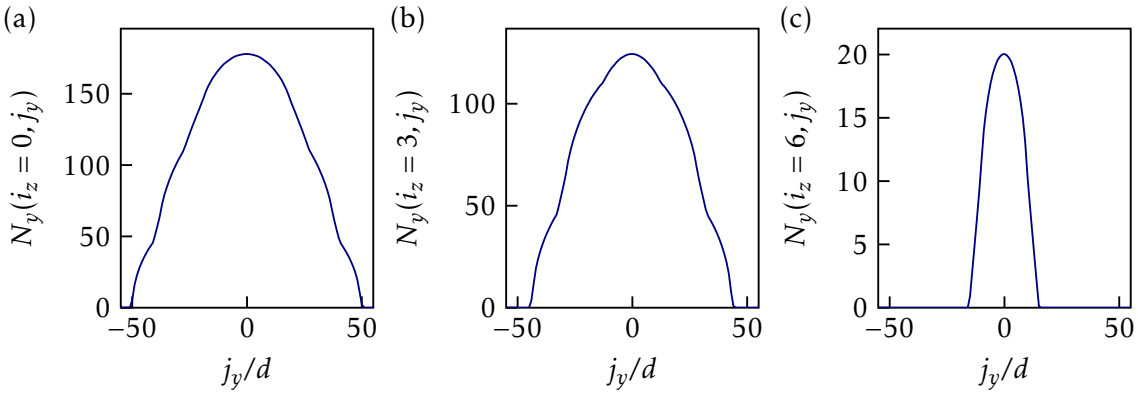

Figure 3.4 Atom number distributions for the stack of 1D gases for $(V_x, V_y, V_z) = (10, 25, 27)\,E_R$ and $N = 6 \times 10^4$ atoms. Only plans $i_z = 0$ (a), 3 (b) and 6 (c) are shown for clarity.

section. To each plane i_z, we assign a chemical potential $\mu_z(i_z)$, and to each tube j_y in this plane we assign a chemical potential

$$\mu_y(j_y) = \mu_z(i_z) - \frac{1}{2} m\omega_y^2 y_{j_y}^2 \tag{3.2.1}$$

with the local density approximation. The density of a tube is also obtained through the local density approximation

$$n_{y_j}(x) = n\left[\mu_y(j_y) - \frac{1}{2} m\omega_x^2 x^2\right]. \tag{3.2.2}$$

By summing the densities of all the tubes of the plane, we obtain the atom number of the plane

$$N_z(i_z) = \sum_{j_y, l_x} n\left[\mu_y(j_y) - \frac{1}{2} m\omega_x^2 x_{l_x}^2\right], \tag{3.2.3}$$

where l_x runs over all the sites of a tube. In practice, we first calculate the atom number $N_z(i_z)$ in plane i_z from the slicing model of Chapter 2. We then determine the chemical potential $\mu_z(i_z)$ by inverting the relation $N(\mu)$ numerically. In figure 3.4(a-c), we show the atom number distribution for 1D stacks in planes $i_z = 0$, 3 and 6 for $(V_x, V_y, V_z) = (10, 25, 27)\,E_R$. From the size of the BEC before turning on the horizontal optical lattices, we estimate that there can be up to ~ 80 tubes in the central plane. We observe cusps in the population distribution of the tubes along y in figure 3.4, which come from the incompressibility of the Mott phases.

3.2.2 Luttinger theory for a harmonically-trapped system

The theory presented in section 3.1 applies for a homogeneous system. In a harmonic trap $V(x) = (1/2)m\omega_x^2 x^2$ without a periodic potential, the density reads $n_{TF}(x) = \max[\mu_0 - V(x)/g, 0]$ in the Thomas-Fermi regime, i.e. if $\gamma \ll 1$ and $k_B T, \hbar\omega_x \ll \mu_0$, as seen in Chapter 1. Within the local density approximation, one defines a local interaction parameter

$$\gamma(x) = \frac{m g_{1D}}{\hbar^2 n_{TF}(x)}, \tag{3.2.4}$$

which is minimal at the center of the trap where the density is the highest. Similarly, the LL Hamiltonian can be generalized to an inhomogeneous system. In the weakly-interacting

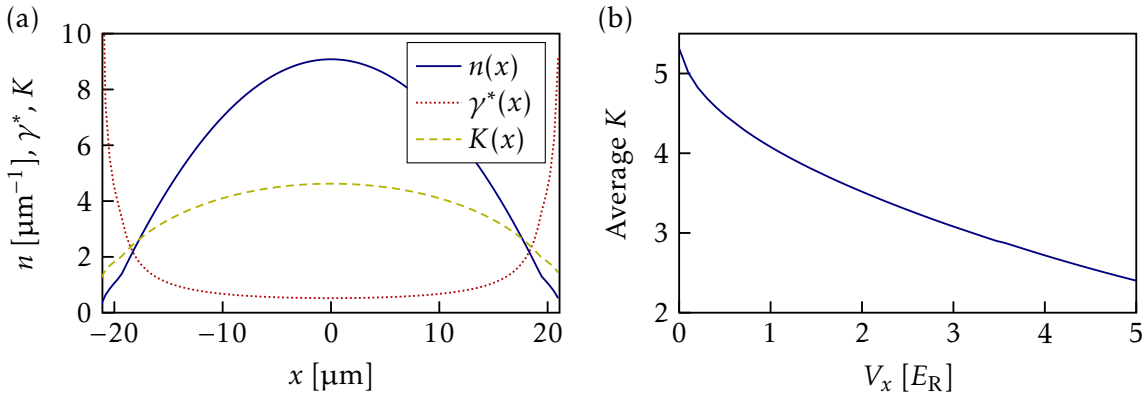

Figure 3.5 (a) Position-dependent parameters in a tube: density distribution $n(x)$ (solid line), interaction parameter $\gamma^*(x)$ (dotted line) and Luttinger exponent $K(x)$ (dashed line). (b) Average K for the stacks of tubes as a function of V_x.

regime, one can use the local density approximation to define $K(x) \approx \pi/\sqrt{\gamma(x)}$ and $v_s \approx \sqrt{g n_{TF}(x)/m}$, both maximal at the center of the trap (Petrov et al. 2004).

If a periodic potential is added, it can be accounted for with a renormalized position-dependent Luttinger parameter

$$\gamma^*(x) = \frac{m^*(Ud)}{\hbar^2(\tilde{n}(x)/d)}. \tag{3.2.5}$$

Using the equation of state and the loading model described above, we determine the population and density distribution of each tube. In figure 3.5(a), we show the density distribution $n(x)$ for the central tube when $V_x = 3E_R$, as well as $\gamma^*(x)$ and $K(x)$. We calculate an average Luttinger exponent $K_{tube} = [\sum_i n(x_i)K(x_i)]/[\sum_i n(x_i)]$ for each tube, and then similarly an average Luttinger exponent for the whole system. This is shown in figure 3.5(b) as a function of the lattice depth V_x. We only study small lattice depths ($V_x < 5E_R$) because Luttinger theory is not expected to apply for large lattice depths. We observe that K does not vary much and is comprised between 2 and 5 for small lattice depths.

The limit of this model of our experiment is that it is a zero-temperature model. In the next section, we study the first-order correlation function of the gas. This will evidence the need for a finite temperature generalization.

3.3 Analysis of the time-of-flight momentum distribution

In this section, we study the time-of-flight (tof) momentum distribution of our stacks of 1D lattices, which is particularly interesting because it corresponds to the initial state of the experiments described in Part II.

3.3.1 Quasi-momentum distribution

We actually go one step further than the tof momentum distribution and study the quasi-momentum distribution, thus removing the Wannier envelope $|\tilde{w}_0|^2$ discussed in Chapter 2. This can be done by fitting the momentum distribution to

$$n_{fit}(k) = |\tilde{w}_0(k)|^2 \sum_{s=1}^{s_{max}} 2\mathcal{C}_s \cos(skd), \tag{3.3.1}$$

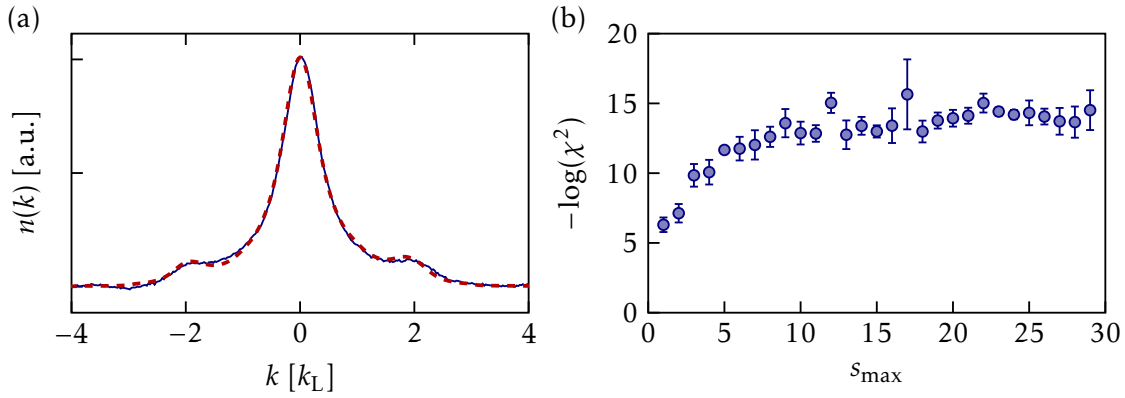

Figure 3.6 (a) 1D momentum distribution $n(k)$ for a lattice depth $V \approx 6.5E_R$. The dashed red line is a fit to equation (3.3.1). (b) χ^2 of the fit in logarithmic scale as a function of the maximum harmonic s_{max}.

where s is the distance (in sites). The quasi-momentum distribution then reads

$$S_{fit}(k) = \sum_{s=1}^{s_{max}} \mathcal{C}_s \cos(skd). \tag{3.3.2}$$

An example of a fit is shown in figure 3.6(a). In figure 3.6(b), we show that the resulting χ^2 of the fit decreases up to $s_{max} \simeq 10$, where a plateau is reached. We set $s_{max} = 10$ hereafter.

The seminal experiment for the analysis of the tof momentum distribution of 1D lattices is that of Paredes et al. (2004). In Appendix A.3, we provide a short comparison of our results with theirs, and we find a good agreement when looking at the tof momentum distribution: we observe a clear power-law behavior $|k|^{-\alpha}$ for $k/k_L \in [0.4, 1]$. However, we find that the convergence of the exponent α to 0.5 (a potential indication of a Luttinger exponent $K = 1$) is coincidental and a byproduct of the Wannier envelope. Note that Paredes et al. (2004) go further than this simple analysis by fitting the full density profile with the temperature and population of the central tube as free parameters. In their loading model, the population of all tubes is a function of that of the central tube. The fits are based on exact Tonks-Girardeau calculations on a lattice (see Appendix A.2) and reproduce the data very well. Although it is possible to reproduce a similar analysis with our data, we choose to focus our attention on unexplored avenues of investigation in the following.

3.3.2 One-body density matrix

We choose to directly study the lattice first-order correlation function $C_s = \langle \hat{a}_s^\dagger \hat{a}_0 \rangle / \bar{n}$, using the results of the fits mentioned above. We show $\mathcal{C}_s$ in figure 3.7 in y-semilogarithmic scale for six different lattice depths. We observe that, while the decay of $\mathcal{C}_s$ at long distance is exponential for all lattice depths, the behavior at short distance changes as we go from the quasi-condensate regime to the Mott insulating phase. A natural first step is to fit with an exponential function

$$\mathcal{C}_s = \exp\left(-\frac{s}{\ell_{exp}}\right), \tag{3.3.3}$$

as shown in figure 3.7 as solid lines. We observe that they only reproduce the data well for large lattice depths. The results of the fits are shown in figure 3.8(a) as circles.

We now want to derive a more appropriate fitting function that can reproduce the data for all lattice depths. To that end, let us first summarize the essential points regarding the

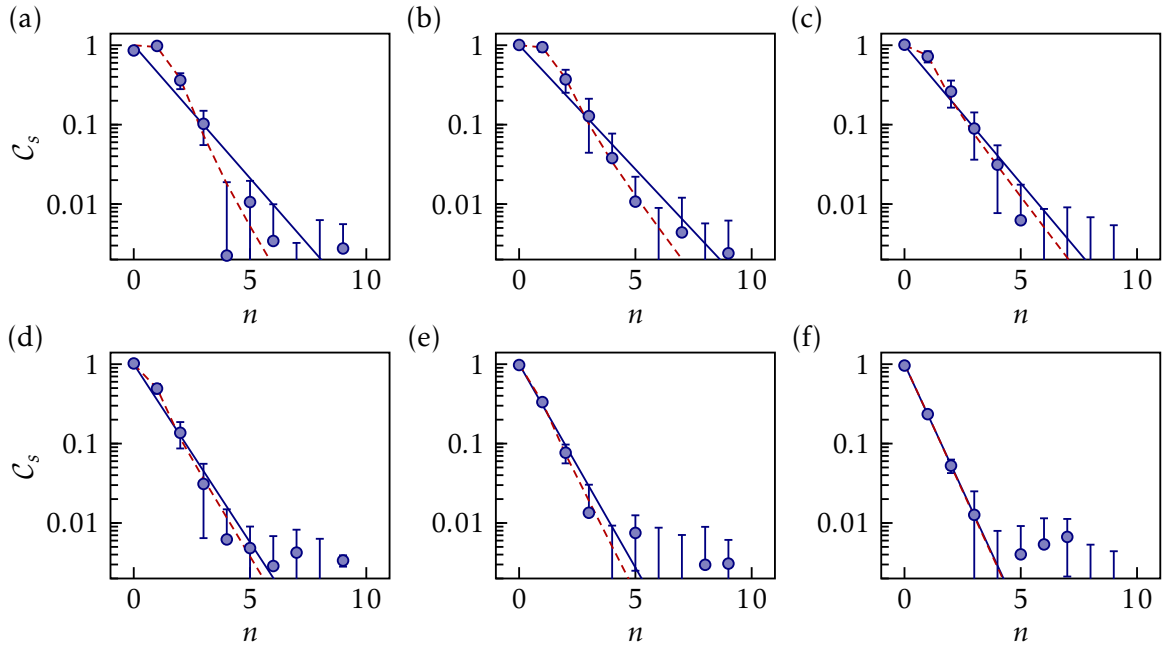

Figure 3.7 (a-f) C_s as a function of s for (a) $V = 0.0E_R$, (b) $V = 3.1E_R$, (c) $V = 5.5E_R$, (d) $V = 8.3E_R$, (e) $V = 10.8E_R$, and (f) $V = 13.3E_R$. The solid line corresponds to an exponential fit, and the dashed line to equation (3.3.8).

first-order correlation function of 1D Bose gases. In Chapter 1, we saw that the first-order correlation function of a finite-temperature quasi-condensate decayed exponentially at long distances

$$g_1(x) \underset{|x|\gg\xi}{\simeq} \exp\left(-\frac{|x|}{l_\phi}\right) \tag{3.3.4}$$

where $\xi = 1/(n\sqrt{2\gamma})$ is the healing length and $l_\phi = 2\hbar^2 n/mk_B T$ is the coherence length. For a shallow lattice, one can extrapolate this behavior and write

$$C_s \underset{s\gg\xi/d}{\simeq} \exp\left(-\frac{s}{l_\phi}\right) \tag{3.3.5}$$

with the coherence length $l_\phi/d = 2\hbar^2\bar{n}/m^* d^2 k_B T$, with $\bar{n}$ the filling and m^* the effective mass. On the other hand, for a zero-temperature Mott insulator with filling $\bar{n}$, one expects a quasi-exponential behavior of the form

$$C_s \simeq \left(\frac{J(\bar{n}+1)}{U}\right)^s = \exp\left[-s\ln\left(\frac{U}{J(\bar{n}+1)}\right)\right]. \tag{3.3.6}$$

The coherence length thus reads

$$l_\phi \approx \frac{d}{\ln\left[\frac{U}{J(\bar{n}+1)}\right]} \tag{3.3.7}$$

up to unspecified numerical corrections. Both predictions agree on an exponential decay at long distances, but the behavior at short distances differs. In particular, the first-order correlation function C_s does not start linearly in the quasi-condensate regime, as shown in figure 3.7(a) and (b) for example. To account for this, we use a heuristic function

$$\mathcal{C}_s = \exp\left[-h(s)\frac{s}{\ell_0}\right] \tag{3.3.8}$$

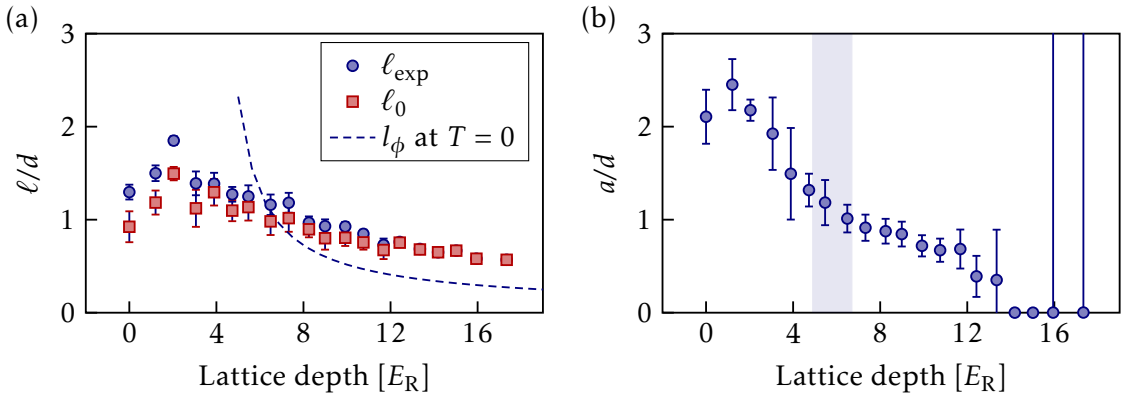

Figure 3.8 Fitting parameters. (a) Coherence length extracted from a simple exponential fit (circles) and from a fit to the heuristic function in equation (3.3.8). The dashed line corresponds to equation (3.3.7) with $\bar{n} = 3$. (b) Fitting parameter a from the heuristic fit. The shaded area corresponds to our estimation of the location of Mott transition: the lower (resp. upper) lattice depth of the area corresponds to the expected Mott transition for $\bar{n} = 1$ (resp. $\bar{n} = 2$).

to fit the data. Here, $h(s)$ is a function chosen to start at zero with a zero slope and quickly tend to 1 to give way to the exponential decay. We have taken (arbitrarily) the function

$$h(s) = \frac{s^4}{a^4 + s^4} \tag{3.3.9}$$

where a is a free fitting parameter, without a particular interpretation.

The results of the fits are shown in figure 3.8. We observe that a decreases with two "jumps" around $4E_\mathrm{R}$ and $13E_\mathrm{R}$ in figure 3.8(b). The first jump qualitatively corresponds to the expected location of the Mott transition, as discussed above. Beyond the second jump, the optimal value $a = 0$ indicates that the decay is exponential for any distance (which can be expected for a system composed only of insulating phases separated by normal regions). Figure 3.8(a) shows that the coherence length ℓ_0 (the relevant physical parameter) slowly decreases as the lattice depth increases. We also observe that it is slightly above the zero-temperature coherence length from equation (3.3.7), taken for $\bar{n} = 3$ (the maximum estimated filling).

Conclusion

In this chapter, we first explained how the first-order correlation function $g_1(x)$ of one-dimensional bosons could be obtained from Luttinger liquid theory applied to both continuum and lattice systems. We discussed into more details the 1D Bose-Hubbard model, including its phase diagram and its equation of state $n(J, U)$. Then, we modeled our experimental system consisting of a 3D stack of 1D tubes of bosons on a lattice. With the local density approximation, we estimated the Luttinger parameter K for small lattice depths by averaging over all the tubes. Finally, by fitting the experimental time-of-flight momentum distribution, we measured the first-order correlation function of the system for different lattice depths. We found that it always decays exponentially at long distances, owing to either the finite temperature or the Mott phase (or both).

Part II

Open Bose gases in optical lattices

CHAPTER 4

Anomalous momentum diffusion in optical lattices

Introduction

No physical system (except the Universe) can be considered closed for all timescales. The interaction of a system with its environment generally results in dissipation and damping, i.e. non-unitary dynamics. This dissipation is the main limit to quantum simulation on large systems. However, dissipation can also be a tool for quantum experiments. For instance, it is commonly used for laser cooling of atoms (Phillips et al. 1982, Raab et al. 1987, Lett et al. 1988). More recently, a number of theoretical studies have shown that a cleverly engineered dissipation can also be used to generate interesting many-body states, such as entangled states and squeezed states (Müller et al. 2012, Daley 2014). While the interaction of a single atom with its environment is well studied (Haroche et al. 2006), much remains to be discovered about the interplay of dissipation and interactions in open many-body systems.

An atomic system interacting with the electromagnetic vacuum is a paradigmatic example of an open quantum system (Cohen-Tannoudji et al. 1992). When an atom is illuminated by a laser field tuned near one of its internal resonances, the laser drives fluorescence cycles, where a laser photon is absorbed, promoting the atom to an internal excited state, and another photon is reemitted later. The emitted photon can be identical to the laser photons (stimulated emission process) or in a different mode of the electromagnetic field (spontaneous emission process). Spontaneous processes provide a relaxation mechanism for the otherwise coherent driving of Rabi oscillations by the laser field. Besides affecting the internal dynamics, spontaneous emission also has a dramatic impact on the motional quantum state of the atom. Beyond this single atom behavior, collective effects such as induced dipole-dipole interactions can take place in dense samples. In Chapter 6, we will focus on collective effects in a bulk system, but in this chapter we concentrate on momentum diffusion in 1D and 2D Bose-Hubbard systems. We show experimentally that short-range coherences exhibit an algebraic decay in presence of interactions, instead of the exponential decay expected for independent atoms. Such an algebraic (sometimes called "critical") decay has been predicted theoretically for several open many-body systems (Poletti et al. 2013, Cai et al. 2013, Henriet et al. 2019).

Section 4.1 introduces the notion of a quantum master equation to describe an open quantum system. In section 4.2, we apply this tool to describe the dissipation caused by spontaneous emission. With a series of approximations, we derive a simple quantum master equation modeling the momentum diffusion of a single atom in an optical lattice. In section 4.3, following Poletti et al. (2013), we study the quantum master equation for a many-body system. Using an adiabatic elimination of the coherences in the Fock basis and a factorization ansatz, we obtain a classical master equation ruling the dynamics of the probability distribution $p(n)$ to find n atoms on a given lattice site. Solving this master equation numerically, we find an algebraic regime of decoherence. Finally, in section 4.4, we present the experimental observation of the predicted algebraic decay of short-range coherences in a stack of 1D and 2D Bose-Hubbard systems. After detailing the experimental setup, we explain the fitting procedure used to analyze the measured momentum distribution. We study the loss of short-range spatial coherence in the system, as well as other dissipative effects such as interband transitions and atomic losses.

4.1 Open quantum systems and the master equation

We consider an open quantum system $\mathcal{S}$ and an environment $\mathcal{E}$, such that $\mathcal{S}+\mathcal{E}$ is a closed system. The total Hamiltonian is

$$\hat{H}_{\text{tot}} = \hat{H} + \hat{H}_{\mathcal{E}} + \hat{V}, \tag{4.1.1}$$

where $\hat{H}$ (resp. $\hat{H}_{\mathcal{E}}$) is the Hamiltonian describing the unitary evolution of $\mathcal{S}$ (resp. $\mathcal{E}$), and where $\hat{V}$ describes the interaction between $\mathcal{S}$ and $\mathcal{E}$. The total system is described by its density matrix $\hat{\rho}_{\text{tot}}(t)$, and we are particularly interested in the evolution of the reduced density matrix of $\mathcal{S}$, $\hat{\rho}(t) = \text{Tr}_{\mathcal{E}}[\hat{\rho}_{\text{tot}}]$.

4.1.1 Born-Markov approximation

To simplify the description of $\hat{\rho}(t)$, we make three essential approximations (Haroche et al. 2006).

- In the Born approximation, the interaction $\hat{V}$ between $\mathcal{S}$ and $\mathcal{E}$ is small and treated perturbatively.
- We also assume that $\mathcal{S}$ and $\mathcal{E}$ are not entangled at time $t = 0$, i.e. $\hat{\rho}_{\text{tot}}(0) = \hat{\rho}(0) \otimes \hat{\rho}_{\mathcal{E}}(0)$. We can then define a superoperator $\mathcal{L}$ called a quantum map describing the evolution of the reduced density matrix $\hat{\rho}(t)$ between times 0 and δt, i.e. $\rho(\delta t) = \mathcal{L}\rho(0)$.
- As they interact, $\mathcal{S}$ and $\mathcal{E}$ build up entanglement, preventing the use of the same quantum map $\mathcal{L}$ to describe the evolution between any time t and $t + \delta t$. In the Markov approximation, the timescale T_R of $\mathcal{S}$ is slow compared to the typical correlation time τ_c of $\mathcal{E}$, so that we can study a coarse-grained evolution of the system with a coarse-graining scale Δt such that $\tau_c \ll \Delta t \ll T_R$. The evolution of the environment is fast enough that correlations are lost between times t and $t + \Delta t$. In addition, the environment is supposed to be "large enough" to be negligibly affected by its interaction with $\mathcal{S}$: $\hat{\rho}_{\text{tot}}(t) \simeq \hat{\rho}(t) \otimes \hat{\rho}_{\mathcal{E}}(0)$. Note that correlations between $\mathcal{S}$ and $\mathcal{E}$ still play a role, but only in the infinitesimal evolution of $\hat{\rho}$ between t and $t + \Delta t$.

4.1.2 Quantum master equation

The coarse-grained evolution of $\hat{\rho}(t)$ is described by the Born-Markov quantum master equation, which is usually put in the generic Lindblad form

$$\frac{\partial \hat{\rho}}{\partial t} = -\frac{\mathrm{i}}{\hbar}[\hat{H}, \hat{\rho}] + \hat{D}[\hat{\rho}], \tag{4.1.2}$$

$$\hat{D}[\hat{\rho}] = \sum_{\alpha} \hat{L}_{\alpha} \hat{\rho} \hat{L}_{\alpha}^{\dagger} - \frac{1}{2} \hat{L}_{\alpha}^{\dagger} \hat{L}_{\alpha} \hat{\rho} - \frac{1}{2} \hat{\rho} \hat{L}_{\alpha}^{\dagger} \hat{L}_{\alpha}. \tag{4.1.3}$$

The $\hat{L}_{\alpha}$ are called quantum jump operators and describe the dissipation events occurring for $\mathcal{S}$ by making the density matrix jump from $\hat{\rho}$ to $\hat{L}_{\alpha} \hat{\rho} \hat{L}_{\alpha}^{\dagger}$. Thanks to the Markov approximation, the $\hat{L}_{\alpha}$ are time independent. We note that the $\hat{L}_{\alpha}$ are not uniquely defined, although there is usually a simple and physically intuitive choice.

4.1.3 Brief state of the art

Experimentally, quantum open-systems have been studied in the greatest details in cavity quantum electrodynamics (QED) experiments, either with atoms (Raimond et al. 2001) or with superconducting qubits (Blais et al. 2021). Using the high level of control on both the environment and the coupling to the environment, much has been unraveled about dissipation and decoherence in single particle systems (Haroche et al. 2006).

In quantum gases, atom losses provide a common example of dissipation. Here, the environment corresponds to states either not trapped or not detected. Although in many-body systems one could naively expect an enhancement of losses, recent experiments have shown that losses can be inhibited by the build-up of correlations through the *quantum Zeno effect*

(Syassen et al. 2008, Barontini et al. 2013, Sponselee et al. 2018). In a project not discussed in this manuscript, we studied the interplay of strong inelastic losses and interactions in a 1D Bose-Hubbard system with ytterbium atoms in the excited metastable state $^3P_0$ introduced in the previous chapter. We found that the two-body losses exhibited by this state can be reduced by several orders of magnitude compared to a non-interacting system due to the build-up of correlations between the atoms (Ghermaoui 2020, Rossini et al. 2021). In another project, also not discussed in this manuscript, we studied how the same losses can be largely avoided in a two-body system through adiabatic preparation (Bosch Aguilera et al. 2022). In this chapter, instead of losses, we focus on the loss of coherence induced by spontaneous emission, an aspect of dissipation that has been less studied in the context of many-body systems.

4.2 Quantum description of spontaneous emission

Spontaneous emission of a single two-level atom is a textbook example of an open quantum system where the Born-Markov approximation works very well. We review in this section the theoretical tools necessary to model the essential aspects pertaining to spontaneous emission.

4.2.1 Evolution of the internal state

We first consider a two-level atom at rest and ignore for the time being the motional degrees of freedom. We write the reduced density matrix

$$\hat{\rho} = \begin{pmatrix} \rho_{ee} & \rho_{eg} \\ \rho_{ge} & \rho_{gg} \end{pmatrix}, \tag{4.2.1}$$

where $\rho_{ee} + \rho_{gg} = 1$ and $\rho_{ge} = \rho_{eg}^*$. In the rotating-wave approximation, the Hamiltonian of an atom interacting with an electromagnetic field with a Rabi frequency Ω_L reads

$$\hat{H} = -\hbar\delta_\mathrm{L} |e\rangle\langle e| + \frac{\hbar\Omega_\mathrm{L}}{2} |e\rangle\langle g| + \frac{\hbar\Omega_\mathrm{L}^*}{2} |g\rangle\langle e|, \tag{4.2.2}$$

where $\delta_\mathrm{L} = \omega_\mathrm{L} - \omega_{eg}$ is the laser detuning. The quantum jump operator

$$\hat{L} = \sqrt{\Gamma_{eg}} |g\rangle\langle e| \tag{4.2.3}$$

describes the demotion of the atom from the excited state to the ground state upon spontaneous emission of a photon. Here, Γ_{eg} is the linewidth of the transition. The resulting Lindblad master equation corresponds to the optical Bloch equations (Metcalf et al. 1999)

$$\frac{\mathrm{d}\rho_{ee}}{\mathrm{d}t} = \mathrm{Im}[\Omega_\mathrm{L}\rho_{eg}] - \Gamma_{eg}\rho_{ee}, \tag{4.2.4}$$

$$\frac{\mathrm{d}\rho_{eg}}{\mathrm{d}t} = \mathrm{i}\delta_\mathrm{L}\rho_{eg} - \frac{\mathrm{i}\Omega_\mathrm{L}}{2}(\rho_{ee} - \rho_{gg}) - \frac{\Gamma_{eg}}{2}\rho_{eg}. \tag{4.2.5}$$

In the steady-state, the solution of these equations leads to the spontaneous emission rate γ_sp

$$\gamma_\mathrm{sp} = \frac{\Gamma_{eg}}{2}\frac{s}{1+s} \quad \text{and} \quad s = \frac{\Omega_\mathrm{L}^2/2}{\delta_\mathrm{L}^2 + (\Gamma_{eg}/2)^2}. \tag{4.2.6}$$

s is called the saturation parameter.

4.2.2 Atomic motion

For ultracold quantum gases, the motional degrees of freedom of the atom must be accounted for. The Hamiltonian then reads

$$\hat{H} = \frac{\hat{\boldsymbol{p}}^2}{2m} - \hbar\delta_{\mathrm{L}}\,|e\rangle\langle e| + \frac{\hbar\Omega_{\mathrm{L}}}{2}\mathrm{e}^{\mathrm{i}\boldsymbol{k}_{\mathrm{L}}\cdot\hat{\boldsymbol{r}}}\,|e;\boldsymbol{q}+\boldsymbol{k}_{\mathrm{L}}\rangle\langle g;\boldsymbol{q}| + \frac{\hbar\Omega_{\mathrm{L}}^*}{2}\mathrm{e}^{-\mathrm{i}\boldsymbol{k}_{\mathrm{L}}\cdot\hat{\boldsymbol{r}}}\,|g;\boldsymbol{q}\rangle\langle e;\boldsymbol{q}+\boldsymbol{k}_{\mathrm{L}}|. \tag{4.2.7}$$

The quantum jump operator $\hat{L}(\boldsymbol{n})$ for the spontaneous emission of a photon of wavevector $\boldsymbol{k} = k_{\mathrm{L}}\boldsymbol{n}$ reads

$$\hat{L}(\boldsymbol{n}) = \sqrt{\Gamma_{eg}}\mathrm{e}^{-\mathrm{i}k_{\mathrm{L}}\boldsymbol{n}\cdot\hat{\boldsymbol{r}}}\,|g;\boldsymbol{q}-k_{\mathrm{L}}\boldsymbol{n}\rangle\langle e;q|. \tag{4.2.8}$$

In the Lindblad equation, $\hat{L}(\boldsymbol{k})$ should be integrated over all the directions of $\boldsymbol{n}$ with a weight reflecting the emission pattern of a driven electric dipole (Dalibard et al. 1985).

To simplify the evolution of the total density matrix, one often considers a weakly saturated transition with $s \ll 1$. The excited state population and the internal coherences can then be adiabatically eliminated to obtain the equation of motion of the reduced density matrix of the ground internal state that captures the effect of spontaneous emission on the motional state of the atoms (Dalibard et al. 1985, Cohen-Tannoudji et al. 1992). The Hamiltonian then is $\hat{H} = \hat{\boldsymbol{p}}^2/2m$, and the quantum jump operator reads

$$\hat{L}(\boldsymbol{n}) = \sqrt{\gamma_{\mathrm{sp}}}\mathrm{e}^{-\mathrm{i}(k\boldsymbol{n}-\boldsymbol{k}_{\mathrm{L}})\cdot\hat{\boldsymbol{r}}}\,|g;\boldsymbol{q}+\boldsymbol{k}_{\mathrm{L}}-k_{\mathrm{L}}\boldsymbol{n}\rangle\langle g;\boldsymbol{q}|. \tag{4.2.9}$$

The quantum jump operator now describes how the absorption of a laser photon and the emission of a spontaneous photon modify the motional state of the atom.

4.2.3 Single-atom master equation in an optical lattice

4.2.3.1 Tight-binding description

As we have seen in Chapter 1, the Hamiltonian describing bosons in optical lattices is the tight-binding Hamiltonian

$$\hat{H}_{\mathrm{TB}} = -J\sum_{\mu,i}(\hat{a}^\dagger_{\mu,i}\hat{a}_{\mu,i+1} + \hat{a}^\dagger_{\mu,i+1}\hat{a}_{\mu,i}) + \sum_{\mu,i}E_\mu\hat{n}_{\mu,i} \tag{4.2.10}$$

Generalizing the spontaneous emission quantum jump operator from equation (4.2.9) to a driven tight-binding system, we write

$$\hat{L}(\boldsymbol{n}) = \sqrt{\gamma_{\mathrm{sp}}}\sum_{\mu,\nu,i,j}|w_i^\mu\rangle\langle w_i^\mu|\mathrm{e}^{-\mathrm{i}(k_{\mathrm{L}}\boldsymbol{n}-\boldsymbol{k}_{\mathrm{L}})\cdot\hat{\boldsymbol{r}}}|w_j^\nu\rangle\langle w_j^\nu|, \tag{4.2.11}$$

$$= \sqrt{\gamma_{\mathrm{sp}}}\sum_{\mu,\nu,i,j}\langle w_i^\mu|\mathrm{e}^{-\mathrm{i}(k_{\mathrm{L}}\boldsymbol{n}-\boldsymbol{k}_{\mathrm{L}})\cdot\hat{\boldsymbol{r}}}|w_j^\nu\rangle\,\hat{a}^\dagger_{i,\mu}\hat{a}_{j,\nu}, \tag{4.2.12}$$

where $\hat{a}_{\mu,i}$ annihilates an atom on site i and in band μ, described by the Wannier state $|w_i^\mu\rangle$, and E_μ is the energy of band μ (Pichler et al. 2010). We consider in this section a 1D lattice model to simplify notations, but the model can be extended to 2D or 3D without conceptual difficulty.

4.2.3.2 Approximations

We make three key approximations to simplify the problem:

- A first approximation consists in neglecting transitions to excited band in a deep lattice

$$\hat{L}(\boldsymbol{n}) = \sqrt{\gamma_{\mathrm{sp}}} \sum_{i,j} \langle w_i | \mathrm{e}^{-\mathrm{i}(k_{\mathrm{L}}\boldsymbol{n}-\boldsymbol{k}_{\mathrm{L}})\cdot\hat{\boldsymbol{r}}} | w_j \rangle \, \hat{a}_i^\dagger \hat{a}_j, \tag{4.2.13}$$

  where $w_i \equiv w_i^0$ and $\hat{a}_i \equiv \hat{a}_{i,0}$. The validity of this single-band approximation is discussed in Bouganne (2018).

- The optical lattice leads the atoms to have well-localized on-site wavefunction, as discussed in Chapter 1. In a deep enough lattice, we have $\langle w_i | \mathrm{e}^{-\mathrm{i}(\boldsymbol{k}-\boldsymbol{k}_{\mathrm{L}})\cdot\hat{\boldsymbol{r}}} | w_j \rangle \simeq \delta_{ij} \mathrm{e}^{-\mathrm{i}(\boldsymbol{k}-\boldsymbol{k}_{\mathrm{L}})\cdot\boldsymbol{r}_i}$, which corresponds to on-site dissipation. In the Lindblad quantum master equation, we can then write

$$\int \mathrm{d}^2 n \, \mathcal{N}(\boldsymbol{n}) \hat{L}(\boldsymbol{n}) \hat{\rho} \hat{L}^\dagger(k\boldsymbol{n}) = \gamma_{\mathrm{sp}} \int \mathrm{d}^2 n \, \mathcal{N}(\boldsymbol{n}) \sum_{ij} \mathrm{e}^{-\mathrm{i}(k\boldsymbol{n}-\boldsymbol{k}_{\mathrm{L}})\cdot(\boldsymbol{r}_i-\boldsymbol{r}_j)} \hat{n}_i \hat{\rho} \hat{n}_j \tag{4.2.14}$$

$$\simeq \gamma_{\mathrm{sp}} \sum_{ij} F(r_i - r_j) \hat{n}_i \hat{\rho} \hat{n}_j, \tag{4.2.15}$$

  where $\mathcal{N}(\boldsymbol{n})$ is the direction factor for dipolar emission. We have defined the function

$$F(\boldsymbol{r}) = \int \mathrm{d}^2 n \, \mathcal{N}(\boldsymbol{n}) \mathrm{e}^{-k\boldsymbol{n}\cdot\boldsymbol{r}} \tag{4.2.16}$$

  and considered a 2D system in the x-y plane and $\boldsymbol{k}_{\mathrm{L}} = k_{\mathrm{L}} \boldsymbol{e}_z$, leading to $\boldsymbol{k}_{\mathrm{L}} \cdot \boldsymbol{r} = 0$.

- Finally, we make a zero-range approximation $F(\boldsymbol{r}_i - \boldsymbol{r}_j) \simeq \delta_{ij}$ for dipolar emission.

After these three approximations, our single-atom model in an optical lattice reads

$$\hat{H}_{\mathrm{TB}} = -J \sum_i (\hat{a}_i^\dagger \hat{a}_{i+1} + \hat{a}_{i+1}^\dagger \hat{a}_i) \tag{4.2.17}$$

$$\hat{L}_i = \sqrt{\gamma_{\mathrm{sp}}} \hat{n}_i. \tag{4.2.18}$$

4.2.4 Exponential decoherence of a single atom

Let us now study the single-atom evolution of the system under the quantum master equation (4.2.18). For a given observable $\hat{O}$, the Lindblad master equation for its expectation value $\langle \hat{O} \rangle = \mathrm{Tr}(\hat{\rho} O)$ can be always rewritten exactly as

$$\frac{\mathrm{d}\langle \hat{O} \rangle}{\mathrm{d}t} = -\frac{\mathrm{i}}{\hbar} \mathrm{Tr}\Big(\hat{H}\hat{\rho}\hat{O} - \hat{\rho}\hat{H}\hat{O} \Big) + \sum_\alpha \mathrm{Tr}\Big(\hat{L}_\alpha \hat{\rho} \hat{L}_\alpha^\dagger \hat{O} - \frac{1}{2} \{ \hat{L}_\alpha^\dagger \hat{L}_\alpha, \hat{\rho} \} \hat{O} \Big) \tag{4.2.19}$$

$$= -\frac{\mathrm{i}}{\hbar} \Big\langle [\hat{O}, \hat{H}] \Big\rangle + \frac{1}{2} \sum_\alpha \Big\langle [\hat{L}_\alpha^\dagger, \hat{O}] \hat{L}_\alpha + \hat{L}_\alpha^\dagger [\hat{O}, \hat{L}_\alpha] \Big\rangle. \tag{4.2.20}$$

For a single atom in an optical lattice, our observable of interest is $\hat{O} = \hat{a}_i^\dagger \hat{a}_j$. The evolution of its expectation value is then given by

$$\frac{\mathrm{d}\langle \hat{a}_i^\dagger \hat{a}_j \rangle}{\mathrm{d}t} = -\frac{\mathrm{i}}{\hbar} \Big\langle [\hat{a}_i^\dagger \hat{a}_j, \hat{H}_{\mathrm{TB}}] \Big\rangle + \frac{\gamma_{\mathrm{sp}}}{2} \sum_m \Big\langle [\hat{n}_m, \hat{a}_i^\dagger \hat{a}_j] \hat{n}_m + \hat{n}_m [\hat{a}_i^\dagger \hat{a}_j, \hat{n}_m] \Big\rangle. \tag{4.2.21}$$

We now consider the first-order correlation function between sites distant by s,

$$C_s = \frac{1}{N_\mathrm{s}} \sum_i \langle \hat{a}^\dagger_{i+s} \hat{a}_i \rangle, \tag{4.2.22}$$

such that the first term in equation (4.2.21) averages out (N_s is the number of sites). Making extensive use of $[\hat{a}^\dagger_i \hat{a}_j, \hat{n}_m] = (\delta_{jm} - \delta_{im}) \hat{a}^\dagger_i \hat{a}_j$, we find that the evolution of C_s is then simply given by

$$\frac{\mathrm{d}C_s}{\mathrm{d}t} = -\gamma_\mathrm{sp}(1 - \delta_{s,0}) C_s. \tag{4.2.23}$$

From this equation, it is clear that $C_0(t) = C_0(0) = 1$ and $C_{s>0}(t) = C_{s>0}(t=0) \exp\left(-\gamma_\mathrm{sp} t\right)$. Moreover, as discussed in Chapter 2, the quasi-momentum distribution $S(\boldsymbol{k})$ is the Fourier transform of the first-order correlation function. We then find

$$S(\boldsymbol{k}, t) = \frac{1}{N} \sum_{ij} \mathrm{e}^{\mathrm{i}\boldsymbol{k}\cdot(\boldsymbol{r}_i - \boldsymbol{r}_j)} \langle \hat{a}^\dagger_i \hat{a}_j \rangle_t = \sum_s \mathrm{e}^{\mathrm{i}ks} C_s(t) \tag{4.2.24}$$

$$= \left(1 - \mathrm{e}^{-\gamma_\mathrm{sp} t}\right) + S(\boldsymbol{k}, 0) \mathrm{e}^{-\gamma_\mathrm{sp} t}. \tag{4.2.25}$$

We thus expect the quasi-momentum distribution of a single atom (or equivalently, of a non-interacting gas of atoms) to converge exponentially to a flat momentum distribution.

4.3 Prediction of an algebraic regime of decoherence

We now turn to the study of an interacting many-atom system. In the single-band approximation and in the presence of interactions, the tight-binding model becomes the Bose-Hubbard model

$$\hat{H}_\mathrm{BH} = -J \sum_i (\hat{a}^\dagger_i \hat{a}_{i+1} + \hat{a}^\dagger_{i+1} \hat{a}_i) + \frac{U}{2} \sum_i \hat{n}_i (\hat{n}_i - 1) \tag{4.3.1}$$

already introduced in Chapter 1. In principle, the Hamiltonian also includes the long-range interaction potential between the induced electric dipoles carried by each atom (O'Dell et al. 2000). We neglect these processes and the analogous collective effects in the dissipative term (Bouganne et al. 2020). Using the same quantum jump operator as in the single-atom case, the dissipative Bose-Hubbard master equation reads

$$\partial_t \hat{\rho} = -\frac{\mathrm{i}}{\hbar} [\hat{H}_\mathrm{BH}, \hat{\rho}] + \gamma_\mathrm{sp} \sum_i \hat{n}_i \hat{\rho} \hat{n}^\dagger_i - \frac{1}{2} \hat{n}^\dagger_i \hat{n}_i \hat{\rho} - \frac{1}{2} \hat{\rho} \hat{n}^\dagger_i \hat{n}_i. \tag{4.3.2}$$

This is the simplified many-body master equation we will study in the remainder of this chapter.

4.3.1 Three different decoherence regimes

In a series of papers (Poletti et al. 2012; 2013), Poletti and collaborators have studied the master equation (4.3.2). In addition to the natural timescale γ_sp^{-1} set by the dissipation rate, they have identified a second emergent timescale

$$t^* = \left(\frac{\bar{n} U}{J}\right)^2 \frac{1}{2z\gamma_\mathrm{sp}} \gg \gamma_\mathrm{sp}^{-1}, \tag{4.3.3}$$

where $\bar{n}$ is the filling and z is the number of nearest-neighbors. The two characteristic timescales define three regimes in the dynamics of the system:

1. At short times ($t \lesssim \gamma_{\rm sp}^{-1}$), long-range coherences decay on the timescale $\gamma_{\rm sp}$. We will focus on this early decay in the next chapter.
2. At intermediate times ($\gamma_{\rm sp}^{-1} \lesssim t \lesssim t^*$), long-range coherences have disappeared and short-range coherences decay algebraically. We focus on this regime in this chapter.
3. At longer times ($t \gtrsim t^*$), glasslike dynamics sets in: the convergence of the system towards the fully-mixed (infinite temperature) steady-state is dominated by rare configurations. This regime is out of experimental reach and we will not discuss it further.

The algebraic regime n°2 results from the balance between the tunneling J, which tends to maintain spatial coherences, the dissipation $\hat{L}_i = \hat{n}_i$ which tends to localize atoms by "measuring" on-site populations, and the interactions U which tend to prevent the build-up of large on-site populations. In the following, we analyze the algebraic regime in more details with the method developed in Poletti et al. (2013).

4.3.2 Adiabatic elimination of coherences and factorization ansatz

We write the density matrix in a Fock-space basis

$$\hat{\rho} = \sum_{\boldsymbol{m},\boldsymbol{n}} \rho_{\boldsymbol{m}}^{\boldsymbol{n}} |\boldsymbol{n}\rangle\langle\boldsymbol{m}|, \tag{4.3.4}$$

where $\boldsymbol{n} = (n_1, ..., n_{N_s})$ is the configuration with n_i atoms on site i (N_s is the number of sites). The steady-state density matrix is diagonal in this basis and

$$\hat{\rho}_{\rm ss} \propto \sum_{\boldsymbol{n}} |\boldsymbol{n}\rangle\langle\boldsymbol{n}|. \tag{4.3.5}$$

Poletti et al. (2013) make two key approximations to study the evolution of $\hat{\rho}$ towards $\hat{\rho}_{\rm ss}$.

The first approximation consists in adiabatically eliminating the dynamics of off-diagonal elements, i.e. the coherences, by using the separation of timescales between dissipation and tunneling ($\gamma_{\rm sp} \gg J$). For timescales $t \gg \gamma_{\rm sp}^{-1}$, the fast evolution of coherences averages out and we have

$$\rho_{\boldsymbol{n}}^{\boldsymbol{n}+\boldsymbol{e}_i^j} = \frac{J\sqrt{n_j(n_i+1)}}{U(n_i - n_j + 1) - \mathrm{i}\hbar\gamma_{\rm sp}} \left(\rho_{\boldsymbol{n}}^{\boldsymbol{n}} - \rho_{\boldsymbol{n}+\boldsymbol{e}_i^j}^{\boldsymbol{n}+\boldsymbol{e}_i^j}\right). \tag{4.3.6}$$

From equation (4.3.6), Poletti et al. (2013) obtain a master equation for the populations

$$\frac{\mathrm{d}}{\mathrm{d}\tau}\rho_{\boldsymbol{n}}^{\boldsymbol{n}} = -\frac{\bar{n}^2}{z} \sum_{(i,j)} \frac{n_j(n_i+1)}{(n_i - n_j + 1)^2 + \epsilon^2} \left(\rho_{\boldsymbol{n}}^{\boldsymbol{n}} - \rho_{\boldsymbol{n}+\boldsymbol{e}_i^j}^{\boldsymbol{n}+\boldsymbol{e}_i^j}\right), \tag{4.3.7}$$

where $\tau = t/t^*$ and $\epsilon = \hbar\gamma_{\rm sp}/U$. We have also defined $\boldsymbol{e}_i^j = (0, ..., 1, ..., -1, ..., 0)$, with 1 and -1 at position i and j respectively. In equation (4.3.7), (i,j) is a double summation over nearest-neighbors.

The second approximation of Poletti et al. (2013) consists in using the factorization ansatz

$$\hat{\rho} \simeq \prod_{\text{sites } i} \left(\sum_{n_i=0}^{\infty} \rho(n_i) |n_i\rangle\langle n_i| \right) \tag{4.3.8}$$

to solve equation (4.3.7). Here, $\rho(n_i)$ is the probability to have n_i atoms on site i, so that $\sum_i \rho(n_i) = 1$ and $\sum_i \rho(n_i) n_i = \bar{n}$. Injecting this ansatz in equation (4.3.7), one finds a classical master equation

$$\frac{\mathrm{d}\rho(n)}{\mathrm{d}\tau} = \sum_{m,\nu=\pm1} \bar{n}^2 \frac{(n+\delta_{1,\nu})(m+\delta_{-1,\nu})}{(n-m+\nu)^2 + \epsilon^2} [\rho(n+\nu)\rho(m-\nu) - \rho(n)\rho(m)], \tag{4.3.9}$$

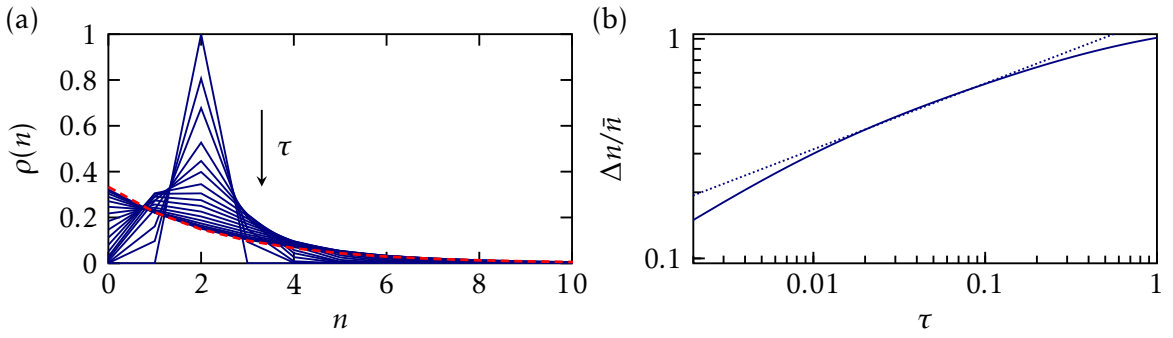

Figure 4.1 (a) Numerical integration of equation (4.3.9). The asymptotic distribution is plotted as a red dashed line. (b) Normalized atom number fluctuations $\Delta n/\bar{n}$. The dotted line is a power-law fit with exponent ~ 0.30.

for the on-site number distribution $\rho(n)$, where $\delta_{\pm1,\nu}$ is the Kronecker delta.

Figure 4.1(a) shows a numerical solution of equation (4.3.9) for $U/J = 10$, $\epsilon = 0.01$ and $\bar{n} = 2$ ($t^* = 250\gamma_{\mathrm{sp}}^{-1}$). The initial state is a Fock state with $\bar{n} = 2$. Asymptotically the distribution $\rho(n)$ converges when $t \to \infty$ towards the steady-state distribution

$$\rho_{\mathrm{ss}}(n) \simeq \frac{\bar{n}^n}{1+\bar{n}^{n+1}}. \tag{4.3.10}$$

Poletti et al. (2013) identify an anomalous power-law behavior for $\tau \ll 1$ by looking at the on-site atom number fluctuations

$$\Delta n^2 = \sum_n (n-\bar{n})^2 \rho(n), \tag{4.3.11}$$

shown in figure 4.1(b) in double-logarithmic scale. The fitted power-law exponent is ~ 0.3, which corresponds to a slower broadening than the Brownian motion exponent 1/2 expected for non-interacting atoms.

4.3.3 Decay of single-particle coherence

Experimentally, we do not have access to the populations of each site and therefore cannot measure Δn. However, we do have access to the momentum distribution, which is directly related to the spatial coherences of the system. Assuming long-range coherences have disappeared, we focus on short-range coherences, and in particular the nearest-neighbor coherence

$$C_1 = \frac{1}{N_{\mathrm{s}}}\sum_i \langle \hat{a}_i^\dagger \hat{a}_{i+1}\rangle = \frac{1}{N_{\mathrm{s}}}\sum_{\boldsymbol{n},\boldsymbol{m},i} \langle \boldsymbol{n}|\hat{a}_i^\dagger \hat{a}_{i+1}|\boldsymbol{m}\rangle = \frac{1}{N_{\mathrm{s}}}\sum_{\boldsymbol{n},i} \sqrt{n_{i+1}(n_i+1)}\,\rho_{\boldsymbol{n}}^{\boldsymbol{n}+\boldsymbol{e}_i^{i+1}}. \tag{4.3.12}$$

In the adiabatic elimination mentioned above, the coherences follow adiabatically the evolution of the populations. Using equation (4.3.6) and the factorization ansatz, one finds

$$C_1 = \frac{J}{U}\sum_{n,m=0}^{\infty} \frac{(m+1)(n+1)}{n-m-\mathrm{i}\epsilon}[\rho(n)\rho(m+1)-\rho(n+1)\rho(m)], \tag{4.3.13}$$

as detailed in Bouganne (2018). Figure 4.2(a) shows a numerical solution of equation (4.3.13) for $U/J = 10$ and $\epsilon = 0.01$. The filling $\bar{n}$ is varied from 2 to 8. We observe a clear power-law behavior, at least for short-enough times.

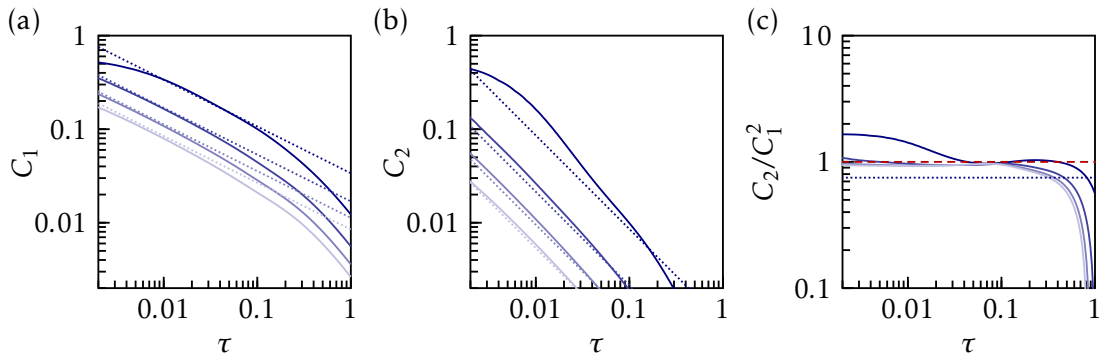

Figure 4.2 Numerical solutions of (a) $C_1(\tau)$, (b) $C_2(\tau)$ and (c) $C_2(\tau)/C_1^2(\tau)$, using equation (4.3.13) and equation (4.3.14) with $U/J = 10$ and $\epsilon = 0.01$. We vary the filling $\bar{n}$: from darker to brighter lines, $\bar{n} = 2$, 4, 6 and 8. The dotted lines correspond to the large filling limit. In (c), the dashed line corresponds to $C_2/C_1^2 = 1$.

We have also computed the next-nearest-neighbor correlator C_2. Applying recursively the same procedure as for C_1, we find

$$C_2 = 2\left(\frac{J}{U}\right)^2 \sum_{m,n,q=0}^{\infty} \frac{(m+1)(n+1)(q+1)}{(q-m-\mathrm{i}\epsilon)(q-n-\mathrm{i}\epsilon)}[\rho(n+1)\rho(q)-\rho(n)\rho(q+1)][\rho(m+1)-\rho(m)]. \quad (4.3.14)$$

Figure 4.2(b) shows a numerical solution of equation (4.3.13) for $U/J = 10$ and $\epsilon = 0.01$.

4.3.4 Scaling regime

4.3.4.1 Large filling limit

In the large filling limit ($\bar{n} \gg 1$), the discrete variable n maps to a continuous variable $x = n/\bar{n}$, the on-site number distribution $\rho(n)$ maps to $p(x)/\bar{n}$, and the classical master equation (4.3.9) maps to a Fokker-Planck equation (Poletti et al. 2013). Making the continuum approximation to also compute C_s, the solution of the Fokker-Planck equation reads

$$p(x,\tau) = \frac{\mathrm{e}^{-(x-1)^4/16\tau}}{4\Gamma(5/4)\tau^{1/4}}, \quad (4.3.15)$$

where Γ is the Gamma function. Thus, instead of a function of x and τ separately, the distribution is a function of the scaling variable $u = (x-1)/\tau^{1/4}$. In the large filling and weak dissipation limit, one then finds the following expression for the nearest and next-nearest-neighbor correlators

$$C_1^{\bar{n}\gg 1} \propto \frac{1}{\sqrt{t}}, \quad (4.3.16)$$

$$C_2^{\bar{n}\gg 1} = \frac{3}{4}\left(C_1^{\bar{n}\gg 1}\right)^2, \quad (4.3.17)$$

as detailed in Bouganne (2018). This large-filling limit is shown as a dotted line in figure 4.2(a-b).

4.3.4.2 Relevance of the scaling solution for small fillings

The idealized limit of large fillings is not reachable experimentally. When $\bar{n} > 2$, two-body light induced losses take place in addition to three-body losses. Bouganne (2018) studied the

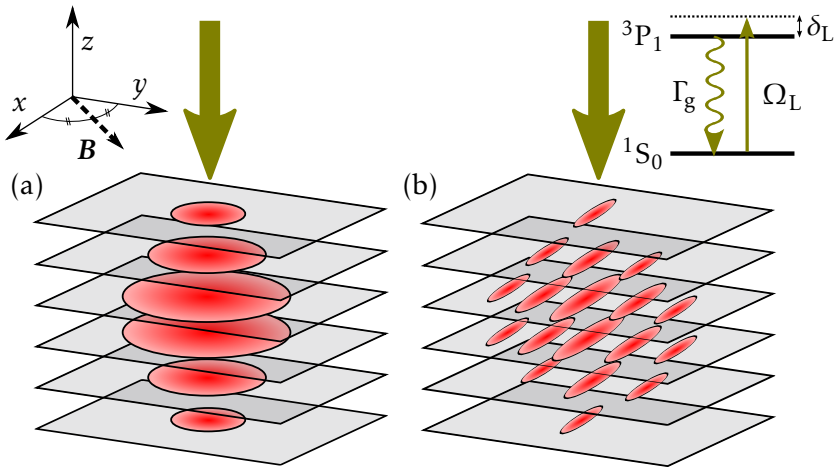

Figure 4.3 Scheme of the experiment for a stack of (a) 2D lattices and (b) 1D lattices. $V_x \simeq V_y$ for 2D lattices, and $V_y \simeq V_z$ for 1D lattices. The dissipation laser is sent from the top and addresses the green transition $^1S_0$–$^3P_1$. Its detuning is δ_L and the Rabi frequency is Ω_L. The polarization is parallel to a small horizontal magnetic field.

influence of two and three-body recombination processes on the dynamics of $\rho(n)$. Numerically, he found that the algebraic exponents for Δn and C_1 were not significantly affected by the losses.

Although we are limited to $\bar{n} = 2 - 3$ at most, we can still observe the algebraic behavior but in a reduced time window, as shown in figure 4.2. Moreover, Bouganne (2018) found that the stronger the losses, the shorter the time window since their effect is to reduce the filling. It is remarkable that the scaling solution provides a very good quantitative prediction in the relevant time window. However, we note that, for finite fillings, numerical solutions find $C_2 \simeq C_1^2$ rather than $C_2 \simeq (3/4)C_1^2$, as shown in figure 4.2(c).

4.4 Experimental study of the algebraic regime

The experimental observation of the algebraic regime for a stack of 2D Mott insulators was previously reported in Bouganne et al. (2020). During my PhD, I studied the algebraic regime for a stack of 1D Mott insulators. I also took data on 2D Mott insulators to compare with the results of Bouganne et al. (2020). Since the results are very similar for 2D and 1D Mott insulators, I present them jointly in this section. The key difference between 2D and 1D is the initial coherence of the system, as shown in Chapter 2.

4.4.1 Experimental procedure

We begin by preparing the stack of 1D or 2D Bose-Hubbard systems described in Chapter 2. The vertical lattice depth is always set to $27\,E_R$, and the horizontal lattice depth in the y direction can be set to $25\,E_R$ to prepare the 1D systems. The dissipation laser is sent from the top of the experiment in the z direction and the atoms are illuminated for a time t. We then release the atoms from all the optical lattices and they are imaged along the vertical axis after a 20 ms tof. A schematic of the experiment is shown in figure 4.3 for both the 1D and 2D configurations.

The dissipation laser is close to resonance with the 556 nm green $J = 0 \leftrightarrow J = 1$ transition. The laser is linearly polarized and the polarization is parallel to a horizontal magnetic field of about 1 G in the direction $(\boldsymbol{e}_x + \boldsymbol{e}_y)/2$, so that we only excite the π transition. The detuning

is fixed at $\delta_L = 15\Gamma_g$. The intensity is also fixed so that the spontaneous emission rate

$$\gamma_{sp} \simeq \frac{\Gamma_g}{2} \frac{\Omega_L^2/2}{\delta_L^2 + \Gamma_g^2/2} \simeq 0.52\,\mathrm{ms}^{-1} \tag{4.4.1}$$

is fixed. The Rabi frequency Ω_L is calibrated experimentally, as shown in Appendix B.1, and is small enough so that $s \ll 1$. Varying γ_{sp} through the intensity, the only observed effect was a rescaling of the dynamics (Bouganne 2018). The chosen γ_{sp} is the same as the one used in Bouganne et al. (2020).

4.4.2 Observation of two decoherence regimes with the peak amplitude of the momentum distribution

Before diving into a more complex analysis in the next subsection, figure 4.4(a) shows that we observe the algebraic regime with simple observables such as the amplitude of the central peak of the momentum distribution. We normalize the peak amplitude to the decaying atom number and to the initial value,

$$\tilde{n}_{k=0}(t) = \frac{n(k=0,t)/N(t)}{n(k=0,0)/N(0)}, \tag{4.4.2}$$

where $N(t) = \int \mathrm{d}k\, n(k,t)$ is the total atom number at time t. By comparing the evolution of $\tilde{n}_{k=0}(t)$ with the exponential decay from equation (4.2.25) expected for non-interacting atoms, we show that correlations play a key role in the dynamics of our Bose-Hubbard systems.

The evolution of $\tilde{n}_{k=0}(t)$ is phenomenologically fitted to a function that decays linearly for short times and as a power law for long times,

$$\tilde{n}_{k=0}(t) = \frac{1}{(1+\gamma_{exp}t/\kappa)^{\kappa}}. \tag{4.4.3}$$

The fits are shown as solid lines in figure 4.4(a). In the following, we use this fit to define the beginning of the algebraic regime as

$$t_{alg} = \frac{\kappa}{\gamma_{exp}}. \tag{4.4.4}$$

In figure 4.4(b), we show t_{alg} for the different lattice depths in 1D and 2D. We observe that the algebraic regime in 2D starts much later than in 1D, at least for small lattice depths where the initial coherence is substantial.

4.4.3 Extraction of the spatial coherences from fits of the momentum distribution

4.4.3.1 Generalized structure factor

In order to better understand the evolution of the system, we now turn to a more comprehensive analysis of the momentum distribution. After a long tof, the momentum distribution is given by

$$n(\boldsymbol{k}) = \sum_{\text{bands}\, n,m} S_{n,m}(\boldsymbol{k}) \tilde{w}_n(\boldsymbol{k}) \tilde{w}_m^*(\boldsymbol{k}), \tag{4.4.5}$$

where $\tilde{w}_n(k)$ is the Fourier transform of the Wannier function of the n-th band (Pedri et al. 2001). We have defined a generalized structure factor

$$S_{n,m}(\boldsymbol{k}) = \sum_{\text{sites}\, i,j} \mathrm{e}^{\mathrm{i}\boldsymbol{k}\cdot(\boldsymbol{r}_i - \boldsymbol{r}_j)} \langle \hat{a}_{\boldsymbol{i},n}^\dagger \hat{a}_{\boldsymbol{j},m} \rangle, \tag{4.4.6}$$

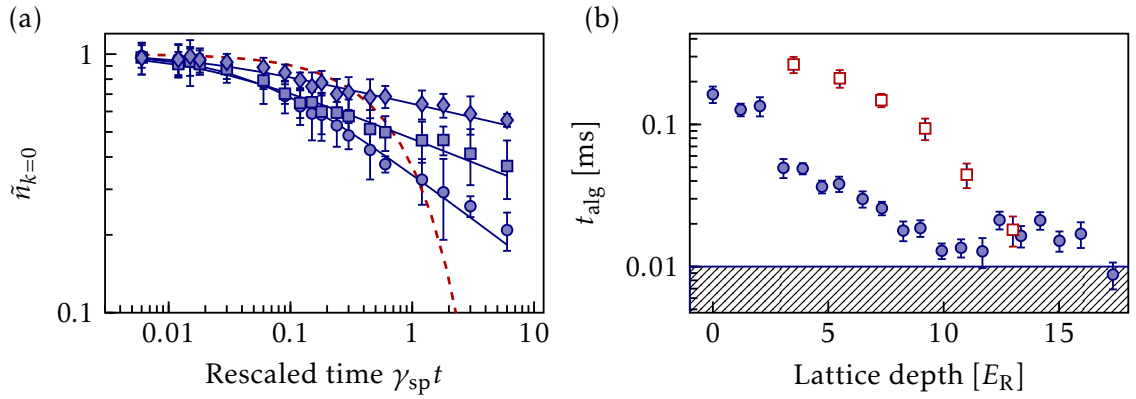

Figure 4.4 (a) Time evolution of the normalized peak amplitude of the momentum distribution for 1D lattices for $V = 3.1E_R$ (circles), $V = 8.3E_R$ (squares) and $V = 13.3E_R$ (diamonds). The solid lines are phenomenological fits to equation (4.4.3). The dashed line shows the exponential decay expected for non-interacting atoms, $e^{-\gamma_{sp}t}$. (b) Starting time of the algebraic regime, $t_{alg} = \kappa/\gamma_{exp}$, in the following analysis, for 1D (circles) and 2D (squares) data. The striped area corresponds to times shorter than 0.01 ms, the shortest experimental dissipation time.

which corresponds to the Fourier-transform of the first-order correlation function $\langle \hat{a}^\dagger_{i,n} \hat{a}_{j,m} \rangle$.

In order to simplify the model, we make a few assumptions. First, we assume that there is no inter-band coherence: this is natural because initially the excited bands are not populated. We also assume that there is no intra-band coherence for excited bands. These two assumptions lead to

$$\langle \hat{a}^\dagger_{i,n} \hat{a}_{j,m} \rangle \neq 0 \quad \text{only if} \quad n = m = 0. \tag{4.4.7}$$

Finally, we assume that the initial long-range coherences have vanished once we are in the algebraic regime. We are left with short-range coherences in the fundamental band $n = 0$, which allows us to truncate the sum in equation (4.4.6) to the first few terms.

4.4.3.2 One dimension

In 1D, the momentum distribution is fitted to the same function as in the previous chapter, with an additional contribution from the first three excited bands that become populated at long times,

$$n_{\text{fit,1D}}(k) = \sum_{m=1}^{m_{\max}} 2\mathcal{C}_m |\tilde{w}_0(k)|^2 \cos(mkd) + \sum_{n=0}^{3} \mathcal{P}_n |\tilde{w}_n(k)|^2, \tag{4.4.8}$$

with the normalization condition $\int \mathrm{d}k\, n_{\text{fit,1D}}(k) = N$. Here, $\mathcal{C}_m$ is the m-th neighbor coherence and $\mathcal{P}_n$ is the population of the n-th band. Typical momentum distributions, as well as corresponding fits are shown on figure 4.5. For short times, typically $t < 0.1$ ms$\sim t_{alg}$, the residuals can be relatively large around $k_x = 0$. However, for longer times corresponding to the algebraic regime of interest, the residuals are comparable to the image noise.

4.4.3.3 Two dimensions

In 2D, next-nearest-neighbors are diagonal sites ($\boldsymbol{j} = \boldsymbol{i} + (\pm 1, \pm 1)$), and next-next-nearest-neighbors are located at $\boldsymbol{j} = \boldsymbol{i} + (\pm 2, 0)$ and $\boldsymbol{j} = \boldsymbol{i} + (0, \pm 2)$. Moreover, because the initial coherence is higher in 2D, some long-range coherence still remains in the "algebraic" regime defined by $t > t_{alg}$. Inspired by the Bogoliubov theory of dilute Bose gases, we assume that the quasi-momentum distribution can be described by two components, a coherent one with

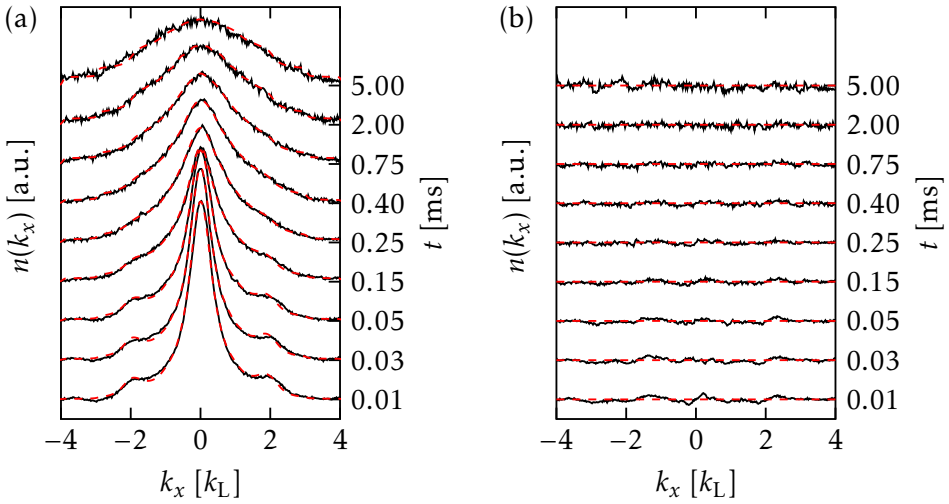

Figure 4.5 (a) 1D momentum distribution $n(k_x)$ as a function of t_p for a lattice depth $V \approx 6.5E_R$. Dashed red lines are fits to equation (4.4.8). For clarity, the momentum distribution is not shown for all measured times t. (b) Residuals of the fits.

long-range coherence characterized by a Bragg pattern with sharp peaks and an incoherent one with only short-range coherence. To model the coherent component, we use a function G taken as a sum of five Gaussian functions. The positions of these Gaussians are fixed, with the main one in the center of the first Brillouin and the four others in the "centers" of the second Brillouin zone. The widths of the Gaussian peaks are also fixed to their value at $t = 0$, and the amplitudes are free parameters. To model the incoherent component, we proceed as in 1D with the nearest-neighbors and the next-nearest-neighbors as defined above. In the end, we fit the momentum distribution to

$$n_{\text{fit,2D}}(k_x, k_y) \approx G(k_x, k_y) + \sum_{i=1}^{m_{\max}} 2\mathcal{C}_i |\tilde{w}_0(k)|^2 \sum_{i_1, i_2} \cos\left(i_1 k_x d + i_2 k_y d\right) + \sum_{n=0}^{3} \mathcal{P}_n |\tilde{w}_n(k)|^2. \tag{4.4.9}$$

Here, i_1 and i_2 account for the geometry of the 2D square lattice. For instance, for $i = 1$, the possible (i_1, i_2) are $(1,0)$, $(0,1)$, $(-1,0)$ and $(0,-1)$. For $i = 2$, the possible (i_1, i_2) are $(1,1)$, $(1,-1)$, $(-1,1)$ and $(-1,-1)$.

4.4.4 Evolution of the spatial coherences

For each dissipation time t, we measure the momentum distribution for 5 repetitions of the experiment. Each distribution is fitted individually. We then take the mean and the standard deviation to determine the fitting parameters and their error bars. The key observables extracted from the momentum distribution fits are the spatial coherences $\mathcal{C}_1$, $\mathcal{C}_2$ and $\mathcal{C}_3$. The time evolution of these coherences is shown in figure 4.6(a) for $V_\perp = 7.3E_R$. In double-logarithmic scale, we clearly observe an algebraic decay of C_1 and C_2.

We perform power-law fits for times greater than $\kappa/\gamma_{\text{exp}}$ and coherences above the detection level, as indicated by the striped area on figure 4.6(a). The detection level of 0.02 comes from the noise of the images. The extracted algebraic exponents α_1 and α_2 are shown in figure 4.6(b-c). We do not fit the time evolution of $\mathcal{C}_3$ since there is typically only one or two points above the detection level in the algebraic regime.

We observe that, as the lattice depth $V_\perp$ increases, the power-law exponent α_1 for $\mathcal{C}_1$ converges from 0.6 to 0.5, the value predicted by the model detailed in the previous section. This means that the decoherence is indeed slowed as interactions are increased. In the model

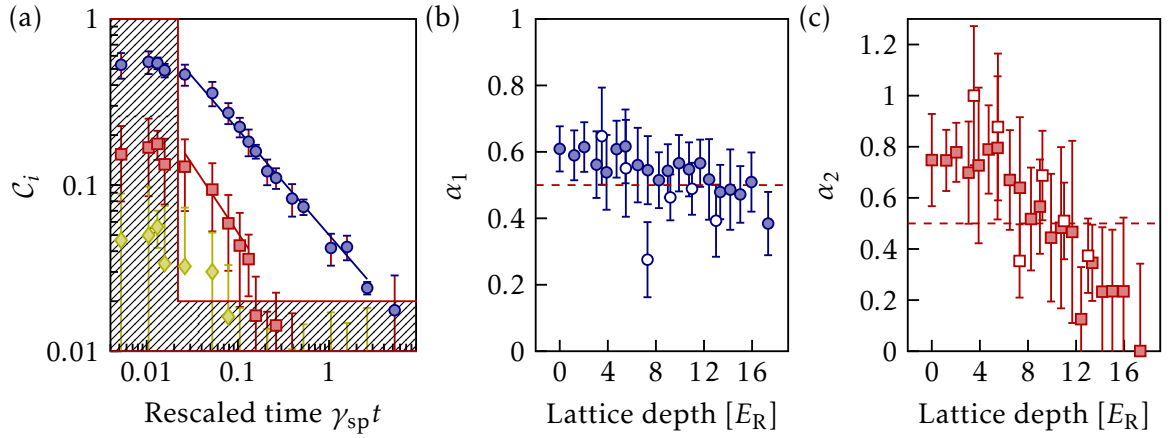

Figure 4.6 (a) First coherences $\mathcal{C}_1$ (circles), $\mathcal{C}_2$ (square) and $\mathcal{C}_3$ (diamonds) with respect to dissipation pulse time for $V = 7.3E_R$. The solid lines correspond to power-law fits of $\mathcal{C}_1$ and $\mathcal{C}_2$. Points in the striped area are excluded from the fits because they are not in the algebraic regime or are below the detection level. (b-c) Fitted exponents for the algebraic decay of the coherences $\mathcal{C}_1$ and $\mathcal{C}_2$ with varying lattice depth in 1D (filled) and 2D (empty). Error bars are determined from a bootstrap procedure.

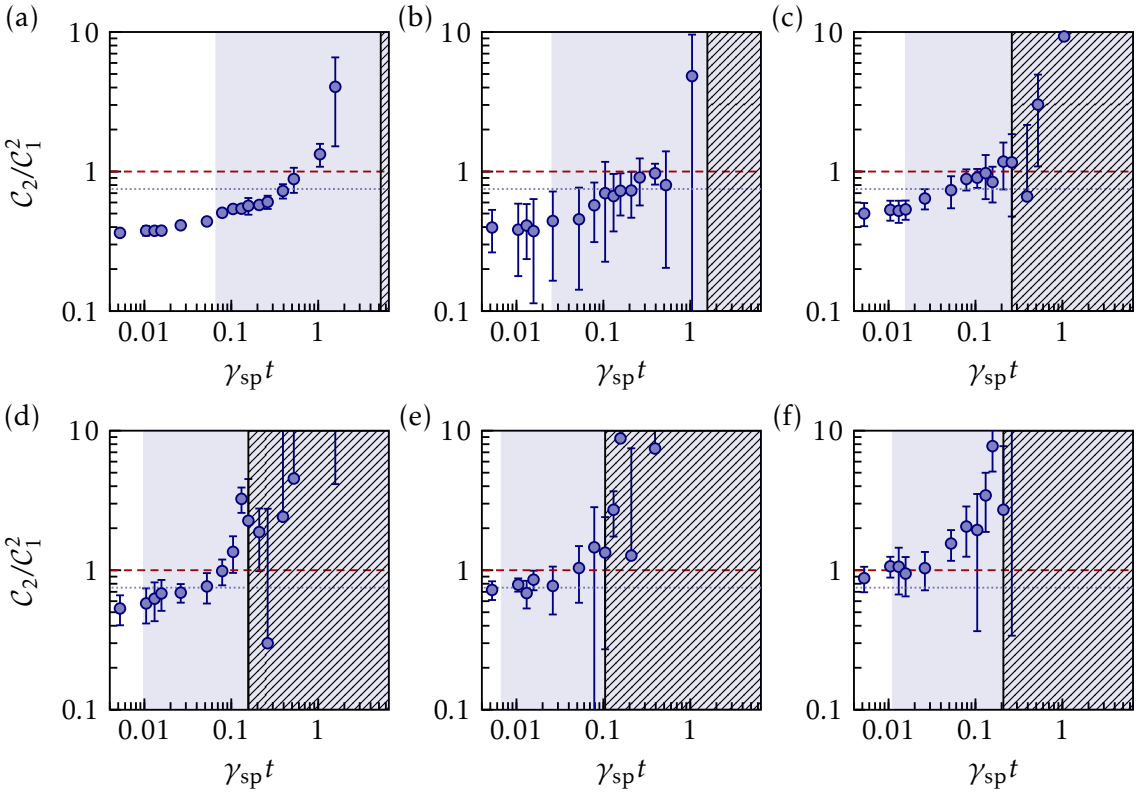

Figure 4.7 $\mathcal{C}_2/\mathcal{C}_1^2$ for 1D data as a function of $\gamma_{sp}t$ for (a) $V = 1.2E_R$, (b) $V = 3.9E_R$, (c) $V = 6.5E_R$, (d) $V = 9.0E_R$, (e) $V = 11.7E_R$, and (f) $V = 14.2E_R$. The dashed line corresponds to numerically expected scaling of 1. The shaded area corresponds to the algebraic regime. The striped area corresponds to points where $\mathcal{C}_2$ falls below the detection level.

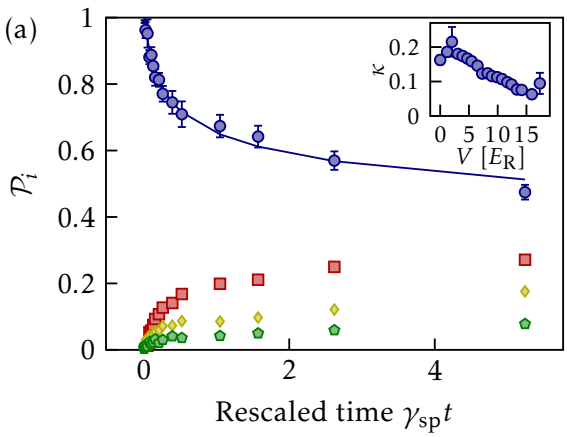

Figure 4.8 Fitted relative populations in the various bands versus rescaled time $\gamma_{sp}t$. Circles are the fundamental band population. Squares, diamonds and pentagons are respectively the first, second and third excited band populations. The solid line is a phenomenological fit of the fundamental band population with equation (4.4.10). Inset: fitted κ as a function of the lattice depth.

by Poletti et al. (2013), the dimension only influences the initial coherences and the starting time of the algebraic regime, but not the exponent of the power-law decay. As expected, 1D and 2D data for α_1 are compatible, as shown in figure 4.6(b).

For $\mathcal{C}_2$, we observe a similar behavior, although the power-law exponent α_2 starts around 0.75 for low lattice depths. It is difficult to determine to which value the power-law exponent converges because $\mathcal{C}_2$ is very close to the detection level for the largest lattice depths ($V > 12E_R$). However, we can study $\mathcal{C}_2/\mathcal{C}_1^2$, which is numerically predicted to be 1 in the algebraic regime, as seen in section 4.3.3. Figure 4.7 shows $\mathcal{C}_2/\mathcal{C}_1^2$ as a function of $\gamma_{sp}t$ for different lattice depths. Points corresponding to $\mathcal{C}_2$ or $\mathcal{C}_1$ below the detection level are discarded. We observe that, as the algebraic starts earlier, the region where $\mathcal{C}_2/\mathcal{C}_1^2 \approx 1$ is also shifted to earlier times. This observation that $\mathcal{C}_2/\mathcal{C}_1^2 \approx 1$ in the algebraic regime, as predicted by theory, is new and was not reported in Bouganne et al. (2020).

4.4.5 Band transitions and atomic losses

In the previous subsection, we showed the coherences of the atoms in the fundamental band. With our fitting procedure, we can also account for atoms being excited to higher bands. As shown in figure 4.8(a), we observe the fundamental band population decay to reach approximately 50 %, while the first three excited band populations increase, the first excited band being the most populated. This is not accounted for in the model by Poletti et al. (2013). The decay of the fundamental band population can be fitted relatively well with the same phenomenological function as the peak amplitude

$$\mathcal{P}_0(t) = \frac{1}{(1+\gamma_{gb}t/\kappa)^\kappa}. \tag{4.4.10}$$

We find $\gamma_{gb} \approx 0.3\gamma_{sp}$ for all lattice depths. On the other hand, as shown in the inset of figure 4.8, κ decreases when the lattice depth increases, indicating a slowing down of interband transitions as the gap between the bands increases.

In addition to decoherence, atomic losses also take place during the dissipation time. A typical atom number curve is shown in figure 4.9, in rescaled time $\gamma_{2B}t$. The two-body loss

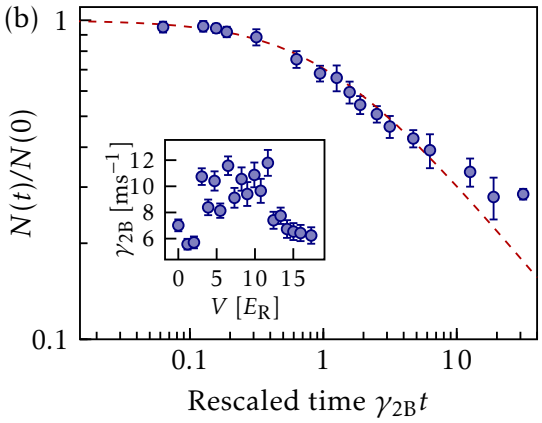

Figure 4.9 Normalized atom number N/N_0 versus rescaled time $\gamma_{2B}t$. The dashed line is $1/(\sqrt{1+\gamma_{2B}t})$. Inset: fitted γ_{2B} as a function of the lattice depth.

rate γ_{2B} is extracted from a fit to

$$N(t) = \frac{N(0)}{\sqrt{1+\gamma_{2B}t}}. \tag{4.4.11}$$

When plotting the atomic losses for all lattice depths in rescaled time $\gamma_{2B}t$, all the curves collapse onto $1/(\sqrt{1+\gamma_{2B}t})$, shown as a dashed line on figure 4.9(b). In the inset of the figure, we show that the two-body loss rate is on the order of a few ms^{-1}. This is one order of magnitude less than γ_{sp}, but not negligible in the entire time span of the experiment. Only 20 % of the atoms remain for the longest dissipation time $\sim 5\gamma_{sp}^{-1} \sim \gamma_{2B}^{-1}$.

Conclusion

In this chapter, we studied the algebraic decay of coherence in 1D and 2D Bose-Hubbard systems. First, we detailed the model used to theoretically investigate dissipation in our system. We have obtained a quantum master equation which we studied using methods developed in Poletti et al. (2013). Although the model ignores a number of experimentally observed effects such as interband transitions and atomic losses, it predicts correctly the dynamics of the single-particle coherence in the fundamental band. In particular, in the algebraic regime of interest, we found a quantitative agreement with the predicted power-law exponent of 1/2 for the decay of nearest-neighbor coherences, which we extracted from a fit to the full momentum distribution of the system. We note that the effects beyond the model of Poletti et al. (2013) are discussed in more detail in chapter 5 of Bouganne (2018).

The dynamics leading to the algebraic regime, that is the early exponential regime, cannot be described with the simple model detailed in this chapter. We found that it depends strongly on the initial state of the system, and thus on the dimension. We also found that the early exponential decay of the central peak of the momentum distribution, i.e. the long-range coherences, is an order of magnitude faster than the spontaneous emission rate γ_{sp}. In the next chapter, we will analyze the data presented in this chapter focusing on the early dynamics of the system. We will also focus on 1D optical lattices, for which many theoretical methods are available to describe complex many-body systems.

CHAPTER 5

Non-Hermitian linear response of one-dimensional Bose gases

Introduction

A very general way of probing the state of a physical system is to apply a perturbation and monitor its response. If the perturbation is small enough, the response will be proportional to the perturbation and can therefore be calculated using linear response theory. Examples are countless in condensed matter: thermal and electrical conductivities, magnetic susceptibility, modulus of elasticity, etc. In optics, linear response theory describes the optical response through the refractive index, as we will see in Chapter 6. In this chapter, we present a method to probe the state of an initially closed quantum system by imposing a small amount of dissipation and studying the initial dynamics.

As opposed to the late algebraic dynamics presented in the previous chapter, we study the early dephasing dynamics for interacting bosons in optical lattices subjected to light scattering, as shown in figure 5.1. To facilitate comparison with theoretical predictions, we specifically focus on 1D systems (Giamarchi 2003). We retrieve information on the initial system by using linear response theory. This measurement, which is complementary to the static one in Chapter 3, can be viewed as a proof of principle of a very general method.

In section 5.1, we present the linear response approach to non-Hermitian systems. In section 5.2, we revisit the light scattering data from the previous chapter, focusing on the early dynamics. In section 5.3, we present an (approximate) version of non-Hermitian linear response theory due to Pan et al. (2020) relating the response to dephasing to the many-body spectral function $A(k,\omega)$ of the initial state. Finally, in section 5.4, we compare the theory from Pan et al. (2020) to our experimental data.

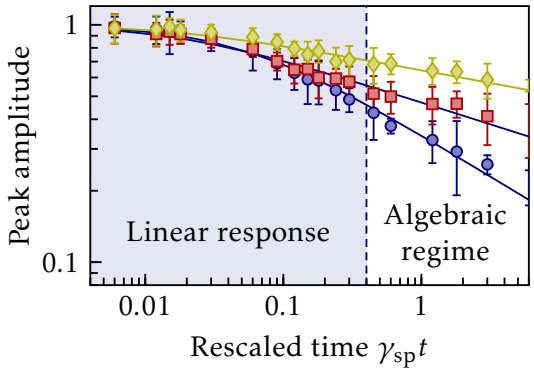

Figure 5.1 Schematic separation of early and late dynamics: normalized central peak amplitude of the momentum distribution as a function of rescaled time $\gamma_{sp}t$.

5.1 Non-Hermitian linear response theory

5.1.1 Reminder on linear response theory

Linear response theory corresponds to the first order of perturbation theory, an essential tool in quantum mechanics. Let us define the time-dependent Hamiltonian $\hat{H}(t) = \hat{H}_0 + \hat{U}(t)$, where $\hat{H}_0$ is time-independent. $\hat{U}(t) \equiv f(t)\hat{U}_0$ corresponds to the time-dependent part of $\hat{H}$ and is Hermitian. We go to the interaction picture (labelled with exponent "I") where

$$\hat{\rho}^{\mathrm{I}}(t) = \mathrm{e}^{-\mathrm{i}\hat{H}_0 t/\hbar}\hat{\rho}\mathrm{e}^{-\mathrm{i}\hat{H}_0 t/\hbar} \quad \text{and} \quad \hat{W}^{\mathrm{I}}(t) = \mathrm{e}^{\mathrm{i}\hat{H}_0 t/\hbar}\hat{W}\mathrm{e}^{-\mathrm{i}\hat{H}_0 t/\hbar}, \tag{5.1.1}$$

where $\hat{\rho}$ is the density-matrix and $\hat{W}$ is any observable, including $\hat{U}(t)$. The equation of motion in the interaction picture, $\partial_t \hat{\rho}^{\mathrm{I}} = [\hat{U}^{\mathrm{I}}, \hat{\rho}^{\mathrm{I}}]/\mathrm{i}\hbar$, can be formally integrated as

$$\hat{\rho}^{\mathrm{I}}(t) = \hat{\rho}_0 + \frac{1}{\mathrm{i}\hbar}\int_0^t \mathrm{d}t' \Big[\hat{U}^{\mathrm{I}}(t'), \hat{\rho}^{\mathrm{I}}(t')\Big], \tag{5.1.2}$$

if the perturbation starts at $t = 0$. Here, we have defined $\hat{\rho}_0 = \hat{\rho}(t = 0)$. In linear response theory, the crucial approximation is to simplify this equation by substituting $\hat{\rho}^{\mathrm{I}}(t)$ with $\hat{\rho}_0$. This translates as

$$\hat{\rho}^{\mathrm{I}}(t) \approx \hat{\rho}_0 + \frac{1}{\mathrm{i}\hbar}\int_0^t \mathrm{d}t' f(t') \Big[\hat{U}_0^{\mathrm{I}}(t'), \hat{\rho}_0^{\mathrm{I}}\Big]. \tag{5.1.3}$$

For a given observable $\hat{W}$, this yields

$$\langle \hat{W} \rangle_t = \mathrm{Tr}[\hat{\rho}^{\mathrm{I}}(t)\hat{W}^{\mathrm{I}}(t)] = \mathrm{Tr}[\hat{\rho}_0 \hat{W}] + \frac{1}{\mathrm{i}\hbar}\int_0^t \mathrm{d}t' \mathrm{Tr}\Big([\hat{U}_0^{\mathrm{I}}(t'), \hat{\rho}_0]\hat{W}^{\mathrm{I}}(t)\Big) \tag{5.1.4}$$

$$= \langle \hat{W} \rangle_0 + \frac{1}{\mathrm{i}\hbar}\int_0^t \mathrm{d}t' f(t') \Big\langle [\hat{W}^{\mathrm{I}}(t), \hat{U}_0^{\mathrm{I}}(t')] \Big\rangle_0 \tag{5.1.5}$$

by using the linear and cyclic properties of the trace. We can then make the linear response appear clearly by writing

$$\Delta\langle \hat{W} \rangle \equiv \langle \hat{W} \rangle_t - \langle \hat{W} \rangle_0 = \int_0^t f(t') \chi_{WU_0}(t - t') \mathrm{d}t', \tag{5.1.6}$$

where we have defined the WU_0 susceptibility

$$\chi_{WU_0}(t - t') = \frac{1}{\mathrm{i}\hbar}\Big\langle [\hat{W}^{\mathrm{I}}(t), \hat{U}_0^{\mathrm{I}}(t')] \Big\rangle_0 = \frac{1}{\mathrm{i}\hbar}\Big\langle [\hat{W}^{\mathrm{I}}(t - t'), \hat{U}_0] \Big\rangle_0. \tag{5.1.7}$$

In order to derive analytical results, it is convenient to make a *quasi-static* approximation. We assume that the state of the system continuously adapts to find a new equilibrium state, allowing us to use equation (5.1.6) to calculate the evolution between any time t and $t + \delta t$

$$\langle \hat{W} \rangle_{t+\delta t} - \langle \hat{W} \rangle_t \approx \int_t^{t+\delta t} f(t') \chi_{WU_0}(t - t') \mathrm{d}t' \approx f(t) \chi_{WU_0}(t) \delta t. \tag{5.1.8}$$

This leads to a coarse-grained differential equation for $\langle \hat{W} \rangle_t$,

$$\frac{\mathrm{d}}{\mathrm{d}t}\langle \hat{W} \rangle_t \approx f(t) \chi_{WU_0}(t), \tag{5.1.9}$$

which indeed corresponds to a first-order response to a time perturbation $f(t)$ with a susceptibility $\chi_{WU_0}(t)$.

5.1.2 Non-Hermitian theory applied to the momentum distribution

Linear response theory can be extended to a non-Hermitian perturbation without conceptual difficulty. Although a non-Hermitian perturbation is not necessarily time-dependent, it induces a time-dependent behavior. We start from the Lindblad equation in the interaction picture

$$\frac{\mathrm{d}\hat{\rho}^{\mathrm{I}}}{\mathrm{d}t} = \sum_\alpha \hat{L}_\alpha \hat{\rho}^{\mathrm{I}} \hat{L}_\alpha^\dagger - \frac{1}{2}\{\hat{L}_\alpha^\dagger \hat{L}_\alpha, \hat{\rho}^{\mathrm{I}}\} \tag{5.1.10}$$

and, by applying the same procedure as in the previous section, we find the general formula of non-Hermitian linear response theory (NHLRT)

$$\Delta\langle\hat{W}\rangle \approx -\sum_\alpha \int_0^t \mathrm{d}t' \xi_{WL_\alpha}(t-t') \quad \text{with} \quad \xi_{WL_\alpha}(\tau) = \left\langle \frac{1}{2}\left\{\hat{L}_\alpha^\dagger \hat{L}_\alpha, \hat{W}^{\mathrm{I}}(\tau)\right\} - \hat{L}_\alpha^\dagger \hat{W}^{\mathrm{I}}(\tau)\hat{L}_\alpha \right\rangle_0 . \tag{5.1.11}$$

Equation (5.1.11) is equivalent to equations (5.1.6) and (5.1.7) for the non-Hermitian case. Once again, the crucial approximation is to take the expectation values in the initial state $\hat{\rho}_0 = \hat{\rho}(t=0)$. This version of the Kubo formula (Kubo 1957) can be readily applied to one-body observables using the first-order correlation function $\langle \hat{a}_i^\dagger \hat{a}_j \rangle$. By taking $\hat{W} = \hat{a}_i^\dagger \hat{a}_j$, we obtain

$$\Delta\langle \hat{a}_i^\dagger \hat{a}_j\rangle \equiv \langle \hat{a}_i^\dagger \hat{a}_j\rangle_t - \langle \hat{a}_i^\dagger \hat{a}_j\rangle_0 \approx -\sum_\alpha \int_0^t \mathrm{d}t' \left\langle \frac{1}{2}\left\{\hat{L}_\alpha^\dagger \hat{L}_\alpha, \hat{a}_i^\dagger \hat{a}_j\right\} - \hat{L}_\alpha^\dagger \hat{a}_i^\dagger \hat{a}_j \hat{L}_\alpha \right\rangle_0 , \tag{5.1.12}$$

where the $\hat{a}_i^\dagger$ and $\hat{a}_j$ under the integral are taken at time $t-t'$ in the interaction picture. We want to study the momentum distribution $n(\boldsymbol{k},t) = \langle \hat{a}_{\boldsymbol{k}}^\dagger \hat{a}_{\boldsymbol{k}}\rangle_t$. On a lattice system with N_s sites, we define

$$\hat{a}_i = \frac{1}{\sqrt{N_\mathrm{s}}} \sum_{\boldsymbol{k}\in \mathrm{BZ1}} \mathrm{e}^{-\mathrm{i}\boldsymbol{k}\cdot\boldsymbol{r}_i} \hat{a}_{\boldsymbol{k}} \quad \text{and} \quad \hat{L}_i = \frac{1}{\sqrt{N_\mathrm{s}}} \sum_{\boldsymbol{k}\in \mathrm{BZ1}} \mathrm{e}^{-\mathrm{i}\boldsymbol{k}\cdot\boldsymbol{r}_i} \hat{L}_{\boldsymbol{k}}. \tag{5.1.13}$$

By defining $\hat{n}_{\boldsymbol{k}} = \hat{a}_{\boldsymbol{k}}^\dagger \hat{a}_{\boldsymbol{k}}$, we obtain

$$\Delta n(\boldsymbol{k}) \equiv n(\boldsymbol{k},t) - n(\boldsymbol{k},0) \approx -\sum_{\boldsymbol{q}} \int_0^t \mathrm{d}t' \left\langle \frac{1}{2}\hat{L}_{\boldsymbol{q}}^\dagger \hat{L}_{\boldsymbol{q}} \hat{n}_{\boldsymbol{k}}^{\mathrm{I}}(t-t') + \frac{1}{2}\hat{n}_{\boldsymbol{k}}^{\mathrm{I}}(t-t')\hat{L}_{\boldsymbol{q}}^\dagger \hat{L}_{\boldsymbol{q}} - \hat{L}_{\boldsymbol{q}}^\dagger \hat{n}_{\boldsymbol{k}}^{\mathrm{I}}(t-t')\hat{L}_{\boldsymbol{q}} \right\rangle_0 . \tag{5.1.14}$$

Finally, with the quasi-static approximation mentioned above, we obtain the coarse-grained differential equation

$$\frac{\mathrm{d}}{\mathrm{d}t} n(\boldsymbol{k},t) \approx -\sum_{\boldsymbol{q}} \xi_{n_{\boldsymbol{k}}L_{\boldsymbol{q}}}(t) \quad \text{with} \quad \xi_{n_{\boldsymbol{k}}L_{\boldsymbol{q}}}(t) = \left\langle \frac{1}{2}\hat{L}_{\boldsymbol{q}}^\dagger \hat{L}_{\boldsymbol{q}} \hat{n}_{\boldsymbol{k}}^{\mathrm{I}}(t) + \frac{1}{2}\hat{n}_{\boldsymbol{k}}^{\mathrm{I}}(t)\hat{L}_{\boldsymbol{q}}^\dagger \hat{L}_{\boldsymbol{q}} - \hat{L}_{\boldsymbol{q}}^\dagger \hat{n}_{\boldsymbol{k}}^{\mathrm{I}}(t)\hat{L}_{\boldsymbol{q}} \right\rangle_0 . \tag{5.1.15}$$

To go beyond equation (5.1.14), we need to define the $\hat{L}_q$ and calculate the $\xi_{n_{\boldsymbol{k}}L_{\boldsymbol{q}}}$. To obtain analytical results, more approximations than the linear response assumption are necessary. In section 5.3, we will propose one way to proceed, following the theoretical work of Pan et al. (2020). But first, let us examine the experimental evolution of the momentum distribution heuristically in the next section.

5.2 Probing the initial state with light scattering

Inspired by the non-Hermitian linear response theory from the previous section, we analyze the early dissipative dynamics of one-dimensional Bose-Hubbard systems undergoing spontaneous emission. The analysis and interpretation of the data in this chapter should be considered preliminary.

5.2.1 Analysis of the momentum diffusion

First, we focus on momentum diffusion in the evolution of the momentum distribution $n(k)$. Let us define the appropriate observable to quantify momentum diffusion. In order to compare with the theory discussed above, we are rather interested in the quasi-momentum distribution $S(k)$, without the Wannier envelope $|w_0(k)|^2$. To do so, we use the results of the fits

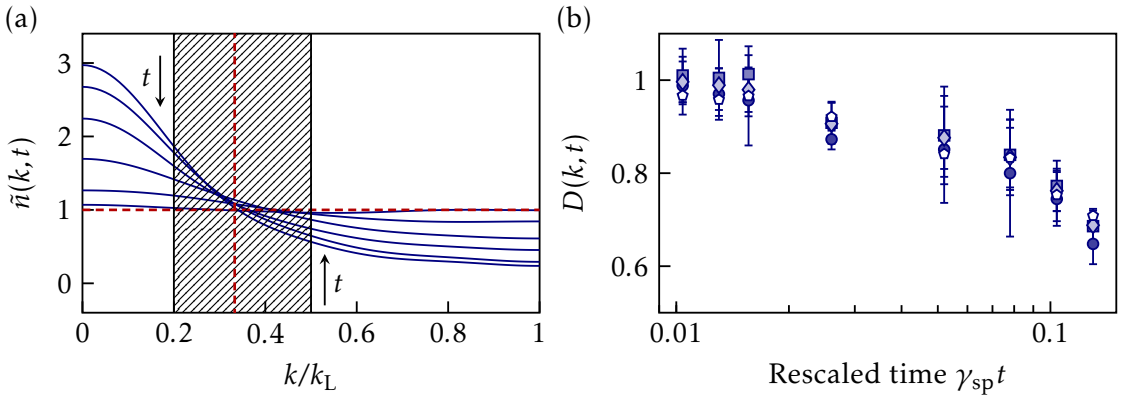

Figure 5.2 (a) Evolution of the normalized momentum distribution $\tilde{n}(k,t)$ for $V = 2E_R$. The horizontal dashed line corresponds to the steady-state normalized momentum distribution, while the vertical dashed line correspond to $k = k_L/3$. The striped area is excluded from the calculation of $D(k,t)$. (b) Renormalized density $D(k,t)$ as a function of time, in x-semilogarithmic scale, for different momenta k in the first Brillouin zone. We observe a similar decay for all momenta.

performed in Chapters 3 and 4. As a reminder, the fitting function reads

$$n(k) = |\tilde{w}_0(k)|^2 \sum_{m=0}^{m_{\max}} 2\mathcal{C}_m \cos(mkd) + \sum_{n=0}^{3} \mathcal{P}_n |\tilde{w}_n(k)|^2, \tag{5.2.1}$$

The quasi-momentum distribution then reads

$$S(k) = \sum_{m=0}^{m_{\max}} 2\mathcal{C}_m \cos(mkd), \tag{5.2.2}$$

and is defined in the first Brillouin zone (BZ1). To study momentum diffusion, we restrict our study to the positive half of the BZ1 and renormalize $S(k)$ by its integral over the BZ1 to compensate losses (which we will study separately later)

$$\tilde{n}(k) = \frac{S(k)}{\int_0^{k_L} \mathrm{d}k' S(k')}. \tag{5.2.3}$$

We have defined $\tilde{n}(k,t)$ so that the flat steady-state normalized momentum distribution $\tilde{n}(k,\infty)$ is 1. We define the distance to the steady-state,

$$D(k,t) = \frac{\tilde{n}(k,t) - 1}{\tilde{n}(k,0) - 1}, \tag{5.2.4}$$

where we have normalized $D(k,t)$ by its value at $t = 0$ so that it monotonously goes from 1 to 0. $D(k,t)$ is our observable for quantifying the momentum diffusion. Although it is a fairly natural quantity to define, its purpose will be clarified in section 5.3.

In figure 5.2(b), we show $D(k,t)$ for different values of k and for $V = 2.0E_R$. We observe that $D(k,t)$ is independent of k at short times ($\gamma_{sp}t \lesssim 1$), which leads us to define the integrated quantity

$$\overline{D}(t) = \int \mathrm{d}k\, D(k,t). \tag{5.2.5}$$

As shown in figure 5.2(a), $\tilde{n}(k,0) \sim 1$ for $k \sim k_L/3$. The observable $D(k,t)$ is then a ratio of two small (and most likely noise-dominated) quantities, and therefore is difficult to measure

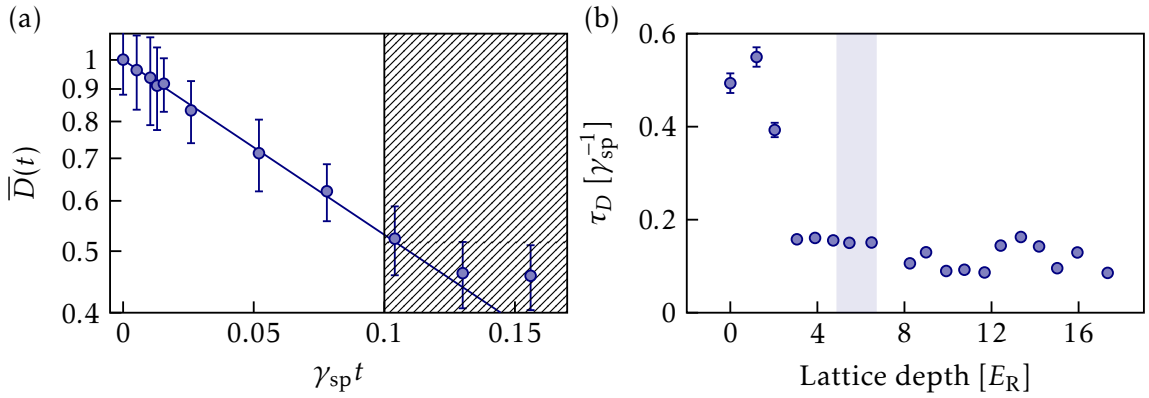

Figure 5.3 (a) Integral renormalized density $\overline{D}(t)$ as a function of time, in y-semilogarithmic scale, for $V = 2.0E_R$. The solid line is a fit to an exponential and, the fit is performed for $t < t_{max} = 0.1\gamma_{sp}^{-1}$, as indicated by the striped area. (b) Fitting parameter τ_D. The shaded area correspond to the approximate location of Mott transition.

accurately around $k \sim k_L/3$. We thus exclude momenta $k \in [0.2k_L, 0.5k_L]$ from the integral. Studying $\overline{D}(t)$ is preferable because the error bars are significantly reduced compared to $D(k,t)$.

Note that we have also analyzed the tof momentum distribution directly instead of the reconstructed quasi-momentum distribution. We observed that the independence of $D(k,t)$ with respect to k worsened significantly at longer times, due to the Wannier envelope and transitions to excited bands. Nevertheless, the results presented below were not qualitatively different.

In figure 5.3(a), we show $\overline{D}(t)$ for $V = 2.0E_R$. In semilogarithmic scale, it is clear that $\overline{D}(t)$ decays exponentially, and we fit it to

$$\overline{D}(t) = e^{-t/\tau_D}. \tag{5.2.6}$$

Hereafter, we limit our study to short times $\gamma_{sp}t < 0.1$ in order to focus on the first-order of the response of the system (i.e. the linear response). The fitted diffusion time τ_D is shown in figure 5.3(b). It gives a clear indication of the superfluid-to-Mott insulator transition, as indicated by the shaded area (see Chapter 3 for a discussion on the Mott transition in 1D). The characteristic diffusion time τ_D decreases as the lattice depths is increased, and is always smaller than γ_{sp}^{-1}. Note that $1/\tau_D$ corresponds a qualitative non-Hermitian susceptibility ξ. By taking $\sum_{\boldsymbol{q}} \xi_{n_k L_{\boldsymbol{q}}}(t) = 1/\tau_D$ in equation (5.1.15), we retrieve a simple exponential behavior for $D(k,t)$.

5.2.2 Analysis of the atomic losses

In the previous chapter, we saw that the momentum diffusion induced by light also resulted in atomic losses. Light-induced atomic losses are not necessarily a hindrance for these measurements. Because they are also a form of controlled dissipation, they can serve as a probe of the initial state of the system within the framework of the non-Hermitian linear response theory of section 5.1. The normalized atom number $\tilde{N}(t) = N(t)/N(0)$ is shown in figure 5.4(a) for $V = 2.0E_R$. We fit $\tilde{N}(t)$ with

$$\tilde{N}(t) = \frac{1}{1 + t/\tau_N} \tag{5.2.7}$$

for reasons that we will clarify below. For now, this fitting function is a reasonable first-order function that captures well the behavior of $\tilde{N}(t)$ at short times, as shown in figure 5.4(a). The

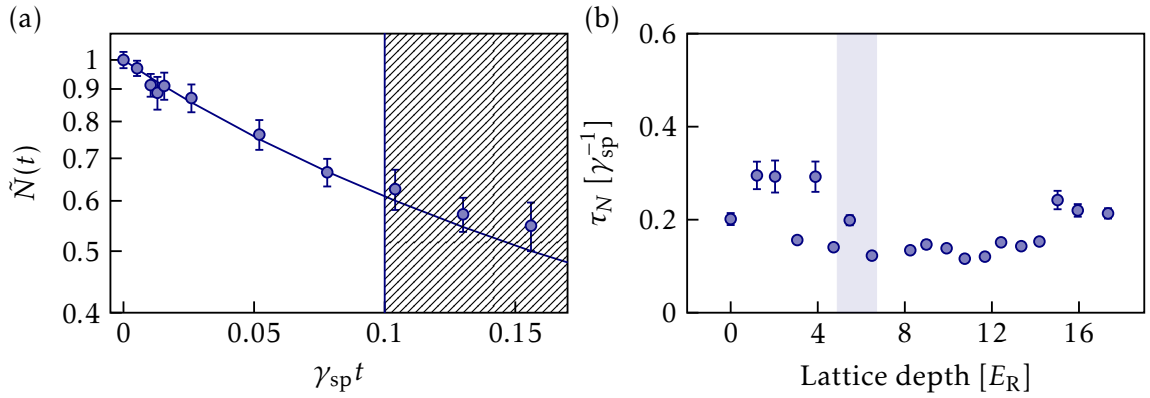

Figure 5.4 (a) Renormalized atom number $\tilde{N}(t)$ as a function of time, in y-semilogarithmic scale, for $V = 2.0E_R$. The solid line is a fit to an exponential. The fit is performed for $t < t_{max} = 0.1\gamma_{sp}^{-1}$, as indicated by the striped area. (b) Fitting parameter τ_N. The shaded area correspond to the approximate location of Mott transition.

fitted loss time τ_N is shown in figure 5.4(b), and seems to indicate the superfluid-to-Mott insulator transition. However, this is less clear than for the fitted diffusion time τ_D.

In conclusion, we have shown experimental data applying the general idea of the non-Hermitian linear response theory presented in section 5.1. By inducing dissipation and measuring characteristic diffusion and loss times, we have shown that we can probe the superfluid-to-Mott insulator transition. In the next section, we propose one way to go further in the analysis of our data, following a proposal by Pan et al. (2020).

5.3 Simplified Non-Hermitian linear response theory from Pan et al. (2020)

Following the publication of Bouganne et al. (2020), Pan et al. (2020) published a proposal to simplify the non-Hermitian linear response theory. In this section, we present this theory, which we call Pan theory hereafter, and its application to light scattering in our experiment. In the next section we will compare the predictions of this theory to our experimental results. Note that Pan theory is not the only proposal for probing a system through its dynamical susceptibility (Hauke et al. 2016, Geier et al. 2022, Laurent et al. 2017).

5.3.1 Essential approximations

Pan theory makes two essential approximations in order to go beyond equation (5.1.14). Pan theory is applicable to any type of dissipation and in any dimension. For concreteness, we detail it here for the quantum jump operator $\hat{L}_i = \sqrt{\gamma_{sp}}\hat{a}_i^\dagger\hat{a}_i$. We used this quantum jump operator in the previous chapter to model the decoherence caused by spontaneous emission in a lattice.

The first approximation of Pan theory is to apply Wick's theorem to equation (5.1.14), which is valid for non-interacting systems but becomes dubious for strong interactions. This leads to

$$\Delta n(\boldsymbol{k}) = \frac{(2\bar{n}+1)\gamma_{sp}}{2}\int_0^t \mathrm{d}\tau |g(\boldsymbol{k},\tau)|^2 + \frac{\gamma_{sp}}{2}\int_0^t \mathrm{d}\tau (\mathrm{i}\hbar)^2\Big[G_{\boldsymbol{k}}^<(-\tau)G_{\boldsymbol{k}}^<(\tau) - G_{\boldsymbol{k}}^>(-\tau)G_{\boldsymbol{k}}^>(\tau)\Big], \quad (5.3.1)$$

where we defined the lesser and greater Green functions

$$G_{\boldsymbol{k}}^<(\tau) = \frac{1}{\mathrm{i}\hbar}\langle\hat{a}_{\boldsymbol{k}}^\dagger(\tau)\hat{a}_{\boldsymbol{k}}(0)\rangle_0\,, \quad G_{\boldsymbol{k}}^>(\tau) = \frac{1}{\mathrm{i}\hbar}\langle\hat{a}_{\boldsymbol{k}}(\tau)\hat{a}_{\boldsymbol{k}}^\dagger(0)\rangle_0. \quad (5.3.2)$$

$g(\boldsymbol{k},t)$ is the Fourier transform of the spectral function $A(\boldsymbol{k},\omega)$

$$g(\boldsymbol{k},t) = \int \mathrm{d}\omega \mathrm{e}^{-\mathrm{i}\omega t} A(\boldsymbol{k},\omega) = \mathrm{i}\hbar\Big[G^{>}_{\boldsymbol{k}}(-\tau) - G^{<}_{\boldsymbol{k}}(\tau)\Big]. \tag{5.3.3}$$

The second approximation of Pan theory is to assume $A(\boldsymbol{k},\omega)$ to be peaked around a certain frequency $\omega_{\boldsymbol{k}}$, which leads to

$$\mathrm{i}\hbar G^{<}_{\boldsymbol{k}}(\tau) \approx n_0(\boldsymbol{k}) g(\boldsymbol{k},t)\,, \quad \mathrm{i}\hbar G^{>}_{\boldsymbol{k}}(\tau) \approx [1+n_0(\boldsymbol{k})] g(\boldsymbol{k},t). \tag{5.3.4}$$

Equation (5.3.1) then takes the simple form

$$\Delta n(\boldsymbol{k}) \approx -\gamma_{\mathrm{sp}}[n_0(\boldsymbol{k}) - \bar{n}] \int_0^t \mathrm{d}\tau |g(\boldsymbol{k},\tau)|^2, \tag{5.3.5}$$

where $\bar{n}$ is the average filling of the system, and also corresponds to the fully-incoherent steady-state of $n_0(\boldsymbol{k})$.

5.3.2 Quasi-static approximation

In order to derive analytical results, we additionally use the quasi-static approximation mentioned in the first section. This leads to the coarse-grained evolution equation

$$\frac{\mathrm{d}}{\mathrm{d}t} n(\boldsymbol{k},t) \approx -\gamma_{\mathrm{sp}}[n(\boldsymbol{k},t) - \bar{n}] |g(\boldsymbol{k},t)|^2, \tag{5.3.6}$$

which can be solved analytically

$$\Sigma(\boldsymbol{k},t) \equiv \frac{n(\boldsymbol{k},t) - \bar{n}}{\bar{n}} = \frac{n(\boldsymbol{k},0) - \bar{n}}{\bar{n}} \mathrm{e}^{-\gamma_{\mathrm{sp}} \mathcal{F}(t)} \quad \text{with} \quad \mathcal{F}(\boldsymbol{k},t) = \int_0^t \mathrm{d}t' |g(\boldsymbol{k},t')|^2. \tag{5.3.7}$$

We retrieve that the linear response of the system $\Sigma(\boldsymbol{k},t)$ is directly linked to properties of the initial systems, which are contained in $\mathcal{F}(\boldsymbol{k},t)$.

5.3.3 Adding two-body losses

In section 5.2, we also observed significant two-body losses in addition to momentum diffusion. Two-body losses are described by the quantum jump operator $\hat{L}_i = \sqrt{\gamma_{2\mathrm{B}}/2}\hat{a}_i^2$. Pan theory can also be applied, by following the same procedure as above, we obtain the coarse-grained equation

$$\frac{\mathrm{d}}{\mathrm{d}t} n(\boldsymbol{k},t) = -\gamma_{2\mathrm{B}} \bar{n}(t) n(\boldsymbol{k},t) |g(\boldsymbol{k},t')|^2. \tag{5.3.8}$$

Note that the filling $\bar{n}(t)$ is now time-dependent. Combining decoherence and losses, we get

$$\Sigma(\boldsymbol{k},t) \equiv \frac{n(\boldsymbol{k},t) - \bar{n}(t)}{\bar{n}(t)} = \frac{n(\boldsymbol{k},0) - \bar{n}_0}{\bar{n}_0} \mathrm{e}^{-\gamma_{\mathrm{sp}} \mathcal{F}(\boldsymbol{k},t)}, \tag{5.3.9}$$

$$\bar{n}(t) = \frac{\bar{n}_0}{1 + \gamma_{2\mathrm{B}} \bar{n}_0 \mathcal{F}(\boldsymbol{k},t)}. \tag{5.3.10}$$

In section 5.4, we will use these two equations to model the early dynamics of 1D Bose-Hubbard systems submitted to light scattering. However, we can already remark that the same function $\mathcal{F}(t)$ determines the behavior of momentum diffusion and losses.

Note that $\Sigma(\boldsymbol{k},t)$ corresponds to $D(\boldsymbol{k},t)$ in section 5.2 with $\bar{n}_0 = 1$, and the fitting functions in section 5.2 simply correspond to equations (5.3.9) and (5.3.10) with $\mathcal{F}(t) = t$.

5.3.4 Dynamical correlation function in Luttinger liquid theory

As mentioned above, the initial state of the system is contained in the function $\mathcal{F}(\boldsymbol{k},t)$, which is related to the spectral function of the system $A(\boldsymbol{k},\omega)$ through equations (5.3.3) and (5.3.7). The spectral function is itself related to the lesser and greater Green functions, which correspond to dynamical first-order correlation functions. As such, they are expected to decay as power-laws for a Luttinger liquid, with an exponent related to the Luttinger exponent K. We described Luttinger liquid theory in Chapter 3. The exact dynamical first-order correlation function of a Luttinger liquid is difficult to express analytically in a simple way. However, at zero temperature, it can be approximated by the following equation

$$g_1(x,t) \equiv \frac{\langle \hat{\Psi}^\dagger(x,t)\hat{\Psi}(0,0)\rangle}{n} \simeq \left(\frac{a^2}{[a+\mathrm{i}(x-vt)][a-\mathrm{i}(x+vt)]}\right)^{1/4K}, \tag{5.3.11}$$

where v is the sound velocity (Giamarchi 2003). The spectral function then reads

$$A(\boldsymbol{k},\omega) \propto \frac{\Theta(\omega-v|k|)-\Theta(-\omega-v|k|)}{|\omega^2-(vk)^2|^\eta} \quad \text{with} \quad \eta = 1-\frac{1}{4K}. \tag{5.3.12}$$

This leads to

$$\mathcal{F}(k,t) \propto t^{2\eta-1} = t^{1-\frac{1}{2K}}. \tag{5.3.13}$$

As discussed in Chapter 3, for a non-interacting gas, $K \to \infty$ and $\eta = 1$: we retrieve the expected exponential behavior $\mathrm{e}^{-\gamma_{\mathrm{sp}}t}$. As interactions increase, $K \to 1$ and η goes from 1 to 0.75, stretching the exponential evolution. By studying the stretched evolution of $n(\boldsymbol{k},t)$ through $\Sigma(\boldsymbol{k},t)$ and $\bar{n}(t)$ for short times $t \lesssim \gamma_{\mathrm{sp}}^{-1}$, we can in principle measure K.

We can already remark that LL theory predicts $\mathcal{F}$ to be independent of $\boldsymbol{k}$, so that the evolution of $\Sigma(\boldsymbol{k},t)$ should also be independent of $\boldsymbol{k}$. Although it does not prove the validity of either Pan theory or LL theory in our system, we did observe that $D(\boldsymbol{k},t)$ evolves independently of $\boldsymbol{k}$ for short times $\gamma_{\mathrm{sp}}t \lesssim 1$.

5.4 Analysis using Pan theory

Let us reanalyze the experimental evolution of the system described in section 5.2 using Pan theory. Once again, this section corresponds to a preliminary analysis and interpretation.

5.4.1 Analysis of the momentum diffusion

Let us first consider momentum diffusion through the quantity $\overline{D}(t)$, as defined in equation (5.2.5). Following Pan theory, we fit $\overline{D}(t)$ with a stretched exponential

$$\overline{D}(t) = \mathrm{e}^{-(t/\tau_D)^{2\eta_D-1}}. \tag{5.4.1}$$

Once again, we limit our study to short times $\gamma_{\mathrm{sp}}t < 0.1$. In figure 5.5(a), we show $\overline{D}(t)$ for $V = 3.1E_{\mathrm{R}}$ and the fit to a stretched exponential as a solid line. We also show the previous fit to a simple exponential as a dashed line. Distinguishing the stretched from the simple exponential is clearly difficult.

The stretched exponential fitting parameters for all lattice depths are shown in figure 5.5(b-c). The exponent η_D is larger than 1 for the most part, which cannot be the case of a Luttinger liquid as it implies $K < 0$. We do not expect the gas to behave as a Luttinger liquid in the Mott insulating phase. This also indicates that we are not able to resolve the algebraic behavior even for a superfluid. This was already the case for the static measurement of the first-order

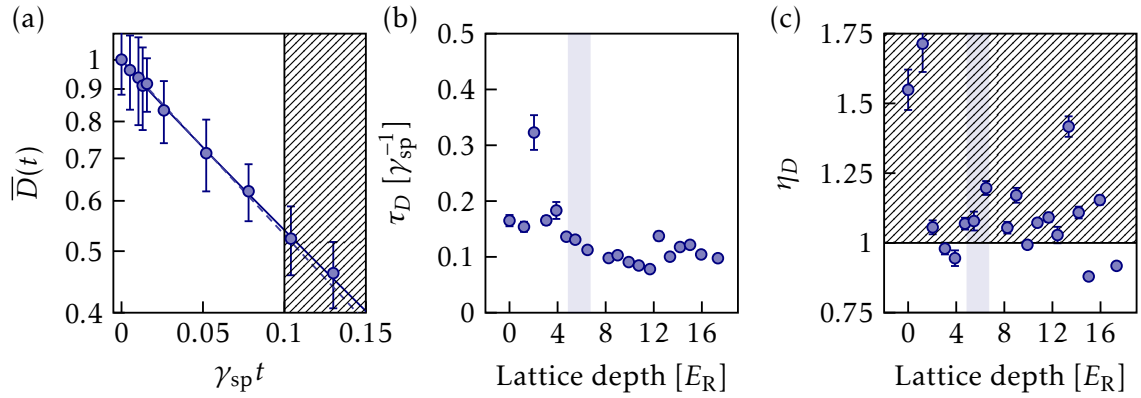

Figure 5.5 (a) Integral renormalized density $\overline{D}(t)$ as a function of time, in y-semilogarithmic scale, for $V = 3.1E_R$. The solid line is a fit to a stretched exponential and the dashed line is a fit to a simple exponential. Here, both fits are performed for $t < t_{max} = 0.1\gamma_{sp}^{-1}$, as indicated by the striped area. (b-c) Fitting parameters from the stretched exponential fits. The shaded area corresponds to the approximate location of Mott transition.

correlation function presented in Chapter 3, and we attributed it to the finite temperature of the system.

As for τ_D, it is very similar to the simple exponential results, apart from the two smallest lattice depths where fitting correlations with η_D prevent an accurate measure of τ_D. For this reason, the simple exponential fit should be preferred.

5.4.2 Analysis of the atomic losses

We now turn to atomic losses, studied through normalized atom number $\tilde{N}(t) = N(t)/N(0)$. Following Pan theory, we fit $\tilde{N}(t)$ with

$$\tilde{N}(t) = \frac{1}{1 + (t/\tau_N)^{2\eta_N - 1}}. \tag{5.4.2}$$

Once again, we limit our study to short times $\gamma_{sp}t < 0.1$. In figure 5.6(a), we show $\tilde{N}(t)$ for $V = 3.1E_R$ and the fit to equation (5.4.2) as a solid line. We also show the previous fit to equation (5.4.2) with $\eta_N = 1$ as a dashed line. It is clear that, in the linear response regime $\gamma_{sp}t < 0.1$, distinguishing the two will also be difficult.

The fitting parameters for all lattice depths are shown in figure 5.6(b-c). The behavior for the exponent η_N is different from that of momentum diffusion: we find $\eta_N \approx 0.9$ for most lattice depths. We remind that Pan theory predicts that the evolution of $\overline{D}$ and $\tilde{N}$ is set by the same function $\mathcal{F} = t^{2\eta-1}$. This indicates that Pan theory does not apply to our system, and that at least one of the two key approximations does not hold.

We note that induced-losses measurements appear to be more precise on our experiment since the error bars on the normalized atom number $\tilde{N}$ are significantly smaller than that on $\overline{D}$. We also note that $\eta_N \approx 0.9$ corresponds to $K \approx 2.5$, a value compatible with the model of the system developed in Chapter 3. As of now, we believe this agreement could be coincidental.

Conclusion

In this chapter, we have shown that, in addition to direct imaging, a quantum system can be probed by inducing controlled dissipation and studying the early linear response. We

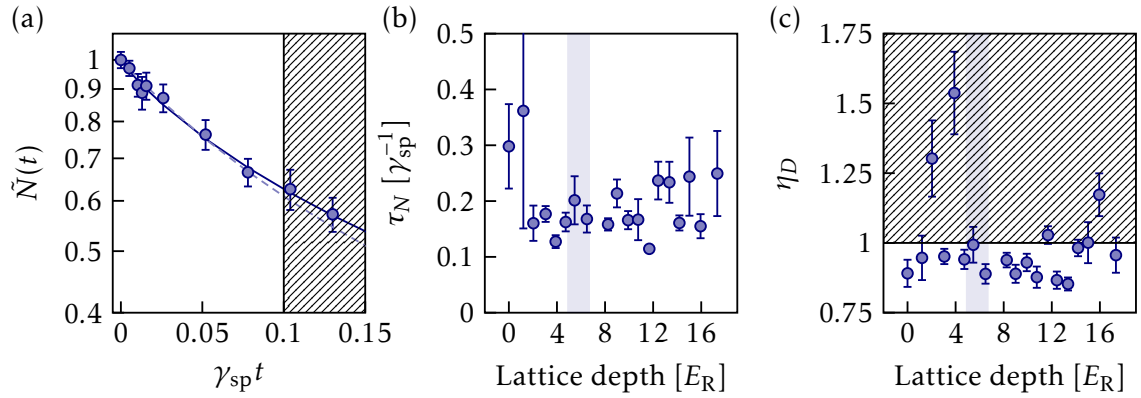

Figure 5.6 (a) Renormalized atom number $\tilde{N}(t)$ as a function of time, in y-semilogarithmic scale, for $V = 3.1E_R$. The solid line is a fit to equation (5.4.2) and the dashed line is a fit where η is fixed to 1. Here, both fits are performed for $t < t_{max} = 0.1\gamma_{sp}^{-1}$, as indicated by the striped area. (b-c) Fitting parameters for $t_{max} = 0.1\gamma_{sp}^{-1}$ (circles). The shaded area corresponds to the approximate location of Mott transition.

presented a theory describing the evolution of a dissipative system using linear response theory, and showed that the initial dynamics of the system can be used as a probe of the initial state. By applying this theory to the experiments presented in Chapter 4, we have clearly observed the 1D Mott insulator transition by measuring the dissipation rate, thus demonstrating that we can indeed probe the initial state of the system with dissipation. The measured non-Hermitian susceptibility drops abruptly to a nearly constant value near $V_x \approx 4E_R$, close to the expected threshold $V_x \simeq 4.9E_R$ where the $n = 1$ Mott transition is expected. This indicates that the non-Hermitian susceptibility is sensitive to the initial equilibrium state.

We have also considered the theory proposed by Pan et al. (2020) that gives a simplified framework to evaluate the non-linear susceptibility. When applied to Luttinger liquids, this theory predicts a stretched exponential behavior $\exp(-t^a)$, but with an exponent a close to 1, and is therefore difficult to distinguish experimentally from a simple exponential. It also predicts that the same function governs the decay of the first-order correlation function in presence of dephasing and of the atom number in presence of two-body losses, but, unfortunately, this does not seem to match our observations.

Further work is underway to calculate the non-Hermitian susceptibility for several models of bosons in optical lattices (Mott insulator state, Gutzwiller model, Luttinger liquid) and compare with experimental results. We note that the measurements of the first-order coherence (in Chapter 3) indicate that the finite temperature of the initial system is not negligibly small and should be taken into account. It would be interesting to extend this study to two-dimensional systems, in the bulk or in lattices.

Part III

A single bulk two-dimensional Bose gas

CHAPTER 6

Experimental realization and characterization of a two-dimensional Bose gas

Introduction

In this part of the manuscript, we discuss technical improvements to the experimental setup that have been implemented in the last part of my thesis work.

The main objective of the upgrades is to enable in-situ imaging of the atoms with a high-resolution microscope objective (MO). Precise access to the density distribution of the atoms could allow us, for example, to resolve the Mott shell structure described in Chapter 2 and to controllably probe different fillings (Gemelke et al. 2009). An important step for high-resolution imaging of quantum gas has been the development of *quantum gas microscopes* (Bakr et al. 2009, Sherson et al. 2010), which, thanks to an optical resolution of a few hundred nm, are able to resolve fluorescence from adjacent sites in an optical lattice. In our case, we do not aim at achieving single-site resolution in our magic retroreflected lattices, as this would require an optical resolution $\lesssim \lambda_m/2 = 0.38\,\mu m$. Such resolutions have only been recently achieved in cold atom experiments with superresolution techniques (McDonald et al. 2019, Subhankar et al. 2019). We have designed and assembled a home-made microscope objective with a numerical aperture NA $\simeq 0.28$ (target resolution of about $0.9\,\mu m$). We installed it on the experiment and estimated the resolution of the imaging system to be about $1\,\mu m$ at $\lambda_b = 399\,nm$, close to the expectations.

In-situ imaging is most relevant for 2D and 1D systems. In Part II, the experiments are performed on stacks of 2D or 1D systems. The integration along the imaging line of sight degrades the resolution and erases correlations for clouds deeper than the depth of field of the imaging system. Therefore, we must first compress our atomic system into a single plane. We chose to perform the 2D compression with a large period lattice (LPL) in which the BEC is loaded. Optical lattices are an excellent tool for 2D compression, and this method is often used, for example in Gemelke et al. (2009). In Sherson et al. (2010), the optical lattice is a standard retroreflected lattice and up to 60 planes are populated. Single plane loading was achieved by a position-dependent microwave transfer and resonant blasting of the other planes. This technique is more difficult to implement in our setup due to the absence of internal structure of the ^{174}Yb ground state, but it could in principle be applied to non-magic lattices using the clock transition (see section 6.2.4). More recently, Ville et al. (2017) have demonstrated 2D compression using an *optical accordion*, i.e. an optical lattice with a controllable lattice spacing. In addition, they use a separate beam for transverse confinement, which they can shape using a digital micromirror device (DMD) and a high-resolution imaging system. In this way, they are able to realize a flat bottom potential with hard walls. In Christodoulou et al. (2021), a similar potential is obtained, but the 2D compression is also achieved using DMD beam shaping.

Section 6.1 describes the optical setup of the new high-resolution imaging system, as well as the different methods we have used to estimate the resolution. Section 6.2 describes the optical setup of the large-period lattice, its characterization, and the loading procedure. We address issues such as single plane loading and stability. In section 6.3, we characterize the 2D cloud with time-of-flight measurements. The vertical expansion of the cloud shows that the atoms are in the vertical ground state of the LPL potential, while the horizontal expansion allowed us to estimate a condensed fraction. We have optimized loading and studied heating while holding the atoms in the LPL. As described in section 6.4, using our new in-situ imaging, we have fully characterized the 2D cloud by fitting the surface density distribution to the known 2D equation of state (Prokof'ev et al. 2002). We find that we can reach temperatures as low as $\approx 25\,nK$, corresponding to entropies per particle as low as $\approx 0.1 k_B$. We discuss what this figure represents and how it can be improved. In section 6.5, we discuss as a perspective the steps needed to make single-plane 2D Mott insulators and the progress we have done so far in this direction.

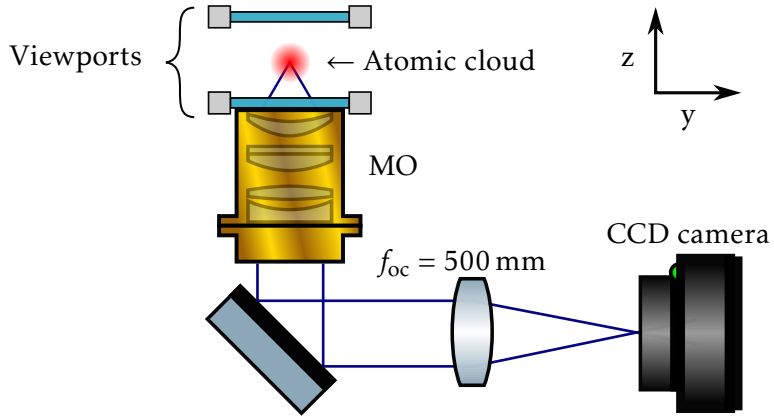

Figure 6.1 Optical setup of the high-resolution vertical imaging system. Distances are not to scale. Adapted from Villain (2021).

6.1 High-resolution imaging system

6.1.1 Optical setup

Figure 6.1 shows the optical setup. The $\lambda_b = 399\,\text{nm}$ imaging beam comes from the top of the science chamber. After passing through the chamber, it passes through a homemade microscope objective (MO) placed below. The MO was designed to have a numerical aperture of 0.28, a focal length of $f_{MO} = 35.8\,\text{mm}$ and a working distance of 31.3 mm (Soave 2016). Together with the MO, a $f_{oc} = 500\,\text{mm}$ occulus lens forms a microscope with a magnification of $M \simeq f_{oc}/f_{MO} \simeq 14.0$.

The MO vertical position was chosen so that focus was achieved when the distance between the relay lens and the camera was equal to the focal length of the lens. It could be adjusted by screwing or unscrewing the MO in its mount, as the science chamber was too low to place a vertical translation mount. Although the MO is placed on the XY horizontal translation mount, the horizontal position is very constrained by the geometry of the vacuum chamber.

Accurate calibration of the magnification is important because it will influence our analysis of distances, optical density, etc. The most precise way to calibrate the magnification is by free falling atoms, but this is not an option for vertical imaging. Since for horizontal imaging, the free-fall measurement gave the expected magnification, we used the calculated magnification of 14 for all the analysis. We have used Kapitza-Dirac measurements to estimate the magnification: the magnification is deduced from the position of atoms diffracted from an optical lattice, as described in Chapter 2. These experiments gave a magnification of 14.5 when 14.0 is expected. We note that interactions between the diffracted components could lead to a systematic shift. With the horizontal imaging system, we have measured a systematic shift of at least 5% with respect to the free fall measurement.

6.1.2 Experimental estimates of the resolution

The MO was designed to have an optical resolution of 0.7 µm at 399 nm. In this manuscript, we define the optical resolution as the half width at half maximum $\Delta r = \sqrt{2\ln(2)}\sigma$ of the Gaussian of $1/\sqrt{e}$-size σ closest to the diffraction limit Airy function. The diffraction-limited optical resolution σ is related to the numerical aperture NA $\simeq 0.28$ by $\sigma \simeq 0.42\lambda/\text{NA}$, yielding

$$\Delta r \approx 0.49 \times \frac{\lambda}{\text{NA}}. \tag{6.1.1}$$

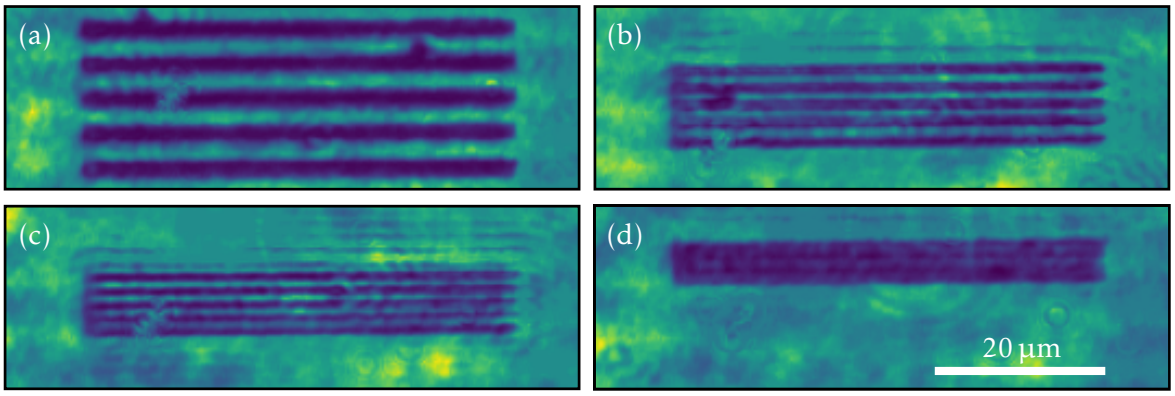

Figure 6.2 Images of the different patterns of the test target, corresponding to lines of width (a) 2, (b) 1, (c) 0.8 and (d) 0.5 µm. Note that the period of the pattern is twice the line width.

We thus expect $\Delta r \approx 0.7\,\mu\text{m}$ for the imaging wavelength $\lambda_b = 399\,\text{nm}$. In this subsection, we discuss the different methods we have used to measure the optical resolution of the MO and of the imaging system as a whole.

6.1.2.1 With resolution targets

Prior to its installation under the science chamber, the MO was calibrated on a test bench with different resolution targets. Images of these targets with the MO are shown in figure 6.2. These tests determined the resolution of the MO was approximately 1 µm: the target with 1 µm width lines could be resolved with a halved contrast while the target with 0.5 µm width lines could not be resolved. Fits of the target images with a convolved Gaussian yielded a resolution of 0.9(1) µm. With these tests, we were also able to measure that the depth of field of the microscope was on the order of ±10 µm. We also noted that, counter-intuitively, a smaller imaging beam waist improved the resolution. More details on these tests can be found in (Villain 2021).

6.1.2.2 With optical lattices

To determine the resolution when imaging the atomic plane, the general idea is to prepare the smallest possible object so that the measured density is the most sensitive to the resolution. A small 3D BEC would seem like a good starting point but the spatial and optical densities in the CDT are too high. As a result, in-situ images of the cloud are 2-3 times larger than the expected Thomas-Fermi radii. Although we could reduce the atom number to alleviate these issues, this makes this method impractical and prone to uncontrolled systematic effects.

We used atoms in optical lattices to fulfill the same role as test targets with periodic patterns. We set up horizontal 1D optical lattices of different periods with 759 nm light by varying the angle between the two beams. We prepared the atoms in the LPL (as described in the rest of the chapter) and then turned on the additional horizontal lattice. We observed that the cloud was split into parallel tubes that we could resolve optically. These experiments showed that the imaging system could resolve atoms in a lattice with 3 µm period, as shown on figure 6.3, but not atoms in a lattice with a 1 µm period. Due to optical access constraints around the science chamber, we cannot produce easily a lattice spacing between those two values. Furthermore, the disadvantage of periodic patterns is that they only provide an upper bound for the resolution: if the lattice spacing is smaller than the resolution, the measured density will not show any modulation. From these measurements, we can only conclude that the resolution of in-situ images is between 0.5 and 1.5 µm.

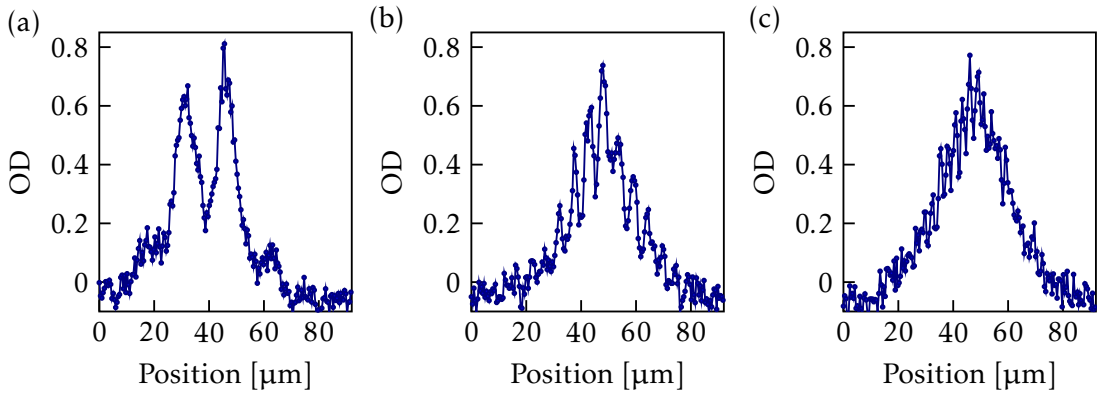

Figure 6.3 Cut of in-situ images of the atoms trapped by the LPL and a lattice of period (a) 15 µm, (b) 6 µm and (c) 3 µm.

6.1.2.3 With density-density correlations

An effective way to measure the resolution is to prepare an object much smaller than the resolution so that its image is given by the PSF of the imaging system. But without interferences, the size of the smallest trap we can prepare is given by the resolution. However, density-density correlations can provide length scales much smaller than our resolution. For example, the density-density correlations of a 2D non-interacting thermal gas will vary with a length scale given by the thermal de Broglie wavelength

$$\lambda_{\mathrm{dB}} = \frac{h}{\sqrt{2\pi m k_{\mathrm{B}} T}} \approx 0.4\,\mu\mathrm{m} \tag{6.1.2}$$

for $T = 100\,\mathrm{nK}$. Density-density correlations can thus be used as a means not only to calibrate the resolution of the imaging system, but also to characterize aberrations in order to reduce them (Hung et al. 2011b). However, in our case, our two-dimensional gases cannot be considered to be non-interacting because the 2D interaction parameter $\tilde{g} \simeq 0.15$ is not small compared to 1 and the surface density n is such that nk^{-2} is comparable to 1. In Hung et al. (2011b), the authors could control the interaction strength with a Feshbach resonance, and they found that the density correlations were strongly affected by the presence of interactions.

A time-of-flight also gets rid of the interactions, but it has two drawbacks. First, the cloud expands vertically very quickly and may be larger than the depth of field. Second, since our high-resolution imaging axis is vertical and gravity cannot be compensated by magnetic fields with Yb, the atoms are displaced from their in-situ position by $\Delta z = 2\,\mathrm{mm}$ in a 20 ms time-of-flight. This can be accounted for by increasing the distance $f = 500\,\mathrm{mm}$ between the relay lens and the camera by $M^2\Delta z = 100\,\mathrm{mm}$, but this could in principle affect the resolution. Despite these two problems, time-of-flight density-density correlation measurements can give an upper bound that should be close to the actual in-situ resolution.

We have performed such measurements on a gas released from a 3D Mott insulator. The average tof distribution is given by the Fourier transform of the Wannier function. Noise analysis can reveal the density-density correlations in momentum space of the trapped gas, which exhibits sharp peaks due to the bosonic quantum statistics (Altman et al. 2004, Fölling et al. 2005). We use a sample of 50 images prepared in identical conditions. For each image n, the autocorrelation function (ACF) is obtained by Fourier-transforming the image, taking the absolute square to obtain the power spectral density and Fourier-transforming it back,

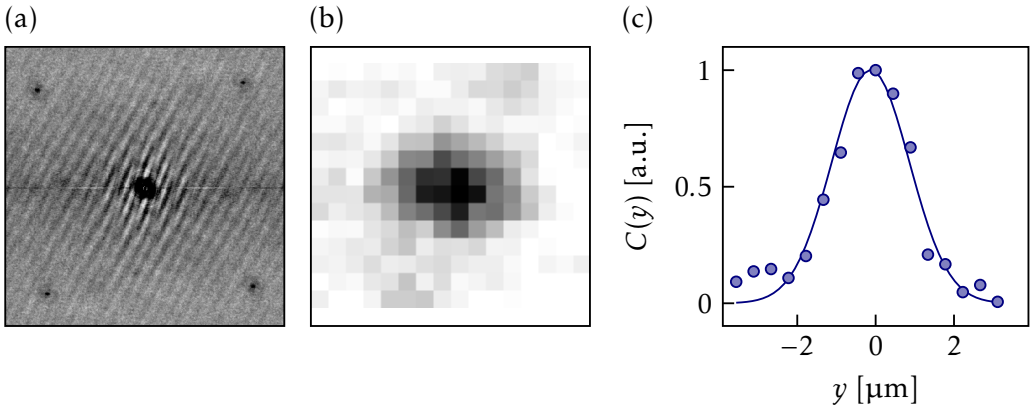

Figure 6.4 Noise analysis to extract density-density correlations. (a) Normalized density-density correlation function $C(x, y)$ of the cloud. (b) Zoom on one secondary peak. One pixel corresponds to $\approx 0.5\,\mu$m. (c) Cut along y of the 2D Gaussian fit of the secondary peak. The fitted Gaussian $1/\sqrt{e}$-size is $1.0\,\mu$m, corresponding to a resolution of $1.2\,\mu$m.

$\mathrm{ACF}(n) = \mathrm{TF}^{-1}\left[|\mathrm{TF(n)}|^2\right]$. Averaging the ACF of all images in the set yields

$$A(\boldsymbol{d}) = \frac{1}{N_{\mathrm{im}}} \sum_n \mathrm{ACF}(n) = \int \langle n(\boldsymbol{x} + \boldsymbol{d}/2) \cdot n(\boldsymbol{x} - \boldsymbol{d}/2) \rangle \mathrm{d}^2 x, \tag{6.1.3}$$

while the ACF of the average of all images yields

$$B(\boldsymbol{d}) = \mathrm{ACF}\left(\frac{1}{N_{\mathrm{im}}} \sum_n n \right) = \int \langle n(\boldsymbol{x} + \boldsymbol{d}/2) \rangle \langle n(\boldsymbol{x} - \boldsymbol{d}/2) \rangle \mathrm{d}^2 x. \tag{6.1.4}$$

In the end, the normalized density-density correlation function of the cloud is

$$C(\boldsymbol{d}) = A(\boldsymbol{d})/B(\boldsymbol{d}). \tag{6.1.5}$$

By fitting the secondary Bragg peaks to a Gaussian, we found a width corresponding to a resolution $1.2\,\mu$m, as shown on figure 6.4.

6.2 Two-dimensional compression in a large-period lattice

6.2.1 Optical setup

The LPL is formed by two 532 nm laser beams focused at the science chamber center with an angle of 7.6°. Both beams come from the same laser source as the DT2 (Verdi V-6, Coherent). They are separated from each other by a polarising beam splitter (PBS), their polarisations are then rematched with a $\lambda/2$ waveplate and they are combined with a 200 mm lens focused on the atoms. The center of the lens is in the horizontal plane containing the atoms, and the two beams hit the lens symmetrically with respect to the horizontal plane so that they both make an angle $\alpha_{\mathrm{LPL}} \approx 3.8°$ with the horizontal, thus ensuring the verticality of the LPL. All the optics allowing the separation and recombination of the two arms of the lattice are contained in a stainless steel box to reduce thermal drifts, as shown in figure 6.5. The box was designed and tested by Raphael Bouganne (Bouganne 2018).

The angle between the two arms of the lattice is chosen so that the lattice spacing is $d_{\mathrm{LPL}} \approx 4\,\mu$m, which is roughly the vertical Thomas-Fermi diameter in the CDT. This way, we expect an adiabatic transfer of the BEC in the CDT to load a single plane of the LPL. This is discussed further in section 6.2.4.

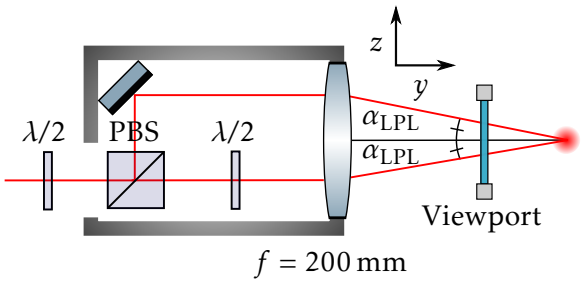

Figure 6.5 Schematic of the stainless steel box containing the optics separating and recombining the two laser beams forming the LPL.

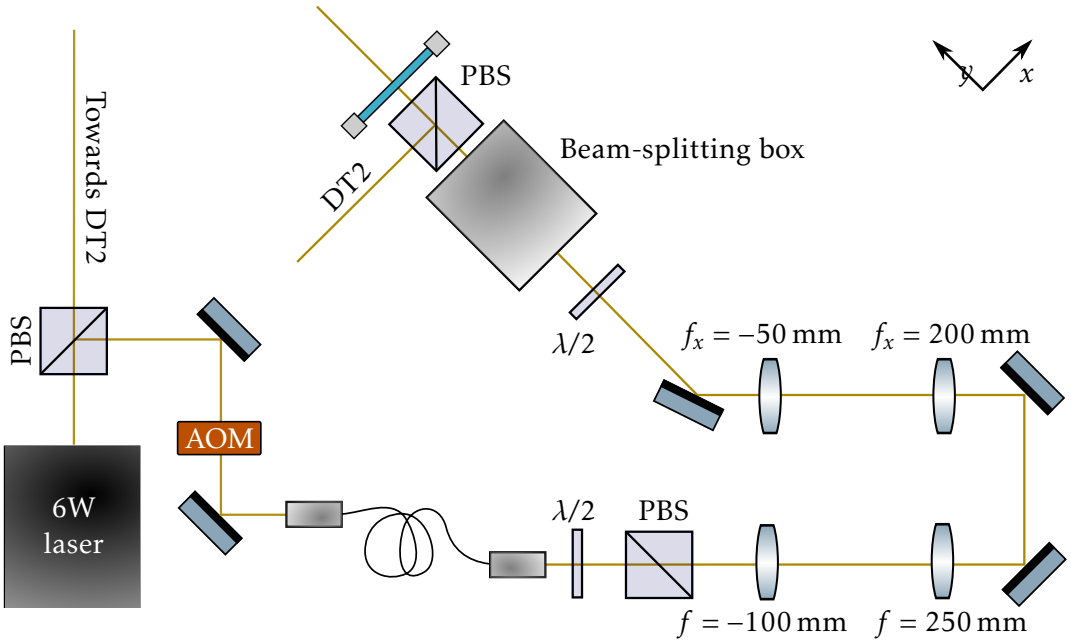

Figure 6.6 Top view of the optical setup. $\lambda/2$ represents a half waveplate, PBS stands for polarizing beam splitter and (f_x) f corresponds to a (cylindrical) lens focal length. AOM stands for acousto-optical modulator.

In order to maximize the vertical frequency and minimize the horizontal frequencies, we want a beam with a small vertical waist but a large horizontal waist, as detailed in the next subsection. We prepare a beam with a waist of 1.8 mm before the box, corresponding to $w_z \simeq 20\,\mu\text{m}$ on the atoms. Then, using a cylindrical telescope, we reduce the horizontal waist of the beam by a factor of 4, so that after a 200 mm focusing lens the waist on the atoms is increased to $w_x \simeq 80\,\mu\text{m}$. The optical setup for the beam shaping is shown on figure 6.6.

6.2.2 Characterization of the large period lattice

Since the atoms are at the bottom of one of the LPL potential minima, the potential seen by the atoms is well described by a 3D harmonic potential, with trapping frequencies given by

$$\omega_x \simeq \sqrt{\frac{4U_{\text{LPL}}}{m}}\frac{1}{w_x}, \quad \omega_y \simeq \sqrt{\frac{4U_{\text{LPL}}}{m}}\frac{\sin(\alpha_{\text{LPL}})}{w_z}, \quad \omega_z \simeq \sqrt{\frac{2U_{\text{LPL}}}{m}}\frac{2\pi\sin(\alpha_{\text{LPL}})}{\lambda}, \tag{6.2.1}$$

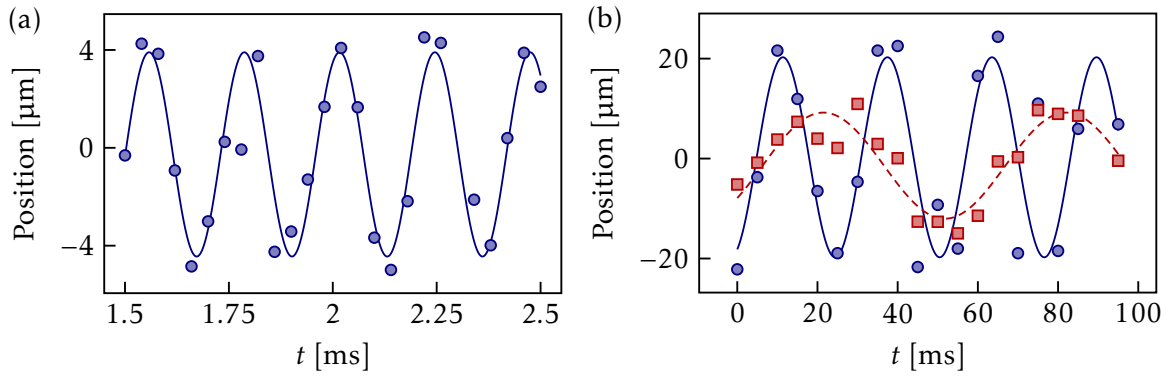

Figure 6.7 Measurement of the LPL trapping frequencies. (a) Vertical oscillation of the cloud measured after of 15 ms time-of-flight. (b) Horizontal oscillations of the cloud measured in-situ. Circles correspond to oscillations in the x direction and squares to the y direction.

where w_i is the waist of the beam along the i direction. We have also defined the depth of the potential

$$U_{\mathrm{LPL}} = \frac{4\alpha_g^{(532)} P_{\mathrm{LPL}}}{\epsilon_0 c \pi w_y w_z} \tag{6.2.2}$$

where $\alpha_g^{(532)} = 235\alpha_0$ is the 532 nm polarizability of the atomic ground state (see Chapter 2) and P_{LPL} the optical power in each arm of the lattice.

By slowly increasing the LPL and abruptly turning off the CDT, we are able to measure fast vertical oscillations of the atomic cloud position after a 15 ms tof. For horizontal trapping frequencies, we use our vertical high resolution imaging to observe the oscillation of the cloud's center of mass position. As shown in figure 6.7, we measure $(\omega_x, \omega_y, \omega_z) = 2\pi \times (17, 38, 4.5 \times 10^3)$ Hz for 200 mW of power in each arm of the LPL, which is the maximum we can achieve with our current setup. We have also performed parametric heating measurements of the vertical trapping frequencies. By modulating the LPL intensity by a few percent, we observe strong heating and losses in the cloud at twice the trapping frequency. We find a vertical trapping frequency in agreement with that measured by abruptly turning off the CDT. We note that these trapping frequencies are very different from the ones in the CDT, $2\pi \times (80, 240, 250)$ Hz, as seen in Chapter 2: not only the cloud is strongly confined in the vertical direction, but the horizontal frequencies are also one order of magnitude smaller than in the CDT. This can make the adiabatic transfer from the CDT to the LPL difficult, as discussed in the following subsection.

One should note that Kapitza-Dirac measurements of the lattice depth of the LPL, like the ones described in Chapter 2, are not really feasible. Indeed, the lattice spacing is more than ten times larger than for retroreflected lattices. The lattice momentum $k = \pi/d$ is then too small to create sufficient displacements over a 20 ms time-of-flight.

In order to finely align the LPL, we built an imaging system to measure the intensity of the LPL in the plane containing the atoms. A 150 mm lens collimates the three 532 nm beams that were focused on the atoms: the DT2 and the two beams forming the LPL. Most of the power is sent to a beam dump but a small fraction is sent on a 750 mm lens and a camera, thus forming an imaging system with a magnification of 5. This allows us to observe one of the beams of CDT on the same camera as the LPL. In order to align the LPL, we want these three beams to overlap in the plane containing the atoms. To determine this plane, we aligned the three beams for different longitudinal positions of the camera, and chose the one maximizing the vertical trapping frequency. A good starting point was to image the atoms with blue light, but the chromatic shifts between the imaging wavelength (399 nm)

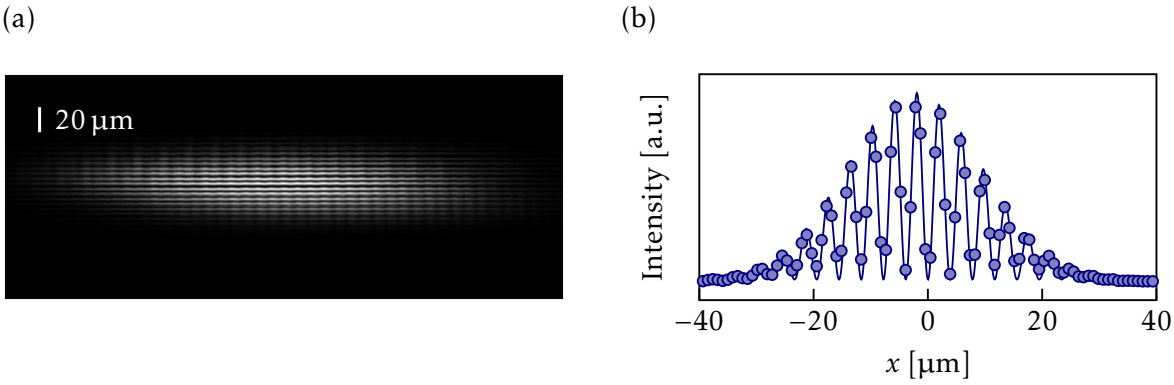

Figure 6.8 (a) Image of the LPL beam profile on a CCD camera. The scale shown accounts for the magnification of the imaging system of the LPL. For comparison, the waist of the crossed dipole trap is 15 µm. (b) Vertical cut of the image and fit.

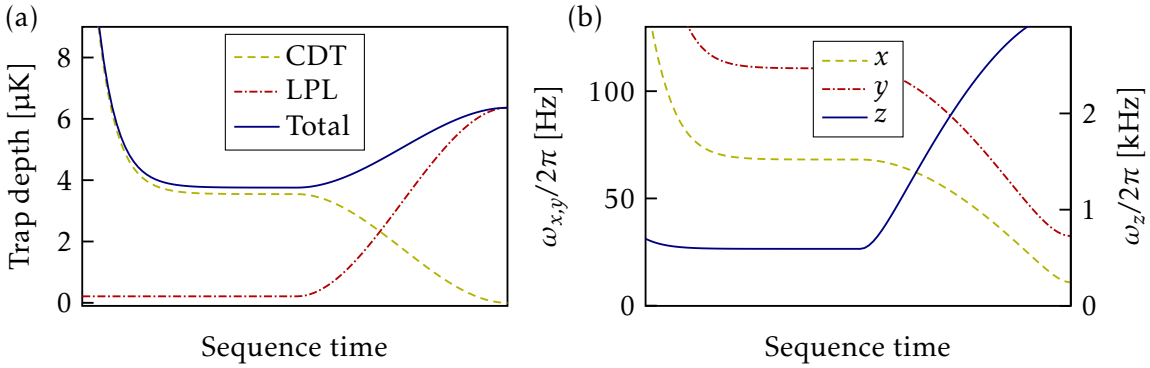

Figure 6.9 Experimental loading sequence. (a) Potential depth and (b) trapping frequencies as a function of time, from 3D evaporation to 2D compression, for the CDT and the LPL.

and the LPL wavelength (532 nm) significantly displace the image plane. Once the plane of the atoms was determined, we finely realigned the LPL each morning on the CDT. An image of the LPL aligned in the plane of the atoms is shown on figure 6.8.

6.2.3 Loading sequence

Starting from the BEC in the CDT, the LPL is ramped up and the CDT is simultaneously ramped down to zero. The determination of the optimal ramp parameters is detailed in section 6.3.3. We found the optimal ramp duration to be approximately 300 ms. In addition, we found that we could increase the condensed fraction after the transfer by turning on the LPL during evaporation. As we discussed in Chapter 2, the CDT final evaporation power is limited by the compensation of gravity. The LPL allowed us to evaporate the CDT to lower values, although we found that evaporating to zero while keeping the LPL at intensity sufficient to trap the atoms by itself resulted in a reduction of the condensed fraction. Finally, we found that ramping up the LPL and ramping down the CDT simultaneously or one after the other had no measurable effect.

The loading sequence of the LPL is shown on figure 6.9. We show the evolution of the trap depths (CDT, LPL and total) during the loading sequence, as well as the evolution of the trapping frequencies of the total trap. A small initial power of the LPL during evaporation is included.

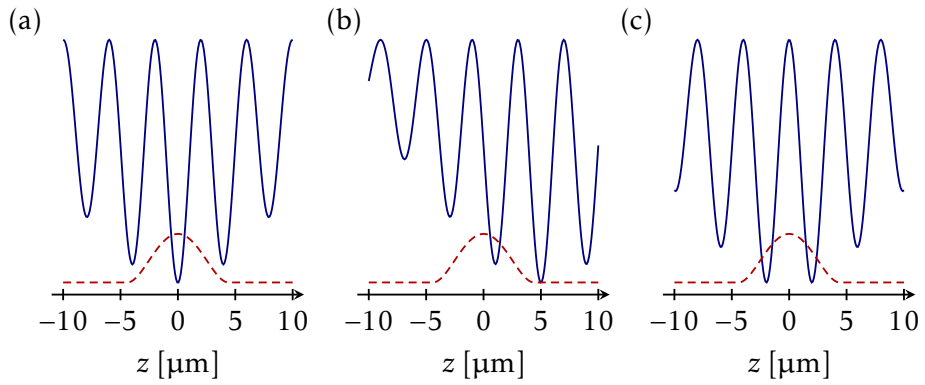

Figure 6.10 Sketch of the loading of the LPL. The solid line represents the LPL trapping potential in the vertical direction, and the dashed line corresponds to the vertical Thomas-Fermi distribution of the BEC in the CDT, with $R_z = 2.5\,\mu\text{m}$. (a) The BEC is aligned with the brightest fringe of the LPL. (b) Envelope misalignment: the BEC is not aligned with the brightest fringe of the LPL. (c) Phase misalignment: the LPL has two brightest fringes.

6.2.4 Loading a single plane

Although we can take side views of the cloud in the LPL using one of the horizontal absorption imaging systems, the optical resolution $\gtrsim 2.4\,\mu\text{m}$ is insufficient to clearly resolve the individual planes of the LPL.

Figure 6.10 shows that there are two ways to misalign the LPL with respect to the BEC. The simplest one is to misalign the position of its envelope, as shown in figure 6.10(b). Also, as shown in figure 6.10(c), there may be not one, but two brightest fringes. We monitor the LPL beam profile to always exclude situation (c).

For simplicity, let us take a sudden loading model such as the one used in Chapter 2 for the retroreflected vertical lattice. The first thing we can note from figure 6.10 is that we can significantly load at most two planes. We first consider situation (a), where the alignment is perfect. The population in the brightest fringe is given by

$$P_0 = \frac{1}{N}\int_{-d_{\text{LPL}}/2}^{d_{\text{LPL}}/2} \mathrm{d}z\, \bar{n}_{\text{TF}}(z) \tag{6.2.3}$$

while the population in the nearest-neighbouring fringes is given by

$$P_1 = \frac{1}{N}\left(\int_{-3d_{\text{LPL}}/2}^{-d_{\text{LPL}}/2} \mathrm{d}z\, \bar{n}_{\text{TF}}(z) + \int_{d_{\text{LPL}}/2}^{3d_{\text{LPL}}/2} \mathrm{d}z\, \bar{n}_{\text{TF}}(z)\right), \tag{6.2.4}$$

where $\bar{n}_{\text{TF}}(z)$ is the density of the BEC integrated along x and y. With this sudden loading model, we find that only 1.8 % of the atoms are loaded in the neighboring planes, regardless of the number of atoms. We next consider situation (b), where the BEC is fixed at $z = 0$ and the brightest fringe is misaligned by z_0. Figure 6.11 shows the populations of the two layers P_0 and P_1 as functions of z_0. We see that the central fringe must not be misaligned by more than 0.8 µm if we want the population of neighboring planes to be less than 10 %. The sudden loading model is a worst-case scenario, but still provides a useful guide.

To experimentally test the loading of a single plane, we can perform spectroscopy on the LPL-trapped cloud using the clock transition presented in Chapter 2. The polarizabilities of the atomic ground and excited states are very different at $\lambda = 532\,\text{nm}$ ($\alpha_g^{(532)} = 253\alpha_0$ and $\alpha_e^{(532)} = 105\alpha_0$ respectively). This leads to a *differential light shift* (DLS) of the resonance compared to the untrapped gas. Experimentally, we find that the resonance is detuned by about

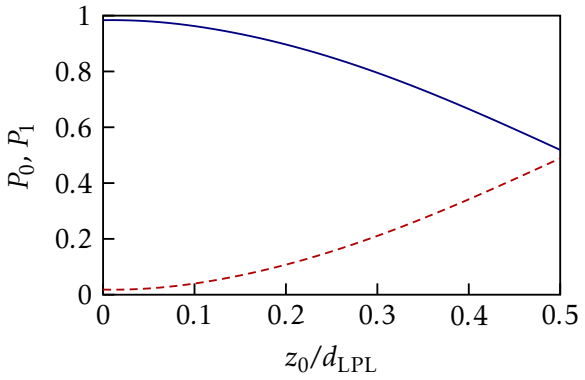

Figure 6.11 Sudden loading model of the LPL: population in the brightest fringe P_0 (solid line) and in the neighbouring fringes (dashed line) as a function of the misalignement z_0 of the LPL.

200 kHz. If U_0 is the trap depth of the brightest fringe for the ground state, the differential light shift is

$$\mathrm{DLS} = \frac{U_0}{h}\left(1 - \frac{\alpha_e}{\alpha_g}\right) \approx 0.58\frac{U_0}{h} \tag{6.2.5}$$

with $U_0 \approx 350$ kHz. Thanks to the small waist in the vertical direction, the differential light shift is sufficiently different between two planes of the LPL that we can resolve it spectroscopically. The situation in figure 6.10(a) is the one we should aim for to maximize the effect of the difference in DLS between two planes: we cannot spectroscopically resolve two planes in situation (c). With a camera image such as the one on figure 6.8, we can see that the intensity difference between the central fringes and its neighbors is about 10 %, which means that we expect a differential DLS of about 20 kHz.

This number must be compared to the resolution of our spectroscopic measurements. The resolution of the clock laser being of the order of 10 Hz, it is more likely that we are limited by the spatial extension of the cloud. The potential energy at the edge of a Thomas-Fermi cloud is equal to the chemical potential μ_0. For a 2D cloud, we have

$$\mu_0 = \sqrt{\frac{N\tilde{g}\hbar^2\omega_x\omega_y}{\pi}} \approx 1.6\,\mathrm{kHz} \tag{6.2.6}$$

for $N = 8 \times 10^4$ atoms. Therefore, this broadening does not pose a problem for the spectroscopic resolution of several populated LPL planes.

We shine the clock laser on the atoms and subsequently measure the ground state population of the cloud. When atoms are transferred to the metastable excited state, they are not imaged and we observe a reduction of the atom number. Examples of clock spectroscopy in the LPL are shown in figure 6.12. We observe a differential DLS of 23 kHz when two planes are loaded. As expected from the sudden loading model, we found that it was not possible to load more than two planes: indeed no significant depletion was ever observed at −46 kHz. The experiment in its current state does not give access to a precise control of the envelope position and the interference phase. For the phase in particular, we could only change it by π using a half-wave plate, as is explained in Appendix C.1. The phase control of the LPL could be improved by using a liquid crystal polarization rotator for example, but we found experimentally that we were able to load a single plane consistently. Furthermore, once single-plane loading was achieved by alignment, we observed that the loading was stable over a day by repeating the spectroscopic measurements.

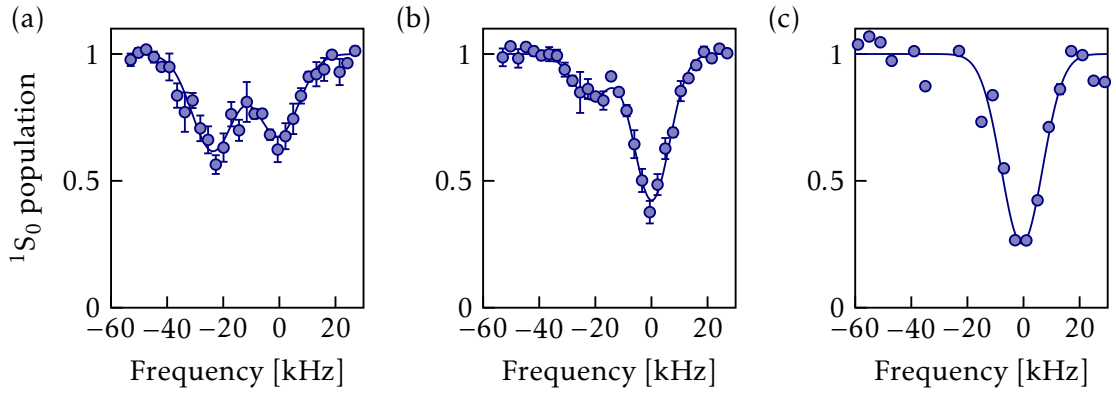

Figure 6.12 Examples of spectroscopy of the LPL: atom number in the ground state as a function of the frequency of the clock laser. Errorbars correspond to the error on the mean. The peak at smaller frequencies corresponds to the second plane, i.e. the one that has less intensity. Using a double Gaussian fit, we estimate that ∼ 55% of atoms are trapped in the second plane for figure (a) and ∼ 25% for figure (b).

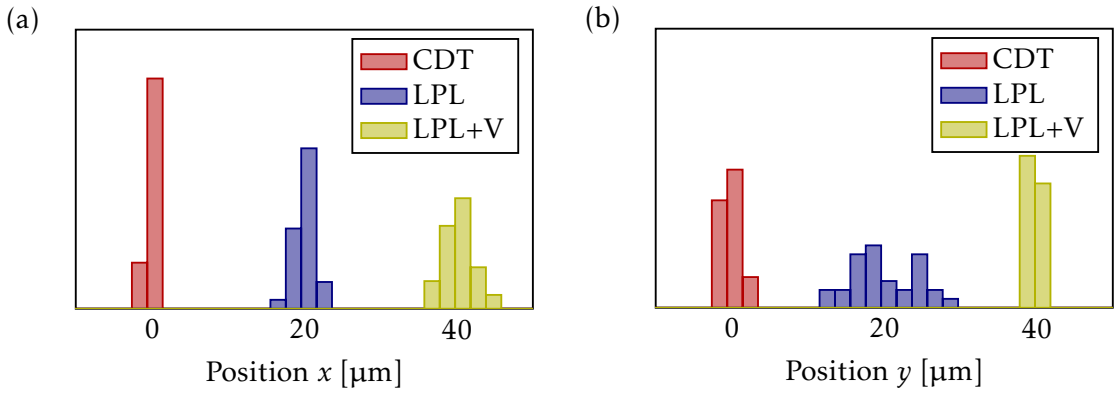

Figure 6.13 Histograms comparing the stability of the cloud in the CDT and in the LPL. (a) and (b) correspond to the transverse and longitudinal direction of LPL respectively. LPL+V corresponds to experiments where a small vertical beam was used in addition to the LPL to stabilize the position of the cloud.

We note that this technique would not work if the LPL was at the magic wavelength λ_m of the clock transition. It would then be necessary to apply an additional light gradient in order to resolve the different planes spectroscopically.

6.2.5 In-plane stability

The horizontal pointing stability of the laser system forming the LPL is crucial because the beam is very wide horizontally, which can lead to large in-plane displacements. Figure 6.13 compares the in-plane stability of the cloud in the CDT and in the LPL, and shows that the center-of-mass fluctuations are up to 4 times larger in the LPL than in the CDT. These fluctuations are slow enough not to heat the cloud significantly, but introduce shot-to-shot variations of cloud position. Initially, the optical setup contained a periscope which we got rid of because it contributed to the pointing instability. However, as we built multiple iterations of the LPL, we found that the determining factor for in-plane stability was the cylindrical telescope. Specifically, we found that the higher the magnification of the cylindrical telescope, the greater the instability.

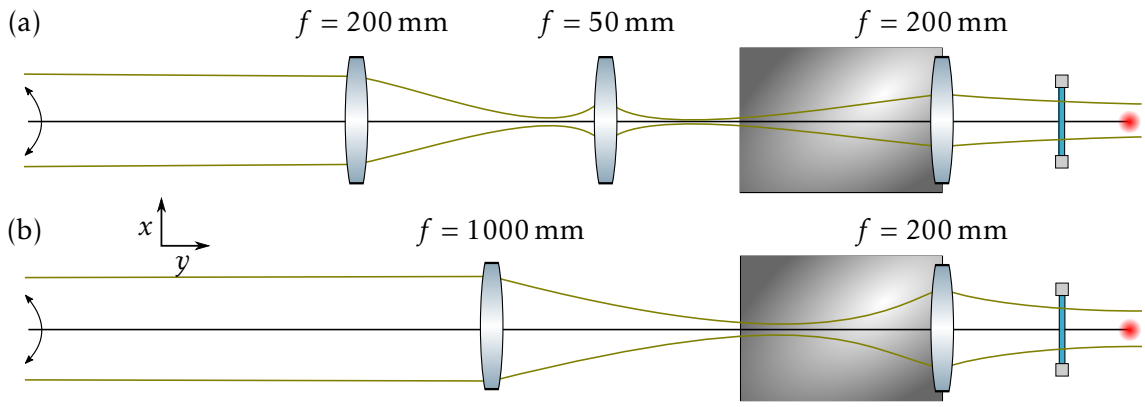

Figure 6.14 Top-view sketch of the two different optical configurations possible to beam shape the LPL. Green lines are a schematic Gaussian optics representation of the LPL. (a) Telescope configuration, favoring instability in the x direction. (b) Single lens configuration, favoring instability in the y direction.

This can be understood if we consider a pointing instability far from the microscope. The cylindrical telescope, which has a magnification $\gamma < 1$ for the beam size, has a magnification $1/\gamma > 1$ for angles, which increases the pointing instability. Due to the $f = 200\,\mathrm{mm}$ focusing lens, this pointing instability of the beam becomes mainly a positional instability in the transverse direction x. On the other hand, one can increase the horizontal waist by using a single cylindrical lens instead of a telescope, as shown in figure 6.14(b). This results in increased angular instability, which translates into instability mainly in the longitudinal direction y. In the end, we chose the optical configuration that compromises between transverse and longitudinal instabilities.

Vertical pointing instability is less problematic because there is no telescope to enhance it and because the depth of field of the imaging system is relatively large (see section 6.1). The stability over several hours of the single-plane loading process indicates that the fluctuations seen by the atoms are negligible.

6.3 Time-of-flight expansion of the compressed cloud

6.3.1 Vertical expansion measurements

The vertical expansion of the cloud can give us important information on the quantum state of the trapped cloud. If $T, \mu \ll \hbar\omega_z$, all the atoms should be in the single-particle ground state of the vertical harmonic oscillator of frequency ω_z created by the LPL

$$\psi_0(z) \propto \exp\left(-\frac{m\omega_z z^2}{2\hbar}\right). \tag{6.3.1}$$

After a long-enough tof t, we image the corresponding momentum distribution, which is

$$|\tilde{\psi}_0(k_z)|^2 \propto \exp\left(-\frac{\hbar k_z^2}{m\omega_z}\right), \tag{6.3.2}$$

where we have $k_z = mz/\hbar t$. Therefore, we expect to measure a Gaussian distribution vertically, with a half-width at $1/\sqrt{e}$

$$\sigma_z(t) \approx \sqrt{\frac{\hbar\omega_z}{2m}}\, t. \tag{6.3.3}$$

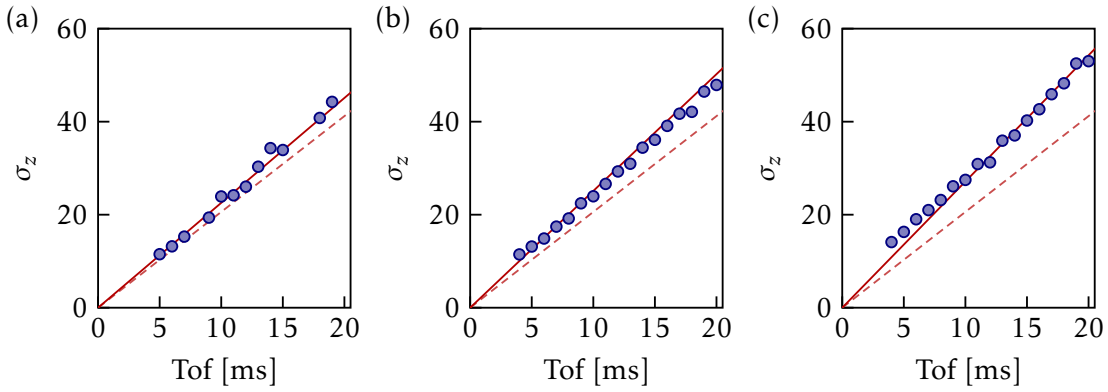

Figure 6.15 Temporal evolution of the vertical cloud size during the tof for (a) 4000, (b) 24 000, (c) 55 000 atoms. The points correspond to $1/\sqrt{e}$ half-lengths extracted from a fit. The dashed lines correspond to $\hbar\omega_z/4$ and the solid lines include a contribution from the interaction energy $\mu_0/2$.

The expansion speed $v_{\mathrm{zpk}} = \sqrt{\hbar\omega_z/2m}$ corresponds to the initial zero-point kinetic energy for an atom in the ground state of the trap,

$$\frac{1}{2}mv_{\mathrm{zpk}}^2 = \frac{\hbar\omega_z}{4}. \tag{6.3.4}$$

As shown on figure 6.15, we observe that the vertical size of the cloud increases linearly for tofs greater than 4 ms. However, the cloud expands faster than the prediction of equation (6.3.4), and the expansion speed slightly increases with the atom number. To understand this, we have done variational calculations to calculate the expected contribution from the interaction energy, as detailed in Appendix C.2. Using the hierarchy

$$\zeta \ll \eta \ll 1 \tag{6.3.5}$$

where $\zeta = \sqrt{\omega_x^2\omega_y^2}/\omega_z$ is the aspect ratio of the trap and $\eta = \mu_0/\hbar\omega_z$ is the normalized chemical potential, we find that the release energy accounting for interactions is

$$E_{\mathrm{release}} = \frac{1}{2}mv_{\mathrm{zpk}}^2\left(1 + \frac{5}{3}\eta\right). \tag{6.3.6}$$

Calculating the chemical potential using the 2D Thomas-Fermi formula

$$\mu_0 = \sqrt{\frac{N\tilde{g}\hbar^2\omega_x\omega_y}{\pi}}, \tag{6.3.7}$$

we find a good agreement with equation (6.3.6): figure 6.16 shows the fitted asymptotic vertical expansion speed v_z (in units of v_{zpk}) as a function of η. We conclude that the atoms are in the ground state of the vertical oscillator created by the LPL, and that we have successfully produced a two-dimensional quantum gas.

6.3.2 Horizontal expansion and condensed fraction estimation

The horizontal momentum distribution of the cloud after a long tof can also yield information on the thermodynamics of the cloud. As explained above, all the interaction energy is approximately released in the vertical direction because of the anisotropy of the LPL. Therefore, the condensed part of the cloud does not expand horizontally, contrary to the thermal

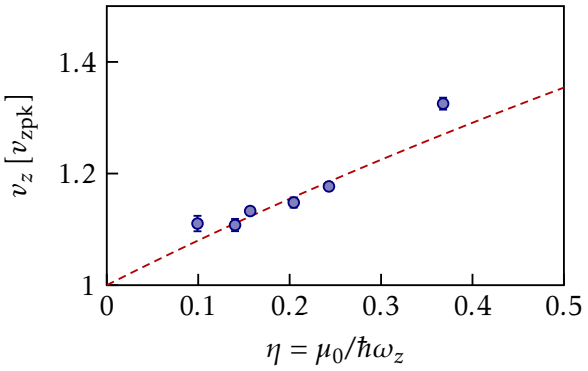

Figure 6.16 Vertical expansion speed as a function of $\eta = \mu_0/\hbar\omega_z$. The experimental data is extracted from a linear fit of the expansion and errorbars are determined with a bootstrap procedure. The dashed line corresponds to $\sqrt{1+2\eta}$, which is expected from equation (6.3.6).

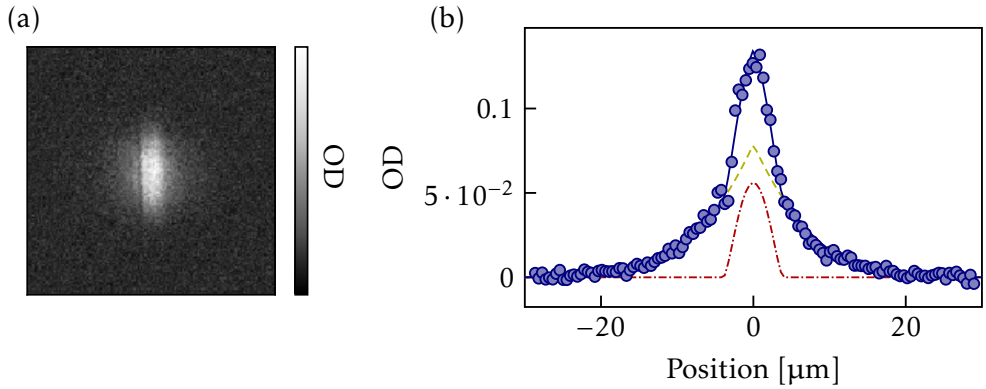

Figure 6.17 (a) Typical density distribution after a tof of 20 ms. We have chosen a hot cloud clearly showing the bimodal distribution. (b) Density distribution integrated along the vertical direction. The solid line corresponds to the total fit to equation (6.3.8). The dashed line corresponds to the fitted thermal fraction and the dash-dotted line to the fitted condensed fraction.

part which expands because of its larger initial kinetic energy. We therefore observe a clear bimodal distribution, as shown on figure 6.17.

We perform 1D fits on the bimodal momentum distribution integrated along the vertical direction. The fitting function is

$$n_{\text{fit}}(x) = A\cdot\Theta\left[1-\frac{(x-x_0)^2}{R_h^2}\right]^{3/2} + B\cdot g_2\left[\exp\left(\frac{(x-x_0)^2}{L_h^2}\right)\right], \tag{6.3.8}$$

where $\Theta(x) = x\theta(x)$ with θ the Heaviside function, and g_α is the polylogarithmic function

$$g_\alpha(x) = \sum_{n=1}^{\infty}\frac{x^n}{n^\alpha}. \tag{6.3.9}$$

The first part of equation (6.3.8) is the Thomas-Fermi distribution and the second part models the density distribution of a thermal gas. Both expressions account for the integration over the imaging direction, hence the exponent 3/2 for the Thomas-Fermi distribution and the g_2 function for the Bose distribution. More details are provided in Appendix C.3.

The fit gives us access to two important observables: the condensed fraction $\text{CF} = A/(A+B)$, and the temperature of the thermal part through $L_h = \sqrt{k_B T/m\omega_h^2}$. For instance, we can

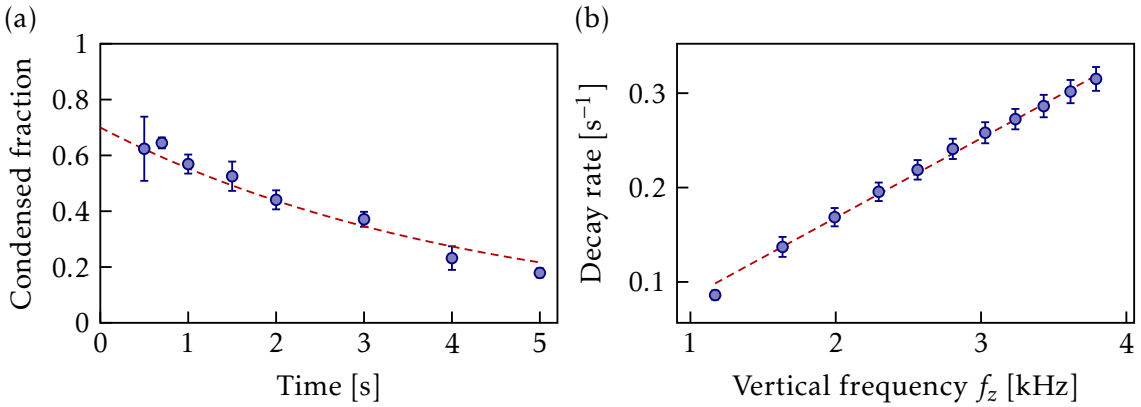

Figure 6.18 (a) Decay of the condensed fraction while maintaining the LPL to its final value. The CF is measured from times 0.5 to 5 s and fitted to an exponential $0.7\exp(-\gamma t)$, shown as a dashed line. (b) Decay rate of the CF in the LPL as a function of the LPL vertical frequency. The dashed line is a linear fit.

measure the heating introduced by maintaining the atoms in the LPL. Figure 6.18(a) shows that over the course of 5 s the CF is significantly reduced. Figure 6.18(b) shows that the reduction rate of the CF increases linearly with the vertical frequency. However, it is always smaller than $0.3\,\mathrm{s}^{-1}$, and thus negligible for the experiments described in the next chapter.

We note, while the horizontal thermal size L_h corresponds to temperatures around $\approx$ 20 nK, the determination of the temperature is not precise enough to quantify the heating. Although the model of equation (6.3.8) is insufficient to do thermometry, the CF is a practical observable for an efficient optimization of the system. Moreover, in section 6.4, we show that we are able to do precise thermometry of the cloud using the in-situ position distribution and the known equation of state.

6.3.3 Optimal loading of the large-period lattice

As mentioned above, the optimal way to maximize the condensed fraction in the LPL is not necessarily to first prepare a 3D BEC with the CDT only, and then turn on the LPL. It might be better to turn on the LPL at very low power during the evaporation and to evaporate the CDT to a lower power. There are actually two extreme cases: either there is no LPL during evaporation and the CDT is evaporated alone, or the power of CDT is reduced to zero and the power of LPL is at the minimum value necessary to trap the atoms without the CDT.

On figure 6.19, we show the results of a 2D scan of the final CDT evaporation power and the LPL evaporation power. We find a variety of configurations that produce a stable and pure 3D Bose-Einstein condensate, indicated by the dashed white line. The LPL is then ramped up to its final power, while the CDT is ramped down to zero. The different configurations mentioned above are not necessarily equivalent once the LPL is ramped up. Figure figure 6.19(b) shows that the condensed fraction in the LPL is about 60 % as long as the CDT and the LPL are both on at the end of evaporation.

We have optimized the transfer ramp duration, as shown in figure 6.20. The optimal ramp duration is about 300 ms. At best, we measure a condensed fraction around 60%. To understand this observation, we have performed experiments where we ramped the LPL to its final value, then back to its evaporation value without ramping down the CDT. We observed a small effect on the purity of the 3D BEC, which indicates that the CDT ramp is likely to be the limiting factor. Unfortunately, we cannot currently perform full back-and-forth experiments where the CDT is ramped down and then up: at very low power, the CDT

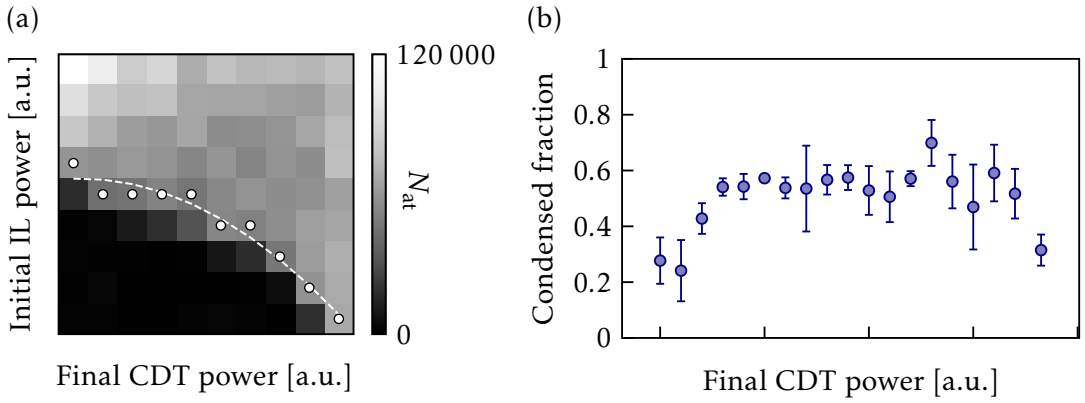

Figure 6.19 (a) 2D scan of the atom number in the 3D BEC as a function of the final CDT evaporation power and the LPL evaporation power. The white points correspond to configurations with a pure and stable BEC with about 50,000 atoms. (b) Condensed fraction in the LPL depending on the CDT evaporation power, the LPL evaporation power being adjusted according to white dashed line on figure (a).

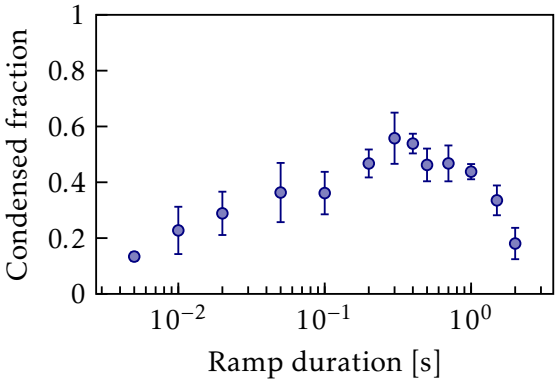

Figure 6.20 Condensed fraction in the LPL as a function of the LPL ramp-up and CDT ramp-down duration.

intensity lock has a lot of hysteresis. This is part of the reason why the "transition" from no atoms to stable condensate is so sharp on figure 6.19(a). We could improve the intensity stability of CDT by using for example another photodiode with a higher gain for the end of evaporation. We also note that we observe strong oscillations of the cloud center of mass up to 0.5 s after an adiabatic transfer. The amplitude of the oscillations decreases with the final power of the LPL. We believe that these oscillations arise from a lack of adiabaticity for the CDT exctinction, which is necessarily abrupt due to the way its intensity is controlled.

6.4 Fitting in-situ images to the two-dimensional equation of state

We now turn to the study of the thermodynamics of our 2D gas using the in-situ density distribution: the cloud is imaged vertically using the high-resolution imaging system described in section 6.1. For absorption imaging to give reliable information about the density distribution of the atoms, the atomic density must be low enough to neglect multiple scatterings of imaging photons. This would also be a problem for imaging the 3D BEC in-situ ($\rho k^{-3} \lesssim 1$) and it is a problem for imaging quasi-2D Bose gases in-situ ($nk^{-2} \lesssim 1$). Moreover, the atomic

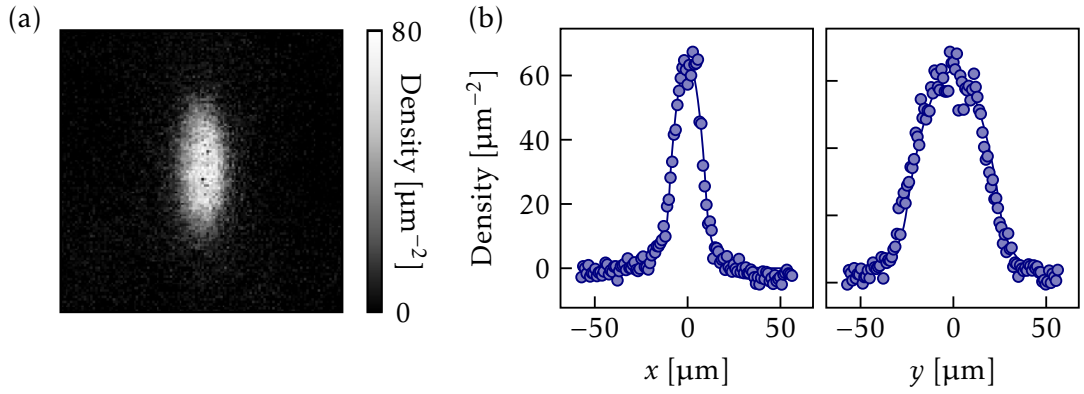

Figure 6.21 Example of a fit to the equation of state. (a) In-situ image of the cloud in the LPL. (b) Cuts of the experimental and fitted atomic density along the x and the y axis.

motion during the imaging pulse should be negligible, whether it is caused by the imaging pulse or not. We adopt the high-intensity imaging approach to circumvent all these issues, as explained in more details in Chapter 7. For now, we admit that we can measure the surface density n of our quasi-2D Bose gases with absorption imaging.

6.4.1 Analysis procedure

The analysis is directly inspired from Yefsah et al. (2011) and Hung et al. (2011a). We start by treating the images with the best-reference algorithm described in Chapter 2. The images are then recentered by finding the maximum of a smoothened image, because of the centre-of-mass fluctuations discussed in section 6.2.5. The images n_{img} are fitted using the 2D equation of state

$$\lambda_{\text{dB}}^2 n = \mathcal{D}(\mu/k_{\text{B}}T) \tag{6.4.1}$$

described in Appendix C.4. To account for the harmonic trap in the plane

$$V_\perp(x,y) = \frac{1}{2}m(\omega_x^2 x^2 + \omega_y^2 y^2), \tag{6.4.2}$$

we use a local-density approximation (LDA) and consider a position-dependent chemical potential

$$\mu(x,y) = \mu_0 - V_\perp(x,y). \tag{6.4.3}$$

In the end, we fit the in-situ density with the function

$$n_{\text{th}}(x,y) = \frac{mk_BT}{2\pi\hbar^2}\mathcal{D}(\alpha(x,y)), \tag{6.4.4}$$

where

$$\alpha(x,y) = \frac{\mu_0 - V_\perp(x,y)}{k_BT}, \tag{6.4.5}$$

with μ_0 and T the two free parameters. Figure 6.21 shows an example of these fits to the 2D equation of state.

For each image, several observables are extracted from the fit, in addition to the chemical potential μ_0 and the temperature T. With equation (6.4.3), each pixel i can be assigned a local $\alpha(i)$ and a local $\mathcal{D}(i)$,

$$\alpha(i) = \frac{\mu_0 - V(i)}{k_BT} \quad \text{and} \quad \mathcal{D}(i) = \frac{2\pi\hbar^2}{mk_BT}n_{\text{img}}(i). \tag{6.4.6}$$

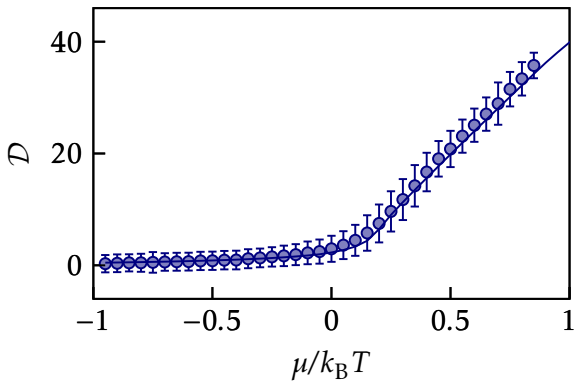

Figure 6.22 Theoretical and experimental 2D equation of state $\mathcal{D}(\alpha)$. The dots correspond to the binned data extracted from a set of in-situ images. The solid line is the theoretical 2D equation of state (Prokof'ev et al. 2002).

We bin the data $(\alpha(i), \mathcal{D}(i))$ extracted from all the pixels from all images where $|\alpha(i)| < 3$. From it, we are able to reconstruct an experimental equation of state, as shown on figure figure 6.22. We note that the experimental points are systematically slightly above the theoretical equation of state in the Thomas-Fermi regime. However, it is difficult to determine whether this comes from a small systematic error in the magnification, in the intensity calibration, etc.

Even more thermodynamic quantities can be extracted from the fits. First, we extract the maximum α, $\alpha_0 = \mu_0/k_B T$ and the maximum phase-space density $\mathcal{D}_0$ (note that we take the fitted maximum phase-space density, not the highest pixel). Following (Yefsah et al. 2011), we also define a reduced pressure

$$\mathcal{P} = \frac{\lambda_{\mathrm{dB}}^2}{k_B T} P. \tag{6.4.7}$$

The reduced pressure is linked to the phase space density through

$$\mathcal{P}(\alpha) = \int_{-\infty}^{\alpha} D(\alpha')\mathrm{d}\alpha'. \tag{6.4.8}$$

The total pressure is therefore the integral over the whole sample, and is thus proportional to the atom number,

$$\mathcal{P}_0 = \left(\frac{\hbar\omega_\perp}{k_B T}\right)^2 N_0, \tag{6.4.9}$$

with $\omega_\perp = \sqrt{\omega_x \omega_y}$. From the fits, we extract the pressure by integrating the fitted density to get a fitted atom number. Knowing $\mathcal{P}_0$ and $\mathcal{D}_0$, we extract the entropy per particle of the cloud

$$\frac{\mathcal{S}}{k_B} = 2\frac{\mathcal{P}_0}{\mathcal{D}_0} - \alpha_0. \tag{6.4.10}$$

We find that we can reach entropies around $0.1 k_B$, as shown on figure 6.23.

6.4.2 Comparison with condensed fraction analysis

With this new analysis, we are able to study heating in the LPL with a different method. We extract the temperature, as well as other thermodynamic quantities, from a fit to the equation of state of in-situ images taken at different hold time between 0.5 and 5s. The results are shown on figure figure 6.24. By fitting the temperature by $T(t) = \gamma t + T_0$, we find an initial temperature of 25 nK and a heating rate of 3.5 nK/s for $f_z = 1.8$ kHz. This is

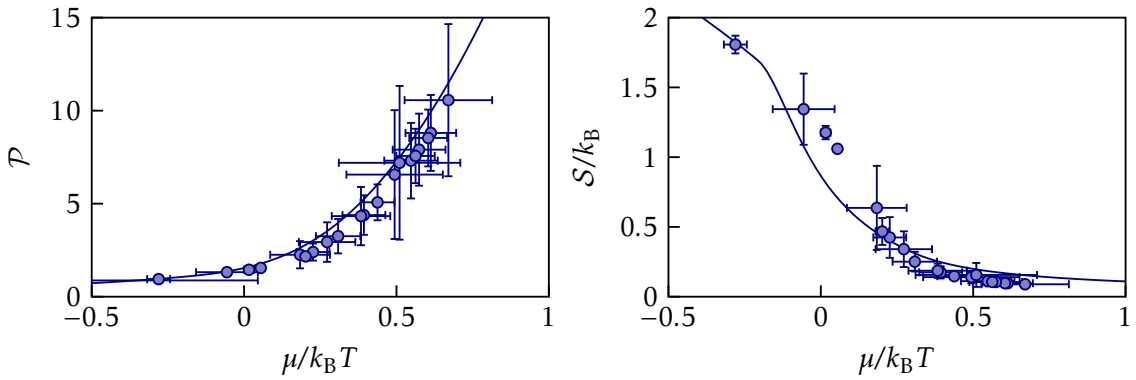

Figure 6.23 Reduced pressure $\mathcal{P}_0$ and entropy per particle $\mathcal{S}/k_B$. For this data set, we varied the final power in the 3D evaporation before the 2D compression in order to vary the temperature and the chemical potential. Solid lines correspond to the 2D equation of state.

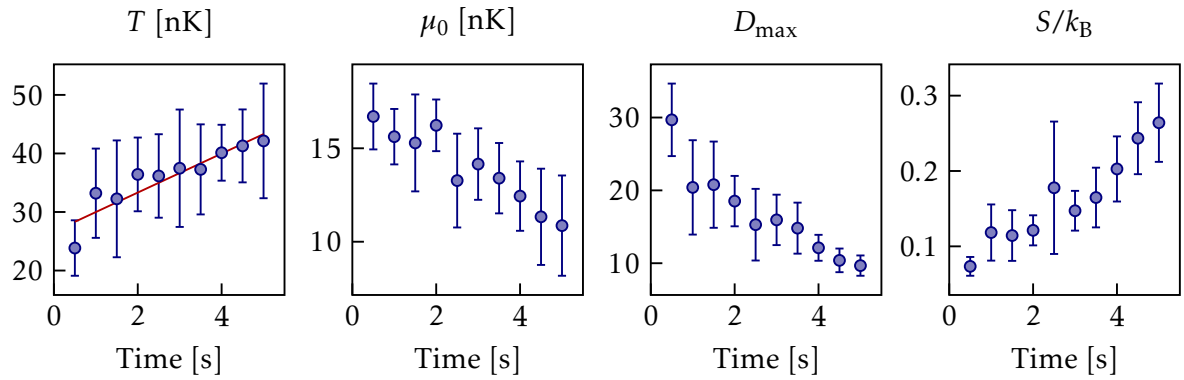

Figure 6.24 Thermodynamic parameters in the LPL as a function of time. For the temperature, the solid line corresponds to a linear fit, from which a heating rate of 3.5 nK/s is extracted. Here, the vertical trapping frequency is $f_z = 1.8$ kHz.

consistent with order of magnitude of the heating rate coming from light scattering (Grimm et al. 2000),

$$\dot{T} = \frac{E_\mathrm{R}}{3k_\mathrm{B}}\left|\frac{\Gamma_\mathrm{g}}{\hbar\Delta_g} + \frac{\Gamma_\mathrm{b}}{\hbar\Delta_b}\right| U_\mathrm{LPL} \approx 2.6\,\mathrm{nK/s}. \tag{6.4.11}$$

For the experiments described in the next chapter, the heating of the cloud in the LPL is not relevant since the typical timescales are well below 1 ms.

We can also optimize the loading ramp duration with this thermometry method. We find results that are consistent with the condensed fraction ones, as shown on figure 6.25.

6.4.3 Discussion

We have seen that we can reach temperatures as low as 25 nK and entropies per particle as low as $0.1k_\mathrm{B}$. As mentioned earlier, we expect that these values could be lowered by improving the adiabaticity of the transfer, and in particular the CDT extinction. For the experiments described in the next chapter, this is not necessary because the initial cloud temperature does not play a significant role. However, if we wanted to make a Mott insulator in the LPL, as described in section 6.5.1, this might not be sufficient. Indeed, it has been predicted that the Mott shell structure disappears around $T \simeq 0.2U/k_\mathrm{B}$, where U is the lattice interaction energy (Gerbier 2007). Typically, we want $U \approx E_\mathrm{R}$ for a Mott insulator, and $E_\mathrm{R}/k_\mathrm{B} = 95$ nK. The

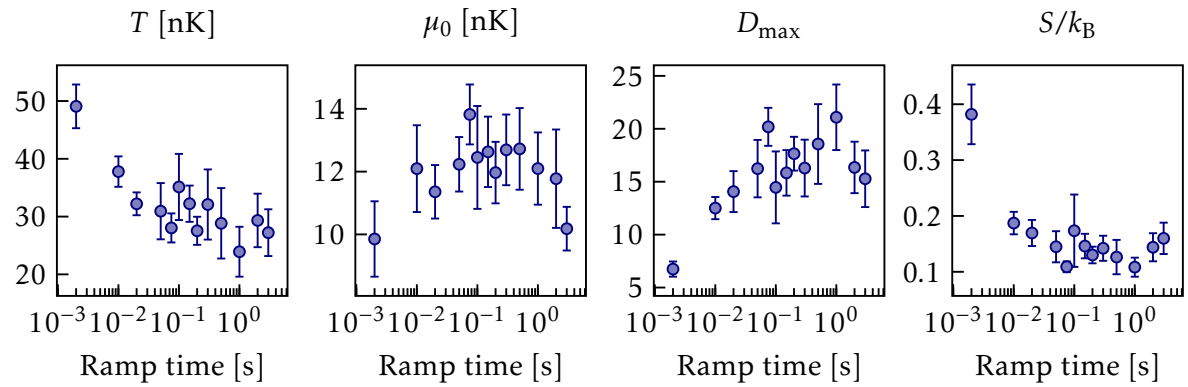

Figure 6.25 Thermodynamic parameters in the LPL as a function of the loading ramp duration. Here, the vertical trapping frequency is $f_z = 1.8\,\text{kHz}$.

temperature of the 2D BEC is therefore at the limit of making a clean Mott insulator, and additing horizontal optical lattices increases the temperature, as discussed in section 6.5.1.

6.5 Outlook

The long-term plan is to use the LPL as an intermediate lattice allowing us to load a single plane of a final 759 nm retroreflected lattice. Indeed, the vertical size of the ground state of the vertical harmonic oscillator created by the LPL,

$$a_z = \sqrt{\frac{\hbar}{m\omega_z}} \approx 0.43\,\mu\text{m}, \tag{6.5.1}$$

is approximately equal to the period of the retroreflected lattice, $d = 0.36\,\mu\text{m}$ and, as we saw in section 6.2.4, this is sufficient to load a single plane. The final goal was to make a single-plane 2D Mott insulator at the magic wavelength. We did not have time to fully reach this goal during this thesis, although first steps were made in this direction. We note that, to our knowledge, there are no experiments with single-plane 2D Mott insulators of ytterbium (or two-electron atoms like strontium). A "clean" Mott insulator requires a small entropy per particle, and we need to do more work to design a cooling scheme in the LPL. Some experiments use radio-frequency evaporation, which is not possible with ^{174}Yb, while others have the ability to lower the trap depth to achieve standard evaporation, but without changing the vertical trapping frequency that is essential for 2D compression. This might be possible on our experiment but would require more heavy-handed technical upgrades (for example, an additional beam for transverse confinement shaped using a digital micromirror (DMD) to create potential barriers at the edge of the cloud).

6.5.1 Two-dimensional Mott insulator in the LPL

As a first step, we attempted to realize a 2D Mott insulator in the LPL by adding the horizontal 759 nm retroreflected lattices. We probed the system by ramping back-and-forth the horizontal lattices. We first optimized the ramp duration and then studied the heating caused by the horizontal lattices for varying horizontal lattice depths as shown on figure 6.26. We observed that the lattice can reduce the condensed fraction by half, from 60 to 30%. We believe this is due, at least in part, to technical problems with the laser producing the $\lambda_m = 759\,\text{nm}$ light (SolsTiS, M Squared), which, in addition to the decreasing power mentioned in Chapter 2, exhibited increasing power fluctuations throughout my PhD, despite being sent to the manufacturer for repair for several months.

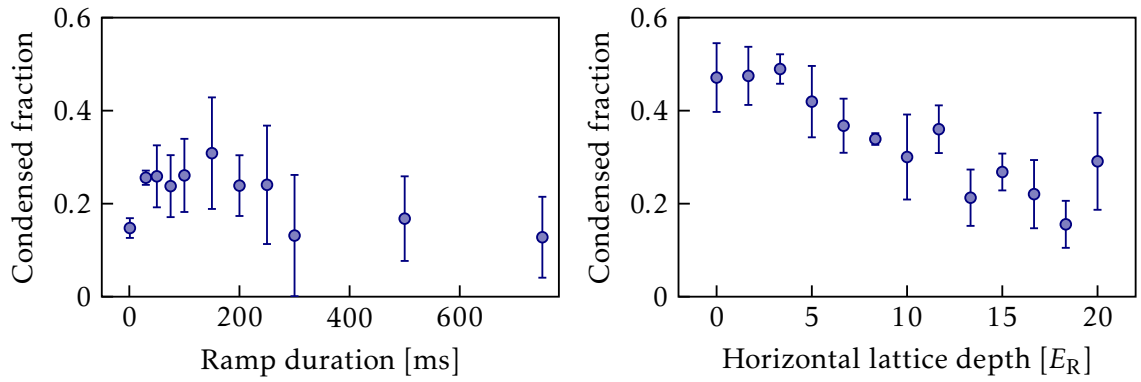

Figure 6.26 (a) Optimisation of the horizontal lattice ramp duration with back-and-forth ramps. Error bars correspond to the standard deviation over 3 repetitions of the experiment. The optimisation is done for the maximum lattice depth. (b) Reduction of the condensed fraction (after a back-and-forth ramp) caused by the horizontal lattices for varying horizontal lattice depths.

On images of the cloud with horizontal lattices, we could not detect sharp edges indicating the cloud had become incompressible, no matter how much we reduced the atom number to reach unit filling. We expect a unit-filling Mott insulator to have a surface density

$$n = \frac{1}{d^2} = 7.7\,\mu\text{m}^{-2}, \tag{6.5.2}$$

which corresponds to an OD of approximately 0.6, which we can measure without difficulty.

Unfortunately, we do not have data with in-situ images in order to extract a temperature and an entropy per particle. However, the data presented in figure 6.26(b) gives a good reason to believe the temperature and the entropy were too high to observe a plateau in density. It is unclear at this point what is exactly the cause, but the poor condition of the laser is strongly suspected.

6.5.2 Rebuilding a vertical retroreflected lattice

We also took steps toward reconstructing a vertical retroreflected lattice. The setup used in the first two parts of this thesis was removed to make room for the new high-resolution imaging system. For the "new" vertical lattice, we aimed for the same waist on the atoms ($\sim 150\,\mu$m). Given the constraints imposed by the presence of the imaging system, the only way to get a large waist on the atoms was to focus the lattice beam down to $\sim 50\,\mu$m at precisely $-f_{\text{MO}}$ from the MO, as depicted on figure 6.27. The retro-reflection, on the upper part of the experiment, was done as previously.

We encountered problems to trap atoms with this setup. Indeed, we observed irregular and time-dependent patterns strongly modulating the density. We noticed that the patterns could not be modified by changing the alignment, but disappeared when reducing the waist on the atoms by a factor of 3, thus increasing the waist on the MO lenses. We thus suspect thermal effects in the MO because the intensity on the MO was then 9 times smaller, and because the last lens of the MO (the closest to the atoms) is not made of N-BK7 like the others, but of CaF_2. We found that this lens to be more absorbent. Since the potential depth of the lattice V is much larger than the chemical potential μ, even small deformations of the beam (on the order of 0.1-1 % of the intensity) can cause strong deformations of the density distribution.

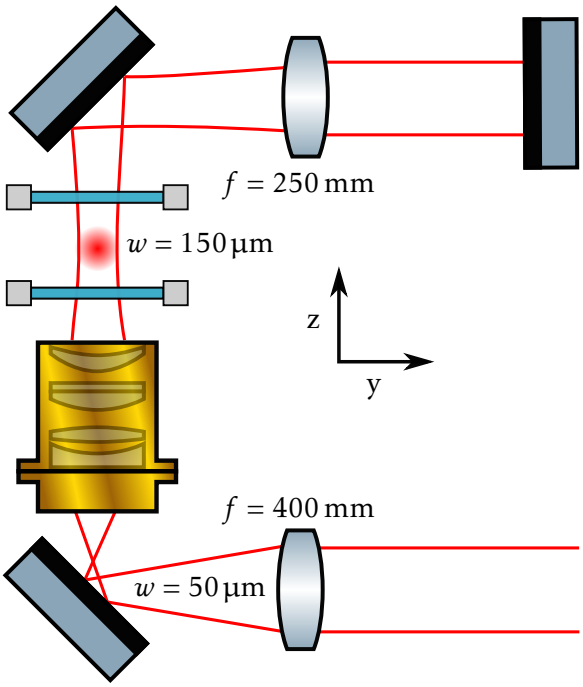

Figure 6.27 Optical setup for a retroreflected vertical lattice. A dichroic mirror (not represented) separates the imaging and lattice light between the MO and the $f = 400\,\mathrm{mm}$ lens. Distances are not to scale.

6.5.3 Painting light potentials

To avoid the problem mentioned in the subsection above, we had to work with a small waist on the atoms, leading to a lower intensity on the MO lenses. This results in a rather strong horizontal confinement, with at most 100-200 atoms in a unit-filling Mott insulator, which is difficult to prepare reliably. To restore the same optical potential for a $\sim 150\,\mu\mathrm{m}$ beam, we have attempted to scan the small waist optical lattice in the horizontal directions. This technique, often referred to as *optical painting* (Roy et al. 2016, Condon et al. 2019), has never been applied to optical lattices to our knowledge. As shown on figure 6.28, two orthogonal AOMs modulate the beam angle. If they are placed at the focal point of the optical system formed by a 1:1 telescope and the MO, the angle modulation on the AOMs corresponds to a position modulation on the atoms. Note that the telescope is only present because the AOMs are too large to be at the focal point of the MO.

For the "painting" to work, the modulation frequency f_{mod} should be much larger than all relevant time scales of the atomic motion, so that the atoms experience an effective potential equal to the time average

$$\overline{V}_{\mathrm{comp}}(\boldsymbol{r}) = \frac{1}{T}\int_0^T V_{\mathrm{comp}}(\boldsymbol{r}, t)\mathrm{d}t, \tag{6.5.3}$$

where $T = f_{\mathrm{mod}}^{-1}$. Painting optical trapping potentials is part of the broader topic of Floquet physics, see Weitenberg et al. (2021) for a review on its applications to quantum gases.

6.5.3.1 Painting a retroreflected vertical lattice

We implemented this scheme and found that we could trap atoms in a painted vertical optical lattice. Note that without retro-reflection, the potential is not strong enough to compensate gravity and trap the atoms. We observed that the size of the cloud increases upon

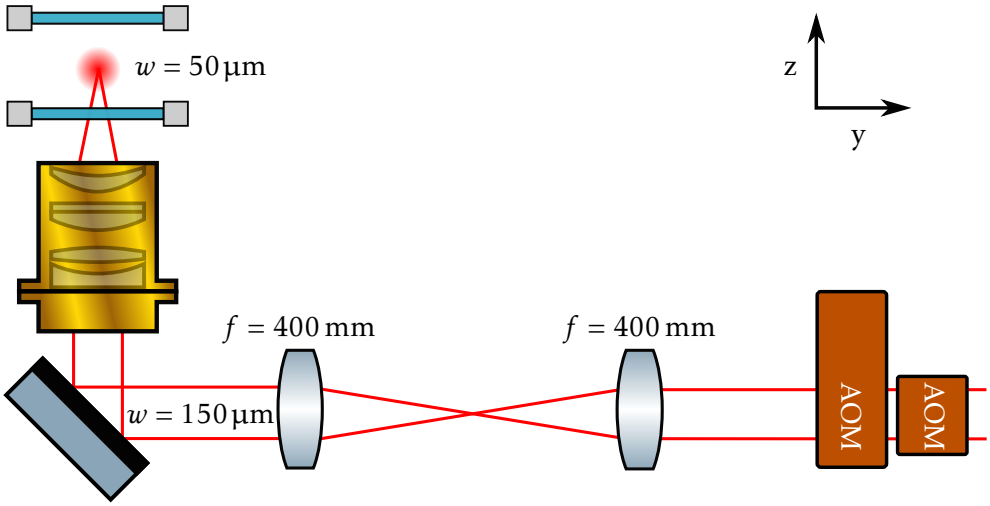

Figure 6.28 Optical setup for painting. The optional retro-reflection is not shown. Distances are not to scale.

modulation and that the painting does not lower the condensed fraction if the modulation frequency is not some resonant frequency which induces strong heating. We did not have time to investigat further the use of a painted optical lattice, but it seems to be a promising tool to push the experiment forward.

6.5.3.2 Painting to compensate the harmonic potential of the LPL

From these experiments with a painted optical lattice came the idea to use the same beam, without retro-reflection, in the LPL in order to flatten the harmonic potential by adding compensating light. The idea is to modulate the $w_{\text{comp}} = 50\,\mu\text{m}$ beam so that it creates a potential made of four gaussians in a rectangle of size $a \times b$,

$$\overline{V}_{\text{comp}}(x,y) = -\frac{U_{\text{comp}}}{4} \sum_{\substack{x_0=a,-a \\ y_0=b,-b}} \exp\left(-\frac{2}{w_{\text{comp}}^2}\left[(x-x_0)^2+(y-y_0)^2\right]\right). \tag{6.5.4}$$

For $V_{\text{tot}} = V_\perp + \overline{V}_{\text{comp}}$ to have zero first and second derivative at $(x,y) = (0,0)$, one needs to chose a and b such that

$$\frac{1}{2}m\omega_x^2 = \frac{2U_{\text{comp}}}{w_{\text{comp}}^2} e^{-\frac{2(a^2+b^2)}{w_{\text{comp}}^2}} \left(\frac{4a^2}{w_0^2} - 1\right), \tag{6.5.5}$$

$$\frac{1}{2}m\omega_y^2 = \frac{2U_{\text{comp}}}{w_{\text{comp}}^2} e^{-\frac{2(a^2+b^2)}{w_{\text{comp}}^2}} \left(\frac{4b^2}{w_0^2} - 1\right). \tag{6.5.6}$$

This system of equations has at least a solution if U_{comp} is not too small. The total potential then looks like the one on figure 6.29.

We have done preliminary tests for applying this idea to our experiments. Early results were promising, but a limiting factor was the instability of the position of the cloud described in section 6.2.5.

Conclusion

In this chapter, we presented the experimental upgrades we performed to prepare and probe two-dimensional Bose gases. These upgrades consisted of a large period lattice to compress

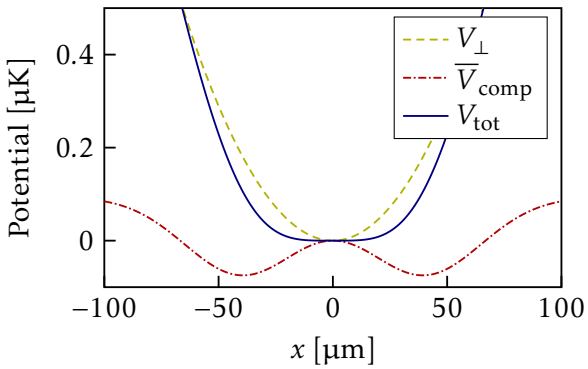

Figure 6.29 Scheme for LPL harmonic trap compensation. The dashed line corresponds to the harmonic potential of the IL in the x direction. The dash-dotted line corresponds to the compensating potential and the solid line corresponds to the total potential.

the BEC into a quasi-2D cloud and a high-resolution system for imaging the cloud. We first have described the new high-resolution imaging system. We have presented the methods used to estimate that the resolution is about 1 μm. We have described the large period lattice used for 2D compression, which is necessary because a 3D system does not really benefit from in-situ imaging. We have characterized the trapping frequencies of the LPL and its stability. We have also presented the optimal loading procedure, and we have studied the loading of a single plane of the LPL.

Next, we have characterized the quasi-2D nature of the compressed cloud: we have found that the vertical expansion of the cloud after being released from the LPL was consistent with all the atoms being in the vertical ground state. We have also estimated a condensed fraction in the LPL by fitting the bimodal momentum distribution after tof. This allowed us to optimize the loading of the LPL. We have also used the new in-situ imaging and fitted the in-situ position distribution of the atoms to the known 2D equation of state. This allowed us to obtain a complete picture of the thermodynamics of the cloud in the LPL, with estimates of the temperature ($\simeq 25$ nK), the chemical potential ($\simeq 10$ nK), the phase-space density ($\simeq 30$), and the entropy per particle ($\simeq 0.1 k_B$). Finally, we discussed the further steps taken towards the realization of the single-plane 2D Mott insulator, as well as an optical painting scheme to achieve a flat bottom potential.

CHAPTER 7

Optical response of a bulk two-dimensional two-level Bose gas

Introduction

In this chapter, we discuss a different aspect of many-body physics, the effect of an atomic cloud on the propagation of a light beam. In the following, we will focus on experimental observable, the complex transmission $t = \sqrt{T}e^{i\Delta\phi}$ of this beam through the cloud. In three dimensions, the 3D atomic density ρ is not the only important parameter of the problem: even if ρ is small, the intensity transmision T of the system is reduced as the density integrated along the propagation axis z, $\int dz\rho(z)$, is increased. This second parameter is usually expressed in dimensionless units through the optical depth $\mathrm{OD} \equiv \sigma_0 \int dz\rho(z)$, with $\sigma_0 = 6\pi k^{-2}$ and $k = 2\pi/\lambda$. In the limit of low density, the physics is single-particle. If in addition we consider a small intensity and a small optical depth, the transmission is simply related to the OD by the well-known Beer-Lambert law $\mathrm{OD} = -\ln(T)$. For large density $\rho k^{-3} \sim 1$, one expects a *cooperative scattering* of light (Guerin et al. 2017), i.e. collective effects such as dipole-dipole coupling begin to occur (Morice et al. 1995). There is debate in the community on whether a large OD (i.e. $\int dz\rho(z)k^{-2}$) is sufficient to introduce cooperative effects.

As mentioned earlier, atomic gases provide good platform to study the interaction between light and matter. Many studies have been done on optically dense samples with small atomic densities ($\mathrm{OD} \gtrsim 1$ and $\rho k^{-3} \ll 1$). The physics becomes even more interesting in the dense regime $\rho k^{-3} \sim 1$. Dense bulk systems have recently been realized with hot vapors (Keaveney et al. 2012) and with cold atoms in microscopic traps (Pellegrino et al. 2014, Jennewein et al. 2016). In particular, Jennewein et al. (2018) used a strong magnetic field to study the two-level case, although their findings could be specific to their microtrap geometry. In this chapter, we consider a bulk system with randomly placed atoms, but many interesting phenomena can be studied when the atoms are arranged in periodic patterns (Bettles et al. 2016, Shahmoon et al. 2017), which can be done with optical lattices (Rui et al. 2020, Glicenstein et al. 2020), tweezer arrays or ion traps (Meir et al. 2014).

A broadening and shift of the resonance line are typical signatures of collective effects in light scattering. Other typical signatures of collective effects include subradiance and superradiance (Guerin et al. 2016, Araújo et al. 2016). Although everyone agrees on the observation of a broadening, there have been conflicting results on the line shift. The effect of the local field leads to a Lorentz-Lorenz redshift of the resonance line, and there is much discussion in the literature of the so-called *cooperative Lamb shift*, a redshift due to photon exchanges between atom pairs (Roof et al. 2016). On the other hand, dipole-dipole interactions lead to a blueshift in a planar geometry that dominates the Lorentz-Lorenz redshift, as measured by **??**. Finally, in microtrap geometries a redshift was observed (Jennewein et al. 2018).

Atomic motion during the interaction with light can be made negligible in the ultracold regime under certain conditions detailed in this chapter. In this direction, Bromley et al. (2016) showed that the cooperative Lamb shift was absent when atomic motion during probing could be neglected in ultracold atomic gases. Moreover, they highlighted that the simple low-energy electronic structure of ^{88}Sr, which is similar to that of ^{174}Yb, is a powerful tool to probe the optical response of atomic gases. As discussed in Chapter 2, not only do alkaline-earth bosons have two transitions with very different linewidths, but they are $J = 0 \leftrightarrow J = 1$ transitions, where all Clebsch-Gordan coefficients are equal to 1 and no optical pumping can occur.

In summary, light-matter interaction experiments with atomic gases can be classified by atom (multi-level vs two-level), by geometry (bulk, wire, slab, microtrap) and temperature (hot, cold, ultracold). Here, we consider a two-dimensional ultracold gas of bosonic ytterbium such as the one characterized in Chapter 5. In the rigorously 2D case (i.e. a gas with an extension $\Delta z = 0$), the optical depth is not as relevant as in 3D because there is a one-to-one

relation between the 2D atomic density n and transmission T, at least in the single-atom regime. However, in practice, our 2D gas has a finite extension $k\Delta z \approx 2.7$ even in its the ground state. In this chapter, we study the complex transmission coefficient $t \equiv \sqrt{T}e^{i\Delta\phi}$ of a light beam near resonance with the large $\lambda_b = 399\,\mathrm{nm}$ $J = 0 \leftrightarrow J = 1$ transition of ^{174}Yb: in addition to transmission measurements of T, we also measure the phase shift $\Delta\phi$ induced by the sample using an interferometer. We compare our results with those of Corman et al. (2017), with who we share the planar geometry. However, Corman et al. (2017) studied a homogeneous 2D gas of ^{87}Rb close to the $F = 2 \leftrightarrow F = 3$ D_2 transition. While the simplicity of our $J = 0 \leftrightarrow J = 1$ transition is an advantage, the fact that our gas is not homogeneous should not be a problem because we perform position-resolved experiments.

In section 7.1, we lay out an independent-atoms model for the optical response of a 2D atomic gas. We use two approaches: a "continuous medium", refractive index approach, which leads to the standard Beer-Lambert law, and the electromagnetic response of a strictly 2D gas considered as an interface. In section 7.2, we present a coupled-dipole model that goes beyond single-atom physics. Using this model, we perform numerical simulations and compare them to the single-atom response. In section 7.3, we detail our experimental methods and image analysis. We discuss possible systematic effects, as well as the calibration of the atomic density. Finally, we present our experimental results in section 7.4.

7.1 Single-atom reponse

An electric field $\boldsymbol{E}_L$ induces a dipole moment $\boldsymbol{d} = \epsilon_0 \alpha \boldsymbol{E}_L$ on an isolated atom, where α is the electric polarizability of the atom at the probe frequency

$$\alpha \simeq -\frac{6\pi c^3}{\omega_A^3}\frac{\Gamma/2}{\delta + i(\Gamma/2)} \simeq -\frac{6\pi}{k^3}\frac{1}{y+i}, \tag{7.1.1}$$

where ω_A is the atomic resonance frequency and where Γ is the full width at half maximum of the excited state. We note the reduced detuning $y \equiv 2\delta/\Gamma$, with $\delta = \omega_L - \omega_A$. For a three-dimensional gas of atoms radiating independently, the polarization per unit volume $\boldsymbol{P}$ is given by

$$\boldsymbol{P} = \rho\epsilon_0\alpha\boldsymbol{E}_L \equiv \epsilon_0\eta\boldsymbol{E}_L, \tag{7.1.2}$$

where ρ is the 3D atomic density and $\eta \equiv \rho\alpha$ is the dielectric susceptibility (Born et al. 1999). This linear response is valid as long as the intensity $I = |\boldsymbol{E}_L|^2$ of the light beam is small enough. This condition reads $s \equiv I/I_{sat} \ll 1$, with $I_{sat} = \hbar\Gamma\omega^3/(12\pi c^2)$ the saturation intensity.

7.1.1 Refractive index description

We first consider the usual refractive index description. The refractive index of the gas is defined by

$$n_{idx}^2 \equiv 1 + \eta = 1 + \rho\alpha. \tag{7.1.3}$$

For low densities $\rho k^{-3} \ll 1$, we approximate $n_{idx} \simeq 1 + \rho\alpha/2$. A plane wave of frequency ω propagates inside the medium as $e^{i(n^2-1)\omega x/c}$. The real part $n'_{idx} \simeq 1 + \rho\,\mathrm{Re}[\alpha]/2$ of the refractive index introduces a phase shift in the light going through the medium, while the imaginary part $n''_{idx} \simeq \rho\,\mathrm{Im}[\alpha]/2$ leads to absorption.

Let us focus on the absorption first. Using the imaginary part of the refractive index, one finds that the attenuation of the intensity I is such that

$$\frac{dI}{dz} = -\frac{\rho\sigma_0}{1+y^2}I \equiv -\rho\sigma I \tag{7.1.4}$$

where we have defined the absorption cross section $\sigma = \sigma_0/(1+y^2)$ and the resonant absorption cross section $\sigma_0 = 6\pi k^{-2} = 3\lambda^2/2\pi$. Hereafter, the light propagation is along the z direction. Integrating equation (7.1.4) leads to the Beer-Lambert law for the intensity transmission,

$$T \equiv \frac{I_\mathrm{f}}{I_\mathrm{i}} = \mathrm{e}^{-\sigma\int\rho\mathrm{d}z}. \tag{7.1.5}$$

It is common to define the optical depth $\mathrm{OD} \equiv \sigma\int\rho\mathrm{d}z$ so that the Beer-Lambert law can be rewritten $\mathrm{OD} = -\ln T$.

Let us now look at the phase shift. Using the real part of the refractive index, one finds that the electric field going through a slice of thickness $\mathrm{d}z$ with a 3D atomic density ρ acquires a phase

$$\mathrm{d}\phi = \frac{\rho\sigma_0}{2}\frac{y}{1+y^2}\mathrm{d}z \tag{7.1.6}$$

with respect to an electric field propagating in vacuum for the same distance $\mathrm{d}z$. Integrating equation (7.1.6) leads to

$$\Delta\phi = \frac{\sigma_0}{2}\frac{y}{1+y^2}\int\rho\mathrm{d}z, \tag{7.1.7}$$

an equivalent of the Beer-Lambert law for the phase.

7.1.2 Electromagnetic description of a strictly two-dimensional gas

Strictly speaking, the Beer-Lambert law applies to smooth and continuous media, i.e. media with features that vary very smoothly at the scale of the light wavelength. It might not hold for a quasi-2D gas because the vertical size of the cloud is usually smaller than the wavelength of the light. In particular, a rigorously 2D system with an extension $\Delta z = 0$ is an interface which can lead to reflection. In the continuous medium description, it is assumed that the system does not have sharp edges (with respect to λ) and there is no reflection. In the following, we present a single-particle electromagnetic description of a strictly-2D gas.

Let us consider a planar dielectric gas in $z = 0$, and an incoming electromagnetic field $[\boldsymbol{E}_\mathrm{i}, \boldsymbol{B}_\mathrm{i}] = [E_\mathrm{i}\boldsymbol{e}_x, E_\mathrm{i}\boldsymbol{e}_y/c]$, as shown in figure 7.1. The incident field can be transmitted, reflected or scattered. We note $[\boldsymbol{E}_1 = (1+r)\boldsymbol{E}_\mathrm{i}, \boldsymbol{B}_1 = (1-r)\boldsymbol{B}_\mathrm{i}]$ the electromagnetic field in the half-space before the gas and $[\boldsymbol{E}_2 = t\boldsymbol{E}_\mathrm{i}, \boldsymbol{B}_2 = t\boldsymbol{B}_\mathrm{i}]$ the electromagnetic field after the gas. The electromagnetic response of the 2D gas is determined by the electromagnetic boundary conditions

$$\boldsymbol{e}_z \times (\boldsymbol{E}_2 - \boldsymbol{E}_1) = 0, \tag{7.1.8}$$

$$\boldsymbol{e}_z \times (\boldsymbol{B}_2 - \boldsymbol{B}_1) = \mu_0 \boldsymbol{j}_s. \tag{7.1.9}$$

where $\boldsymbol{j}_s$ is the surface current. Equation (7.1.8) leads to

$$E_1 = E_2 = tE_\mathrm{i} \quad \text{and} \quad t = 1 + r. \tag{7.1.10}$$

This implies that, because of the reflected field, the electric field "seen" by the atoms $E_1 = E_2$ is the transmitted field and not the incident field.

For a purely dielectric material with vanishing electrical conductivity (no free charges), the current is entirely due to surface polarization currents such that $\boldsymbol{j}_s = \partial_t \boldsymbol{P}_s$. Using the definition of the monochromatic dielectric susceptibility $\eta(\omega)$ in equation (7.1.2), this yields

$$\boldsymbol{j}_s(\omega)\mathrm{e}^{-\mathrm{i}\omega t} = \mathrm{i}\omega\epsilon_0\eta(\omega)\boldsymbol{E}(\omega)\mathrm{e}^{-\mathrm{i}\omega t}. \tag{7.1.11}$$

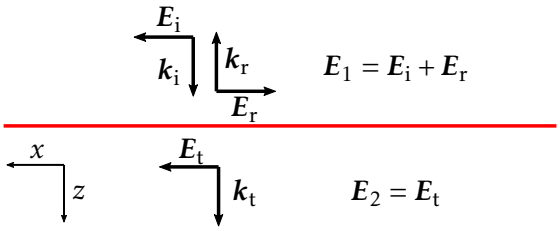

Figure 7.1 Scheme of the rigorously 2D description. The 2D gas is viewed as an infinite interface, here in red, separating space in regions 1 and 2. In region 1, the total electric field $\boldsymbol{E}_1$ is the sum of the incident field $\boldsymbol{E}_\mathrm{i}$ and of the reflected field $\boldsymbol{E}_\mathrm{r}$. In region 2, the total electric field $\boldsymbol{E}_2$ is simply the transmitted field $\boldsymbol{E}_\mathrm{t}$.

Equation (7.1.9) then yields $t = 1 - r + \mathrm{i}k\eta t$, or $t = 1/(1 - \mathrm{i}k\eta/2)$. For a 2D gas with planar density n, the dielectric susceptibility reads

$$\eta = -\frac{1}{k}\frac{2x}{y+\mathrm{i}} \quad \text{with} \quad x = n\sigma_0/2 = 3\pi n k^{-2}, \tag{7.1.12}$$

as can be seen from equation (7.1.1). This leads to

$$t = \frac{1}{1 - \mathrm{i}k\eta/2} = \frac{1}{1 + \mathrm{i}x/(y+\mathrm{i})}. \tag{7.1.13}$$

Using $t = \sqrt{T}\exp(\mathrm{i}\Delta\phi)$, we deduce a formula for the transmission

$$T = |t|^2 = \frac{1+y^2}{(1+x)^2+y^2}, \tag{7.1.14}$$

as well as for the phase shift

$$\Delta\phi = \arctan\left(\frac{xy}{1+x+y^2}\right). \tag{7.1.15}$$

We compare equation (7.1.14) and equation (7.1.15) to the Beer-Lambert predictions in the next section. In summary, for small densities we observe the same behavior for the intensity transmission and the phase shift, but there are significant differences outside of this regime.

7.1.3 Description of a quasi-two-dimensional gas

The strictly-2D response derived above might be appropriate for monolayer condensed matter systems where the transverse extension Δz is on the order of the Bohr radius (Nair et al. 2008, Fang et al. 2013). For quasi-2D quantum gases, the situation is less clear: Δz is set by the size of the ground state of the vertical trapping potential, and is typically barely smaller than λ. For this reason, past experimental works (Hung et al. 2011a, Yefsah et al. 2011) on quasi-2D atomic gases used an analogous equation

$$T = \exp(-n\sigma) = \exp\left(-\frac{2x}{1+y^2}\right), \tag{7.1.16}$$

for the transmission, and

$$\Delta\phi = \frac{n\sigma_0}{2}\frac{y}{1+y^2} = \frac{xy}{1+y^2} \tag{7.1.17}$$

for the phase. This approach will be justified by the numerical simulations presented in the next section.

7.2 Beyond the single-atom response

We can go one step further than the single-atom description by considering the effect on one atom of the mean electric field generated by nearby atoms. In a model where the atom is in an empty sphere surrounded by an homogeneously polarised medium, one defines a local field which is the field seen by an atom "excluding itself". One find that this contribution is such that $\boldsymbol{E}_{\text{eff}} = \boldsymbol{E}_{\text{L}} + \boldsymbol{P}/3$ (Born et al. 1999). By using $\boldsymbol{P} = \rho\epsilon_0\alpha\boldsymbol{E}_{\text{eff}}$, we obtain the Lorentz-Lorenz formula for the dielectric susceptibility

$$\eta = \frac{\rho\alpha}{1-\rho\alpha/3}. \tag{7.2.1}$$

This equation leads to the prediction of a redshift of the resonance line.

7.2.1 Model

Following Morice et al. (1995) and Chomaz et al. (2012), we consider N identical atoms at rest in interaction with the electromagnetic field. The fully-quantum Hamiltonian reads $\hat{H} = \hat{H}_{\text{F}} + \hat{H}_{\text{A}} + \hat{V}$, with

$$\hat{H}_{\text{F}} = \sum_{\boldsymbol{q},\boldsymbol{s}} \hbar c q \hat{a}^{\dagger}_{\boldsymbol{q},\boldsymbol{s}} \hat{a}_{\boldsymbol{q},\boldsymbol{s}}, \tag{7.2.2}$$

$$\hat{H}_{\text{A}} = \sum_{i=1}^{N} \sum_{\alpha=x,y,z} \hbar\omega_{\text{A}} |i:e_\alpha\rangle\langle i:e_\alpha|, \tag{7.2.3}$$

$$\hat{V} \simeq -\sum_{i=1}^{N} \hat{\boldsymbol{D}}_i^{(+)} \cdot \hat{\boldsymbol{E}}^{(+)}(\boldsymbol{r}_i) + \text{h.c.}, \tag{7.2.4}$$

where N is the atom number, $\boldsymbol{s}$ the polarization, and $|e_\alpha\rangle$ the three Zeeman sublevels of the excited state (Cohen-Tannoudji et al. 1997). The rotating-wave approximation has been used in the expression of $\hat{V}$, and we have defined the forward electric field

$$\hat{\boldsymbol{E}}^{(+)}(\boldsymbol{r}) = \mathrm{i} \sum_{\boldsymbol{q},\boldsymbol{s}} \sqrt{\frac{\hbar c q}{2\epsilon L^3}} \hat{a}_{\boldsymbol{q}} e^{\mathrm{i}\boldsymbol{q}\cdot r} \boldsymbol{s} \tag{7.2.5}$$

and the raising dipole operator

$$\hat{\boldsymbol{D}}_i^{(+)} = d \sum_{\alpha=x,y,z} |i:e_\alpha\rangle\langle i:g| \boldsymbol{u}_\alpha. \tag{7.2.6}$$

Let us now consider an incident monochromatic plane wave $E_{\text{L}}\boldsymbol{\epsilon}e^{i(kz-\omega_{\text{L}}t)}$ with a small saturation parameter $s \ll 1$. After some algebra, Morice et al. (1995) obtained the following set of equations

$$e_\alpha(\boldsymbol{r}) = E_{\text{L}}\epsilon_\alpha e^{\mathrm{i}kz} + \frac{k^3}{6\pi\varepsilon_0} \sum_{i,\beta} g_{\alpha,\beta}(\boldsymbol{u}_i) d_{i,\beta}, \tag{7.2.7}$$

$$\left(\frac{2\delta}{\Gamma} + \mathrm{i}\right) d_{i,\alpha} + \sum_{j\neq i,\beta} g_{\alpha\beta}(\boldsymbol{u}_{ij})\, d_{j,\beta} = -\frac{6\pi\varepsilon_0}{k^3} E_{\text{L}}\epsilon_\alpha e^{\mathrm{i}kz_i}, \tag{7.2.8}$$

where $\langle\hat{\boldsymbol{E}}(\boldsymbol{r},t)\rangle = \boldsymbol{e}(\boldsymbol{r})e^{-\mathrm{i}\omega t} + \text{c.c.}$ and $\langle\hat{\boldsymbol{D}}_j(t)\rangle = \boldsymbol{d}_j e^{-\mathrm{i}\omega t} + \text{c.c.}$, $\boldsymbol{u}_i = k(\boldsymbol{r}-\boldsymbol{r}_i)$, and $g_{\alpha\beta}(\boldsymbol{u})$ is a function describing the field radiated by a classical dipole along $\boldsymbol{e}_x$ located at the origin and oscillating at frequency ω.

$$g_{\alpha\beta}(\boldsymbol{u}) = \frac{3\mathrm{e}^{\mathrm{i}u}}{2u^3}\left[\delta_{\alpha\beta}(u^2+\mathrm{i}u-1) + \frac{u_\alpha u_\beta}{u^2}(-u^2-3\mathrm{i}u+3)\right]. \tag{7.2.9}$$

For a given incident field, the solution of the set of $3N$ equations (7.2.8) provides the value of each dipole $\boldsymbol{d}_i$, which can then be injected into equation (7.2.7) to obtain the total field at any point in space.

Note that Morice et al. (1995) also derived a perturbative expression of the susceptibility η up to order 2 in the density. This expression included the effect of quantum statistics, which were studied in Bons et al. (2016). The Lorentz-Lorenz formula was retrieved, as well as an additional term corresponding to the resonant van der Waals interaction coming from multiple scatterings of photons.

7.2.2 Numerical simulations

In this section, following Chomaz et al. (2012), we provide a numerical solution of equations (7.2.7) and (7.2.8) for a random spatial distribution of the dipoles. We start by randomly drawing the positions of N atoms in a disk of radius R chosen to match the desired 2D atomic density n. The system can also have a longitudinal extension Δz with a Gaussian distributon $p(z) = \mathrm{e}^{-z^2/2\Delta z^2}$. Hereafter, we will refer to this system as a Gaussian slab.The draw is typically repeated for 10 iterations. For each iteration, we obtain a set of $3N$ positions (x_i, y_i, z_i). We then put equation (7.2.8) in matrix form $MB = A$, where

$$A_{i,\alpha} = \epsilon_\alpha e^{\mathrm{i}kz_i}, \qquad B_{i,\alpha} = -\frac{k^3}{6\pi\varepsilon_0} d_{i,\alpha}, \tag{7.2.10}$$

and M has diagonal elements equal to $(2\delta/\Gamma + \mathrm{i})$ and off-diagonal elements equal to $g_{\alpha\beta}(\boldsymbol{u}_{ij})$. We calculate the latter using the drawn random positions of the atoms. We obtain B by solving $MB = A$ numerically. Chomaz et al. (2012) found that the amplitude transmission coefficient reads

$$t \simeq 1 - \frac{\mathrm{i}}{2}\sigma_0 n \times \frac{A^* \cdot B}{N}, \tag{7.2.11}$$

when neglecting edge effects. The transmission is then given by $T = |t|^2$, while the phase shift is given by the phase of t.

As M is a $3N \times 3N$ matrix, realistic numbers of atoms (up to 6×10^4) are out of reach. We are restricted to $N = 2000$, which gives a radius of about 2.6 µm in the atom plane for the highest experimental atomic density $nk^{-2} \simeq 0.5$. In principle this much lower number of atom should not be a problem because we are interested in the local response of the system in the bulk. However, for a fixed 2D density n, the radius of the simulated disk increases as $\sqrt{N}$ and, if N is too small, finite size effects dominate the optical response. An atom number $N = 2000$ is probably not high enough to neglect finite size corrections, but this is difficult to estimate because we cannot test higher values of N.

We compare the numerical simulations with the different analytical approaches in figure 7.2 for the transmission and in figure 7.3 for the phase shift. Looking first at the transmission, we observe that numerical simulations for a strictly 2D gas ($k\Delta z = 0$, filled circles) show a larger transmission than expected from the Beer-Lambert law. This larger transmission is in relatively good agreement with the single-particle response of a strictly-2D gas. However, the simulations also predict a blueshift that cannot be obtained from single-particle calculations. We do not observe the redshift predicted by the Lorentz-Lorenz formula, probably because it is hidden behind stronger collective effects.

When simulating a gas closer to a 3D regime with $Deltaz = 2.7k^{-1}$ (i.e. a Gaussian slab), we retrieve the Beer-Lambert law (empty squares). Here, we have taken the experimental vertical extension of the gas, $k\Delta z = 2.7$. The blueshift is suppressed for Gaussian slabs with thickness $k\Delta z \gtrsim 1$, and the optical response is a single-particle one. We observe a similar behavior for the phase shift, as can be expected from the fact that the transmission and the phase shift are derived from the same quantity $t = \sqrt{T}\exp(\mathrm{i}\Delta\phi)$.

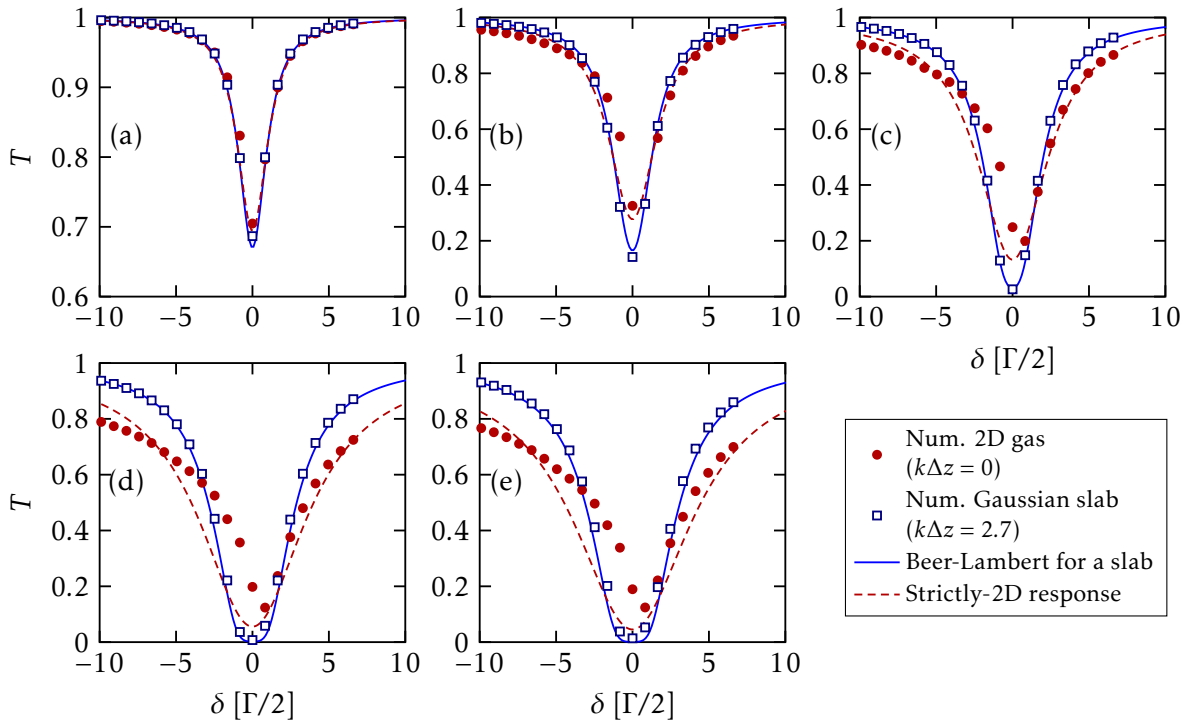

Figure 7.2 Numerical simulation of the transmission T for $N = 1000$ atoms and, from (a) to (f), a 2D density $nk^{-2} = 0.02$, 0.1, 0.2, 0.35 and 0.4. Circles correspond to a strictly 2D gas ($k\Delta z = 0$) and squares to a Gaussian slab ($k\Delta z = 2.7$). The Beer-Lambert response is shown as a solid line and the single-particle response of a strictly-2D gas as a dashed line.

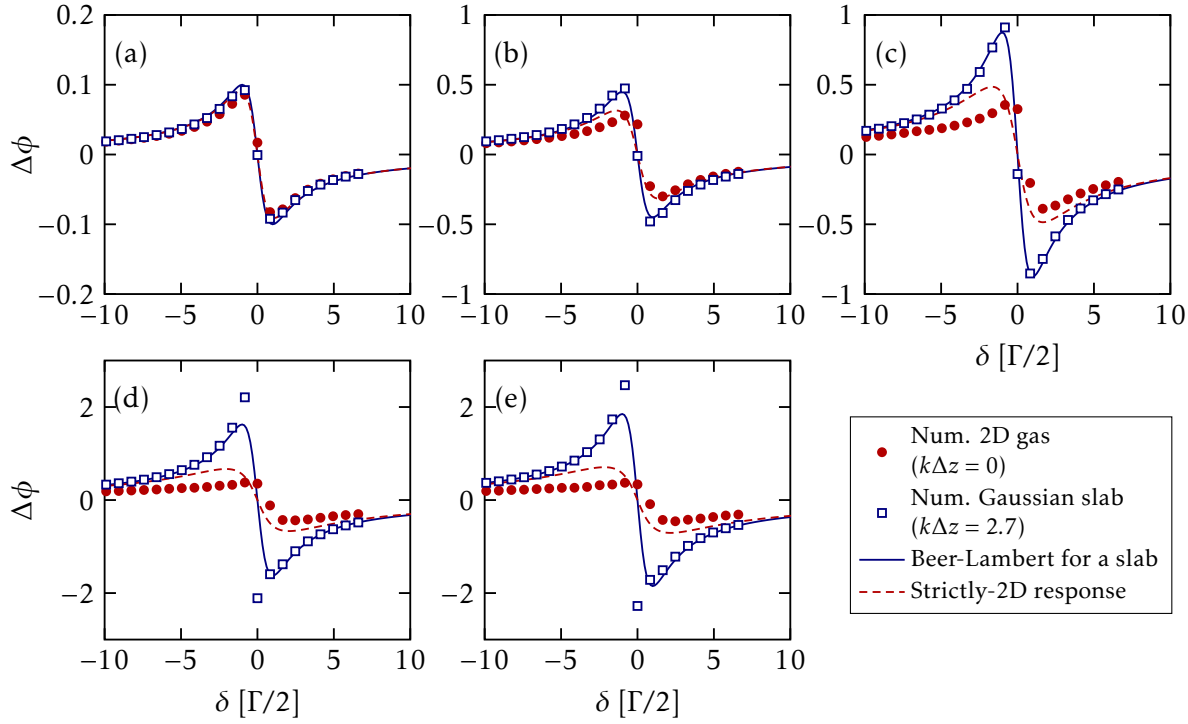

Figure 7.3 Numerical simulation of the phase shift $\Delta\phi$ for $N = 1000$ atoms and, from (a) to (f), a 2D density $nk^{-2} = 0.02$, 0.1, 0.2, 0.35 and 0.4. Circles correspond to a strictly 2D gas ($k\Delta z = 0$) and squares to a Gaussian slab ($k\Delta z = 2.7$). The Beer-Lambert response is shown as a solid line and the single-particle response of a strictly-2D gas as a dashed line.

As of now, we have only simulated samples with a homogeneous distribution in the $x-y$ plane. It would be interesting to simulate samples with Thomas-Fermi distributions because, when the detuning is non-zero, the gas has a refractive index different from 1 and lensing effects are expected. However, the difference in atom number between the simulations and the experiment could make it difficult to obtain satisfactory quantitative results.

7.3 Measurement procedure

7.3.1 Optical setup

We now turn to the presentation of our experimental setup and methods. The optical setup, shown in figure 7.4, is very similar to the imaging setup presented in the previous chapter. The essential difference is the presence of an interferometer in order to measure the phase shift induced by the atomic cloud. The two arms of the interferometer are separated from each other by a polarizing beam splitter (PBS). Their polarizations are rematched with a half-wave plate, and set to a circular polarization with a quarter-wave plate. The two beams are aligned to be parallel with two mirrors. In the plane of the atoms, the two beams have a $w_{\mathrm{at}} = 180\,\mu\mathrm{m}$ waist and they are 1.5 mm apart. Since the atomic cloud is smaller than 50 µm, only one of the arms of the interferometer goes through the atoms.

After the science chamber, the two arms pass through the imaging system described in Chapter 5: a microscope objective ($f_{\mathrm{MO}} = 35.8\,\mathrm{mm}$) and a recombining lens ($f_{\mathrm{r}} = 500\,\mathrm{mm}$). The beam waist is then $w_{\mathrm{cam}} = 2.5\,\mathrm{mm}$, and the two arms are recombined on the CCD camera with two mirrors. They arrive on the camera at an angle so that we observe interferences with a fringe spacing of 27.8 µm, corresponding to 3.6 pixels per fringe.

We use the same experimental procedure as described in Chapter 2 for absorption imaging. We send two pulses of near-resonant light and image them on the camera. On the first image, which we call image 1, one of the two arms of the interferometer crosses the atomic cloud. On the second image, which we call image 2, the cloud has been released for 200 ms and the two arms do not cross any cloud.

7.3.2 Image analysis

As shown in figure 7.5(a), we extract two squares of 10×15 pixels ($\approx 4\times6\,\mu\mathrm{m}^2$ in the plane of the atoms) from each image: one square where the center of the atomic cloud is located, and another about 70 µm further along the y-direction (the direction of the fringes). We integrate each square along the y-direction, thus obtaining 10-point profiles as shown in figure 7.5(b-c). The size of the squares is chosen to be large enough to reduce noise (in particular average out photon shot noise), but small enough that the density can be considered uniform. We call $S_{\mathrm{at},i}$ the profile on the atoms of image i and $S_{\mathrm{bg},i}$ the profile away from the atoms of image i.

Transmission To measure the intensity transmission T, we block the second arm of the interferometer and compute

$$T = \frac{I_{\mathrm{f}}}{I_{\mathrm{i}}} = \frac{\overline{S}_{\mathrm{at},1}/\overline{S}_{\mathrm{at},2}}{\overline{S}_{\mathrm{bg},1}/\overline{S}_{\mathrm{bg},2}}, \tag{7.3.1}$$

where the $\bar{S}_i$ are the mean of y-integrated profiles. We cannot compute the transmission from a single image (i.e. $T = \overline{S}_{\mathrm{at},1}/\overline{S}_{\mathrm{bg},1}$) since the beam profile is not uniform. The denominator in equation (7.3.1) corrects intensity differences between the two pulses and is close to 1. This is equivalent to the scaling treatment discussed in Chapter 2.

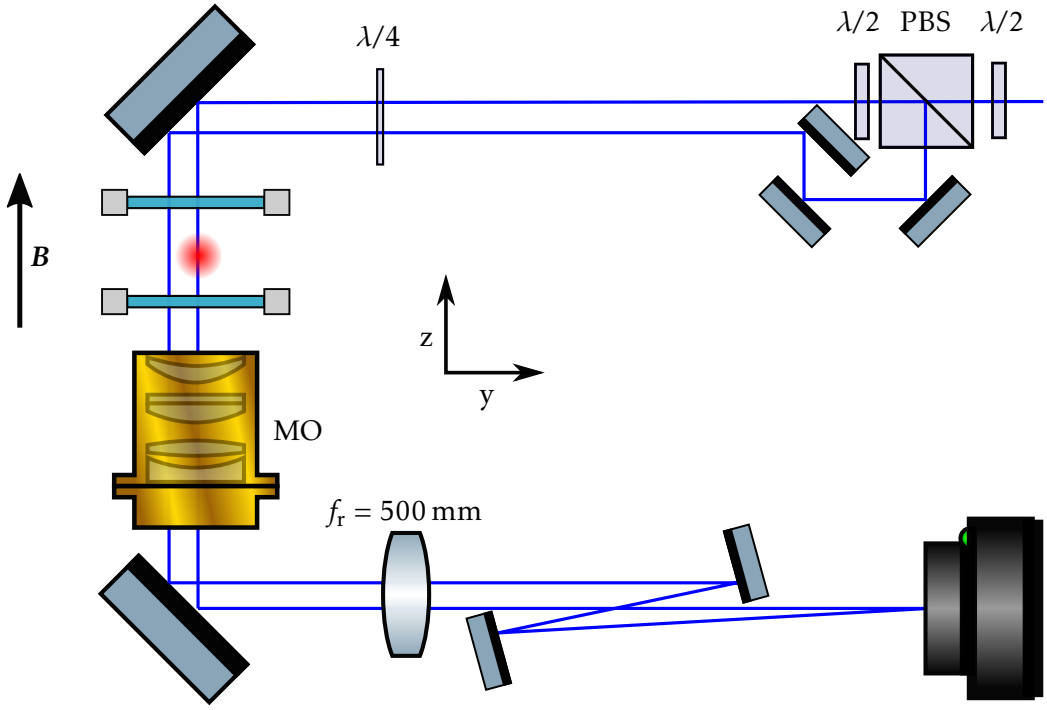

Figure 7.4 Schematic of the interferometer used to measure the optical response of a 2D BEC. PBS corresponds to polarizing beam splitter, $\lambda/2$ ($\lambda/4$) corresponds halfwave (quarterwave) plate, MO corresponds to microscope objective. f_r corresponds to the recombination lens.

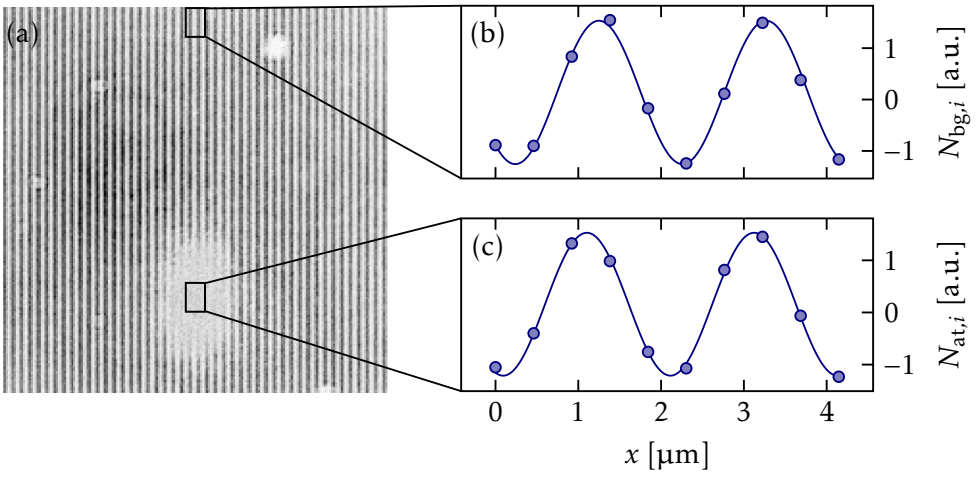

Figure 7.5 Image analysis. (a) Raw image of the beam. The lighter region corresponds to the atoms, where the transmission is not 1. The squares correspond to the 10×15-pixels regions-of-interest: the top one without atoms, the bottom one at the center of the cloud. The profiles are obtained by vertical integration. (b) Intensity profile of 10 points away from the atoms $N_{bg,i}$. (c) Intensity profile of 10 points on the atoms $N_{at,i}$. The profiles are normalized.

Phase shift On the other hand, we measure the phase shift by fitting the four profiles with the function

$$S(x) = A\sin[2\pi(x/\ell + \phi)] + B. \tag{7.3.2}$$

An example of such a fit is shown in figure 7.5(b-c). The fringe spacing ℓ is determined once and for all with a first pass where it is set as a free parameter. A, B and ϕ are free parameters. For each image i, the phase shift is then the phase difference between the profile on the atoms $S_{\mathrm{at},i}$ and the profile away from the atoms $S_{\mathrm{bg},i}$. Image 2 (on which there were no atoms on both paths) is used as a control image. We thus measure the phase shift by computing

$$\Delta\phi = (\phi_{\mathrm{at},1} - \phi_{\mathrm{bg},1}) - (\phi_{\mathrm{at},2} - \phi_{\mathrm{bg},2}). \tag{7.3.3}$$

The second term of this equation can correct a small angle of the fringes and ensures the phase shift is zero when there are no atoms. To determine the uncertainty on $\Delta\phi$, we use a bootstrap procedure. For each profile, the 10 points are drawn randomly 100 times (with replacement) and each set of drawn points is fitted individually. We then take the mean and the standard deviation of the 100 fitting results to compute $\Delta\phi$ and its error bar.

7.3.3 Estimation of systematic effects

In this section, we highlight the different challenges posed by the blue $\lambda_{\mathrm{b}} = 399\,\mathrm{nm}$ and the green $\lambda_{\mathrm{g}} = 556\,\mathrm{nm}$ transitions. Since their wavelengths are somewhat similar, the essential difference between the transitions is their linewidth $\Gamma_{\mathrm{b}} \simeq 29.1\,\mathrm{MHz}$ and $\Gamma_{\mathrm{g}} \simeq 182\,\mathrm{kHz}$.

7.3.3.1 Amplitude of the light signal

From the perspective of the light signal, the blue transition is easier to work with. In figure 7.6, we show the precision of the phase measurement (obtained from the bootstrap procedure) as a function of the pulse intensity both in units of s and number of photons per pixel. We observe that we need about $N_{\mathrm{ph,min}} \sim 20$ photons per pixels to measure the phase accurately. This means that there is a minimum pulse duration

$$t_{\mathrm{p}} > \frac{1}{I} \times N_{\mathrm{ph,min}} \frac{\hbar\omega}{(p_s/M)^2}, \tag{7.3.4}$$

where p_s is the pixel size and M is the magnification. This limit corresponds to the striped area for small saturation parameters in figure 7.7. As mentioned above, we want the saturation parameter s to remain small compared to 1 in order to probe the linear response of the cloud. As shown in figure 7.6, this is a challenge for the green transition, but not for the blue transition. Indeed, while the saturation intensity is $60\,\mathrm{mW/cm^2}$ for the blue transition, it is only $0.14\,\mathrm{mW/cm^2}$ for the green transition.

7.3.3.2 Atomic movement

We have not considered the movement of the atoms so far. In the vertical direction, the typical velocity of the ground state reads $v_z = h/m\Delta z$ where Δz is the vertical harmonic oscillator size. This velocity introduces a Doppler shift

$$2\pi \times \Delta f = \frac{hk_L}{m\Delta z}, \tag{7.3.5}$$

which for relevant experimental parameters corresponds to 0.13Γ for the green transition and $10^{-3}\Gamma$ for the blue transition. Transverse motion leads to even smaller Doppler shifts. We therefore neglect the effect of the initial momentum distribution on the optical response.

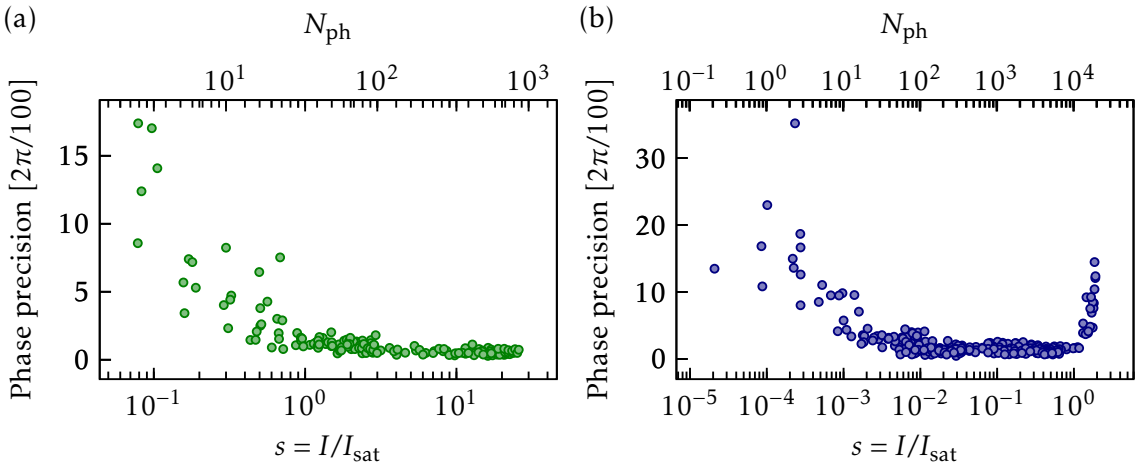

Figure 7.6 Phase precision as a function of $s = I/I_{\mathrm{sat}}$ (bottom axis), or equivalently the number of photons per pixel (top axis). Without any atomic cloud, a pulse of duration 40 µs was sent in the interferometer, with (a) green light and (b) blue light.

As we discussed extensively in Part II, the probing light pulse also alters the momentum distribution through momentum diffusion and the direct pushing force (radiation pressure) exerted by the probe beam. These effects impose upper limits to the pulse duration. Following Chomaz (2014), we now provide a simple single-atom description in order to estimate atomic movement due to the light pulse. Each absorption of a photon imparts a momentum kick to an atom, resulting in an average acceleration

$$a = \frac{\hbar k}{m}\frac{\Gamma}{2}\frac{s}{1+s}. \tag{7.3.6}$$

The atom can thus acquire a velocity $v_p = at_{\mathrm{p}}$ and be pushed by $d_{\mathrm{ver}} = at_{\mathrm{p}}^2/2$ in the vertical direction. To neglect radiation pressure, the Doppler shift kv_p should be much smaller than the linewidth $\Gamma\sqrt{1+s}$ of the transition, or equivalently

$$t_{\mathrm{p}} \ll \frac{2m}{\hbar k^2}\sqrt{s(1+1/s)^3}. \tag{7.3.7}$$

The atomic displacement along z should also be smaller than the half depth of field $D_{\mathrm{f}} \approx 20\,\mu\mathrm{m}$ of the imaging system. This condition translates as

$$t_{\mathrm{p}} < \sqrt{\frac{2mD_{\mathrm{f}}}{\hbar k\Gamma}\left(1+\frac{1}{s}\right)}. \tag{7.3.8}$$

This condition is normally weaker than the one on the Doppler shift. Finally, spontaneously emitted photons lead to momentum diffusion in the transverse plane, as discussed in the Part II. Neglecting many-body effects, we can estimate a momentum broadening

$$\Delta p \approx \hbar k\sqrt{\frac{1}{3}\frac{\Gamma t_{\mathrm{p}}}{2}\frac{s}{1+s}}. \tag{7.3.9}$$

The displacement $d_{\mathrm{hor}} \approx t_{\mathrm{p}}\Delta p/m$ should be smaller than the pixel size $p_s/M \approx 0.5\,\mu\mathrm{m}$. When we combine all the constraints together, we find that the probing the atoms with green light imposes much stronger constraints than with blue light, as shown in figure 7.7. In particular, neglecting the Doppler shifts for small saturation parameters seems difficult. For this reason, we will focus on the blue transition in the following. In figure 7.7(a), we show typical experimental parameters for probing the transmission as a blue line.

The above calculations offer only a simple single-atom description of the effect of the pulse on the atomic cloud. In particular, near-resonant light can induce strong dipole forces.

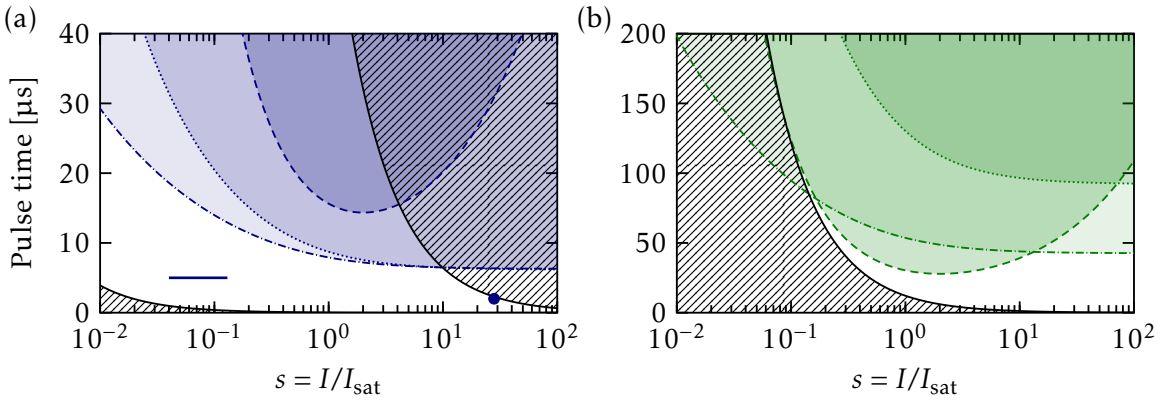

Figure 7.7 Summary of the constraints on the pulse intensity and duration for (a) blue $\lambda_b = 399\,\text{nm}$ light and (b) green $\lambda_g = 556\,\text{nm}$ light. The striped areas correspond to the camera limitations: for small s the solid line corresponds to the camera detectivity and for larger s the solid line corresponds to the camera saturation. The other areas correspond to atomic movement. The dashed line corresponds to a Doppler shift of $0.25\Gamma\sqrt{1+s}$. The dotted line corresponds to a vertical movement of $10\,\mu\text{m}$, which is roughly half of the depth of field. The dash-dotted lign corresponds to an in-plane atomic diffusion of $0.5\,\mu\text{m}$, which is roughly the size of a pixel. In figure (a), the blue line corresponds to the typical experimental parameters for probing the transmission for $s \ll 1$, and the blue dot corresponds to the experimental parameters for atomic density calibrations at high-intensity.

7.3.3.3 Fluorescence from the cloud

The single-atom responses described in section 7.1 do not account for the spontaneous emission of absorbed photons. Because of the finite numerical aperture NA = 0.28, photons with a wavevector different from $\boldsymbol{k}_L$ will also be captured by the imaging system. The ratio of captured photons is given by

$$\Omega = \frac{1-\sqrt{1-\text{NA}^2}}{2} \approx 2.0\,\%. \tag{7.3.10}$$

Note that this simple expression for Ω assumes that the fluorescence is isotropic and does not account for the spatial pattern of dipolar emission. We expect that accounting for the correct emission pattern will only change the forthcoming results by a numerical factor.

Accounting for the magnification ($M = 14$), the backward image of a pixel on the atoms is a square of side length $d_{px} = 0.46\,\mu\text{m}$. We collect

$$N_{ph,fluo} = \Omega\frac{\Gamma s}{2}\frac{1}{1+y^2}t_p N_{px} \tag{7.3.11}$$

photons per pixel, where $N_{px} = n d_{px}^2$ is the number of atoms within the area d_{px}^2 mapped to a single pixel by the imaging system. Here, we assumed the same model leading to the Beer-Lambert law, where each atom is radiating independently. Comparing $N_{ph,fluo}$ to the number of incident photons per pixel,

$$N_{ph,i} = \frac{s I_{sat} t_p d_{px}^2}{\hbar\omega_L}, \tag{7.3.12}$$

we have

$$F \equiv \frac{I_{fluo}}{I_i} = \frac{N_{ph,fluo}}{N_{ph,i}} = \frac{3\Omega n\lambda^2}{2\pi(1+y^2)} = \frac{2\Omega x}{1+y^2} = \Omega n\sigma. \tag{7.3.13}$$

We note that, for a given 2D density n, the resonant fluorescence rate only depends on λ^2 (not on Γ, or rather the dipole strengh d). Hence, the blue transition with a smaller wavelength yields a lower amount of fluorescence in relative terms. At resonance with the blue $\lambda_b \simeq 399\,\mathrm{nm}$ transition, $F \approx 0.15$ for a typical density $n = 100\,\mu\mathrm{m}^{-2}$. However, note that such a single-atom description is a rather rough approximation: because of the finite extension of the gas, some of the fluoresced light will be absorbed by other atoms.

7.3.4 Scanning the detuning near the blue transition

We have seen that the broad blue transtion at $\lambda_b \simeq 399\,\mathrm{nm}$ presents many advantages. However, because it is very broad, it is difficult to scan large detunings with common acousto-optical modulators (AOMs), which typically have a bandwidth of about $\pm 1.5\Gamma_b$. Moreover, within their bandwidth, their efficiency can be very frequency dependent.

In order to circumvent these issues, we chose to separate the three Zeeman sublevels of the $^1P_1$ state with a large vertical magnetic field, as indicated in figure 7.4. With a circular polarization (prepared with a quarter wave-plate, also shown in figure 7.4), we adress one of the extreme Zeeman states $J = 1, m_J = \pm 1$. Instead of varying the frequency of the light beam, we vary the magnetic field and thus the atomic frequency in order to vary the detuning. The available current for the magnetic field coils allows us to roughly probe a $[-20\Gamma_b, 10\Gamma_b]$ range. The conversion from magnetic field to frequency is calibrated by performing spectroscopy with the AOM for different magnetic fields B and recording the shift of the resonance line with B.

7.3.5 Measurement of the density

The many-body effects we want to study prevent an accurate measurement of high atomic densities at small intensities $s \ll 1$. Instead, we use high intensities and short pulses to calibrated the atomic density. This approach was first applied to 2D Bose gases by Hung et al. (2011a) and Yefsah et al. (2011). The idea of high-intensity imaging is that, when the cloud is saturated, the density of atoms absorbing photons is small even at high densities, and thus the single-particle response is retrieved: the effects of dipole-dipole interactions (broadening, shift) is then small compared to the effects of saturation broadening. The effect of saturation on the single-particle optical response of a 2D Bose gas is discussed in Appendix C.5 in more details. However, note for alkali (or other multi-level) atoms, the cross-section for high intensity imaging is known only up to a prefactor, stemming from polarization and optical pumping effects (Hung et al. 2011a, Yefsah et al. 2011). As mentioned earlier, this problem does not exist for bosonic ytterbium (or other atoms with a simple $J = 0 \leftrightarrow J = 1$ transition). High-absorption imaging gives direct access to the atomic density without the need for additional calibration.

Because high-intensity absorption imaging is a destructive measurement, we cannot calibrate the density and measure the low-intensity optical response on the same atomic cloud. In practice, we vary the density with a controlled pulse of resonant light (called a *blast* pulse) on the 3D BEC (before the LPL loading). The density as a function of the duration of the blast is calibrated with high-intensity absorption imaging. A fit to the 2D equation of state is used to verify a posteriori the procedure, as described in Chapter 5. In figure 7.7(a), we show typical experimental parameters for high-intensity imaging as a blue dot.

7.4 Experimental results

We now turn to the results of experiments performed with the broad blue transition at $\lambda_b = 399\,\mathrm{nm}$. However, note that we have successfully performed preliminary experiments with

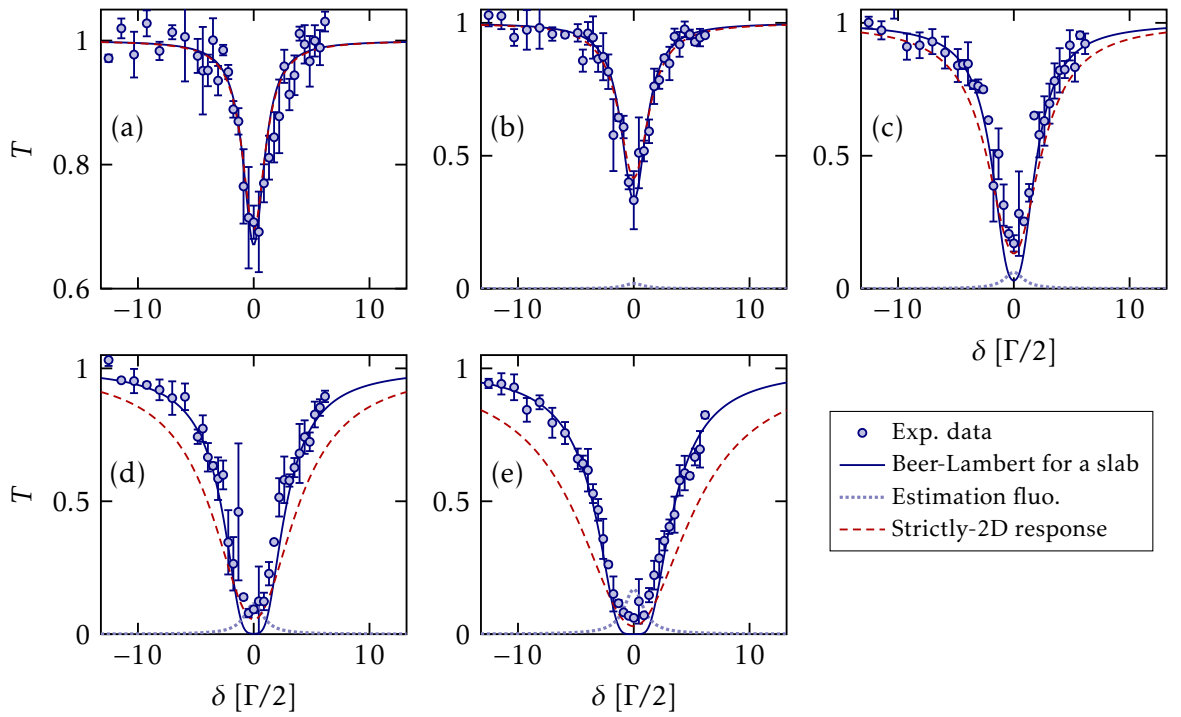

Figure 7.8 Transmission as a function of the detuning for different atomic densities: (a) $nk^{-2} = 0.02$, (b) $nk^{-2} = 0.06$, (c) $nk^{-2} = 0.18$, (a) $nk^{-2} = 0.33$, and (a) $nk^{-2} = 0.51$. The Beer-Lambert response is shown as a solid line and the single-particle response of a strictly-2D gas as a dashed line. The estimation of the fluorescence is shown as a dotted line.

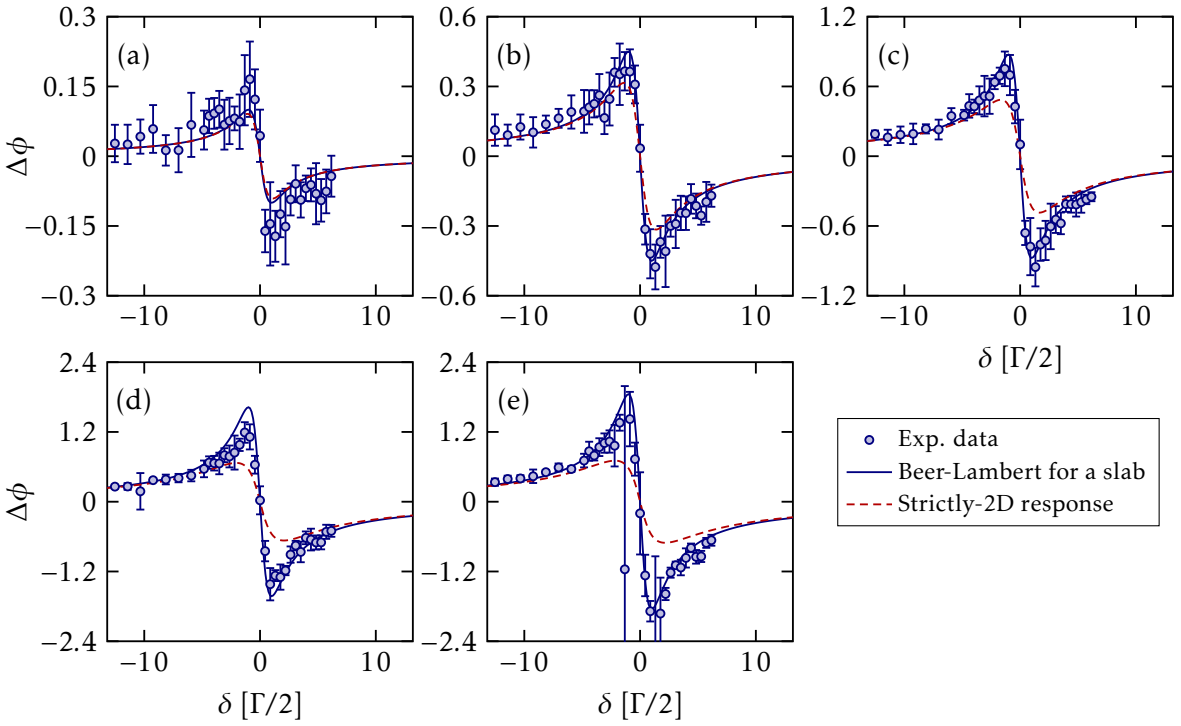

Figure 7.9 Phase shift as a function of the detuning for different atomic densities: (a) $nk^{-2} = 0.02$, (b) $nk^{-2} = 0.1$, (c) $nk^{-2} = 0.18$, (a) $nk^{-2} = 0.34$, and (a) $nk^{-2} = 0.39$. The Beer-Lambert response is shown as a solid line and the single-particle response of a strictly-2D gas as a dashed line.

the narrow green transition at $\lambda_g = 556\,\text{nm}$. The analysis and the interpreation of the data presented in this section are preliminary.

Our main point of comparison are the experiments reported in Corman et al. (2017), where the transmission of near-resonant light at $\lambda = 780\,\text{nm}$ was probed in quasi-2D gases of ^{87}Rb. By scanning the detuning and the density, Corman et al. (2017) observed a saturation of the optical density as well as a broadening and a significant blueshift of the resonance line. Note that, despite similar atomic densities n, Corman et al. (2017) could reach $nk^{-2} \approx 1.5$ while we can reach at most $nk^{-2} \approx 0.5$. The difference stems from different resonance wavelengths.

7.4.1 Transmission as a function of detuning

We start by studying the transmission T of the gas as a function of the detuning, as shown in figure 7.8. We probe the gas with pulses of duration $5\,\mu\text{s}$ and intensity $I/I_{\text{sat}} \approx 0.13$. We consider five different densities, from $nk^{-2} \approx 0.02$ to $nk^{-2} \approx 0.5$, calibrated with high-intensity imaging. The errorbars correspond to the standard deviation over three repetitions of the experiment.

Comparing first with the Beer-Lambert prediction, we observe a good quantitative agreement for the lowest densities. This makes the experimental protocol, including the intensity and density calibrations, convincing. For higher densities, the 3D Beer-Lambert prediction agrees well with our measurements on the wings of the resonance line, but predicts a lower intensity transmission at resonance than the measured one. Comparing with the strictly 2D gas, the resonant T is in good agreement with data, but there is a significant disagreement away from resonance.

The behavior at resonance can be explained by including in the prediction the fact that the measured signal also includes a fraction of fluoresced light on top of the transmission light. The dotted line corresponds to the estimation of the fluorescence given in section 7.3.3.3: although the agreement with the experimental data is not quantitative, the fluorescence correction corresponds to the right order of magnitude and qualitative behavior. Aside from the behavior at resonance, the agreement with the Beer-Lambert prediction can be understood with the numerical simulations shown in figure 7.2. Indeed, the finite size of the gas in the vertical direction makes the gas interact with light as a single-particle 3D cloud would.

We do not observe any significant shift of the transition. Considering the experimental data from Corman et al. (2017), this is to be expected in our regime of densities $nk^{-2} < 0.5$. This is also consistent with the experiments of Bromley et al. (2016), which did not observe any significant shifts in diluted 3D gases of ^{88}Sr when probing the broad $^1\text{S}_0$-$^1\text{P}_1$ transition. However, Bromley et al. (2016) observed a redshift when probing the intercombination transition. Because of the much smaller linewidth of this transition, the Doppler shifts due to atomic movement are far from negligible. It would be interesting to see if the same result holds in our quasi-2D geometry.

Finally, we note that we apparently do not observe any effects due to the inhomogeneity of the gas. Indeed, effects such as lensing should be asymmetric with respect to resonance because the refractive index of the BEC changes sign.

7.4.2 Phase shift as a function of detuning

We now turn to the study of the phase shift $\Delta\phi$ induced by the gas as a function of the detuning, as shown in figure 7.9. We perform the same experimental sequence as for transmission, except for the addition of the second arm of the interferometer. We consider five different densities, from $nk^{-2} \approx 0.02$ to $nk^{-2} \approx 0.4$. Note that some densities are slightly different

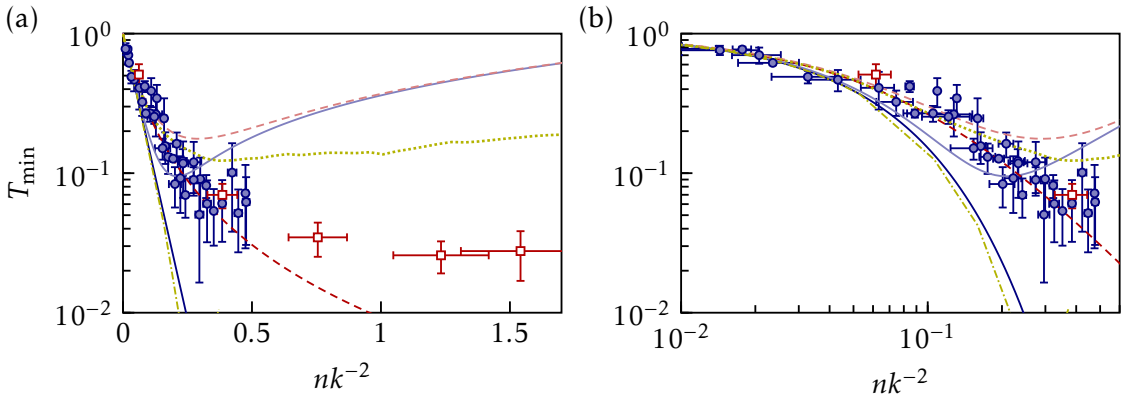

Figure 7.10 Minimum transmission as a function of the atomic density. Our experimental data is represented as circles while experimental data from Corman et al. (2017) is reproduced as squares. We compare these data with analytical formulas such as the Beer-Lambert law (solid line) and the single-particle response of a strictly-2D gas (dashed line). The lighter solid (resp. dashed) line corresponds to the Beer-Lamber law (resp. strictly-2D gas) including isotropic fluorescence at a rate $\approx \Gamma s/2$. We also compare them to numerical simulations for a planar gas ($k\Delta z = 0$, dotted line) and for a quasi-2D gas ($k\Delta z = 2.7$, dash-dotted line). Figure (b) is a close-up of figure (a) in double-logarithmic scale.

from the transmission ones because the phase shift data was taken on a different day. For the phase shift, the errorbars correspond to the standard deviation over the results of the bootstrap fitting procedure accumulated for three repetitions of the experiment.

For all densities, we observe a good quantitative agreement with the 3D Beer-Lambert prediction, rather than the 2D electromagnetic response. The collected fluorescence does not contribute to the phase shift, so that the phase shift measurements tend to confirm our interpretation of the transmission results. As for the intensity transmission, we do not observe any shift of the resonance.

7.4.3 Transmission of the gas at resonance

Overall, the 3D Beer-Lambert law seems to account for the observations except for the intensity transmission near resonance. We therefore focus on this quantity. We fix the probing laser frequency at resonance ($\delta = 0$) and vary the density more finely. Note that, since there are no significant shifts of the transition in our regime of densities, we are thus studying the minimum of transmission of the system. We probe the atomic cloud with pulses of duration 5 µs and intensity $I/I_{\text{sat}} = 0.04$.

As shown in figure 7.10, we observe that the experimental data at resonance is in good quantitative agreement with the single-particle response of a 2D gas, as well as with the numerical simulations for $\Delta z = 0$. However, we believe this agreement with the 2D electromagnetic response to be coincidental. Indeed, numerical simulations for the experimental value of $k\Delta z = 2.7$ show that no reflection is expected, and that the transmission should follow the Beer-Lambert law. On the other hand, we observe that, if we add our simple fluorescence model at a rate $\approx \Gamma s/2$ to the Beer-Lambert law (light blue solid line), we do not find a good quantitative agreement with the experimental data. The transmission is then overestimated and, in fact, we cannot fit the data even if the fluorescence rate is left as a free parameter. Our simple fluorescence model cannot explain the slope at relatively low densities, and we have yet to find a complete model which quantitatively accounts for all the data.

The saturation of the optical depth $\text{OD} = -\ln(T)$ is one of the main results of Corman et al. (2017), and we reproduce their experimental data in figure 7.10. We observe that the

two points from their data that are in our regime of nk^{-2} are consistent with our data. This is to be expected since the transverse extension of their gas is close to ours ($k\Delta z \simeq 2.4$), and they report a similar numerical aperture (NA ≈ 0.2). Whether the saturation of the optical depth comes from the 2D nature of the gas, fluorescence, or many-body effects is not clear at the moment. In any case, many-body effects are necessary to explain the significant blueshift that Corman et al. (2017) measured at higher densities.

In the section on density calibration, we said that in-situ imaging of two-dimensional gases is better with a high intensity ($s \gg 1$) than with a low intensity ($s \ll 1$). Our results seem to indicate that, at least in our experiment where $nk^{-2} \leqslant 0.5$, the reason is the fluorescence of the gas rather than a collective scattering. Increasing the intensity beyond I_{sat}, the fluorescence rate saturates and quickly becomes negligible compared to the probing intensity.

Conclusion

In this chapter, we studied the transmission of a quasi-two-dimensional Bose gas. First, we presented two different single-particle descriptions: one based on the Beer-Lambert law, and a second one considering the 2D gas as an electromagnetic boundary condition. In order to go beyond single-particle physics, we presented a coupled-dipole model on which we performed numerical calculations. We found that the 3D Beer-Lambert prediction was retrieved when the simulated gas had an experimentally relevant transverse extension. When the simulated gas was strictly 2D, we observed a qualitative agremeent for observables such as the minimum transmission and the maximum phase shift, but the simulations also predicted a blueshift of the resonance line that cannot come from single-particle formulas. Finally, we reported our experimental results. We found that the transmission and the phase shift induced by the gas were in good quantitative agreement with the 3D Beer-Lambert prediction for the most part. The only discrepancy was the behavior of the transmission at resonance, where the 3D Beer-Lambert law predicts an intensity transmission higher than observed. This discrepancy could be explained by the fluorescence of the gas.

A first natural perspective would be to study the fluorescence in more detail. For example, the fluorescence could be measured independently with a photodiode in the plane of the atoms, or with polarization-selective optics in the interferometer path. Rui et al. (2020) reported on the transmission and reflection of a 2D gas of Rb on an optical lattice. It would be interesting to perform similar experiments with ytterbium because we could study two different ratios of probing wavelength to lattice spacing using the blue and green transitions. Finally, a stimulating prospect could be the Anderson localization of light (Wiersma et al. 1997, Störzer et al. 2006): Skipetrov et al. (2015) have predicted that light resonant with a $J = 0 \leftrightarrow J = 1$ transition can be localized in a dense ultracold atomic sample submitted to a large magnetic field.

Conclusion

Summary

In this manuscript, I have presented a series of experimental studies on light-matter interaction in atomic quantum gases. After describing in Part I the general theoretical and experimental characteristics of the bosonic ytterbium ultracold gases I studied, I reported on experiments studying decoherence in a dissipative Bose-Hubbard system in Part II, and on the optical response of a planar Bose gas in Part III.

Part I provides the theoretical and experimental background necessary to describe the experiments reported in this manuscript. Regarding the theoretical aspects, we first introduced the concept of Bose-Einstein condensation using the ideal gas, and then we presented the mean-field formalism that describes a 3D Bose-Einstein condensate in the weakly-interacting regime and at zero temperature. Then, we delved into the description of Bose gases in lower dimensions, i.e. 2D and 1D, and in particular their correlation properties, with emphasis on the differences between 2D and 1D. Although true Bose-Einstein condensation does not occur in lower dimensions, we discussed the concepts of quasi-Bose-Einstein condensates and quasi-long-range order. Finally, we examined the behavior of bosons in optical lattices using band theory and the Bose-Hubbard Hamiltonian. We discussed the phase diagram of the Bose-Hubbard model and the validity regime of this model.

Turning to experimental considerations, we first outlined the fundamental characteristics of the atom chosen for our experiment, ^{174}Yb. We then detailed the experimental protocol we used to prepare Bose-Einstein condensates of Yb, which involves the generation of an atomic beam, Zeeman slowing, magneto-optical trapping, transport, and evaporative cooling. We presented the imaging system used probe the gases and discussed the time-of-flight absorption imaging technique that we use to measure the momentum distribution. Finally, we described cubic optical lattices into which the BEC is loaded, which we use to generate stacks of 2D or 1D Bose-Hubbard systems. These stacks serve as the starting point for the experiments in Part II.

In a third chapter, we provided a more complete description of the physics of bosons in one-dimension, from both a theoretical and experimental point of view. We first introduced Luttinger liquid theory to obtain the first-order correlation function $g_1(x)$ of one-dimensional bosons for both continuum and lattice systems. We provided a more in-depth analysis of the 1D Bose-Hubbard model, including its phase diagram and equation of state $n(J, U)$. Next, we presented a loading model of our experimental system, which is composed of a 2D stack of 1D tubes of bosons on a lattice. Using the local density approximation, we estimated the Luttinger parameter K for small lattice depths by averaging over all the tubes. Finally, we

measured the first-order correlation function of the system by fitting the experimental time-of-flight momentum distribution. We found that the correlation function always decayed exponentially at long distances, due to either the finite temperatures or the gap in the Mott phase.

Part II reports on a series of experiments on momentum diffusion in a quantum gases of bosons in an optical lattice subjected to many cycles of absorption and spontaneous emission by near-resonant laser light. Similar experiments have been previously reported in Bouganne et al. (2020) for 2D Bose-Hubbard systems specifically. After providing theoretical background on open quantum systems and the quantum description of spontaneous emission, we have shown that these experiments demonstrate the existence of an algebraic regime of decoherence at long times. By fitting the time-of-flight distribution of the system, we found that nearest-neighbor coherences decayed as a power-law with the predicted exponent of 1/2, and that the next-nearest-neighbor coherences were simply related to the nearest-neighbor coherences. This non-trivial dissipative dynamics, predicted byPoletti et al. (2013), shows that decoherence can be slowed by strong correlations and interactions.

Another way to view this series of experiments is to use the controlled dissipation at early times as a tool to probe the equilibrium state of the system before the application of dissipation. Specifically, we presented a theory describing the evolution of a dissipative system using linear response theory. By applying this non-Hermitian linear response theory to our 1D experiments, we obtained a response function that appears to be sensitive to the 1D Mott insulator transition. We showed that this method could be used in principle to estimate the Luttinger parameter in the superfluid phase. However, the estimate relies on the determination of the exponent α of a stretched exponential $\exp\left(t^{\alpha+1}\right)$ with α small. We also stressed experimental difficulties such as the finite temperature of the system or the averaging of observables over many independent and different systems, and concluded that our experimental system requires improvements in the precision of the measurement to perform this determination.

Part III presents a series of experiments on the optical response of the 2D Bose gas. First, we described the experimental improvements made to the setup in order to probe a single 2D Bose gase in-situ, including a large-period optical lattice to prepare it and a high-resolution microscope to image it. We presented the techniques used to determine the resolution of approximately 1 µm. We described and characterized the large-period lattice used for 2D compression and we presented its loading procedure. We examined the 2D nature of the compressed cloud by studying its vertical expansion after being released from the trap, and found that the atoms were indeed in the ground state of the motion along the vertical transverse axis. We used in-situ imaging to fit the position distribution of the atoms to the known 2D equation of state, which allowed us to fully characterize the thermodynamic properties of the cloud in the large-period lattice. Finally, we discussed experimental perspectives for further improvements and optical lattice loading.

Having described the preparation of a 2D Bose gas, we explored the transmission of light through this slab of atoms. First, we presented two single-particle models: one based on the 3D Beer-Lambert law, and the other considering the 2D gas as an infinitely thin layer. To go further, we carried out numerical simulations using a coupled-dipole model. Comparing the simulations with the single-atom descriptions, we found that simulations of strictly 2D Bose gases were in qualitative agreement with the interface description (except a blueshift and a distortion of the line coming for collective effects). However, simulations of Gaussian slabs, i.e. quasi-2D Bose gases with a finite extension typically found in experiments, simply behaved according to the 3D Beer-Lambert law, at least in the regime of densities explored in our experiment. Finally, after presenting our experimental setup and methods, we reported our experimental results. We found that the transmission and the phase shift induced by

the gas were largely consistent with the 3D Beer-Lambert prediction, as suggested by the simulations. The only exception was the transmission at resonance, for which we suggested the fluorescence of the gas as a possible explanation.

Perspectives

Artificial gauge fields As mentioned in the general introduction, the ytterbium project at Laboratoire Kastler Brossel was initiated to study artificial gauge fields on optical lattices, more specifically to realize the 2D Harper Hamiltonian

$$\hat{H}_{\text{Harper}} = -J \sum_{i,j,\pm} \mathrm{e}^{\pm \mathrm{i} 2\pi\alpha i} \hat{a}^\dagger_{i\pm1,j} \hat{a}_{i,j} + \hat{a}^\dagger_{i,j\pm1} \hat{a}_{i,j} + \text{h.c.}, \tag{7.4.1}$$

that describes particles in a tight-binding lattice subjected a constant magnetic field $B = h\alpha/ed^2$ (Harper 1955). Here, d is the lattice spacing and $\hat{a}^\dagger_{i,j}$ creates an atom at position $(x, y) = (id, jd)$. The quantity α corresponds to the magnetic flux going through a unit cell of the lattice. Jaksch et al. (2003) first proposed a scheme to realize this Hamiltonian with ultracold quantum gases, and Gerbier et al. (2010) adapted it to alkaline-earth and alkaline-earth-like atoms, which feature a clock transition as discussed in Chapter 1.

Our progress towards realizing of the Harper Hamiltonian was slowed by the discovery of fast two-body inelastic losses for atoms in the $^3\mathrm{P}_0$ metastable excited state (Bouganne et al. 2017). In order to study how we could get around this problem, we studied two instances of the Quantum Zeno effect, as mentioned in Chapter 4. We found that, due to the build-up of correlations between the atoms, the two-body loss rate is lower than that of a non-interacting system by several orders of magnitude in 1D Bose-Hubbard systems (Ghermaoui 2020, Rossini et al. 2021). In Bosch Aguilera et al. (2022), we also report on how the Quantum Zeno effect can contribute to an adiabatic preparation when two atoms are present at the same site. As a first step, we believe that these two studies can help us realize a minimal instance of artificial gauge fields by using the clock transition as a synthetic dimension (Mancini et al. 2015, Stuhl et al. 2015), effectively realizing the Harper Hamiltonian on a ladder. Note that using polarized fermionic ytterbium could also be a way to eliminate two-body losses thanks to the Pauli principle.

Single homogeneous open quantum system In Chapters 3 and 5, we pointed out that some features of the momentum distribution are lost when they are averaged over many different and independent systems. Using the technical upgrades of the experimental setup, we can prepare a single 2D Bose-Hubbard system (although achieving low entropies is still challenging as discussed in Chapter 6). In addition, it would be even better to prepare homogeneous Bose-Hubbard systems, for example with the optical painting scheme described in Chapter 6. To prepare a single tube, additional work would be required to design an appropriate scheme, but optical painting (as discussed in Chapter 6) could also be a means to achieve this goal.

With similar experimental tools, we could also gain a deeper understanding of the dynamics of 1D Bose-Hubbard systems exhibiting the strong inelastic two-body losses mentioned above. This open quantum system problem is described by the Bose-Hubbard Hamiltonian $\hat{H}_{\text{BH}}$ and the quantum jump operator

$$\hat{L}_i = \sqrt{\frac{\gamma_{2\text{B}}}{2}} \hat{a}_i^2 \tag{7.4.2}$$

In particular, we have not yet found a satisfying explanation for why the decay of the atom number observed experimentally (Ghermaoui 2020) is much slower than predicted theoretically (Rossini et al. 2021). One possibility that we are not able to rule out is that the actual

λ_{latt}	759 nm	1064 nm	617 nm
$\lambda_b = 399$ nm	0.95	1.33	0.77
$\lambda_g = 556$ nm	0.68	0.98	0.56
$\lambda = 1379$ nm	0.27	0.39	0.22

Table 7.1: Values of d/λ for the two main transitions of ^{174}Yb and for different possible lattice constants $d = \lambda_{\text{latt}}/2$.

density in the experiment is much lower than we think. Being able to probe the local density with high-resolution imaging wouuld allow us to eliminate this systematic effect (among others).

Optical response of a 2D Mott insulator In Chapter 7, we studied the optical response of a quasi-two-dimensional Bose gas where the spatial distribution of the atom scan be considered random. By ordering our bosons in a square optical lattice, we could study cooperative subradiance or superradiance. Rui et al. (2020) reported such effects by probing the D_2 line of ^{87}Rb atoms in a square optical lattice with a lattice constant d such that $d/\lambda \simeq 0.68$. For such a study, the two $J = 0 \leftrightarrow J = 1$ transitions of ^{174}Yb could be an asset. In table 7.1, we compile values of d/λ that could be achieved on our experiments. We can see that by repeating the experiments of Chapter 6 on a lattice, we can already study a new value $d/\lambda \simeq 0.95$. By using a common $\lambda = 1064$ nm laser for the lattice, we could also probe $d/\lambda \simeq 1.33$. Finally, using a trapping laser around the anti-magic wavelength $\lambda \simeq 617$ nm, we could have $d/\lambda \simeq 0.77$, a value close to the value of 0.8 where the transmission of the cloud is expected to go to zero (Shahmoon et al. 2017).

In addition, by transferring the atoms in the $^3P_0$ excited state, we could study the $^3P_0$-$^3D_1$ transition at $\lambda = 1389$ nm. We already use this open transition to repump excited atoms to the ground state (Bouganne 2018). The large wavelength of this transition would allow us to enter the $nk^{-2} \sim 1$ regime that we could not reach with the $\lambda_b = 399$ nm blue transition. Moreover, Perczel et al. (2017) have predicted the existence of photonic topological states that could be engineered in a 2D atom array by using such a transition in the presence of the magnetic field. Topological robustness against dissipation and long-lived edge states constitute exciting prospects of versatile quantum optical systems such as ours.

Appendices

Appendix A of Part I

A.1 Kapitza-Dirac measurement of the lattice depth

Our chosen method for the calibration of the lattice depth is Kapitza-Dirac diffraction (Kapitza et al. 1933, Ovchinnikov et al. 1999). The optical lattice is pulsed onto the 3D BEC, which is subsequently released from the CDT. After tof, the absorption image exhibits a series of peaks at integer multiples of $\pm 2k_\mathrm{L}$, as shown in figure A.1(a). A peak at momentum $2k_\mathrm{L}$ can be interpreted as the virtual absorption of a photon from the forward lattice beam and the subsequent stimulated emission of a photon in the reflected beam.

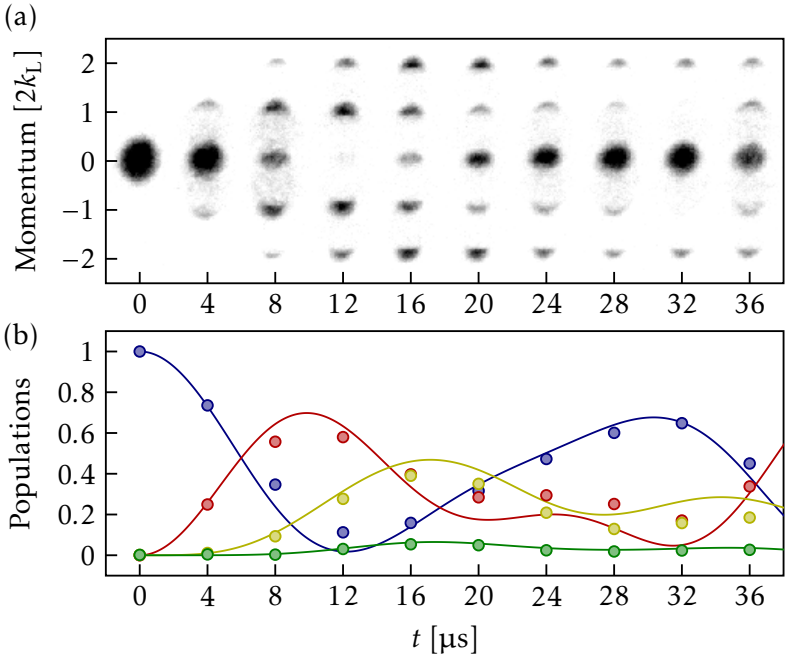

Figure A.1 Calibration of the lattice depth with Kapitza-Dirac diffraction. (a) Images taken after a time-of-flight expansion, as a function of the Kapitza-Dirac pulse duration t. The diffracted orders are separated by $2mk_\mathrm{L}$, with m an integer. (b) Relative populations of the diffracted orders as a function of the pulse duration t. The lines correspond to a fit to the data. Adapted from Bosch Aguilera (2019).

The evolution of the populations $P_m = f(t, V_0)$ in each order m can be computed numerically (Denschlag et al. 2002, Gadway et al. 2009), and is used to extract the lattice depth. A typical example is shown in figure A.1(b). In practice, optical lattices in each direction are calibrated independently for simplicity.

A.2 The Tonks-Girardeau gas

A.2.1 Fermionization

The strongly-interacting limit $\gamma \gg 1$ provides a rather simple description of 1D Bose gases. The infinitely-interacting 1D Bose gas is called the Tonks-Girardeau gas, and the bosons are referred to as hardcore bosons. Girardeau (1960) noted that the constraint imposed by infinite interactions resembled the Pauli principle for a fermionic gas, and wrote the many-body wavefunction as

$$\Psi(x_1,...,x_n) = \Psi^{\mathrm{F}}(x_1,...,x_n)A(x_1,...,x_n) \tag{A.2.1}$$

where $\Psi^{\mathrm{F}}(x_1,...,x_n)$ describes a gas of spinless fermions and $A(x_1,...,x_n) = \sum_{i<j}\mathrm{sign}(x_j - x_i)$ maintains Bose statistics regarding particle exchange. Equation (A.2.1) implies that the density distribution $n = |\Psi|^2$ of a infinitely-interacting Bose gas is the same as a non-interacting Fermi gas. This approach, called *fermionization*, simplifies greatly the calculation of many observables like the second-order correlation function

$$g_2(x) \equiv \frac{\langle \hat{n}(x)\hat{n}(0)\rangle}{n^2} = 1 - \left[\frac{\sin(\pi n x)}{\pi n x}\right]^2. \tag{A.2.2}$$

However, the first-order correlation function is much more difficult to compute, as it is different from that of free fermions. One description, which we will not detail, involves so-called Töplitz determinant (Lenard 1964, Ovchinnikov 2009) and yields at long distance

$$g_1(x) \equiv \frac{\langle \hat{\Psi}^\dagger(x)\hat{\Psi}(0)\rangle}{n} \sim \left[\frac{1}{2nL|\sin(\pi x/L)|}\right]^{1/2}. \tag{A.2.3}$$

Since they are more relevant for our experiment, we now focus on fermionized Bose-Hubbard gases in a lattice rather than continuous gases. Our goal is to obtain a generalization of equation (A.2.3).

A.2.2 Hardcore bosons on a lattice

For a filling $\bar{n} \leqslant 1$, infinitely-interacting bosons on a 1D lattice can be described by the hardcore-boson Hamiltonian

$$\hat{H}_{\mathrm{HCB}} = -J\sum_l (\hat{b}_l^\dagger \hat{b}_{l+1} + \hat{b}_{l+1}^\dagger \hat{b}_l), \tag{A.2.4}$$

where the hardcore creation-annihilation operators $(\hat{b}_l^\dagger, \hat{b}_l)$ obey a mix of bosonic and fermionic commutation relations

$$[\hat{b}_l, \hat{b}_m] = [\hat{b}_l^\dagger, \hat{b}_m^\dagger] = [\hat{b}_l, \hat{b}_m^\dagger] = 0, l \neq m \tag{A.2.5}$$

$$\hat{b}_l^2 = (\hat{b}_l^\dagger)^2 = 0 \tag{A.2.6}$$

$$\{\hat{b}_m, \hat{b}_m^\dagger\} = 1. \tag{A.2.7}$$

Hardcore bosons can be mapped to free fermions through the Jordan-Wigner transformation (Lieb et al. 1961), the lattice equivalent of equation (A.2.1). We define the fermionic operators

$$\hat{c}_m = \exp\left(\pi i \sum_{l<m} \hat{b}_l^\dagger \hat{b}_l\right)\hat{b}_m\,, \quad \hat{c}_m^\dagger = \exp\left(-\pi i \sum_{l<m} \hat{b}_l^\dagger \hat{b}_l\right)\hat{b}_m^\dagger. \tag{A.2.8}$$

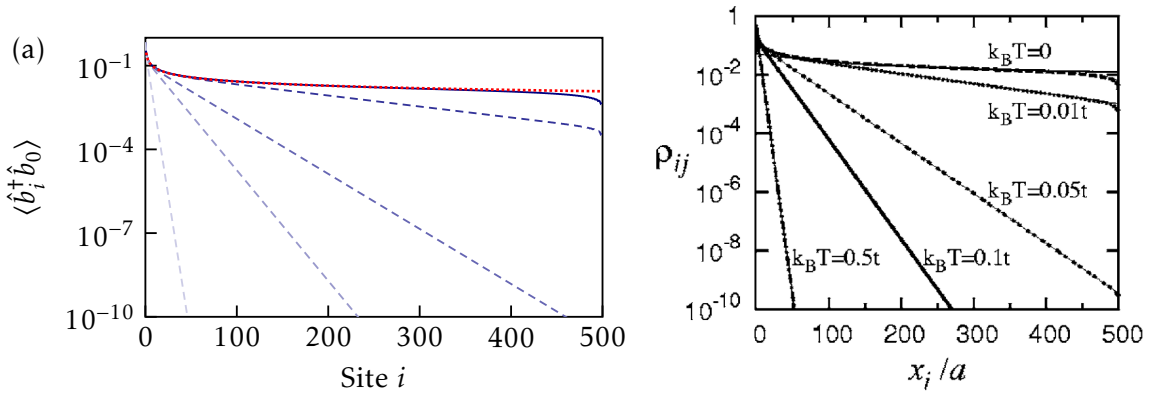

Figure A.2 (a) $\langle b_i^\dagger b_0 \rangle$ for $\mu = J$ and $T = 0$ (solid black), calculated with Töplitz determinants. The red dotted line corresponds to a fit to $1/\sqrt{i}$. The dashed blue lines correspond, from darker to brighter, to $k_B T = 0.01J$, $0.05J$, $0.1J$ and $0.5J$. (b) First-order correlation function calculated using exact diagonalization for $\bar{n} = 0.5$ and $N_s = 1000$. The zero-temperature curve decays as $1/\sqrt{x}$. From Rigol (2005).

Substituting in equation (A.2.4), we obtain a free-fermion Hamiltonian, which is diagonal in momentum space

$$H_{\mathrm{FF}} = -J \sum_l (\hat{c}_l^\dagger \hat{c}_{l+1} + \hat{c}_{l+1}^\dagger \hat{c}_l) = -\frac{2J}{N_s} \sum_q \cos(qd) \hat{c}_q^\dagger \hat{c}_q, \tag{A.2.9}$$

with the momentum space creation-annihilation operators

$$c_q = \frac{1}{\sqrt{N_s}} \sum_l e^{-iqx_l} c_l \,, \quad c_q^\dagger = \frac{1}{\sqrt{N_s}} \sum_l e^{iqx_l} c_l^\dagger, \tag{A.2.10}$$

where $x_l = ld$ is the position of site l and N_s is the size of the system.

We can also link the first-order correlation function of hardcore bosons to the known first-order correlation function of free fermions. From equation (A.2.8), it is clear that $\langle b_l^\dagger b_l \rangle = \langle c_l^\dagger c_l \rangle$, so we only need to study the case $l \neq m$. Using again the Jordan-Wigner transformation, we write

$$\langle b_l^\dagger b_m \rangle = \langle c_l^\dagger \exp\left(\pi i \sum_{l>n>m} c_n^\dagger c_n \right) c_m \rangle, \quad l > m \tag{A.2.11}$$

Using Wick's theorem, Gangardt et al. (2006) expressed the first-order correlation function in the form of a Töplitz determinant

$$\langle b_l^\dagger b_m \rangle_{l \neq m} = \begin{vmatrix} G_1 & G_2 & G_3 & \dots & G_{l-m} \\ G_0 & G_1 & G_2 & \dots & G_{l-m-1} \\ G_{-1} & G_0 & G_1 & \dots & G_{l-m-2} \\ \vdots & \vdots & \vdots & \ddots & \vdots \\ G_{2-(l-m)} & G_{3-(l-m)} & G_{4-(l-m)} & \dots & G_1 \end{vmatrix} \tag{A.2.12}$$

where $G_{l-m} \equiv \langle c_l^\dagger c_m \rangle - \frac{1}{2}\delta_{lm}$, and can be readily calculate from the known first-order correlation function of free fermions $\langle c_l^\dagger c_m \rangle$. For example, for bulk free fermions with periodic boundary conditions, one has

$$g_1^{\mathrm{FF}}(l-m) \equiv \frac{\langle c_l^\dagger c_m \rangle}{\bar{n}} = \frac{\sin[\pi \bar{n}(l-m)]}{\pi \bar{n}(l-m)}. \tag{A.2.13}$$

Even at finite temperature and with an additional trapping potential, $g_1(l-m)$ can be calculated numerically without difficulty (Paredes et al. 2004) in the thermodynamic limit and in the grand-canonical ensemble. In figure A.2(a), we show calculations of $\langle b_i^\dagger b_0\rangle$ as a function of i for different temperatures.

We also note that other approaches are also available to calculate the first-order correlation function of hardcore bosons for finite systems at finite temperature without the grand-canonical ensemble and the thermodynamic limit. We show the result of such a calculation, from Rigol (2005), in figure A.2(b).

A.2.3 Equation of state of the Bose-Hubbard model in the Tonks limit

We now use the tools introduced above to calculate the equation of the state of the Bose-Hubbard model in the limit of hardcore bosons, which are mapped to free fermions. The ground state of the ideal Fermi gas is constructed by filling all available states up to the Fermi energy E_F. Introducing the Fermi momentum k_F such that $E_\mathrm{F} = -2J\cos(k_\mathrm{F}d)$, the N-fermions state is given by

$$|\Psi_0\rangle = \prod_{|k|<k_\mathrm{F}} \hat{c}_k^\dagger |\varnothing\rangle. \tag{A.2.14}$$

The associate momentum distribution is simply

$$n(k) = \Theta(k_\mathrm{F} - |k|), \tag{A.2.15}$$

with Θ the Heaviside step function. Integrating over all momenta, we obtain the total particle number as $N = N_\mathrm{s}\int_{-k_\mathrm{F}}^{k_\mathrm{F}} \frac{\mathrm{d}k}{2\pi}$. We thus obtain the Fermi momentum and energy,

$$k_\mathrm{F} = \pi\bar{n}, \qquad E_\mathrm{F} = 2J\cos(\pi\bar{n}), \tag{A.2.16}$$

with $\bar{n} = N/N_\mathrm{s}$ the mean lattice filling. Since the chemical potential equals the Fermi energy at $T = 0$, the relation between E_F and $\bar{n}$ can be inverted to obtain the equation of state,

$$\bar{n} = \frac{1}{\pi}\arccos\left(-\frac{\mu}{2J}\right). \tag{A.2.17}$$

The two limits $\bar{n}\to 0$ and $\bar{n}\to 1$ are obtained when $\mu\to -2J$ and $\mu\to 2J$, respectively.

A.3 Momentum distribution of one-dimensional lattices

In figure A.3(a-e), we show the experimental time-of-flight (tof) momentum distribution $n(k)$ in double-logarithmic scale, normalized by $n(k=0)$. We fit a power-law behavior $|k|^{-\alpha}$ for $k/k_\mathrm{L}\in[0.4,1]$ to extract the algebraic exponent α, shown in figure A.3(f). This analysis method was first used in Paredes et al. (2004), and we show their values for comparison (empty squares).

Paredes et al. (2004) observed a slow convergence to $\alpha = 1/2$, which they attribute to the entry in the Tonks-Girardeau regime. Indeed, $\alpha = 1/2$ implies $\langle \hat{a}_l^\dagger \hat{a}_m\rangle \propto |l-m|^{-1/2K}$, with $1/2K = 1-\alpha = 1/2$. This corresponds to $K = 1$, i.e. to the Tonks-Girardeau regime $\gamma \gg 1$ as discussed in the previous section. On the other hand, $\alpha > 0.5$ corresponds to $K < 1$, which is not physical. Although this is not necessarily an issue in the Mott insulating regime ($V > 3E_\mathrm{R}$) because LL theory is not expected to apply, this is more puzzling in the superfluid regime.

Looking first at the data from Chapter 4 (filled circles), we observe that, although the qualitative behavior is the same as in Paredes et al. (2004), there is no quantitative agreement. This can be explained by the high number of atoms used in our experiments, leading

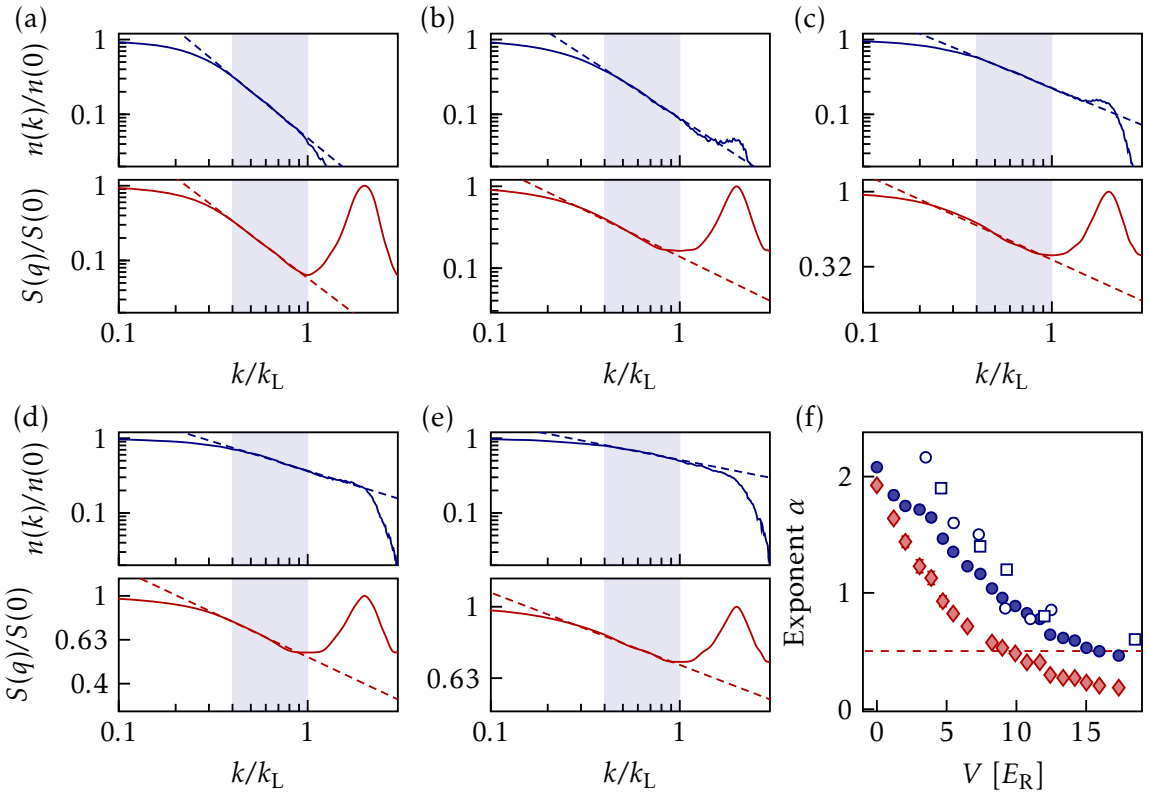

Figure A.3 Normalized 1D tof momentum distribution $n(k)/n(0)$ (blue solid line) and reconstructed quasi-momentum distribution $S(q)/S(0)$ (red solid line) for (a) $V = 0$, (b) $V = 3.9E_R$, (c) $V = 8.3E_R$, (d) $V = 11.7E_R$, and (e) $V = 15.9E_R$. The dashed lines corresponds to power-law fits and the shaded area to the fit window. (f) Extracted exponents α for maximum filling $\bar{n} = 2$ (full circles) and $\bar{n} = 1$ (empty circles). Empty squares coresspond to values reported in Paredes et al. (2004). Red diamonds correspond to the exponents extracted from the quasi-momentum distribution. The dashed line corresponds to the exponent $1/2$ for an ideal Tonks-Girardeau gas.

to a $\bar{n} = 3$ maximum filling in most of the tubes. To confirm this hypothesis, we have repeated the experiment with a reduced atom number so that the maximum filling is $\bar{n} = 1$ (empty circles). The quantitative agreement with the values of Paredes et al. (2004) is much better. Note that it is not surprising that we observe the same qualitative behavior even if $\bar{n} > 1$. For a Tonks-Girardeau gas with $\bar{n} \in [1, 2]$, the atoms corresponding to $\bar{n} = 1$ can be ignored and only the surplus of atoms needs to be considered. For this surplus of atoms behaving as hardcore bosons, the interaction energy U is larger, which could explain why the exponent α converges slightly faster to $1/2$.

The reconstructed quasi-momentum distribution is shown in red in figure A.3(a-e), and the algebraic exponent of the central peak is shown in figure A.3(f) as red diamonds. Performing the same power-law fit, we observe that that the exponent actually converges to 0. Thus, the "power-law" decay reported in Paredes et al. (2004) is most likely an artifact of the Wannier envelope and not a genuine signature of fermionization. The a priori more accurate analysis of Chapter 3 further shows that the finite temperature should wash out the power-law behavior anyway.

Appendix B of Part II

B.1 Calibration of the Rabi frequency for light scattering

For experimental convenience, we perform Rabi oscillations by varying the power of the dissipation laser rather than the duration of the dissipation pulse, which we fix to $T = 400\,\mathrm{ns}$. Images are taken after a time-of-flight which is long compared to the lifetime of the excited state Γ_g^{-1}, and thus all atoms are present on the images. To measure the effect of the dissipation pulse, we rather look at the tof size of the BEC, which serves as a proxy of the population transfered to the excited state.

As shown in figure B.1, we indeed observe oscillations of the BEC size. As expected, the Rabi frequency is proportional to the square root of the power, $\Omega_L = a\sqrt{P_L}$. With a sinusoidal fit to $\sin\left(a\sqrt{P_L}T\right)$, we extract $a \approx 2\pi \times 2.5\,\mathrm{MHz/mW^{1/2}}$, which is consistent with beam waist calibration $w_L \sim 1\,\mathrm{mm}$. For more details, see the supplemental material of Bouganne et al. (2020).

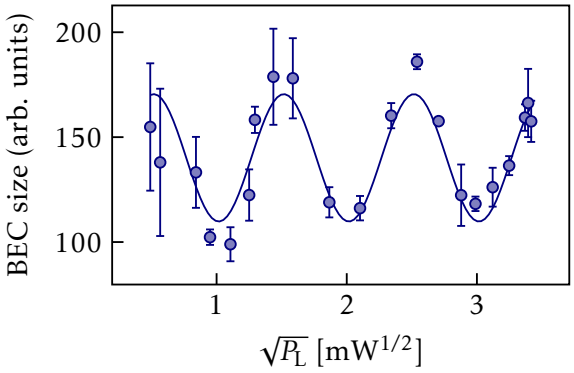

Figure B.1 Calibration of the Rabi frequency: Rabi oscillations on the green transition with a fixed pulse time $T = 400\,\mathrm{ns}$ and a varying laser power P_L.

Appendix C of Part III

C.1 Half-wave plate for the large period lattice

In this section, we show that a horizontal half-wave plate can change the phase of the large period lattice by π. We use Jones formalism, where light propagating in the y direction is described with vector $\left(E_{0x}\mathrm{e}^{\mathrm{i}\phi_x}, E_{0z}\mathrm{e}^{\mathrm{i}\phi_z}\right)$.

Before the polarizaing beam splitter (PBS), we start with a beam polarized linearly at a 45° angle from x and z

$$|0\rangle = \frac{1}{\sqrt{2}}\begin{pmatrix}1\\1\end{pmatrix}, \tag{C.1.1}$$

where we have normalized the intensity to 1 for convenience. The PBS creates two arms

$$|1\rangle = \frac{1}{\sqrt{2}}\begin{pmatrix}1\\0\end{pmatrix}, \quad |2\rangle = \frac{1}{\sqrt{2}}\begin{pmatrix}0\\1\end{pmatrix} \tag{C.1.2}$$

For them to interfere when they are recombined on the atoms with a lens, we place a half-wave plate on arm 1. Its fast axis is set to be at 45° from the horizontal, yielding

$$|3\rangle = \mathrm{e}^{-\mathrm{i}\frac{\pi}{2}}\begin{pmatrix}0 & 1\\1 & 0\end{pmatrix}|1\rangle = \frac{\mathrm{e}^{-\mathrm{i}\frac{\pi}{2}}}{\sqrt{2}}\begin{pmatrix}0\\1\end{pmatrix}. \tag{C.1.3}$$

We observe that $|3\rangle$ is dephased by $-\pi/2$ with respect to $|2\rangle$ in this configuration.

Let us now change $|0\rangle$ to $|0\rangle'$ with a half-wave plate with a horizontal fast axis

$$|0\rangle' = \mathrm{e}^{-\mathrm{i}\frac{\pi}{2}}\begin{pmatrix}1 & 0\\0 & -1\end{pmatrix}|0\rangle = \frac{\mathrm{e}^{-\mathrm{i}\frac{\pi}{2}}}{\sqrt{2}}\begin{pmatrix}1\\-1\end{pmatrix}. \tag{C.1.4}$$

Keeping the same notations, this yields

$$|3\rangle' = \frac{1}{\sqrt{2}}\begin{pmatrix}0\\-1\end{pmatrix}, \quad |2\rangle' = \frac{\mathrm{e}^{-\mathrm{i}\frac{\pi}{2}}}{\sqrt{2}}\begin{pmatrix}0\\-1\end{pmatrix}, \tag{C.1.5}$$

meaning that $|3\rangle'$ is dephased by $+\pi/2$ with respect to $|2\rangle'$ in this configuration. We have thus changed the phase of the large period lattice by π.

C.2 Expansion of a two-dimensional condensate

We consider a 2D gas in the ground state of a vertical harmonic oscillator of frequency ω_z, with a size $a_z = \sqrt{\hbar/m\omega_z}$. As explained in Chapter 1, the interactions are described with an effective interation strength $\tilde{g} = \sqrt{8\pi}a/a_z$, where a is the 3D scattering length.

C.2.1 Method

To describe the 2D gas, we use a *hybrid Lagrangian variational model* (Pérez-García et al. 1996, Edwards et al. 2005). The condensate is described by a classical field ansatz

$$\Psi(\boldsymbol{r}) = G(z,t)\chi(\rho,t), \tag{C.2.1}$$

where we have separated the vertical and horizontal wavefunctions. The vertical wavefunction is described by a Gaussian

$$G(z,t) = \frac{\mathrm{e}^{-\frac{z^2}{2\sigma^2}+\mathrm{i}\frac{m\alpha z^2}{2\hbar}}}{(\pi\sigma^2)^{1/4}} \tag{C.2.2}$$

where σ is an effective width and α is an expansion parameter, while the horizontal wavefunction χ remains unspecified. In 3D, the Schrödinger Lagrangian reads

$$L[\Psi,\Psi^*] = \int d^3\boldsymbol{r}\left\{\frac{\mathrm{i}\hbar}{2}\left(\Psi^*\dot{\Psi}-\dot{\Psi}^*\Psi\right)+\frac{\hbar^2}{2M}\Psi^*\Delta\Psi - V\Psi^*\Psi+\frac{g_{3\mathrm{D}}}{2}\left(\Psi^*\right)^2\Psi^2\right\} \tag{C.2.3}$$

where $g_{3\mathrm{D}} = 4\pi\hbar^2 a/m$. Finally, we remind that the Euler-Lagrange equations read

$$\frac{\mathrm{d}}{\mathrm{d}t}\frac{\partial L}{\partial\dot{\Psi}} = \frac{\partial L}{\partial\Psi}. \tag{C.2.4}$$

We use the notation $\dot{\Psi} = \partial_t\Psi$.

C.2.2 Equations of motion

We apply the Euler-Lagrange equations to the variational ansatz. By varying with respect to x^* for each variational parameter x, we obtain three equations of motion. We use the convenient parametrization

$$\omega_z(t) = \sqrt{f(t)}\omega_z\,, \quad \tau = \omega_z t\,, \quad b_z = \frac{\sigma}{a_z}, \tag{C.2.5}$$

The equation of motion for α reads

$$\alpha = \frac{\dot{b}_z}{b_z}. \tag{C.2.6}$$

The equation of motion for σ reads

$$\frac{\mathrm{d}^2 b_z}{\mathrm{d}\tau^2} + f(t)b_z = \frac{1}{b_z^3} + \frac{1}{b_z^2}K[\chi] \tag{C.2.7}$$

where we have defined

$$K[\chi] = \frac{\tilde{g}a_z^2}{N}\int \mathrm{d}^2\rho|\chi(\boldsymbol{\rho})|^4 \tag{C.2.8}$$

Finally, the equation of motion for χ reads

$$\mathrm{i}\hbar\omega_z\frac{\partial\chi}{\partial\tau} = -\frac{\hbar^2}{2m}\Delta_\perp\chi + V_\perp\chi + \frac{\hbar\omega_z\tilde{g}a_z^2}{b_z}|\chi|^2\chi, \tag{C.2.9}$$

which corresponds to an effective 2D Gross-Pitaevskii equation for χ. Here, $\Delta_\perp$ and $V_\perp$ hare the horizontal components of the 3D Δ and V.

C.2.3 Solution

At equilibrium, we take $b_z(t) = b_0$, $f(0) = 1$ and $\chi = \chi_0$. For a non-interacting system, $sigma_0 = a_z$ and $b_0 = 1$. To account for interactions, we use equation (C.2.7) which becomes

$$b_0^4 = 1 + b_0 K[\chi_0]. \tag{C.2.10}$$

To solve this equation, we make use of the separation of energy scales

$$\hbar\omega_\perp \ll \mu_0 \ll \hbar\omega_z. \tag{C.2.11}$$

We define $\eta = \mu_0/(\hbar\omega_z)$. Using $\mu_0 \gg \hbar\omega_\perp$, we treat equation (C.2.9) in the Thomas-Fermi approximation, and we obtain

$$|\chi_0|^2 = \frac{b_0\eta}{\tilde{g}a_z^2}\Upsilon\left[1 - \left(\frac{\rho}{R}\right)\right]^2 \tag{C.2.12}$$

with the Thomas-Fermi radius $R = \sqrt{2\mu_0/M\omega_\perp^2}$. This leads to

$$K[\chi_0] = \frac{2\eta}{3} b_0^{1/2}. \tag{C.2.13}$$

Equation (C.2.10) becomes

$$b_0^4 = 1 + b_0^{3/2}\frac{2\eta}{3}. \tag{C.2.14}$$

Using $\eta \ll 1$, we get

$$b_0 \simeq 1 + \frac{\eta}{6}. \tag{C.2.15}$$

When the cloud is released from the trap, the released energy is the sum of the kinetic and interaction energies at equilibrium

$$e_{\rm rel} = e_{\rm K,0} + e_{\rm int,0} = \frac{\hbar\omega_z}{4b_0^2} + \frac{\eta\hbar\omega_z}{3b_0}. \tag{C.2.16}$$

Using equation (C.2.15), we finally obtain

$$e_{\rm rel} \simeq \frac{\hbar\omega_z}{4}\left(1 + \frac{5}{3}\eta\right). \tag{C.2.17}$$

C.3 Integrated Bose and Thomas-Fermi distributions

We consider a Bose gas trapped in a 3D harmonic trap

$$V(x,y,z) = \frac{1}{2}m(\omega_x^2x^2 + \omega_y^2y^2 + \omega_z^2z^2). \tag{C.3.1}$$

C.3.1 Thermal gas

The 3D density distribution of a thermal Bose gas in the trap reads

$$n_{\rm th}(x,y,z) = \left(\frac{m}{2\pi\hbar^2\beta}\right)^{3/2} g_{3/2}\left[\phi\exp\left(-\frac{x^2}{L_x^2} - \frac{y^2}{L_y^2} - \frac{z^2}{L_z^2}\right)\right] \tag{C.3.2}$$

where the thermal length are given by $L_\alpha = \sqrt{2k_{\rm B}T/m\omega_\alpha}$, $\phi = \exp(\beta\mu)$ is the fugacity and $\beta = 1/k_{\rm B}T$. After integration along the line of sight z, the imaged density distribution reads

$$\bar{n}_{\rm th}(x,y) = \frac{m}{2\pi\hbar^3\beta^2\omega_z} g_2\left[\phi\exp\left(-\frac{x^2}{L_x^2} - \frac{y^2}{L_y^2}\right)\right]. \tag{C.3.3}$$

After a long time-of-flight $t_g g\omega_\alpha^{-1}$, the density in the three directions will be dilated by $d_\alpha(t) = \sqrt{1 + \omega_\alpha^2 t^2}$.

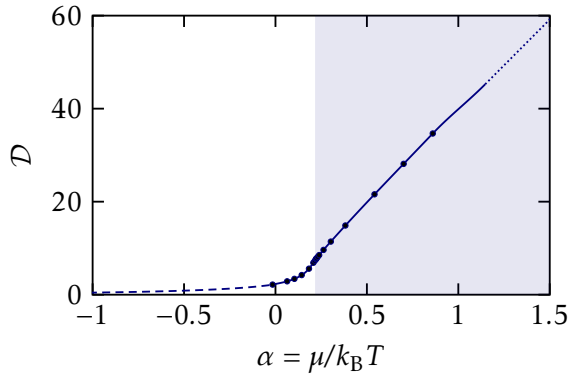

Figure C.1 2D equation of state $\mathcal{D}(\mu/k_B T)$ for $\tilde{g} = 0.15$, with Hartree-Fock (dashed) and Thomas-Fermi asymptotes (dotted). The circles correspond Monte-Carlo calculations from Prokof'ev et al. (2002). The solid line is a numerical interpolation. The shaded area corresponds to the superfluid regime $\mathcal{D} > \mathcal{D}_c \simeq 7.3$.

C.3.2 Bose-Einstein condensate

The 3D density distribution of a Bose-Einstein condensate in the trap reads

$$n_{\mathrm{TF}}(x,y,z) = n_0 \Upsilon\left(1 - \frac{x^2}{R_x^2} - \frac{y^2}{R_y^2} - \frac{z^2}{R_z^2}\right) \tag{C.3.4}$$

where n_0 is the peak density and the Thomas-Fermi radius is given by $R_\alpha = \sqrt{2\mu/m\omega_\alpha^2}$. After integration along the line of sight z, the imaged density distribution reads

$$\bar{n}_{\mathrm{TF}}(x,y) = \frac{4}{3} n_0 R_z \Upsilon\left(1 - \frac{x^2}{R_x^2} - \frac{y^2}{R_y^2}\right)^{3/2}. \tag{C.3.5}$$

After a long time-of-flight $t \gg \omega_\alpha^{-1}$, the density in the three directions will be dilated by $b_\alpha(t)$. For more details, see Castin et al. (1996).

C.4 Equation of state of the two-dimensional Bose gas

The thermodynamics of weakly-interacting Bose gases is described by equations of states for quantities such as the phase-space density $\mathcal{D}$ (or the pressure $\mathcal{P}$, the entropy S, etc.). In general, for a fixed n-dimensional interaction parameter ($n_{3\mathrm{D}} a^3$, $\tilde{g}$ or γ), the equations of states depend on two intensive parameters, the chemical potential μ and the temperature T.

The 2D case is special, so let us discuss it in more detail. Because of the scale invariance, all 2D equations of state are functions of $\mu/k_B T$ (Dalibard 2017). For example, we can cast the Thomas-Fermi density in equation (1.2.4) into an equation of state for the phase-space density

$$\mathcal{D}_{\mathrm{TF}} \simeq n_{\mathrm{TF}} \lambda_{\mathrm{th}}^2 \simeq \frac{2\pi}{\tilde{g}} \frac{\mu}{k_B T} \tag{C.4.1}$$

using the local chemical potential $\mu(x,y) = \mu_0 - V_{2\mathrm{D}}(x,y)$. This $T = 0$ description is relevant when $\mathcal{D} \gg \mathcal{D}_c$, where $\mathcal{D}_c = \ln(360/\tilde{g})$ is the critical point of the superfluid transition (see above), calculated by Prokof'ev et al. (2002). In the opposite limit $\mathcal{D} \ll \mathcal{D}_c$, called the Hartree-Fock limit, the density of state can be calculated with a self-consistent equation

$$\mathcal{D}_{\mathrm{HF}} \simeq -\ln[1 - \exp(\beta\mu - \tilde{g}\mathcal{D}_{\mathrm{HF}}/\pi)]. \tag{C.4.2}$$

where $-\tilde{g}\mathcal{D}_{\mathrm{HF}}/\pi$ is a mean-field correction to the ideal gas. The general 2D equation of state $\mathcal{D} = \mathcal{D}(\mu/k_{\mathrm{B}}T)$ was calculated by Prokof'ev et al. (2002) with Monte-Carlo simulations. We obtain a numerical equation of state by interpolating their points with the two known limits[1]. The result is shown in figure C.1. Although trapped gases are not scale invariant, within the local density approximation, we consider a homogeneous system with potential $\mu = \mu_0 - V_{2\mathrm{D}}$ at every position (x, y), and can thus apply the 2D equation of state locally. In Chapter 5, we use this equation of state to analyze the 2D density distribution of 2D Bose gases.

C.5 Optical single-particle response of a saturated cloud

C.5.1 Single-atom saturation

If the intensity is comparable to the saturation intensity, the optical Bloch equations predict that the steady state probability of the atom to be in the excited state is

$$p_e = \frac{s/2}{1+s}. \tag{C.5.1}$$

Here we have introduced the saturation parameter s.

$$s = \frac{2\Omega^2}{\Gamma^2}\frac{1}{1+(4\delta^2/\Gamma^2)} = \frac{I}{I_{\mathrm{sat}}}\frac{1}{1+(4\delta^2/\Gamma^2)} = \frac{s_0}{1+y^2}. \tag{C.5.2}$$

where Ω is the Rabi frequency, $y \equiv 2\delta/\Gamma$ and $s_0 \equiv I/I_{\mathrm{sat}}$. The average induced-dipole moment is

$$\boldsymbol{d} = \epsilon_0 \frac{\alpha}{1+s}\boldsymbol{E}_{\mathrm{L}}, \tag{C.5.3}$$

and α is the electric polarizability in the small saturation linear response.

C.5.2 Refractive index approach

When $s \sim 1$, the 3D Beer-Lambert law for absorption is modified according to

$$\frac{\mathrm{d}I}{\mathrm{d}z} = -\frac{\rho\sigma}{1+s}I = -\frac{\rho\sigma_0}{1+s_0}\frac{1}{1+4\delta^2/(\Gamma\sqrt{1+s_0})^2}I \tag{C.5.4}$$

Even before integration along z, one can see that if the transition is saturated, less intensity will be absorbed and the linewidth will be broadened by a factor $\sqrt{1+I/I_{\mathrm{sat}}}$. In 3D, after integration, one finds

$$\frac{\sigma_0}{1+4\delta^2/\Gamma^2}\int \rho \mathrm{d}z = -\ln\left(\frac{I_{\mathrm{f}}}{I_{\mathrm{i}}}\right) + \frac{1}{1+4\delta^2/\Gamma^2}\frac{I_{\mathrm{i}}-I_{\mathrm{f}}}{I_{\mathrm{sat}}}. \tag{C.5.5}$$

Past experimental works on quasi-2D atomic gases (Hung et al. 2011a, Yefsah et al. 2011) used an analogous equation,

$$\mathrm{OD} \equiv n\sigma_0 = -\ln\left(\frac{I_{\mathrm{f}}}{I_{\mathrm{i}}}\right) + \frac{I_{\mathrm{i}}-I_{\mathrm{f}}}{I_{\mathrm{sat}}} = -\ln(T) + s_0(1-T), \tag{C.5.6}$$

when using high-absorption imaging.

[1] Quantum corrections are not included in these classical field calculations. However, they are small in our case and mostly change the slope of $\mathcal{D}(\alpha)$ on the percent level for our highest densities.

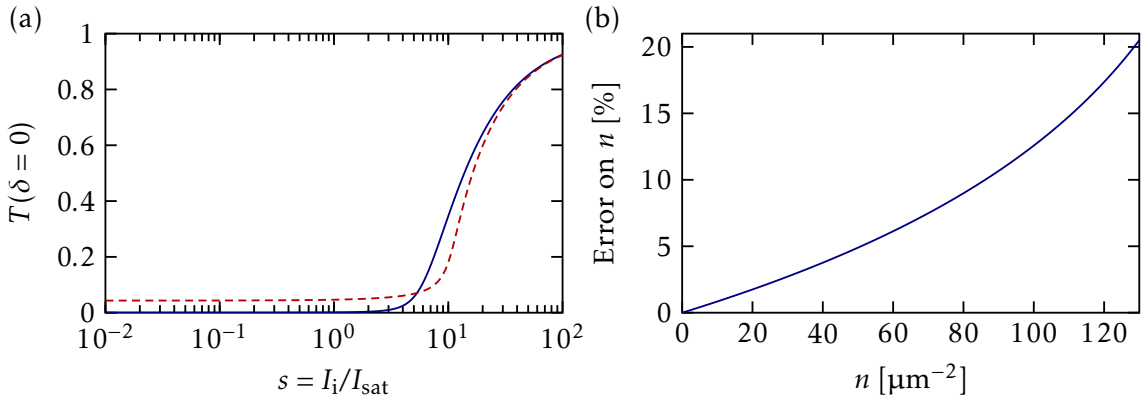

Figure C.2 (a) Transmission as a function of the saturation parameter s according to equation (C.5.6) (solid line) and equation (C.5.9) (dashed line). Calculation for a 2D gas with density $n = 100\,\mu\text{m}^{-2}$. (b) Error on density measurements if the (saturated) Beer-Lambert law is applied when the transmission is given by the 2D electromagnetic response. Calculation for $s = 20$.

C.5.3 Electromagnetic boundary conditions description

We now consider a strictly 2D gas and we follow the same electromagnetic boundary condition approach as in Chapter 6. For simplicity, for consider the resonant case $\delta = 0$. The dielectric susceptibility is modified by the saturation and we have

$$\eta = -2k^{-1}\frac{x}{\mathrm{i}(1+Ts_0)} \tag{C.5.7}$$

where Ts_0 is the actual saturation parameter in the gas, considering that the field in the gas is equal to the transmitted field (see Chapter 6). This yields

$$t = \frac{1}{1+x/(1+Ts_0)} \quad \text{and} \quad T = \frac{(1+Ts_0)^2}{(1+Ts_0+x)^2}. \tag{C.5.8}$$

This quadratic equation can be solved without difficulty and we find

$$n\sigma_0 = 2x = 2(1+Ts_0)\left(\sqrt{1+\frac{1-T}{T}}-1\right). \tag{C.5.9}$$

For a strictly 2D gas, this is the formula one should use to calibrate the atomic density for high intensity imaging. Figure C.2(a) compares the transmission for a 2D gas with density $n = 100\,\mu\text{m}^{-2}$ as a function of s_0 according to the 3D Beer-Lambert law and the 2D electromagnetic response. Figure C.2(b) shows the overestimation of the density from the Beer-Lambert law as a function of s_0 for a typical saturation parameter $s_0 = 20$. We find that the error is maximal at high densities, and reaches at most 20 %.

References

[Abanin et al. 2019] D. A. Abanin, E. Altman, I. Bloch & M. Serbyn; "Colloquium: Many-body localization, thermalization, and entanglement"; Rev. Mod. Phys. **91**, p. 021001 (2019). Cited on page 2

[Aikawa et al. 2012] K. Aikawa, A. Frisch, M. Mark, S. Baier, A. Rietzler, R. Grimm & F. Ferlaino; "Bose-Einstein Condensation of Erbium"; Phys. Rev. Lett. **108**, p. 210401 (2012). Cited on page 2

[Altman et al. 2004] E. Altman, E. Demler & M. D. Lukin; "Probing many-body states of ultracold atoms via noise correlations"; Phys. Rev. A **70**, p. 013603 (2004). Cited on page 85

[Anderson et al. 1995] M. H. Anderson, J. R. Ensher, M. R. Matthews, C. E. Wieman & E. A. Cornell; "Observation of Bose-Einstein Condensation in a Dilute Atomic Vapor"; Science **269**, pp. 198–201 (1995). Cited on page 1

[Araújo et al. 2016] M. O. Araújo, I. Krešić, R. Kaiser & W. Guerin; "Superradiance in a Large and Dilute Cloud of Cold Atoms in the Linear-Optics Regime"; Phys. Rev. Lett. **117**, p. 073002 (2016). 2 citations on pages 3 and 108

[Aspuru-Guzik et al. 2012] A. Aspuru-Guzik & P. Walther; "Photonic quantum simulators"; Nature Physics **8**, pp. 285–291 (2012). Cited on page 1

[Ates et al. 2012] C. Ates, B. Olmos, J. P. Garrahan & I. Lesanovsky; "Dynamical phases and intermittency of the dissipative quantum Ising model"; Phys. Rev. A **85**, p. 043620 (2012). Cited on page 3

[Bagnato et al. 1987] V. Bagnato, D. E. Pritchard & D. Kleppner; "Bose-Einstein condensation in an external potential"; Phys. Rev. A **35**, pp. 4354–4358 (1987). Cited on page 8

[Bakr et al. 2009] W. S. Bakr, J. I. Gillen, A. Peng, S. Fölling & M. Greiner; "A quantum gas microscope for detecting single atoms in a Hubbard-regime optical lattice"; Nature **462**, pp. 74–77 (2009). 3 citations on pages 2, 18, and 82

[Barontini et al. 2013] G. Barontini, R. Labouvie, F. Stubenrauch, A. Vogler, V. Guarrera & H. Ott; "Controlling the Dynamics of an Open Many-Body Quantum System with Localized Dissipation"; Phys. Rev. Lett. **110**, p. 035302 (2013). 2 citations on pages 3 and 52

[Barreiro et al. 2011] J. T. Barreiro, M. Müller, P. Schindler, D. Nigg, T. Monz, M. Chwalla, M. Hennrich, C. F. Roos, P. Zoller & R. Blatt; "An open-system quantum simulator with trapped ions"; Nature **470**, pp. 486–491 (2011). Cited on page 3

[Baumann et al. 2010] K. Baumann, C. Guerlin, F. Brennecke & T. Esslinger; "Dicke quantum phase transition with a superfluid gas in an optical cavity"; Nature **464**, pp. 1301–1306 (2010). Cited on page 3

[Berezinsky 1972] V. L. Berezinsky; "Destruction of Long-range Order in One-dimensional and Two-dimensional Systems Possessing a Continuous Symmetry Group. II. Quantum Systems." Sov. Phys. JETP **34**, p. 610 (1972). 2 citations on pages 2 and 12

[Bettles et al. 2016] R. J. Bettles, S. A. Gardiner & C. S. Adams; "Enhanced Optical Cross Section via Collective Coupling of Atomic Dipoles in a 2D Array"; Phys. Rev. Lett. **116**, p. 103602 (2016). Cited on page 108

[Blais et al. 2021] A. Blais, A. L. Grimsmo, S. M. Girvin & A. Wallraff; "Circuit quantum electrodynamics"; Rev. Mod. Phys. **93**, p. 025005 (2021). 2 citations on pages 3 and 51

[Blatt et al. 2012] R. Blatt & C. F. Roos; "Quantum simulations with trapped ions"; Nature Physics **8**, pp. 277–284 (2012). Cited on page 1

[Bloch et al. 2008] I. Bloch, J. Dalibard & W. Zwerger; "Many-body physics with ultracold gases"; Rev. Mod. Phys. **80**, pp. 885–964 (2008). 2 citations on pages 1 and 22

[Bloch et al. 2012] I. Bloch, J. Dalibard & S. Nascimbène; "Quantum simulations with ultracold quantum gases"; Nature Physics **8**, pp. 267–276 (2012). Cited on page 1

[Bockrath et al. 1999] M. Bockrath, D. H. Cobden, J. Lu, A. G. Rinzler, R. E. Smalley, L. Balents & P. L. McEuen; "Luttinger-liquid behaviour in carbon nanotubes"; Nature **397**, pp. 598–601 (1999). Cited on page 36

[Bons et al. 2016] P. C. Bons, R. de Haas, D. de Jong, A. Groot & P. van der Straten; "Quantum Enhancement of the Index of Refraction in a Bose-Einstein Condensate"; Phys. Rev. Lett. **116**, p. 173602 (2016). Cited on page 113

[Borkowski et al. 2017] M. Borkowski, A. A. Buchachenko, R. Ciuryło, P. S. Julienne, H. Yamada, Y. Kikuchi, K. Takahashi, Y. Takasu & Y. Takahashi; "Beyond-Born-Oppenheimer effects in sub-kHz-precision photoassociation spectroscopy of ytterbium atoms"; Phys. Rev. A **96**, p. 063405 (2017). Cited on page 27

[Born et al. 1999] M. Born & E. Wolf; *Principles of Optics: Electromagnetic Theory of Propagation, Interference and Diffraction of Light* (Cambridge University Press). (1999). 3 citations on pages 3, 109, and 112

[Bosch Aguilera et al. 2022] M. Bosch Aguilera, A. Ghermaoui, R. Vatré, R. Bouganne, J. Beugnon & F. Gerbier; "Adiabatic quantum Zeno dynamics of bosonic atom pairs with large inelastic losses"; Phys. Rev. A **106**, p. 053304 (2022). 2 citations on pages 52 and 127

[Bosch Aguilera 2019] M. Bosch Aguilera; *Coherence and relaxation of an optically-driven bosonic quantum gas: experiments with ultracold ytterbium atoms*; Ph.D. thesis; Sorbonne Université (2019). 2 citations on pages 22 and 131

[Bouganne et al. 2017] R. Bouganne, M. B. Aguilera, A. Dareau, E. Soave, J. Beugnon & F. Gerbier; "Clock spectroscopy of interacting bosons in deep optical lattices"; New Journal of Physics **19**, p. 113006 (2017). 2 citations on pages 23 and 127

[Bouganne et al. 2020] R. Bouganne, B. Aguilera, A. Ghermaoui, J. Beugnon & F. Gerbier; "Anomalous decay of coherence in a dissipative many-body system"; Nature Physics **16**, pp. 21–25 (2020). 7 citations on pages 55, 59, 60, 64, 73, 126, and 137

[Bouganne 2018] R. Bouganne; *Probing ultracold ytterbium in optical lattices with resonant light: from coherent control to dissipative dynamics*; Ph.D. thesis; Sorbonne Université (2018). 12 citations on pages 22, 26, 27, 30, 54, 57, 58, 59, 60, 65, 86, and 128

[Bradley et al. 1995] C. C. Bradley, C. A. Sackett, J. J. Tollett & R. G. Hulet; "Evidence of Bose-Einstein Condensation in an Atomic Gas with Attractive Interactions"; Phys. Rev. Lett. **75**, pp. 1687–1690 (1995). Cited on page 1

[Bromley et al. 2016] S. Bromley, B. Zhu, M. Bishof, X. Zhang, T. Bothwell, J. Schachenmayer, T. Nicholson, R. Kaiser, S. Yelin, M. Lukin, A. Rey & J. Ye; "Collective atomic scattering and motional effects in a dense coherent medium"; Nat. Commun. **7**, p. 11039 (2016). 4 citations on pages 2, 3, 108, and 122

[Büchler et al. 2003] H. P. Büchler, G. Blatter & W. Zwerger; "Commensurate-Incommensurate Transition of Cold Atoms in an Optical Lattice"; Phys. Rev. Lett. **90**, p. 130401 (2003). Cited on page 41

[Cai et al. 2013] Z. Cai & T. Barthel; "Algebraic versus Exponential Decoherence in Dissipative Many-Particle Systems"; Phys. Rev. Lett. **111**, p. 150403 (2013). Cited on page 50

[Capogrosso-Sansone et al. 2007] B. Capogrosso-Sansone, N. V. Prokof'ev & B. V. Svistunov; "Phase diagram and thermodynamics of the three-dimensional Bose-Hubbard model"; Phys. Rev. B **75**, p. 134302 (2007). Cited on page 33

[Capogrosso-Sansone et al. 2008] B. Capogrosso-Sansone, i. m. c. G. m. c. Söyler, N. Prokof'ev & B. Svistunov; "Monte Carlo study of the two-dimensional Bose-Hubbard model"; Phys. Rev. A **77**, p. 015602 (2008). Cited on page 33

[Carr et al. 2009] L. D. Carr, D. DeMille, R. V. Krems & J. Ye; "Cold and ultracold molecules: science, technology and applications"; New Journal of Physics **11**, p. 055049 (2009). Cited on page 1

[Castin et al. 1996] Y. Castin & R. Dum; "Bose-Einstein Condensates in Time Dependent Traps"; Phys. Rev. Lett. **77**, pp. 5315–5319 (1996). 3 citations on pages 22, 29, and 142

[Castin 2001] Y. Castin; "Bose-Einstein Condensates in Atomic Gases: Simple Theoretical Results"; in "Coherent atomic matter waves," , edited by R. Kaiser, C. Westbrook & F. Davidpp. 1–136 (Springer Berlin Heidelberg, Berlin, Heidelberg) (2001). Cited on page 8

[Castin 2004] Y. Castin; "Simple theoretical tools for low dimension Bose gases"; J. Phys. IV France **116**, pp. 89–132 (2004). Cited on page 12

[Cazalilla et al. 2011] M. A. Cazalilla, R. Citro, T. Giamarchi, E. Orignac & M. Rigol; "One dimensional bosons: From condensed matter systems to ultracold gases"; Rev. Mod. Phys. **83**, pp. 1405–1466 (2011). 3 citations on pages 2, 36, and 38

[Cazalilla 2004a] M. A. Cazalilla; "Bosonizing one-dimensional cold atomic gases"; Journal of Physics B: Atomic, Molecular and Optical Physics **37**, p. S1 (2004). 3 citations on pages 37, 38, and 39

[Cazalilla 2004b] M. A. Cazalilla; "Differences between the Tonks regimes in the continuum and on the lattice"; Phys. Rev. A **70**, p. 041604 (2004). Cited on page 41

[Chang 2003] A. M. Chang; "Chiral Luttinger liquids at the fractional quantum Hall edge"; Rev. Mod. Phys. **75**, pp. 1449–1505 (2003). Cited on page 36

[Chin et al. 2010] C. Chin, R. Grimm, P. Julienne & E. Tiesinga; "Feshbach resonances in ultracold gases"; Rev. Mod. Phys. **82**, pp. 1225–1286 (2010). Cited on page 2

[Chomaz et al. 2012] L. Chomaz, L. Corman, T. Yefsah, R. Desbuquois & J. Dalibard; "Absorption imaging of a quasi-two-dimensional gas: a multiple scattering analysis"; New Journal of Physics **14**, p. 055001 (2012). 2 citations on pages 112 and 113

[Chomaz et al. 2022] L. Chomaz, I. Ferrier-Barbut, F. Ferlaino, B. Laburthe-Tolra, B. L. Lev & T. Pfau; "Dipolar physics: a review of experiments with magnetic quantum gases"; Reports on Progress in Physics **86**, p. 026401 (2022). Cited on page 2

[Chomaz 2014] L. Chomaz; *Coherence and superfluidity of Bose gases in reduced dimensions : from harmonic traps to uniform fluids*; Theses; Ecole normale supérieure - ENS PARIS (2014). Cited on page 118

[Christodoulou et al. 2021] P. Christodoulou, M. Galka, N. Dogra, R. Lopes, J. Schmitt & Z. Hadzibabic; "Observation of first and second sound in a BKT superfluid"; Nature **594**, pp. 191–194 (2021). Cited on page 82

[Cohen-Tannoudji et al. 1992] C. Cohen-Tannoudji, J. Dupont-Roc & G. Grynberg; *Processus d'interaction entre photon et atomes* (EDP Sciences – CNRS Editions). (1992). 3 citations on pages 3, 50, and 53

[Cohen-Tannoudji et al. 1997] C. Cohen-Tannoudji, J. Dupont-Roc & G. Grynberg; *Photons and Atoms* (John Wiley and Sons, Ltd) (1997). Cited on page 112

[Condon et al. 2019] G. Condon, M. Rabault, B. Barrett, L. Chichet, R. Arguel, H. Eneriz-Imaz, D. Naik, A. Bertoldi, B. Battelier, P. Bouyer & A. Landragin; "All-Optical Bose-Einstein Condensates in Microgravity"; Phys. Rev. Lett. **123**, p. 240402 (2019). Cited on page 103

[Corman et al. 2017] L. Corman, J. L. Ville, R. Saint-Jalm, M. Aidelsburger, T. Bienaimé, S. Nascimbène, J. Dalibard & J. Beugnon; "Transmission of near-resonant light through a dense slab of cold atoms"; Phys. Rev. A **96**, p. 053629 (2017). 5 citations on pages 3, 109, 122, 123, and 124

[Daley 2014] A. J. Daley; "Quantum trajectories and open many-body quantum systems"; Advances in Physics **63**, pp. 77–149 (2014). Cited on page 50

[Dalfovo et al. 1999] F. Dalfovo, S. Giorgini, L. P. Pitaevskii & S. Stringari; "Theory of Bose-Einstein condensation in trapped gases"; Rev. Mod. Phys. **71**, pp. 463–512 (1999). Cited on page 1

[Dalibard et al. 1985] J. Dalibard & C. Cohen-Tannoudji; "Atomic motion in laser light: connection between semiclassical and quantum descriptions"; Journal of Physics B: Atomic and Molecular Physics **18**, p. 1661 (1985). 2 citations on pages 3 and 53

[Dalibard et al. 1989] J. Dalibard & C. Cohen-Tannoudji; "Laser cooling below the Doppler limit by polarization gradients: simple theoretical models"; J. Opt. Soc. Am. B **6**, pp. 2023–2045 (1989). Cited on page 23

[Dalibard et al. 2011] J. Dalibard, F. Gerbier, G. Juzeliūnas & P. Öhberg; "Colloquium: Artificial gauge potentials for neutral atoms"; Rev. Mod. Phys. **83**, pp. 1523–1543 (2011). Cited on page 2

[Dalibard 2017] J. Dalibard; "Fluides quantiques de basse dimension et transition Kosterlitz-Thouless"; (2017); Collège de France lectures. Cited on page 142

[Dalibard 2021] J. Dalibard; "Les interactions entre atomes dans les gaz quantiques: De l'universalité de van der Waals aux résonances de Fano-Feshbach"; (2021); Collège de France lectures. Cited on page 9

[Danshita et al. 2011] I. Danshita & A. Polkovnikov; "Superfluid-to-Mott-insulator transition in the one-dimensional Bose-Hubbard model for arbitrary integer filling factors"; Phys. Rev. A **84**, p. 063637 (2011). Cited on page 33

[Dareau 2015] A. Dareau; *Manipulation cohérente d'un condensat de Bose-Einstein d'ytterbium sur la transition horloge: de la spectroscopie aau magnétisme artificiel*; Ph.D. thesis; École Normale Supérieure - Paris (2015). 2 citations on pages 22 and 26

[Davis et al. 1995] K. B. Davis, M. O. Mewes, M. R. Andrews, N. J. van Druten, D. S. Durfee, D. M. Kurn & W. Ketterle; "Bose-Einstein Condensation in a Gas of Sodium Atoms"; Phys. Rev. Lett. **75**, pp. 3969–3973 (1995). Cited on page 1

[Denlinger et al. 1999] J. D. Denlinger, G.-H. Gweon, J. W. Allen, C. G. Olson, J. Marcus, C. Schlenker & L.-S. Hsu; "Non-Fermi-Liquid Single Particle Line Shape of the Quasi-One-Dimensional Non-CDW Metal $Li_{0.9}Mo_6O_{17}$: Comparison to the Luttinger Liquid"; Phys. Rev. Lett. **82**, pp. 2540–2543 (1999). Cited on page 36

[Denschlag et al. 2002] J. H. Denschlag, J. E. Simsarian, H. Häffner, C. McKenzie, A. Browaeys, D. Cho, K. Helmerson, S. L. Rolston & W. D. Phillips; "A Bose-Einstein condensate in an optical lattice"; Journal of Physics B: Atomic, Molecular and Optical Physics **35**, p. 3095 (2002). Cited on page 131

[Dzuba et al. 2010] V. A. Dzuba & A. Derevianko; "Dynamic polarizabilities and related properties of clock states of the ytterbium atom"; Journal of Physics B: Atomic, Molecular and Optical Physics **43**, p. 074011 (2010). 2 citations on pages 22 and 24

[Edwards et al. 2005] M. Edwards, L. M. DeBeer, M. Demenikov, J. Galbreath, T. J. Mahaney, B. Nelsen & C. W. Clark; "A hybrid Lagrangian variational method for Bose–Einstein condensates in optical lattices"; Journal of Physics B: Atomic, Molecular and Optical Physics **38**, p. 363 (2005). Cited on page 140

[Einstein 1905] A. Einstein; "Über einen die Erzeugung und Verwandlung des Lichtes betreffenden heuristischen Gesichtspunkt"; Annalen der Physik **322**, pp. 132–148 (1905). Cited on page 2

[Einstein 1924] A. Einstein; "Quantentheorie des einatomigen idealen Gases"; in "Sitzungsberichte der Preussischen Akademie der Wissenschaften," pp. 261–267 (1924). 2 citations on pages 1 and 8

[Ejima et al. 2011] S. Ejima, H. Fehske & F. Gebhard; "Dynamic properties of the one-dimensional Bose-Hubbard model"; Europhysics Letters **93**, p. 30002 (2011). Cited on page 33

[Elstner et al. 1999] N. Elstner & H. Monien; "A numerical exact solution of the Bose-Hubbard model"; (1999). https://arxiv.org/abs/cond-mat/9905367. Cited on page 33

[Endres et al. 2011] M. Endres, M. Cheneau, T. Fukuhara, C. Weitenberg, P. Schauss, C. Gross, L. Mazza, M. C. Bañuls, L. Pollet, I. Bloch & S. Kuhr; "Observation of Correlated Particle-Hole Pairs and String Order in Low-Dimensional Mott Insulators"; Science **334**, pp. 200–203 (2011). Cited on page 36

[Fang et al. 2013] H. Fang, H. A. Bechtel, E. Plis, M. C. Martin, S. Krishna, E. Yablonovitch & A. Javey; "Quantum of optical absorption in two-dimensional semiconductors"; Proceedings of the National Academy of Sciences **110**, pp. 11688–11691 (2013). Cited on page 111

[Feynman 1982] R. P. Feynman; "Simulating physics with computers"; International Journal of Theoretical Physics **21**, pp. 467–488 (1982). Cited on page 1

[Fölling et al. 2005] S. Fölling, F. Gerbier, A. Widera, O. Mandel, T. Gericke & I. Bloch; "Spatial quantum noise interferometry in expanding ultracold atom clouds"; Nature **434**, pp. 481–484 (2005). Cited on page 85

[Freericks et al. 1994] J. K. Freericks & H. Monien; "Phase diagram of the Bose-Hubbard Model"; Europhysics Letters **26**, p. 545 (1994). Cited on page 39

[Gadway et al. 2009] B. Gadway, D. Pertot, R. Reimann, M. G. Cohen & D. Schneble; "Analysis of Kapitza-Dirac diffraction patterns beyond the Raman-Nath regime"; Opt. Express **17**, pp. 19173–19180 (2009). Cited on page 131

[Gangardt et al. 2006] D. M. Gangardt & G. V. Shlyapnikov; "Off-diagonal correlations of lattice impenetrable bosons in one dimension"; New Journal of Physics **8**, p. 167 (2006). Cited on page 133

[Geier et al. 2022] K. T. Geier & P. Hauke; "From Non-Hermitian Linear Response to Dynamical Correlations and Fluctuation-Dissipation Relations in Quantum Many-Body Systems"; PRX Quantum **3**, p. 030308 (2022). Cited on page 73

[Gemelke et al. 2009] N. Gemelke, X. Zhang, C.-L. Hung & C. Chin; "In situ observation of incompressible Mott-insulating domains in ultracold atomic gases"; Nature **460**, pp. 995–998 (2009). Cited on page 82

[Gerbier et al. 2010] F. Gerbier & J. Dalibard; "Gauge fields for ultracold atoms in optical superlattices"; New Journal of Physics **12**, p. 033007 (2010). 2 citations on pages 2 and 127

[Gerbier et al. 2008] F. Gerbier, S. Trotzky, S. Fölling, U. Schnorrberger, J. D. Thompson, A. Widera, I. Bloch, L. Pollet, M. Troyer, B. Capogrosso-Sansone, N. V. Prokof'ev & B. V. Svistunov; "Expansion of a Quantum Gas Released from an Optical Lattice"; Phys. Rev. Lett. **101**, p. 155303 (2008). 2 citations on pages 22 and 29

[Gerbier 2007] F. Gerbier; "Boson Mott Insulators at Finite Temperatures"; Phys. Rev. Lett. **99**, p. 120405 (2007). Cited on page 100

[Ghermaoui 2020] A. Ghermaoui; *Many-body dynamics of laser-driven ultracold atoms in optical lattices: from strong interactions to the quantum Zeno regime in a bosonic quantum gas*; Ph.D. thesis; Sorbonne Université (2020). 4 citations on pages 3, 22, 52, and 127

[Giamarchi 2003] T. Giamarchi; *Quantum Physics in One Dimension* (Oxford University Press) (2003). 3 citations on pages 2, 68, and 75

[Giorgini et al. 2008] S. Giorgini, L. P. Pitaevskii & S. Stringari; "Theory of ultracold atomic Fermi gases"; Rev. Mod. Phys. **80**, pp. 1215–1274 (2008). Cited on page 1

[Girardeau 1960] M. Girardeau; "Relationship between systems of impenetrable bosons and fermions in one dimension"; Journal of Mathematical Physics **1**, pp. 516–523 (1960). Cited on page 132

[Glicenstein et al. 2020] A. Glicenstein, G. Ferioli, N. Šibalić, L. Brossard, I. Ferrier-Barbut & A. Browaeys; "Collective Shift in Resonant Light Scattering by a One-Dimensional Atomic Chain"; Phys. Rev. Lett. **124**, p. 253602 (2020). Cited on page 108

[Greiner et al. 2002] M. Greiner, O. Mandel, T. Esslinger, T. Hänsch & I. Bloch; "Quantum phase transition from a superfluid to a Mott insulator in a gas of ultracold atoms"; Nature **415**, pp. 39–44 (2002). 3 citations on pages 2, 18, and 33

[Grimm et al. 2000] R. Grimm, M. Weidemüller & Y. B. Ovchinnikov; "Optical Dipole Traps for Neutral Atoms"; ; pp. 95–170 (Academic Press) (2000). 3 citations on pages 22, 24, and 100

[Gross et al. 2017] C. Gross & I. Bloch; "Quantum simulations with ultracold atoms in optical lattices"; Science **357**, pp. 995–1001 (2017). Cited on page 2

[Guerin et al. 2016] W. Guerin, M. O. Araújo & R. Kaiser; "Subradiance in a Large Cloud of Cold Atoms"; Phys. Rev. Lett. **116**, p. 083601 (2016). 2 citations on pages 3 and 108

[Guerin et al. 2017] W. Guerin, M. Rouabah & R. Kaiser; "Light interacting with atomic ensembles: collective, cooperative and mesoscopic effects"; Journal of Modern Optics **64**, pp. 895–907 (2017). 2 citations on pages 3 and 108

[Hadzibabic et al. 2006] Z. Hadzibabic, P. Krüger, M. Cheneau, B. Battelier & J. Dalibard; "Berezinskii–Kosterlitz–Thouless crossover in a trapped atomic gas"; Nature **441**, pp. 1118–1121 (2006). Cited on page 2

[Haldane 1981a] F. D. M. Haldane; "Effective Harmonic-Fluid Approach to Low-Energy Properties of One-Dimensional Quantum Fluids"; Phys. Rev. Lett. **47**, pp. 1840–1843 (1981). Cited on page 36

[Haldane 1981b] F. D. M. Haldane; "'Luttinger liquid theory' of one-dimensional quantum fluids. I. Properties of the Luttinger model and their extension to the general 1D interacting spinless Fermi gas"; Journal of Physics C: Solid State Physics **14**, p. 2585 (1981). Cited on page 36

[Haller et al. 2010] E. Haller, R. Hart, M. J. Mark, J. G. Danzl, L. Reichsöllner, M. Gustavsson, M. Dalmonte, G. Pupillo & H.-C. Nägerl; "Pinning quantum phase transition for a Luttinger liquid of strongly interacting bosons"; Nature **466**, pp. 597–600 (2010). Cited on page 41

[Haroche et al. 2006] S. Haroche & J.-M. Raimond; *Exploring the Quantum: Atoms, Cavities, and Photons* (Oxford University Press). (2006). 3 citations on pages 2, 50, and 51

[Harper 1955] P. G. Harper; "Single Band Motion of Conduction Electrons in a Uniform Magnetic Field"; Proceedings of the Physical Society. Section A **68**, p. 874 (1955). Cited on page 127

[Hasan et al. 2010] M. Z. Hasan & C. L. Kane; "Colloquium: Topological insulators"; Rev. Mod. Phys. **82**, pp. 3045–3067 (2010). Cited on page 1

[Hauke et al. 2016] P. Hauke, M. Heyl, L. Tagliacozzo & P. Zoller; "Measuring multipartite entanglement through dynamic susceptibilities"; Nature Physics **12**, pp. 778–782 (2016). Cited on page 73

[Henriet et al. 2019] L. Henriet, J. S. Douglas, D. E. Chang & A. Albrecht; "Critical open-system dynamics in a one-dimensional optical-lattice clock"; Phys. Rev. A **99**, p. 023802 (2019). Cited on page 50

[Hofferberth et al. 2007] S. Hofferberth, I. Lesanovsky, B. Fischer, T. Schumm & J. Schmiedmayer; "Non-equilibrium coherence dynamics in one-dimensional Bose gases"; Nature **449**, pp. 324–327 (2007). Cited on page 36

[Hofferberth et al. 2008] S. Hofferberth, I. Lesanovsky, T. Schumm, A. Imambekov, V. Gritsev, E. Demler & J. Schmiedmayer; "Probing quantum and thermal noise in an interacting many-body system"; Nature Physics **4**, pp. 489–495 (2008). Cited on page 36

[Hohenberg 1967] P. C. Hohenberg; "Existence of Long-Range Order in One and Two Dimensions"; Phys. Rev. **158**, pp. 383–386 (1967). Cited on page 11

[Honda et al. 1999] K. Honda, Y. Takahashi, T. Kuwamoto, M. Fujimoto, K. Toyoda, K. Ishikawa & T. Yabuzaki; "Magneto-optical trapping of Yb atoms and a limit on the branching ratio of the $^1P_1$ state"; Phys. Rev. A **59**, pp. R934–R937 (1999). Cited on page 25

[Houck et al. 2012] A. A. Houck, H. E. Türeci & J. Koch; "On-chip quantum simulation with superconducting circuits"; Nature Physics **8**, pp. 292–299 (2012). Cited on page 1

[Hung et al. 2011a] C.-L. Hung, X. Zhang, N. Gemelke & C. Chin; "Observation of scale invariance and universality in two-dimensional Bose gases"; Nature **470**, pp. 236–239 (2011). 4 citations on pages 98, 111, 120, and 143

[Hung et al. 2011b] C.-L. Hung, X. Zhang, L.-C. Ha, S.-K. Tung, N. Gemelke & C. Chin; "Extracting density–density correlations from in situ images of atomic quantum gases"; New Journal of Physics **13**, p. 075019 (2011). Cited on page 85

[Itano et al. 1990] W. M. Itano, D. J. Heinzen, J. J. Bollinger & D. J. Wineland; "Quantum Zeno effect"; Phys. Rev. A **41**, pp. 2295–2300 (1990). Cited on page 3

[Jaksch et al. 2003] D. Jaksch & P. Zoller; "Creation of effective magnetic fields in optical lattices: the Hofstadter butterfly for cold neutral atoms"; New Journal of Physics **5**, p. 56 (2003). 2 citations on pages 2 and 127

[Jaksch et al. 1998] D. Jaksch, C. Bruder, J. I. Cirac, C. W. Gardiner & P. Zoller; "Cold Bosonic Atoms in Optical Lattices"; Phys. Rev. Lett. **81**, pp. 3108–3111 (1998). 2 citations on pages 2 and 33

[Jeltes et al. 2007] T. Jeltes, J. M. McNamara, W. Hogervorst, W. Vassen, V. Krachmalnicoff, M. Schellekens, A. Perrin, H. Chang, D. Boiron, A. Aspect & C. I. Westbrook; "Comparison of the Hanbury Brown–Twiss effect for bosons and fermions"; Nature **445**, pp. 402–405 (2007). Cited on page 12

[Jennewein et al. 2016] S. Jennewein, M. Besbes, N. J. Schilder, S. D. Jenkins, C. Sauvan, J. Ruostekoski, J.-J. Greffet, Y. R. P. Sortais & A. Browaeys; "Coherent Scattering of Near-Resonant Light by a Dense Microscopic Cold Atomic Cloud"; Phys. Rev. Lett. **116**, p. 233601 (2016). Cited on page 108

[Jennewein et al. 2018] S. Jennewein, L. Brossard, Y. R. P. Sortais, A. Browaeys, P. Cheinet, J. Robert & P. Pillet; "Coherent scattering of near-resonant light by a dense, microscopic cloud of cold two-level atoms: Experiment versus theory"; Phys. Rev. A **97**, p. 053816 (2018). 2 citations on pages 3 and 108

[Kapitza et al. 1933] P. L. Kapitza & P. A. M. Dirac; "The reflection of electrons from standing light waves"; Mathematical Proceedings of the Cambridge Philosophical Society **29**, p. 297–300 (1933). Cited on page 131

[Keaveney et al. 2012] J. Keaveney, A. Sargsyan, U. Krohn, I. G. Hughes, D. Sarkisyan & C. S. Adams; "Cooperative Lamb Shift in an Atomic Vapor Layer of Nanometer Thickness"; Phys. Rev. Lett. **108**, p. 173601 (2012). Cited on page 108

[Ketterle et al. 1999] W. Ketterle, D. S. Durfee & D. M. Stamper-Kurn; "Making, probing and understanding Bose-Einstein condensates"; (1999). https://arxiv.org/abs/cond-mat/9904034. 2 citations on pages 22 and 28

[Kiely et al. 2022] T. G. Kiely & E. J. Mueller; "Superfluidity in the one-dimensional Bose-Hubbard model"; Phys. Rev. B **105**, p. 134502 (2022). Cited on page 38

[Kinoshita et al. 2004] T. Kinoshita, T. Wenger & D. S. Weiss; "Observation of a One-Dimensional Tonks-Girardeau Gas"; Science **305**, pp. 1125–1128 (2004). Cited on page 36

[Kitagawa et al. 2008] M. Kitagawa, K. Enomoto, K. Kasa, Y. Takahashi, R. Ciuryło, P. Naidon & P. S. Julienne; "Two-color photoassociation spectroscopy of ytterbium atoms and the precise determinations of *s*-wave scattering lengths"; Phys. Rev. A **77**, p. 012719 (2008). Cited on page 27

[Klanjšek et al. 2008] M. Klanjšek, H. Mayaffre, C. Berthier, M. Horvatić, B. Chiari, O. Piovesana, P. Bouillot, C. Kollath, E. Orignac, R. Citro & T. Giamarchi; "Controlling Luttinger Liquid Physics in Spin Ladders under a Magnetic Field"; Phys. Rev. Lett. **101**, p. 137207 (2008). Cited on page 36

[Kosterlitz et al. 1973] J. M. Kosterlitz & D. J. Thouless; "Ordering, metastability and phase transitions in two-dimensional systems"; Journal of Physics C: Solid State Physics **6**, p. 1181 (1973). 2 citations on pages 2 and 12

[Kubo 1957] R. Kubo; "Statistical-Mechanical Theory of Irreversible Processes. I. General Theory and Simple Applications to Magnetic and Conduction Problems"; Journal of the Physical Society of Japan **12**, pp. 570–586 (1957). Cited on page 70

[Kühner et al. 1998] T. D. Kühner & H. Monien; "Phases of the one-dimensional Bose-Hubbard model"; Phys. Rev. B **58**, pp. R14741–R14744 (1998). 3 citations on pages 17, 33, and 39

[Kühner et al. 2000] T. D. Kühner, S. R. White & H. Monien; "One-dimensional Bose-Hubbard model with nearest-neighbor interaction"; Phys. Rev. B **61**, pp. 12474–12489 (2000). 2 citations on pages 39 and 41

[Laurent et al. 2017] S. Laurent, M. Pierce, M. Delehaye, T. Yefsah, F. Chevy & C. Salomon; "Connecting Few-Body Inelastic Decay to Quantum Correlations in a Many-Body System: A Weakly Coupled Impurity in a Resonant Fermi Gas"; Phys. Rev. Lett. **118**, p. 103403 (2017). Cited on page 73

[Lenard 1964] A. Lenard; "Momentum Distribution in the Ground State of the One-Dimensional System of Impenetrable Bosons"; Journal of Mathematical Physics **5**, pp. 930–943 (1964). Cited on page 132

[Lett et al. 1988] P. D. Lett, R. N. Watts, C. I. Westbrook, W. D. Phillips, P. L. Gould & H. J. Metcalf; "Observation of Atoms Laser Cooled below the Doppler Limit"; Phys. Rev. Lett. **61**, pp. 169–172 (1988). Cited on page 50

[Lieb et al. 1961] E. Lieb, T. Schultz & D. Mattis; "Two soluble models of an antiferromagnetic chain"; Annals of Physics **16**, pp. 407–466 (1961). Cited on page 132

[Lu et al. 2011] M. Lu, N. Q. Burdick, S. H. Youn & B. L. Lev; "Strongly Dipolar Bose-Einstein Condensate of Dysprosium"; Phys. Rev. Lett. **107**, p. 190401 (2011). Cited on page 1

[Ludlow et al. 2015] A. D. Ludlow, M. M. Boyd, J. Ye, E. Peik & P. O. Schmidt; "Optical atomic clocks"; Rev. Mod. Phys. **87**, pp. 637–701 (2015). Cited on page 23

[Luttinger 1963] J. M. Luttinger; "An Exactly Soluble Model of a Many-Fermion System"; Journal of Mathematical Physics **4**, pp. 1154–1162 (1963). Cited on page 36

[Mancini et al. 2015] M. Mancini, G. Pagano, G. Cappellini, L. Livi, M. Rider, J. Catani, C. Sias, P. Zoller, M. Inguscio, M. Dalmonte & L. Fallani; "Observation of chiral edge states with neutral fermions in synthetic Hall ribbons"; Science **349**, pp. 1510–1513 (2015). Cited on page 127

[McDonald et al. 2019] M. McDonald, J. Trisnadi, K.-X. Yao & C. Chin; "Superresolution Microscopy of Cold Atoms in an Optical Lattice"; Phys. Rev. X **9**, p. 021001 (2019). Cited on page 82

[Meir et al. 2014] Z. Meir, O. Schwartz, E. Shahmoon, D. Oron & R. Ozeri; "Cooperative Lamb Shift in a Mesoscopic Atomic Array"; Phys. Rev. Lett. **113**, p. 193002 (2014). Cited on page 108

[Mermin et al. 1966] N. D. Mermin & H. Wagner; "Absence of Ferromagnetism or Antiferromagnetism in One- or Two-Dimensional Isotropic Heisenberg Models"; Phys. Rev. Lett. **17**, pp. 1133–1136 (1966). Cited on page 11

[Metcalf et al. 1999] H. J. Metcalf & P. van der Straten; *Laser Cooling and Trapping* (Springer-Verlag New-York). (1999). 2 citations on pages 22 and 52

[Misra et al. 1977] B. Misra & E. C. G. Sudarshan; "The Zeno's paradox in quantum theory"; Journal of Mathematical Physics **18**, pp. 756–763 (1977). Cited on page 3

[Mora et al. 2003] C. Mora & Y. Castin; "Extension of Bogoliubov theory to quasicondensates"; Phys. Rev. A **67**, p. 053615 (2003). Cited on page 12

[Morice et al. 1995] O. Morice, Y. Castin & J. Dalibard; "Refractive index of a dilute Bose gas"; Phys. Rev. A **51**, pp. 3896–3901 (1995). 4 citations on pages 3, 108, 112, and 113

[Müller et al. 2012] M. Müller, S. Diehl, G. Pupillo & P. Zoller; "Engineered Open Systems and Quantum Simulations with Atoms and Ions"; in "Advances in Atomic, Molecular, and Optical Physics," , *Advances In Atomic, Molecular, and Optical Physics*, volume 61, edited by P. Berman, E. Arimondo & C. Lin ; pp. 1–80 (Academic Press) (2012). Cited on page 50

[Nair et al. 2008] R. R. Nair, P. Blake, A. N. Grigorenko, K. S. Novoselov, T. J. Booth, T. Stauber, N. M. R. Peres & A. K. Geim; "Fine Structure Constant Defines Visual Transparency of Graphene"; Science **320**, pp. 1308–1308 (2008). Cited on page 111

[Ockeloen et al. 2010] C. F. Ockeloen, A. F. Tauschinsky, R. J. C. Spreeuw & S. Whitlock; "Detection of small atom numbers through image processing"; Phys. Rev. A **82**, p. 061606 (2010). 2 citations on pages 22 and 30

[O'Dell et al. 2000] D. O'Dell, S. Giovanazzi, G. Kurizki & V. M. Akulin; "Bose-Einstein Condensates with $1/r$ Interatomic Attraction: Electromagnetically Induced "Gravity""; Phys. Rev. Lett. **84**, pp. 5687–5690 (2000). Cited on page 55

[Olshanii 1998] M. Olshanii; "Atomic Scattering in the Presence of an External Confinement and a Gas of Impenetrable Bosons"; Phys. Rev. Lett. **81**, pp. 938–941 (1998). Cited on page 11

[Ovchinnikov et al. 1999] Y. B. Ovchinnikov, J. H. Müller, M. R. Doery, E. J. D. Vredenbregt, K. Helmerson, S. L. Rolston & W. D. Phillips; "Diffraction of a Released Bose-Einstein Condensate by a Pulsed Standing Light Wave"; Phys. Rev. Lett. **83**, pp. 284–287 (1999). Cited on page 131

[Ovchinnikov 2009] A. Ovchinnikov; "Fisher–Hartwig conjecture and the correlators in the impenetrable Bose gas"; Physics Letters A **373**, pp. 305–307 (2009). Cited on page 132

[Pan et al. 2020] L. Pan, X. Chen, Y. Chen & H. Zhai; "Non-Hermitian linear response theory"; Nat. Phys. (2020). 6 citations on pages v, 67, 68, 70, 73, and 77

[Paredes et al. 2004] B. Paredes, A. Widera, V. Murg, O. Mandel, S. Fölling, I. Cirac, G. V. Shlyapnikov, T. W. Hansch & I. Bloch; "Tonks-Girardeau gas of ultracold atoms in an optical lattice"; Nature **429**, pp. 277–281 (2004). 4 citations on pages 36, 44, 134, and 135

[Pedri et al. 2001] P. Pedri, L. Pitaevskii, S. Stringari, C. Fort, S. Burger, F. S. Cataliotti, P. Maddaloni, F. Minardi & M. Inguscio; "Expansion of a Coherent Array of Bose-Einstein Condensates"; Phys. Rev. Lett. **87**, p. 220401 (2001). Cited on page 60

[Pellegrino et al. 2014] J. Pellegrino, R. Bourgain, S. Jennewein, Y. R. P. Sortais, A. Browaeys, S. D. Jenkins & J. Ruostekoski; "Observation of Suppression of Light Scattering Induced by Dipole-Dipole Interactions in a Cold-Atom Ensemble"; Phys. Rev. Lett. **113**, p. 133602 (2014). Cited on page 108

[Penrose et al. 1956] O. Penrose & L. Onsager; "Bose-Einstein Condensation and Liquid Helium"; Phys. Rev. **104**, pp. 576–584 (1956). Cited on page 11

[Perczel et al. 2017] J. Perczel, J. Borregaard, D. E. Chang, H. Pichler, S. F. Yelin, P. Zoller & M. D. Lukin; "Topological Quantum Optics in Two-Dimensional Atomic Arrays"; Phys. Rev. Lett. **119**, p. 023603 (2017). Cited on page 128

[Pérez-García et al. 1996] V. M. Pérez-García, H. Michinel, J. I. Cirac, M. Lewenstein & P. Zoller; "Low Energy Excitations of a Bose-Einstein Condensate: A Time-Dependent Variational Analysis"; Phys. Rev. Lett. **77**, pp. 5320–5323 (1996). Cited on page 140

[Petrov et al. 2001] D. S. Petrov & G. V. Shlyapnikov; "Interatomic collisions in a tightly confined Bose gas"; Phys. Rev. A **64**, p. 012706 (2001). Cited on page 11

[Petrov et al. 2000] D. S. Petrov, M. Holzmann & G. V. Shlyapnikov; "Bose-Einstein Condensation in Quasi-2D Trapped Gases"; Phys. Rev. Lett. **84**, pp. 2551–2555 (2000). Cited on page 11

[Petrov et al. 2004] D. Petrov, D. Gangardt & G. Shlyapnikov; "Low-dimensional trapped gases"; arXiv (2004). 2 citations on pages 2 and 43

[Phillips et al. 1982] W. D. Phillips & H. Metcalf; "Laser Deceleration of an Atomic Beam"; Phys. Rev. Lett. **48**, pp. 596–599 (1982). 2 citations on pages 25 and 50

[Pichler et al. 2010] H. Pichler, A. J. Daley & P. Zoller; "Nonequilibrium dynamics of bosonic atoms in optical lattices: Decoherence of many-body states due to spontaneous emission"; Phys. Rev. A **82**, p. 063605 (2010). Cited on page 53

[Pitaevskii et al. 2003] L. Pitaevskii & S. Stringari; *Bose-Einstein condensation* (Oxford University Press). (2003). Cited on page 1

[Poletti et al. 2012] D. Poletti, J.-S. Bernier, A. Georges & C. Kollath; "Interaction-Induced Impeding of Decoherence and Anomalous Diffusion"; Phys. Rev. Lett. **109**, p. 045302 (2012). Cited on page 55

[Poletti et al. 2013] D. Poletti, P. Barmettler, A. Georges & C. Kollath; "Emergence of Glasslike Dynamics for Dissipative and Strongly Interacting Bosons"; Phys. Rev. Lett. **111**, p. 195301 (2013). 8 citations on pages 50, 55, 56, 57, 58, 64, 65, and 126

[Pollet 2012] L. Pollet; "Recent developments in quantum Monte Carlo simulations with applications for cold gases"; Reports on Progress in Physics **75**, p. 094501 (2012). Cited on page 17

[Prokof'ev et al. 2002] N. Prokof'ev & B. Svistunov; "Two-dimensional weakly interacting Bose gas in the fluctuation region"; Phys. Rev. A **66**, p. 043608 (2002). 4 citations on pages 82, 99, 142, and 143

[Raab et al. 1987] E. L. Raab, M. Prentiss, A. Cable, S. Chu & D. E. Pritchard; "Trapping of Neutral Sodium Atoms with Radiation Pressure"; Phys. Rev. Lett. **59**, pp. 2631–2634 (1987). Cited on page 50

[Raimond et al. 2001] J. M. Raimond, M. Brune & S. Haroche; "Manipulating quantum entanglement with atoms and photons in a cavity"; Rev. Mod. Phys. **73**, pp. 565–582 (2001). 2 citations on pages 3 and 51

[Raitzsch et al. 2009] U. Raitzsch, R. Heidemann, H. Weimer, B. Butscher, P. Kollmann, R. Löw, H. P. Büchler & T. Pfau; "Investigation of dephasing rates in an interacting Rydberg gas"; New Journal of Physics **11**, p. 055014 (2009). Cited on page 3

[Rigol 2005] M. Rigol; "Finite-temperature properties of hard-core bosons confined on one-dimensional optical lattices"; Phys. Rev. A **72**, p. 063607 (2005). 2 citations on pages 133 and 134

[Roof et al. 2016] S. J. Roof, K. J. Kemp, M. D. Havey & I. M. Sokolov; "Observation of Single-Photon Superradiance and the Cooperative Lamb Shift in an Extended Sample of Cold Atoms"; Phys. Rev. Lett. **117**, p. 073003 (2016). 2 citations on pages 3 and 108

[Rossini et al. 2021] D. Rossini, A. Ghermaoui, M. B. Aguilera, R. Vatré, R. Bouganne, J. Beugnon, F. Gerbier & L. Mazza; "Strong correlations in lossy one-dimensional quantum gases: From the quantum Zeno effect to the generalized Gibbs ensemble"; Phys. Rev. A **103**, p. L060201 (2021). 2 citations on pages 52 and 127

[Roy et al. 2016] R. Roy, A. Green, R. Bowler & S. Gupta; "Rapid cooling to quantum degeneracy in dynamically shaped atom traps"; Phys. Rev. A **93**, p. 043403 (2016). Cited on page 103

[Rui et al. 2020] J. Rui, D. Wei, A. Rubio-Abadal, S. Hollerith, J. Zeiher, D. M. Stamper-Kurn, C. Gross & I. Bloch; "A subradiant optical mirror formed by a single structured atomic layer"; Nature **583**, pp. 369–374 (2020). 3 citations on pages 108, 124, and 128

[Saint-Jalm et al. 2019] R. Saint-Jalm, P. C. M. Castilho, E. Le Cerf, B. Bakkali-Hassani, J.-L. Ville, S. Nascimbene, J. Beugnon & J. Dalibard; "Dynamical Symmetry and Breathers in a Two-Dimensional Bose Gas"; Phys. Rev. X **9**, p. 021035 (2019). Cited on page 11

[Scholl 2014] M. Scholl; *Probing an ytterbium Bose-Einstein condensate using an ultranarrow optical line : towards artificial gauge fields in optical lattices*; Ph.D. thesis; Paris 6 (2014). 2 citations on pages 22 and 27

[Schwartz et al. 1998] A. Schwartz, M. Dressel, G. Grüner, V. Vescoli, L. Degiorgi & T. Giamarchi; "On-chain electrodynamics of metallic $(TMTSF)_2X$ salts: Observation of Tomonaga-Luttinger liquid response"; Phys. Rev. B **58**, pp. 1261–1271 (1998). Cited on page 36

[Shahmoon et al. 2017] E. Shahmoon, D. S. Wild, M. D. Lukin & S. F. Yelin; "Cooperative Resonances in Light Scattering from Two-Dimensional Atomic Arrays"; Phys. Rev. Lett. **118**, p. 113601 (2017). 2 citations on pages 108 and 128

[Sherson et al. 2010] J. Sherson, C. Weitenberg, M. Endres, M. Cheneau, I. Bloch & S. Kuhr; "Single-atom-resolved fluorescence imaging of an atomic Mott insulator"; Nature **467**, pp. 68–72 (2010). 3 citations on pages 2, 18, and 82

[Sieberer et al. 2016] L. M. Sieberer, M. Buchhold & S. Diehl; "Keldysh field theory for driven open quantum systems"; Reports on Progress in Physics **79**, p. 096001 (2016). Cited on page 3

[Skipetrov et al. 2015] S. E. Skipetrov & I. M. Sokolov; "Magnetic-Field-Driven Localization of Light in a Cold-Atom Gas"; Phys. Rev. Lett. **114**, p. 053902 (2015). Cited on page 124

[Soave 2016] E. Soave; *Production and High-Resolution Imaging of a quantum degenerate Ytterbium atomic gas*; Università degli studi di Pisa (2016). Cited on page 83

[Spielman et al. 2007] I. B. Spielman, W. D. Phillips & J. V. Porto; "Mott-Insulator Transition in a Two-Dimensional Atomic Bose Gas"; Phys. Rev. Lett. **98**, p. 080404 (2007). Cited on page 33

[Sponselee et al. 2018] K. Sponselee, L. Freystatzky, B. Abeln, M. Diem, B. Hundt, A. Kochanke, T. Ponath, B. Santra, L. Mathey, K. Sengstock & C. Becker; "Dynamics of ultracold quantum gases in the dissipative Fermi–Hubbard model"; Quantum Science and Technology **4**, p. 014002 (2018). 2 citations on pages 3 and 52

[Stellmer et al. 2009] S. Stellmer, M. K. Tey, B. Huang, R. Grimm & F. Schreck; "Bose-Einstein Condensation of Strontium"; Phys. Rev. Lett. **103**, p. 200401 (2009). Cited on page 1

[Stöferle et al. 2004] T. Stöferle, H. Moritz, C. Schori, M. Köhl & T. Esslinger; "Transition from a Strongly Interacting 1D Superfluid to a Mott Insulator"; Phys. Rev. Lett. **92**, p. 130403 (2004). Cited on page 33

[Störzer et al. 2006] M. Störzer, P. Gross, C. M. Aegerter & G. Maret; "Observation of the Critical Regime Near Anderson Localization of Light"; Phys. Rev. Lett. **96**, p. 063904 (2006). Cited on page 124

[Stuhl et al. 2015] B. K. Stuhl, H.-I. Lu, L. M. Aycock, D. Genkina & I. B. Spielman; "Visualizing edge states with an atomic Bose gas in the quantum Hall regime"; Science **349**, pp. 1514–1518 (2015). Cited on page 127

[Subhankar et al. 2019] S. Subhankar, Y. Wang, T.-C. Tsui, S. L. Rolston & J. V. Porto; "Nanoscale Atomic Density Microscopy"; Phys. Rev. X **9**, p. 021002 (2019). Cited on page 82

[Syassen et al. 2008] N. Syassen, D. M. Bauer, M. Lettner, T. Volz, D. Dietze, J. J. García-Ripoll, J. I. Cirac, G. Rempe & S. Dürr; "Strong Dissipation Inhibits Losses and Induces Correlations in Cold Molecular Gases"; Science **320**, pp. 1329–1331 (2008). 2 citations on pages 3 and 52

[Teichmann et al. 2009] N. Teichmann, D. Hinrichs, M. Holthaus & A. Eckardt; "Process-chain approach to the Bose-Hubbard model: Ground-state properties and phase diagram"; Phys. Rev. B **79**, p. 224515 (2009). Cited on page 33

[Tomonaga 1950] S.-i. Tomonaga; "Remarks on Bloch's Method of Sound Waves applied to Many-Fermion Problems"; Progress of Theoretical Physics **5**, pp. 544–569 (1950). Cited on page 36

[Trebbia et al. 2006] J.-B. Trebbia, J. Esteve, C. I. Westbrook & I. Bouchoule; "Experimental Evidence for the Breakdown of a Hartree-Fock Approach in a Weakly Interacting Bose Gas"; Phys. Rev. Lett. **97**, p. 250403 (2006). Cited on page 36

[Vassen et al. 2012] W. Vassen, C. Cohen-Tannoudji, M. Leduc, D. Boiron, C. I. Westbrook, A. Truscott, K. Baldwin, G. Birkl, P. Cancio & M. Trippenbach; "Cold and trapped metastable noble gases"; Rev. Mod. Phys. **84**, pp. 175–210 (2012). Cited on page 1

[Villain 2021] T. Villain; "M2 internship report: High-resolution imaging of ytterbium atoms in a two-dimensional optical lattice"; E.N.S. de Lyon (2021). 2 citations on pages 83 and 84

[Ville et al. 2017] J. L. Ville, T. Bienaimé, R. Saint-Jalm, L. Corman, M. Aidelsburger, L. Chomaz, K. Kleinlein, D. Perconte, S. Nascimbène, J. Dalibard & J. Beugnon; "Loading and compression of a single two-dimensional Bose gas in an optical accordion"; Phys. Rev. A **95**, p. 013632 (2017). Cited on page 82

[Weimer et al. 2021] H. Weimer, A. Kshetrimayum & R. Orús; "Simulation methods for open quantum many-body systems"; Rev. Mod. Phys. **93**, p. 015008 (2021). Cited on page 3

[Weitenberg et al. 2021] C. Weitenberg & J. Simonet; "Tailoring quantum gases by Floquet engineering"; Nat. Phys. **17**, pp. 1342–1348 (2021). Cited on page 103

[Wiersma et al. 1997] D. S. Wiersma, P. Bartolini, A. Lagendijk & R. Righini; "Localization of light in a disordered medium"; Nature **390**, pp. 671–673 (1997). Cited on page 124

[Yefsah et al. 2011] T. Yefsah, R. Desbuquois, L. Chomaz, K. J. Günter & J. Dalibard; "Exploring the Thermodynamics of a Two-Dimensional Bose Gas"; Phys. Rev. Lett. **107**, p. 130401 (2011). 5 citations on pages 98, 99, 111, 120, and 143

[Zakrzewski et al. 2008] J. Zakrzewski & D. Delande; "Accurate determination of the superfluid-insulator transition in the one-dimensional Bose-Hubbard model"; AIP Conference Proceedings **1076**, pp. 292–300 (2008). Cited on page 33

[Zwerger 2003] W. Zwerger; "Mott–Hubbard transition of cold atoms in optical lattices"; Journal of Optics B: Quantum and Semiclassical Optics **5**, p. S9 (2003). 2 citations on pages 17 and 33